PROCEEDINGS

The Institution of Engineers (India)

99 Years of Relentless Journey towards Engineering Advancement for Nation Building

Thirty-third National Convention of Aerospace Engineers and National Conference on

"Emerging Technologies in Aerospace Structures, Materials and Propulsion Systems"

ISBN No. : 978-81-942561-9-9

Organised by

The Institution of Engineers (India)

Pune Local Centre

Under the Aegis of

Aerospace Engineering Division Board, IEI

Edited by : Hon. Secretary, Pune Local Centre

November 16-17, 2019
Pune

The Institution of Engineers (India),

Pune Local Centre

1332, Shivaji Nagar, J.M.Road, , Pune - 411 005.

Tel.: 020-25533376 / 25520239.

Email: punelc@ieindia.org

The Institution of Engineers (India)

99 Years of Relentless Journey towards Engineering Advancement for Nation Building

Thirty-third National Convention of Aerospace Engineers
and
National Conference on

"Emerging Technologies in Aerospace Structures, Materials and Propulsion Systems"

November 16-17, 2019
Pune

PROCEEDINGS

ISBN No. : 978-81-942561-9-9

Under the Aegis of

Aerospace Engineering Division Board, IEI

Organised by

The Institution of Engineers (India)
Pune Local Centre

In association with

Defence Institute of Technology (DIAT), Pune
&
ASM International, Pune Chapter

index

SN	TITLE OF PAPER	Page
	Propulsion System	
1	A Comparative Study on the Generation of Flame Structure During Burning of Sooting and Non-Sooting Liquid Fuels *Abhinandan Singh and Ajay V. Singh*	**1**
2	Performance Evaluation of Boron Particles with Wax–HTPB-Based Solid Fuels For the Primary Combustor in Ducted Rocket Applications *Srinibas Karmakar, Arnab Roy,and Shifa Sheikh*	**7**
3	Sensitizing Gaseous Mixtures for Practical Applications in RDEs *D. Santosh Kumar and Ajay V. Singh*	**14**
4	Sensitising Ethylene-Air and Ethylene-Oxygen for Optimal Performance of Detonation Cycle Engines *Kiran Ivin and Ajay V.Singh*	**20**
5	Study the Effect of Axi-swirl Injector on the Regression Rate of the Hybrid Rocket *Pragya and Shelly Biswas*	**27**
6	CFD Analysis of Convergent-Divergent Jet Nozzle of a Fighter Aircraft Gas Turbine Engine *Ved Prakash,Sunil Chandel and R K Mishra*	**32**
7	Turbulent Boundary Layer Combustion in a Free Convective Environment *Akash Malaviya, Abhinandan Singh and Ajay V.Singh*	**36**
8	Turbulent fuel-air mixing investigations within a cavity based hydrogen inoculated scramjet combustor *Kodamasimham Bharadwajan and DP Mishra*	**42**
	Airships	
9	Design and Fabrication of a High Endurance, Cost-Effective, Auto-Stabilised Airship *Sohan Suvarna, Amogh S.Joshi, Avinash Dubey and Rajkumar S.Pant*	**52**
10	Design And Fabrication Of An Indoor Tethered Aerostat System *M.Suhel U Karkun Aashna Seth, Raman Verma and Raj kumar S. Pant*	**57**
11	Design And Fabrication Of Pluto-X Controlled Indoor Non rigid Airship *Saumya Sarawagi,Krishnakant Zope,Shreyas Sivan and Avneet Singh*	**64**
12	Design of Winching System for Tethered Aerostat *Saurabh Verma, Avesh Cheulkar Rajkumar S Pant*	**68**
13	A Generic Approach For Geometry Generation Of Multi-Lobed Airship Envelopes *Abhishek Kumar Shanklesha, Manikandan Murugaiah and Rajkumar S. Pant*	**78**
14	Hybrid Airship: More of a Faster Ship, Than a Slower Aircraft *Saurabh V Bagare*	**82**
	Materials & Miscellaneous	
15	Study of the Mechanical Properties of an Additively Manufactured IN718 Submitted to Tensile Tests *Mahesh Naik and Dr D G Thakur*	**88**
16	Topology optimization of aircraft fuselage wing lug bracket attachment *Akshay S and Dr D G Thakur*	**92**
17	System Engineering For Electrical Integration In Aerospace Industries: An Overview *Uttam G Salawade*	**97**
18	Design and Analysis of Parachutes using PARAZ Software *Aniket Antre, Sumit Jana andBasant Gupta*	**103**

A Comparative Study on the Generation of Flame Structure During Burning of Sooting and Non-Sooting Liquid Fuels

Abhinandan Singh[1], Graduate Student, IIT Kanpur and Ajay V. Singh[2], Assistant Professor, IIT Kanpur

***Abstract* – A detailed numerical study is conducted on square-shaped pool fires burning ethanol (non-sooting) and n-heptane (sooting). The difference in the flame behavior due to the sharply varying sooting propensity of the two fuels is analyzed by plotting temperature, velocity and soot volume fraction along the centerline. Also, to understand the influence of turbulence, two different pool sizes (10cm x 10cm and 25cm x 25cm) are studied and a comparison is presented. To understand the difference in turbulent behavior of ethanol and heptane, auto spectral density for 10cm x 10cm pool fires is plotted at three different locations along the flow.**

***Index Terms* – Pool Fire; Soot; Turbulence; Radiation; Auto spectral Density**

1. INTRODUCTION

Mankind is in many ways reliant on fire for its energy requirements. Fire under controlled conditions is used domestically, industrially and even for recreational activities, but if it is not administered meticulously it can become diabolical leading to a substantial loss of both life and property. These uncontrolled fires usually start at a very small scale and is sometimes initiated by a small spark which seems to be inconsequential. This small fire can quickly become an inferno if not encumbered at the right time. Numerous methods have been developed to control such a fire, but to estimate the right location and time to utilize a fire-suppressant with highest efficiency is still a thought to ponder upon.

Any fire, whatever the scale, requires air and fuel for the formation along with heat and mass transfer for its sustenance and growth. Most of the commonly occurring fires have an accompanying visible flame which radiates (convection or conduction can be dominating depending upon the scale) heat to the surroundings(outwards) and unburnt fuel(inwards). This inward heat transfer helps in sustaining the flame as it heats up the incoming fuel to its fire point. For most cases combustion occurs in gas phase, so the conversion of solid or liquid fuels in their respective gaseous forms becomes an essential process. This inward heat flow also assists in pyrolysis and evaporation of solid and liquid fuel producing gaseous products which combine/react with oxidizer to form the flame. This reaction can occur in two ways, either the fuel and oxidizer combine before reaching the flame (premixed flame), or they combine right at the flame (diffusion flame); latter flame in buoyant conditions will be the main focus of this paper.

A diffusion flame can occur in various orientations - Wall fire, Ceiling fire or Pool fire. The orientation as well as the size of the fuel surface have a strong effect on the flame structure and spread rate. As the name suggests - a wall fire is the one where fuel is kept vertical, ceiling fire has a downward facing fuel-orientation and a pool fire has an upward facing fuel-orientation. In each case buoyancy and gravity play a vital role; but under forced flow conditions, inertia forces produced by the air current strongly affect the flame structure and flame spread. In this study we focus our attention towards flames with horizontal fuel surface, i.e. Pool fires.

A medium scale pool fire is inherently turbulent[1] with fluctuations emanating from the base/fuel surface and extended to the tip of the flame. These fluctuations encounter a necking region during their movement, where along with air entrainment they lead to bifurcation of the flame. The separated flame tends to move farther than the main flame, leading to an increase in the average flame height. A major ramification of

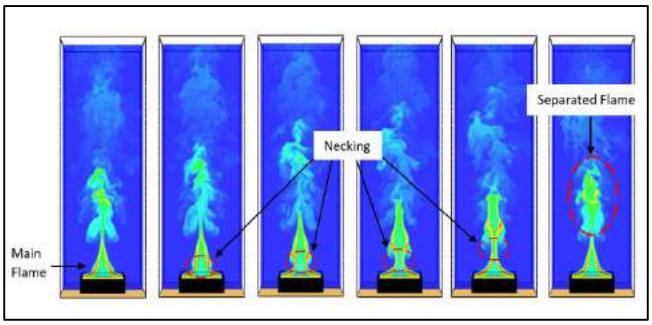

Fig. 1: Process of flame bifurcation as seen in a 10cm x 10cm ethanol pool fire.

fluctuations initiated at the fuel surface is *puffing phenomena*. This occurs in almost every fire irrespective of its scale or orientation, meaning it could help decipher many unknown features of pool fire, which can be generalized for different orientations just by taking into account the difference in the buoyant and inertia forces. This puffing phenomenon is characterized by flame bifurcation which is easily observed in the visible flame. It is, as the name suggests

[1] Abhinandan Singh is a student of MS by Research in the Department of Aerospace Engineering, IIT Kanpur
Email: abisingh@iitk.ac.in

[2] Ajay V. Singh is an Assistant Professor in the Department of Aerospace Engineering, IIT Kanpur
Email: ajayvs@iitk.ac.in

a break-up of flame into two, namely: main flame and separated flame. This bifurcation of flame plays an important role in determining the rate at which flame will spread. For example, when a pool fire is subjected to a cross-air flow it tends to behave more like a boundary layer flame; this flame structure, as mentioned earlier, is also prone to puffing phenomena which would ultimately cause a bifurcation of the flame. The separated flame flows farther than the main flame, engulfing more spatial region and increasing the rate at which flame spreads. This kind of flame is very common in wildfires, industrial fires and to be able to control such an obstreperous flame, a detailed understanding of flame spread is vital, which makes turbulence study for different fuel types a necessity.

Figure 1 which represents the temperature distribution in an ethanol pool fire shows the bifurcation of flame. This bifurcation is initiated near the fuel surface in the form of neck-in(necking) region. This region moves along the flame, concurrently intensifying and reducing the flame width. It is experimentally observed that large air entrainment occurs at the visible flame tip (about 10 times the stoichiometric mass requirement), it can be theorized that this strong mass flow which occurs radially to the flame surface appears to pinch the flame, producing separated flame. Since air entrainment itself depends upon different parameters for a turbulent fire [2], flame bifurcation should at least be a function of these parameters.

A detailed review presented by P. Joulain [3],[4] provides a detailed insights about the variation of various properties in buoyant plumes, in particular pool fires. Recent studies[5],[6] on the soot behavior of jet flames shows the variation of soot along the fuel surface and its influence on the flame behavior and radiation. This study can be continued further to study the effect of soot volume fraction on radiative heat transfer to the surroundings. Classical studies [7],[8],[9] about soot generation in buoyant flames suggest a strong effect of soot on radiative transfer by the flame.

2. Computational

2.1. Governing Equations

Numerical study of liquid-pool fires (ethanol and heptane) in an open atmosphere is conducted using Fire Dynamics Simulator (FDS), which is a widely used Computational Fluid Dynamics (CFD) code developed by National Institute of Standards and Technology (NIST). It is specifically designed to cater to the study of buoyancy-driven low Mach number (incompressible) flows in a high heat release or combusting environment. It can be used to perform both LES (Large Eddy Simulation) and DNS (Direct Numerical Simulation) to study the effect of turbulence on the flow field; the present study utilizes LES which makes it cheaper in terms of computational cost when compared with DNS.

A large eddy simulation utilizes discretized governing equations - mass, momentum, energy and species - passed through a low pass filter to filter out small scale eddies. The equations are numerically solved up to the filter width but require semi-empirical turbulence models to include the effect of small-scale eddies. These turbulence models, also known as sub-grid scale (SGS) models, are used to furnish the value of turbulent viscosity ultimately leading to the closure of each governing equation. FDS provides an eclectic mix of SGS models to solve the closure problem. Appropriate model was selected depending upon the fuel, physical parameters, and the details are presented in further sub-sections [10]. The general form of governing equations for a chemically reacting flow, with N participating species, in conservation form are stated below:

A. Mass Conservation:

$$\frac{\partial \rho}{\partial t} + \nabla \cdot (\rho \mathbf{v}) = 0 \tag{1}$$

B. Momentum Conservation:

$$\frac{\partial \rho \mathbf{v}}{\partial t} + \nabla \cdot (\rho \mathbf{v} \times \mathbf{v}) = -\nabla p + \nabla \cdot \tau + \rho \sum_{i=1}^{N} Y_i f_i \tag{2}$$

C. Energy Conservation:

$$\rho \frac{\partial \rho e_t}{\partial t} + \nabla \cdot \{(\rho e_t + p)\mathbf{v}\} = -\nabla . \mathbf{q} + \nabla \cdot (\tau \cdot \mathbf{v}) + \rho \sum_{i=1}^{N} Y_i \mathbf{f}_i \cdot \mathbf{v} + \sum_{i=1}^{N} \mathbf{f}_i \cdot \mathbf{j}_i \tag{3}$$

$$e_t = h - \frac{p}{\rho} + \frac{1}{2}\mathbf{v} \cdot \mathbf{v} \tag{4}$$

D. Species Conservation:

$$\frac{\partial \rho Y_i}{\partial t} + \nabla \cdot (\rho Y_i \mathbf{v}) = -\nabla \cdot \mathbf{j}_i + w_i \tag{5}$$

E. Equation of State:

$$p = \rho R T M^{-1} \tag{6}$$

where,

$$M = \left(\sum_{i=1}^{N} \frac{Y_i}{M_i}\right)^{-1} \tag{7}$$

In FDS, the above-mentioned equations are discretized using finite difference method and solved for a computational domain broken into a myriad of square shaped grids. FDS employs uniform, structured and staggered mesh structure, meaning scalar, 1st-order tensor and 2nd-order tensor are assigned to body-center, face-center(s) and edge(s) of grid, respectively.

2.2. Hydrodynamic Model

Pool fires of medium size(>=7cm) are inherently turbulent, so it is cardinal to include a turbulent study to understand the nature of flow. As it has been previously mentioned, present study focuses on Large Eddy Simulation of square shaped liquid pool fires of two different sizes i.e. 10cm x 10cm and 25cm x 25cm,

which fall in the range of medium-scale pool fires. For each fuel, simulation is conducted for three different grid sizes (4mm, 2mm, 1mm) to corroborate that the results are grid-independent. It can be clearly observed in figure 1 that the burning rate for ethanol pool fire becomes grid-independent at a grid size of 2mm.

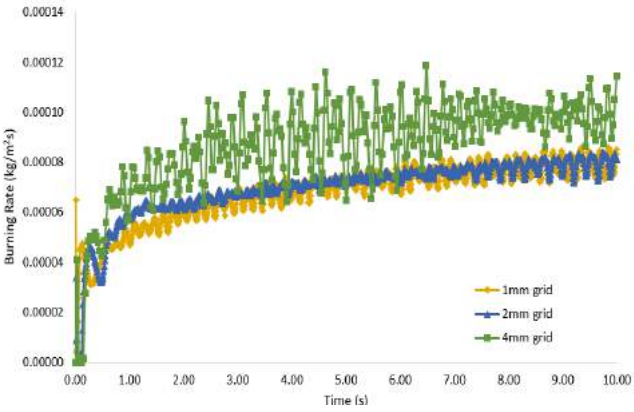

Fig. 2: Mass burning rate measurements for three different grid sizes - 4mm, 2mm and 1mm show grid independence is achieved after 2mm.

LES turbulence model used in this study is **Deardorff's Model** which uses the following equation to calculate the value of turbulent viscosity[10],

$$\mu_t = \rho C_v \Delta \sqrt{k_{sgs}} \tag{8}$$

$$k_{sgs} = 0.5((\bar{u} - \hat{\bar{u}})^2 + (\bar{v} - \hat{\bar{v}})^2 + (\bar{w} - \hat{\bar{w}})^2) \tag{9}$$

where μ_t is the turbulent viscosity, ρ is the density, C_v is a model constant with a value of 0.1, $\Delta = (\delta x \delta y \delta z)^{1/3}$ is the filter width, $\bar{u}$ is the average value of velocity at the cell center and $\hat{\bar{u}}$ is a weighted average of u over the adjacent cells.
For validation of numerical results, average mass loss rate data of ethanol and heptane pools has been compared with the experiments conducted by the author using baked super-wool wicks soaked with liquid fuels. Both the data are in good agreement with a maximum percentage error of 16%.

2.3. Pyrolysis Model

Fuel burning rate is the major governing parameter for flame spread and is directly influenced by the pyrolysis/evaporation model used. This model is a function of liquid fuel temperature and fuel vapor concentration above the fuel surface. These controlling parameters themselves depend upon the heat transfer from the flame - making it a closed-loop mechanism. For simplicity, convection within the liquid fuel is neglected by assuming it to be a thermally-thick solid fuel where only conduction occurs. Radiation heat transfer from the flame is taken into account at the fuel surface and in many cases plays a critical role to determine the fuel burning rate. Pyrolysis model for a solid fuel is comparatively complex and is not a part of present study.

2.4. Combustion Model

In the combustion model, it is assumed that chemical reactions occur at an infinitely fast rate making mixing (of fuel and oxidizer) the controlling parameter. Since combustion is mixing-controlled, it is convenient to define species in terms of mixture fraction(Z), a conserved scalar. Reaction between Fuel and Oxygen occurs along an infinitely thin sheet of flame (because of infinitely fast reaction) where Z takes up its stoichiometric value determined by the solution of transport equation for Z. Heat Release Rate (HRR) per unit flame area is given by [11]:

$$\dot{q}''_C = \Delta H_O (\rho D) \nabla Z \cdot \mathbf{n} \frac{dY_O}{dZ}|_{Z<Z_f} \tag{10}$$

where, ΔH_O is the energy released per unit Oxygen consumed which is almost constant for a wide variety of fuels , n is the unit vector normal (facing outward) to the fuel surface.

2.5. Radiation Model

The radiative transport equation (RTE) for a non-scattering gas can be written as [10]:

$$s \cdot \nabla I_\lambda(x,s) = \kappa_\lambda(x)[I_b(x) - I_\lambda(x,s)] \tag{11}$$

where $I_\lambda(x,s)$ is radiation intensity at λ wavelength, **s** is unit normal direction vector, κ_λ is spectral absorption coefficient and $I_b(x)$ is the source term obtained from the Planck function. For a fuel with low soot yield, it becomes necessary to break the radiation spectrum into a small number of bands, N. The band specific RTE's can be written as:

$$s \cdot \nabla I_n(x,s) = \kappa_n(x)[I_{b,n}(x) - I_n(x,s)] \tag{12}$$

where, n = 1,2,3, …..N, I_n is the intensity integrated over the band n and κ_n is the appropriate mean absorption coefficient. The source can be written as [11]:

$$I_{b,n}(x) = F_n(\lambda_{min} - \lambda_{max})\sigma T(x)^4 \tag{13}$$

Even for a small number of bands, the solution for RTE's is computationally and temporally demanding but to obtain high-fidelity results for radiative behavior wide band model becomes inevitable.

2.6. Boundary Conditions

Square shaped pools of side length 10cm and 25cm are kept flush with the bottom surface with zero lip height. The domain size is different for both the fuel sizes; 10cm pool fire has a domain of dimension 12cmx12cmx60cm and 25cm pool fire has a domain size of 27cmx27cmx100cm.The simulation is conducted in a domain closed at the bottom with other five faces open to the atmosphere and maintained at 298.15K and 101325Pa.

3. Results and Discussion

3.1. Mean Centerline Variation

Mean variation of temperature and soot volume fraction along the centerline are presented in figure 3. The variation is presented for four different cases to understand the fuel and pool scale effect. A peak in the temperature profile is present after a certain distance from the fuel surface because of the presence of the flame, this trend is seen in all the four cases. Another common trend is seen in the soot volume fraction

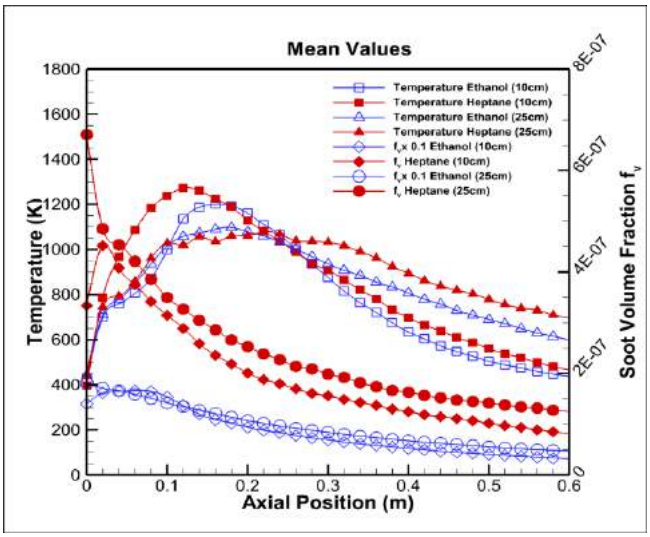

Fig. 3: Mean temperature and soot volume fraction centreline profile for four different pool fires.

profiles which attain a high at the fuel surface because of strong thermophoretic forces pushing the soot particles away from the flame and towards the fuel surface.

To understand the influence of fuel on the flame behavior, same sized pool is compared for both the fuels. The 10cm x 10cm heptane and ethanol temperature profiles show that they both follow a very similar trend with heptane having a higher peak than ethanol. Also, the rise of temperature for heptane is stepper with a slow decent after attaining the peak when compared with ethanol. This trend can be understood by comparing the soot volume fraction profiles of heptane and ethanol. As heptane has a high sooting propensity, the value of soot volume fraction for heptane is greater by an order of magnitude than ethanol. This difference increases the heat trapped within the heptane flame as soot is the major source and sink of heat in any flame, further leading to a higher and steeper temperature rise along the centerline.

This steep rise is not seen in the 25cm x 25cm heptane pool but the trend is very similar for both the fuels. This difference is because of the change in the size of pool. As pool size increases, heat losses to the atmosphere increase. These increased losses lead to a lower peak temperature for both the fuels. Also, for the bigger pool, a prominent peak cannot be seen but a flat high-temperature curve is observed. This suggests that the flame bifurcation does not occur at one particular location but it changes for different cycles. In some cases, flame bifurcation would occur at a distance of 0.1m while in other cases the flame would be stretched to a distance of 0.3m (from the fuel surface) before generating the separated flame.

Figure 4 shows the variation of lateral and axial velocity along the centerline. Lateral velocity is zero at the fuel surface due to the no-slip condition whereas away from the fuel surface it attains negative and positive values depending upon air entrainment. On comparing the axial velocity profiles, the behavioral difference obtained due to the pool scale is clearly seen. The axial velocity drops sharply for the 10cm x 10cm pool fire for both the fuels whereas the 25cm x 25cm pool fire does not show any dip up to 0.6m. This is because the larger pool has a longer flame and these longer flames have a strong flow along the axial direction. The plots are presented up to 0.6m only for comparison but the simulation domain is kept at 1m for 25cm x 25cm pool. A dip in the axial velocity is seen at around 0.8m for both the fuels for 25cm x 25cm pool. It is also seen that axial velocity values are not strongly affected by the fuel's sooting propensity.

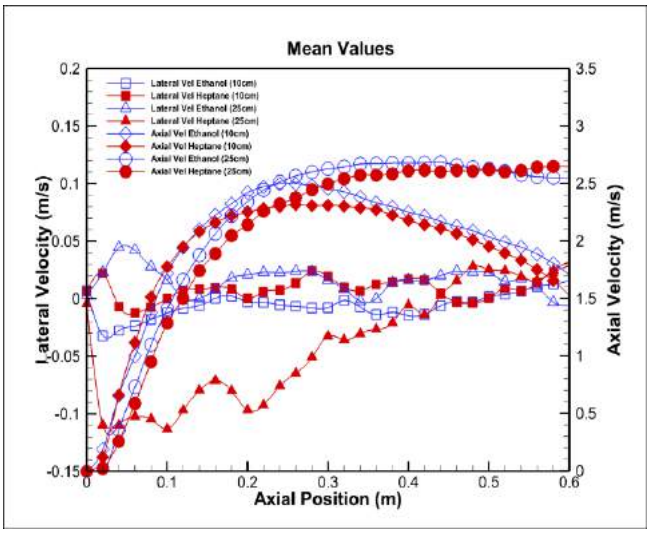

Fig. 4: Mean lateral and axial velocity centreline profile for four different pool fires.

3.2. RMS Variation along the centerline

Figure 5 shows the RMS variation of temperature and soot volume fraction for four different pool fires. Trends are similar for both the fuels for a constant size of the pool fire but the magnitude varies due the change in fuel. It can be seen that throughout the flow domain, heptane shows stronger fluctuations when compared to ethanol and the same behavior is seen for soot volume fraction. Since, temperature directly controls soot oxidation RMS soot volume fraction follows a similar trend to the RMS temperature variation. The pool scale

increases the RMS values for both the fuels meaning that turbulence increases with the pool size.

A similar scale effect can be seen in figure 6 for RMS values of lateral and axial velocities. It can also be seen that the lateral velocity has lower RMS values than the axial velocity suggesting that turbulence effects are weak in the lateral direction whereas stronger along the axial. Heptane again shows a stronger turbulent

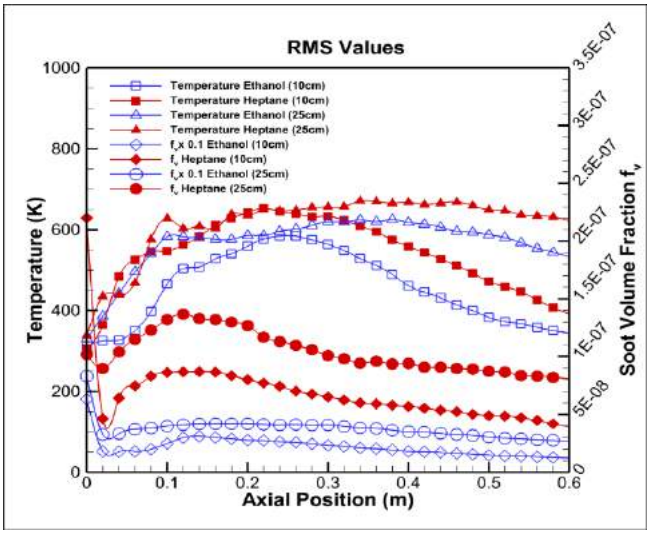

Fig. 6: RMS profiles of temperature and soot volume fraction along the centreline for four different pool fires.

behavior than ethanol.

3.3. Auto-spectral Density at various locations

The auto-spectral density values are calculated for lateral velocity (u) and axial velocity (w) at three different locations, i.e. 0cm, 20cm and 40cm from the fuel surface along the centerline. The values are plotted against frequency in a loglog curve for 10cm x 10cm pool fire using both ethanol and heptane. These plots

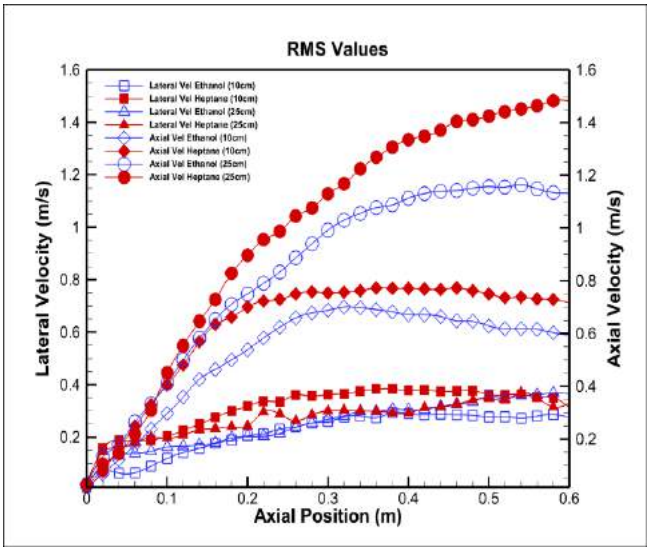

Fig. 5: RMS profiles of lateral and axial velocity along the centreline for four different profiles.

help identify the prominent frequency at which the flame fluctuates and the different locations show which region has the strongest fluctuation and how this fluctuation dies down along the flow.

Comparing the auto-spectral density of ethanol and heptane at Z=0 cm, we see that ethanol develops a peak with a very small magnitude whereas heptane does not have a peak. This shows that for ethanol, fluctuations in the lateral and axial velocity are generated at a frequency of around 6Hz and 9Hz at the fuel surface whereas heptane does not have any prominent fluctuations. On moving away from the fuel surface we observe a stronger peak for both the fuels and it can be seen in the second column of figures 7 and 8 showing the auto-spectral density variation at Z = 20cm. This peak is prominent for axial velocity at around 6Hz for both the fuels with heptane having a higher magnitude than ethanol. The 9Hz peak observed in ethanol at surface dies down at Z = 20cm for both the velocities. Moreover, there are no prominent peaks for lateral velocity.

At Z = 40cm peaks are observed at the same frequency for both the fuels as the ones observed at Z = 20cm. The magnitude of peak sees a decrease with ethanol showing a stronger decrease than heptane.

4. Conclusions

This study focuses on the turbulent behavior in a medium scale pool fire and the effect turbulence generates on the flame structure. Flame bifurcation is conceptualized and the cyclic variation with the generated necking is presented. On comparing the two fuels, namely ethanol and heptane it can be concluded that the soot generated by heptane is 10 times more than soot generation in ethanol by volume. This higher soot volume fraction leads to a steeper temperature rise and higher peak temperatures in heptane. It is also shown that with the size of the pool soot generation increases but the steeper rise is not seen in heptane because of higher heat loss to the surroundings.

RMS profiles are also compared for all the four cases which show that heptane has higher fluctuations as compared to ethanol and these fluctuations increase as the pool size increases. A similar conclusion about turbulent behavior is seen from the auto-spectral density plots.

5. Acknowledgment

The authors would like to thank High Performance Computing Facility of Indian Institute of Technology Kanpur for providing the necessary hardware for CFD simulations. This work is supported by the Startup Research Grant of Indian Institute of Technology Kanpur.

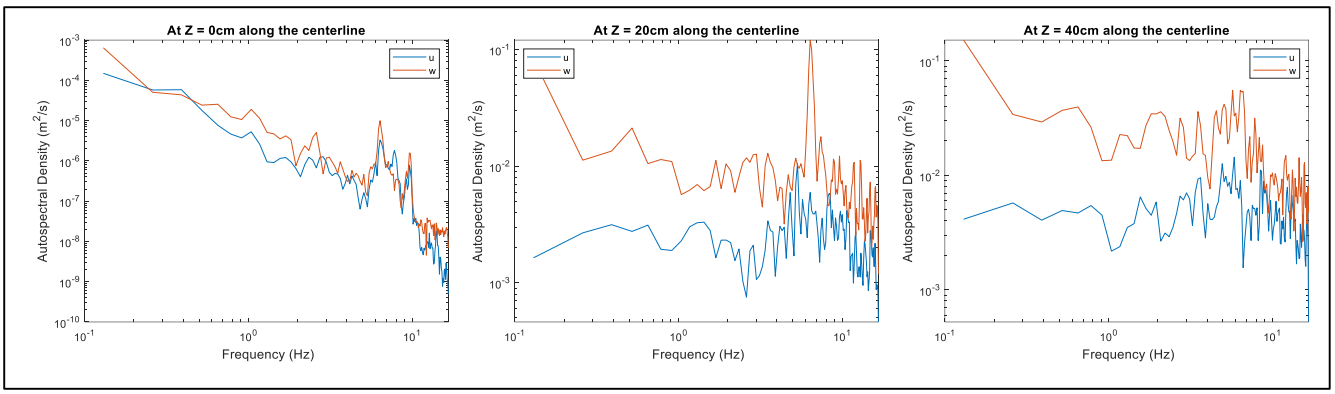

Fig. 8: Auto-spectral density for lateral velocity (u) and axial velocity (w) for ethanol 10cm x 10cm pool fire at Z = 0cm, Z = 20cm and Z = 40cm.

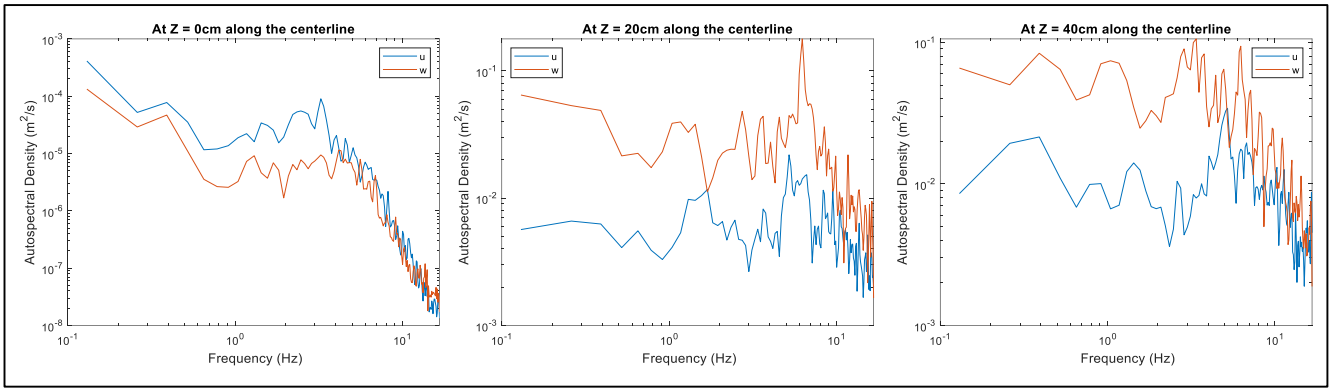

Fig. 7: Auto-spectral density for lateral velocity (u) and axial velocity (w) for ethanol 10cm x 10cm pool fire at Z = 0cm, Z = 20cm and Z = 40cm.

6. References

[1] E. J. Weckman, A. B. Strong, "Experimental investigation of the turbulence structure of medium-scale methanol pool fires," *Combust. Flame*, vol. 105, no. 3, pp. 245–266, 2002.

[2] M. A. Delichatsios, "Air entrainment into buoyant jet flames and pool fires," *Combust. Flame*, vol. 70, no. 1, pp. 33–46, 1987.

[3] P. Joulain, B. P. Te, "The behavior of pool fires: state of the art and new insights," pp. 2691–2706, 1998.

[4] P. Joulain, "Convective and radiative transport in pool and wall fires: 20 years of research in Poitiers," *Fire Saf. J.*, vol. 26, no. 2, pp. 99–149, 1996.

[5] F. Nmira, J. L. Consalvi, M. A. Delichatsios, "Radiant fraction from sooting jet fires," *Combust. Flame*, vol. 208, pp. 51–62, 2019.

[6] F. Nmira, D. Burot, J. L. Consalvi, "Soot emission radiation–turbulence interactions in diffusion jet flames," *Combust. Sci. Technol.*, vol. 191, no. 1, pp. 126–136, 2019.

[7] J. De Ris, "Fire radiation—a review," *Symp. Combust.*, 1979.

[8] A. T. Modak, "Thermal radiation from pool fires," *Combust. Flame*, vol. 29, no. C, pp. 177–192, 1977.

[9] A. T. Modak, "Radiation from products of combustion," *Fire Saf. J.*, vol. 1, no. 6, pp. 339–361, 1979.

[10] K. McGrattan, S. Hostikka, R. McDermott, J. Floyd, C. Weinschenk, K. Overholt, "Fire Dynamics Simulator Technical Reference Guide Volume 1: Mathematical Model (Sixth Edition)," *NIST Spec. Publ. 1018*, vol. 1, 2015.

[11] S. Hostikka, K. B. McGrattan, A. Hamins, "Numerical modeling of pool fires using les and Finite Volume Method for radiation," *Fire Saf. Sci.*, vol. M, pp. 383–394, 2003.

Performance Evaluation of Boron Particles with Wax–HTPB-Based Solid Fuel for the Primary Combustor in Ducted Rocket Applications

1. Syed Alay Hashim, Member, *IEI*, 2. Srinibas Karmakar, 3. Arnab Roy, 4. Shifa Imtiaz Shaikh

***Abstract*-- From past several decades opposed flow burner (OFB) has been considered a cost-effective as well as a rapid screening instrument for the evaluation of solid fuels. The present investigation deals with boron particles impregnated with wax and HTPB mixture which work as a binder and fuel as well. Boron is known as a high energy material on both volumetric and gravimetric basis, therefore its presence in solid fuel might be useful as an ingredient in the application of ducted rocket (DR)/ramjet. Although due to the formation of boron oxide (B_2O_3) on the surface of boron particles, boron has certain problems during its ignition and combustion. These complications open a way of research worldwide on boron to understand the combustion performance and energy release. In the present investigation, a total of four solid fuel samples are processed which include pure-HTPB, wax with HTPB, boron with HTPB, and boron with mixture of wax and HTPB. The content of wax and boron is 10% each in the sample and the remaining is HTPB. In this investigation, OFB is connected with gaseous oxygen (GOX) supply line for impinging oxygen jet on the top surface of the solid fuel pellet. The range of oxygen mass flux has been varied from 20-57 kg/m^2-s. The present study includes material characterization (FE-SEM, EDX, XRD, and TGA) of ingredients and regression rate of solid fuel samples. It is presumed that the current investigation on boron-based solid fuel would become an economical as well as strong guideline for the fuel selection of a lab-scale rocket motor for the preliminary investigation in ducted rocket/ramjet.**

***Keywords*: Boron; Wax; HTPB; Solid fuel; Regression rate; Ducted rocket/Ramjet.**

1. Dr. Syed Alay Hashim, Associate Professor, Department of Aerospace Engineering, Sandip University, Nashik, India. (e-mail: aviator123hash@gmail.com).
2. Dr. Srinibas Karmakar, Associate Professor, Department of Aerospace Engineering, Indian Institute of Technology Kharagpur, India. (e-mail: skarmakar@aero.iitkgp.ac.in).
3. Dr. Arnab Roy, Associate Professor, Department of Aerospace Engineering, Indian Institute of Technology Kharagpur, India. (e-mail: arnab@aero.iitkgp.ac.in).
4. Miss. Shifa Sheikh, B. Tech student, Department of Aerospace Engineering, Sandip University, Nashik, India. (e-mail: shaikhshifa2000@gmail.com).

1. INTRODUCTION

DESIGN level modifications in ramjet produce a modern and more effective propulsive device which is recommended for missile applications. Essentially, this design is named as ducted rocket (DR). Ducted rockets work with two combustors: primary and secondary. In the existing DR, combustion of working substance (solid fuel or propellant) is commenced first in primary combustor followed by secondary with the help of atmospheric (energized) ducted air (as shown in Fig. 1a) [1], [2]. Various hydroxyl-terminated polybutadiene (HTPB) based metalized solid fuels/propellants have been experimented in solid fuel ducted rockets (SFDR). Previous research on DRs explores mainly the presence and benefits of Al, Mg, Ti, and B in the fuel. Although, for DR applications boron-based fuel combinations have been highly appreciated, it is mainly due to its burning nature and high energy density [2], [4], [5], [6], [7]. Boron has problem during its ignition and combustion, hence, for the stabilized performance in DR, boron-based solid fuels have been investigated for its full implementation over past several years [2], [4], [5], [6], [7]. Actually, boron is prone to react with oxygen (O_2) and whenever boron comes in contact with O_2 forms boron oxide (B_2O_3). In this way, B_2O_3 covers boron and acted as a protective layer. As a result, B_2O_3 prevents/restricts boron's ignition and combustion [8], [9].

The solid fuel grain must possess adequate structural integrity so that it can be placed in the combustion chamber. In order to provide mechanical strength, the powder fuel or additive requires a binder. Most of the binders used in rockets are hydrocarbon fuels; therefore, they not only provide strength but also liberate energy on combustion. Among them, paraffin-wax (nonpolymeric) and HTPB (polymeric) are widely used in rocket and ramjet applications. Previous study reveals that paraffin-wax provides better fuel burning rates than HTPB but HTPB has better structural integrity than paraffin-wax [10]. To avail both the benefits, the fuel in the present study is processed on mixing powder-wax

with HTPB. In this context, significant research has been conducted so far to improve mechanical properties by mixing polymers and other additives to paraffin-wax. It is also found that most thermoplastics increase the viscosity and surface tension of the liquid melt layer. Therefore, the entrainment rate decreases but combustion efficiency of fuel increases. Sisi and Gany [11] studied a solid fuel having paraffin-wax and HTPB mixture (1:1). As compared to pure paraffin-wax the regression rate reduces around 50% with gaseous oxygen (GOX) and 60% with N_2O respectively. In another study, paraffin-wax and HTPB as baseline fuel are mixed with $LiAlH_4$ and MgH_4 [12]. It has been found that regression rates decrease for both the additives compared to their baseline (wax-HTPB) but higher (~350-475%) than the conventional HTPB-based hybrid fuel.

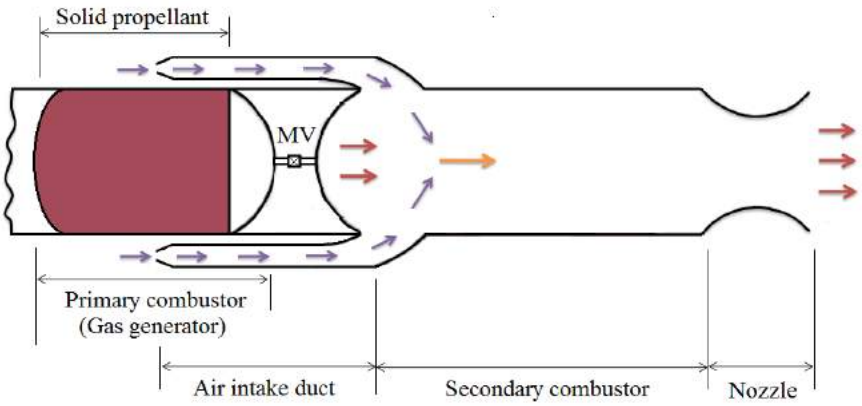

a. Solid fuel ducted rocket (SFDR) [2]

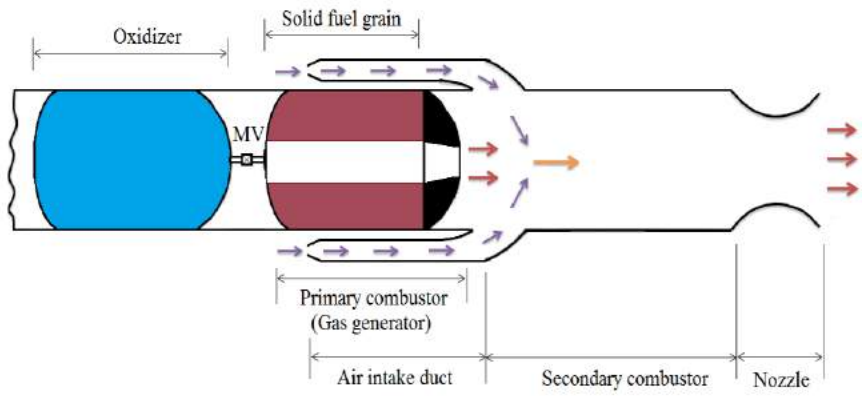

b. Hybrid fuel ducted rocket [13]

Fig. 1: Conceptual designs of ducted rocket (DR)

Among various performance evaluating tools, generally small-scale rocket test bed has been used for solid fuel investigations prier to use in rocket motor/gas generator. However, costly ingredients to solid fuels need more economical system before investigation even in a small scale rocket motor [10]. Nano and micro size metalized additives used in solid fuels are expansive and may not readily available; therefore, a more economical tool can be used. In previous literatures, a small-scale instrument called opposed flow burner (OFB) system has been used extensively to screen the performance of the solid fuels [10], [14], [15], [16], [17]. OFB is not only a low cost but also a rapid data collecting instrument. The concept of OFB is existing in literature since 1950s and it is analogous to a strand burner system [14], [15], [16], [17].

The primary objective of the present study is to investigate the performance of boron-based solid fuel which is in the matrix of wax-HTPB mixture. The purpose of investigation is to find the possibilities of the present fuel combination to introduce in the primary combustor of a hybrid fuel ducted rocket (Fig. 1b). A total of four fuel combinations are studied using an opposed flow burner (OFB) which run with gaseous oxygen. The oxygen flux in OFB is set between 20-56 kg/m^2-s. Field emission scanning electron microscope (FE-SEM), X-ray spectroscopy (EDS), X-ray diffraction (XRD), particle size analyzer (PSA), and thermogravimetric analysis (TGA) are use to characterize the as-received boron particles. The major focus of the research is held on regression rate profiles of the solid fuels.

2. EXPERIMENTAL METHODS

2.1 Material

The major ingredients such as boron particles (advertised size: ≤1 μm, purity: ≥95%), Isophorone diisocyanate (IPDI), and HTPB were procured from Sigma Aldrich (B: product no. 15580), Alfa Essar (IPDI: product no. L13759, purity: > 97.5%) and Anabond Ltd., Chennai, India respectively.

2.2 Material Characterizations

Various diagnostic techniques and instruments were used for performing the analysis on feed particles. For examining the various geometric and agglomeration attributes of the particles, a field emission scanning electron microscope (FE-SEM/JSM-7610F) was used. Due to high voltage applied during sample analysis, the charging effects were to be minimised. Thus, a conductive coating method (ion sputtering) was used to coat the particle specimen. Herein, gold was taken as the conductive material as it is highly stable and capable of emitting high secondary electrons during analysis. The thickness of the conductive coating was a few nm (<10nm approx.) which basically depends on the specimen morphology. Also, an energy dispersive X-ray spectroscopy (EDX/EDS) was utilized for analyzing the characteristic X-ray spectra by measuring the energy of the X-ray. Thus, the elemental composition of the specimen was identified using EDX. The particles were also examined for their size distribution by using a particle size analyzer (PSA: Zetasizer, Nano series/ZEN3600). For exploring the constituent components and also the structure (amorphous/crystalline) of the specimen, X-ray diffraction (XRD) analysis was performed on a Pan analytic system (X'Pert³ Powder, using Cu Kα (λ=1.5418Å) radiation) where angle (2θ) varied from 10 to 50^0 with a scanning rate of 5°/min and a step size of 0.05^0. To ascertain the active boron content in the as-received boron particles, a thermogravimetric analysis (TGA) in air environment was performed using Perkin Elmer Instrument (Pyris Diamond TG/DTA). An alumina crucible of 10-15 mg capacity was used as a sample pan; a constant air supply of 100 ml min^{-1} and a predetermined heating rate of 10° C min^{-1} were used in the experiment to oxidize the sample in the temperature range of 30–1350°C.

2.3 Fuel Sample Preparation

A total of four solid fuel samples were processed; these are Neat-HTPB, HTPB with powder-wax, HTPB with boron, and HTPB with wax and boron. The content of boron and wax was 10 % each of the total sample wt. Wax and HTPB carries the role of both binder as well as fuel. The fuel samples were prepared as given below: first HTPB was introduced to a curing agent IPDI (10% of HTPB) and the mixture was hand mixed by around 20 minutes. For getting the pellet shape, the fuel slurry was transferred into plastic bottles (Dia: ∅12.6 mm) and finally bottles were placed in a vacuum oven for degassing and curing. Degassing is done to remove all pockets in the slurry formed during mixing. The mixture was cured in two stages: first 5 days in the oven at 60°C and then 25 days at room temperature (30°C) [16], [17], [18]. Based on the observations of each day, it was noted that the pellets completely solidify after completing 30 days from the processing date. Similar process was carried out for fuel combinations carrying wax and boron. To protect the boron particles from local exposure (mainly oxidation), a glove bag (nitrogen filled) was used throughout while measuring and mixing. In our previous study [16], sample homogeneity test was conducted through EDS analysis where degree of homogeneity of particle on the fuel surface was appreciable. Since same procedure has been applied for the present sample preparation, therefore, similar homogeneity is expected for all the samples processed here.

2.4 OFB Design and Measurement Techniques

A schematic representation of an opposed flow burner (OFB) system is shown in Fig. 2 which is used in the present investigation based on the design and dimensions reported in the previous study [17]. The prime components of the OFB are stand with a nozzle guide, nozzle (for oxygen impingement), and a pellet holder unit. In all the sample tests, 10 mm of pellet length was exposed above the pellet holder and remaining was pushed into the holder; holder was kept at the centre of the dish. The exposed outer boundary except for the top surface was polished by a thin layer of silicone gel (Metroark 14 compound) which works as a fire inhibitor for limit the fuel pellet to burn only through the surface normal to oxygen impingement. The other important components used in controlling the OFB are shown in the experimental setup diagram. For all samples that were tested, the distance between the top surface of the pellet and the nozzle exit plane was maintained at 10 mm. A tungsten wire was connected to the sample using a Variac (supply: 6V) for its ignition and for measuring the flow rate, a rotameter was placed in the oxygen supply line. The oxygen mass flux in the present investigations was varied from 20 to 57 kg/m^2-s where flux is the ratio of oxidizer mass flow rate to the cross-sectional area of the nozzle exit. To control the oxygen supply and for initiating the ignition process of the burner, LabVIEW software was programmed in such a way that by a single command oxygen supplied first and after 1s, the ignition process initiated automatically.

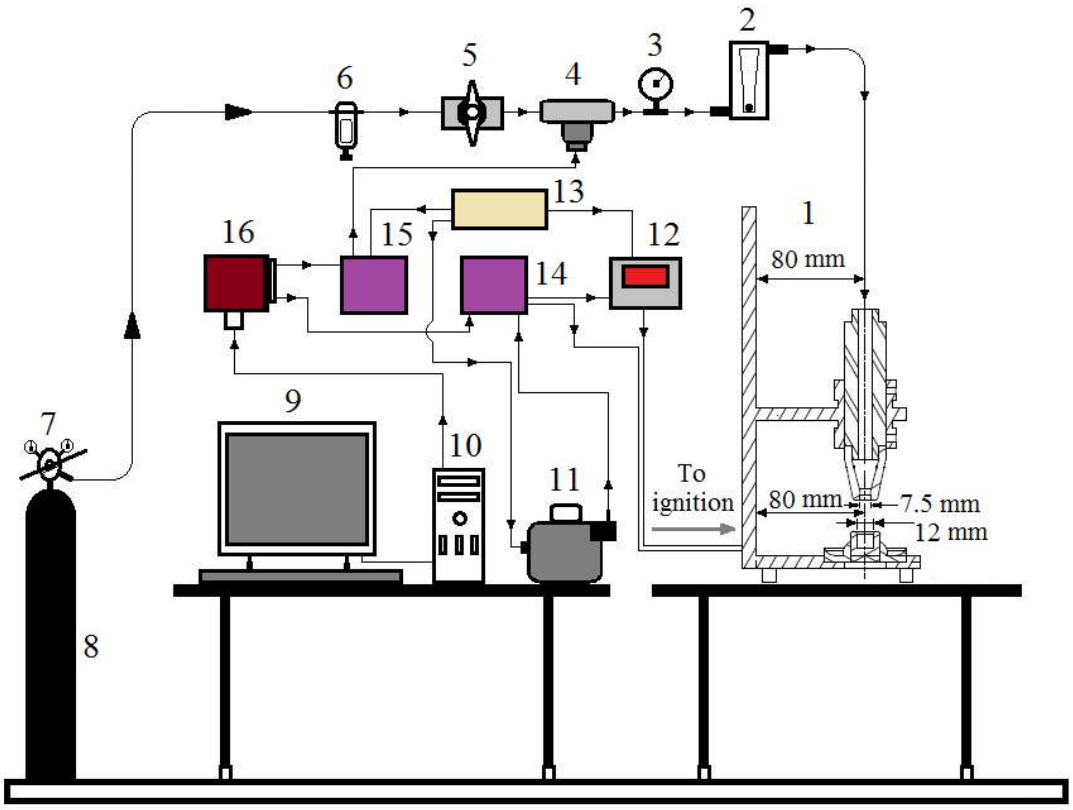

Fig. 2: Schematic illustration of opposed flow burner system: (1) OFB; (2) rotameter; (3) pressure gauge; (4) solenoid valve; (5) valve; (6) humidifier/filter; (7) regulator; (8) oxygen cylinder; (9) PC monitor; (10) CPU; (11) variac; (12) amp. Meter; (13) supply board (AC); (14 and 15) relay; (16) DAQ [17]

2.5 Regression Rate Measurement

In the present investigation, regression rate was measured by weight difference method. The mass of the pellet holder unit was taken before and after conducting experiment and pre-test/post-test weight difference (burned length) was used in regression rate calculation. Thus, the regression was determined by the burned length and the total sample burning duration.

3. RESULTS AND DISCUSSION

3.1 Characterization of Boron Powder

Figure 3 shows FE-SEM images of boron (B) particles, these images have been taken at two different magnifications. The morphology of boron powder (Fig. 3) shows that particles are in agglomerated form. These agglomerates are made up of several nano and micro size boron particles. The reason behind the appearance of agglomerates in boron powder is due to untouched sample (no pre-processing) while performing FE-SEM analysis.

Figure 4(a) shows the particle size distribution, during PSA analysis boron particles were well sonicated in ethanol for minimizing the agglomeration. The boron particle size has been evaluated between 200-1000 nm, although, average particle size is around 400 nm. Figure 4(b) shows the XRD pattern of boron particle, most of the peaks show in the figure match well with elemental boron and few peaks (low intensity) only represent boron oxide (B_2O_3). Major peaks match well the standard data (ICDD PDF # 00-011-0617) of elemental boron.

Figure 5 shows the plot between temperature and weight gain percentage of boron powder. This plot is actually shows gradual events of boron oxidation. The weight of the sample reduces marginally (<100%) up to the temperature of ~192 °C, on further increase of temperature shows a gain in wt. %. Marginal loss in wt. % means the sample contains less moisture which vaporizes on heating. Gain in wt. % in TG plot shows due to reaction of uncoated boron with oxygen. Hence boron oxide (B_2O_3) starts forming during reaction and the wt. % increases in slow rate upto 450 °C (melting temperature of B_2O_3). Beyond this temperature, there is a rapid increase in the formation of B_2O_3, along with this there is an evaporation of B_2O_3 as well. Although, formation reaction dominates evaporation, thus the TG curve keeps on increasing till temperature of around 1220 °C. Consequently, based on molar analysis using TG curve the active boron content in the sample is found to be ~77%.

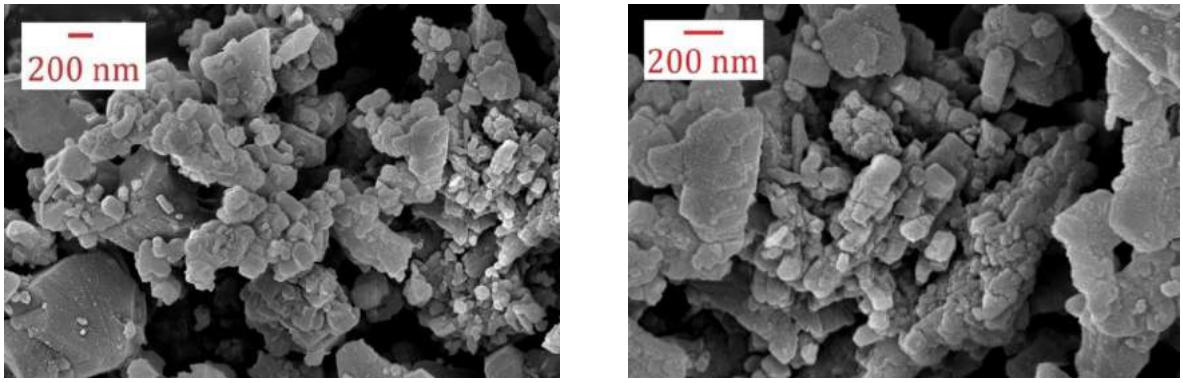

a. b.

Fig. 3: FE-SEM images of boron particle at 50k (a) and 100k (b) magnifications

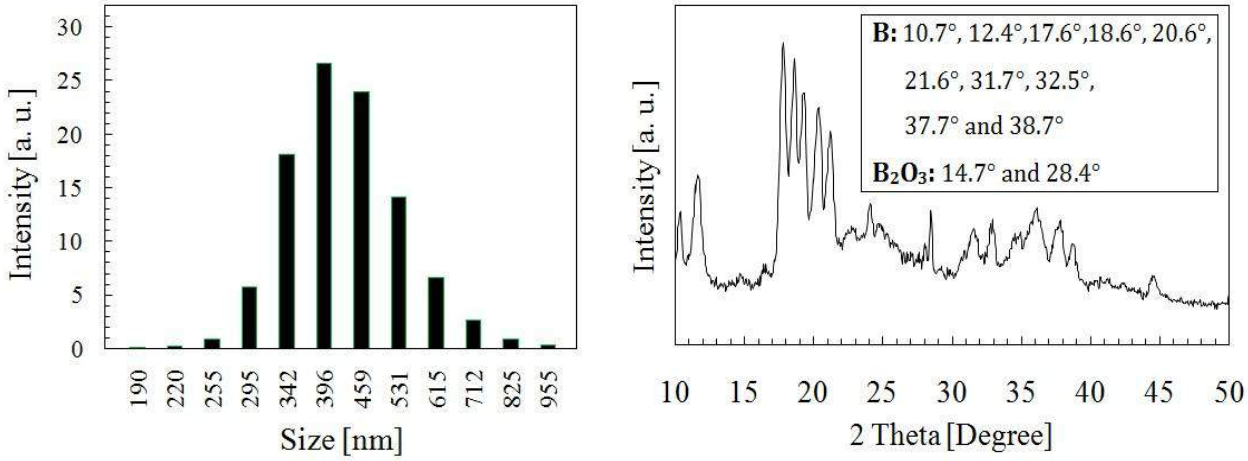

a. b.

Fig. 4: (a) Particle size distribution of B and (b) XRD pattern of B-powder

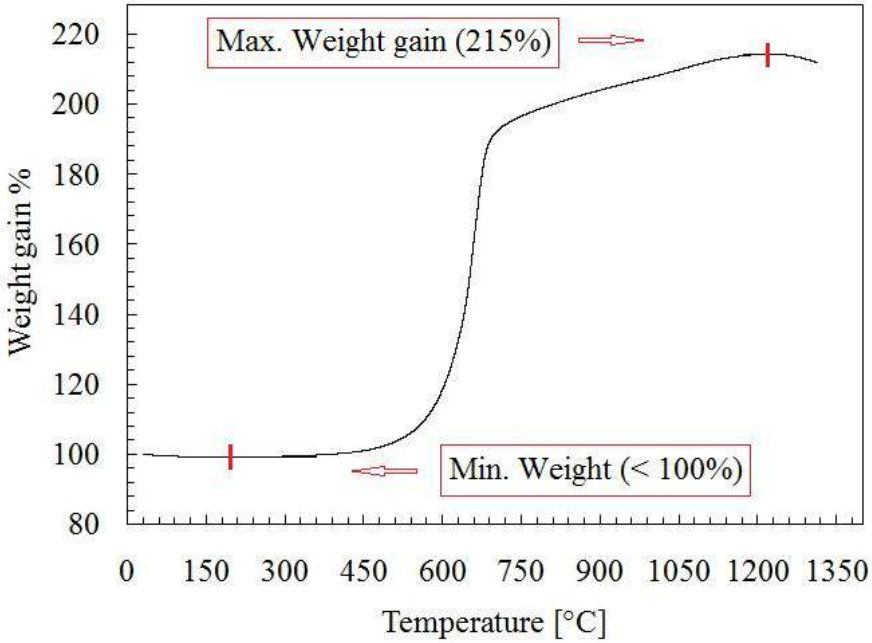

Fig. 5: TGA curve of boron powder

3.2 Regression Rate Measurement and Analysis

Figure 6 shows the color picture of OFB during ignition and combustion. It is clearly visible that green emission is available in the flame. This is an important phenomenon for boron ignition and combustion because it confirms the presence of boron's intermediate species (BO, BO_2) during oxidation [16]. On the burning surface, burning of boron particles can be seen which are actually ejected from the burning surface and travel a small distance. It is presumed that, if those particles could burn on the burning surface they helped to increase the heat/temperature of the burning surface [10].

Figure 7 shows the regression rate profiles of solid fuels. Maximum regression rate is found for Neat-HTPB and lowest for B/HTPB combination at all fluxes (20-56 kg/m^2-s). Although, it was assumed that regression rate for wax/HTPB mixture will give maximum. But this is not happened due to some reasons observed from the previous literatures [10]. The wax used in the present study is in powder form and has less oil content as compared to paraffin-wax. It is observed that neat pellets of both types of wax (paraffin-wax and powder wax); paraffin-wax is sticky where as pellet made by powder wax is brittle in nature. Therefore, burning quality of present wax used in the sample preparation cannot be counted its burning quality same as paraffin-wax [10]. Hence, it might be the reason of lower regression rate of wax/HTPB mixture than that of Neat-HTPB sample. The heat of combustion of both the wax is also different, paraffin-wax has ~46 MJ/kg where as powder wax is ~40 MJ/kg. Therefore, these reasons might be considered for the reduction in present regression rate data. The regression rate of wax/B/HTPB combination is slightly higher than that of B/HTPB. If we see both the boron-based samples the regression rate is lesser than their baseline samples. The reason behind reduction in regression rate recalls the problems associated with the boron which has been discussed in the introduction section. The ejection of agglomerates from the burning surface has major affects on regression rate as burning is effected due to loss of energy on the burning surface.

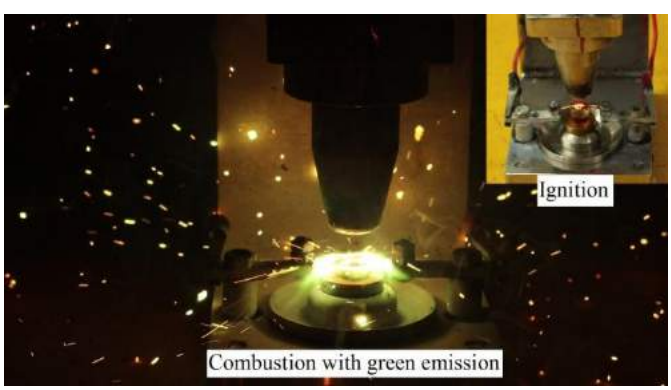

Fig. 6: Ignition and combustion of OFB

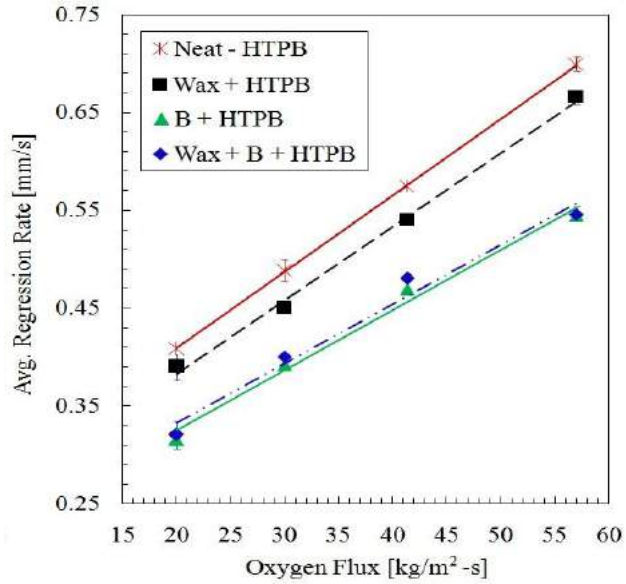

Fig. 7: Regression rate profile of the solid fuels

4. CONCLUSION

An opposed flow burner is used in the experimental investigation of boron-based solid fuel for the primary combustor of a ducted rocket. As-received boron particle are characterized using various material characterization techniques such as FE-SEM, XRD, TGA. Boron particles are found in submicron size in morphological analyses (FE-SEM) and size distribution (PSA). In XRD analysis most of the major peaks match well with elemental B. From TG analysis, it is found that the active boron content in the sample is ~77%. The study is concentrated on regression rate. The regression rate calculated in OFB is found lesser than that of regression rate of a rocket motor because only vaporization regression rate is involved in OFB. But in case of a rocket motor, vaporization as well as entrainment both has kept their influence on regression rate. Although, the data obtained from the present study cannot be compared directly with that of a rocket motor/primary combustor as the two systems work on very different conditions. The concept of OFB is easy to understand. Therefore, it can be used by a very established research group as well as one who limits the research due to funding constraint. Because the basic OFB design is comparatively cheaper than a strand burner setup/rocket motor, hence some useful performance parameters can be determined even in the absence of costly equipment.

5. ACKNOWLEDGMENT

We would like to express our sincere gratitude to the Department of Aerospace Engineering of IIT Kharagpur for providing the necessary funding for carrying the research work.

6. REFERENCES

[1] A. Gany and A. Netzer, "Burning and flame holding characteristics of a miniature solid fuel ramjet combustor," Journal of Propulsion and Power, vol. 7, no. 3, pp. 357–363, May 1991.

[2] Y. M. Timnat, "Advanced air breathing propulsion," Krieger Publishing Company, 1996.

[3] N. Kubota and T. Kuwahara, "Combustion of Energetic Fuel for Ducted Rockets (I)," Propellants, Explosives, Pyrotechnics, vol. 16, no. 2, pp. 51–54, Apr. 1991.

[4] D. Liu, Z. Xia, L. Huang, and J. Hu, "Boron Particle Combustion in Solid Rocket Ramjets," Journal of Aerospace Engineering, vol. 28, no. 4, p. 04014112, Jul. 2015.

[5] K. Schadow, "Experimental investigation of boron combustion in air-augmented rockets," AIAA Journal, vol. 7, no. 10, pp. 1870–1876, Oct. 1969.

[6] B. Natan and A. Gany, "Combustion characteristics of a boron-fueled solid fuel ramjet with aft-burner," Journal of Propulsion and Power, vol. 9, no. 5, pp. 694–701, Sep. 1993.

[7] S. Balas and B. Natan, "Boron Oxide Condensation in a Hydrocarbon-Boron Gel Fuel Ramjet," Journal of Propulsion and Power, vol. 32, no. 4, pp. 967–974, Jul. 2016.

[8] A. Ulas, K. K. Kuo, and C. Gotzmer, "Ignition and combustion of boron particles in fluorine-containing environments," Combustion and Flame, vol. 127, no. 1–2, pp. 1935–1957, Oct. 2001.

[9] A. Mačeic and J. M. Semple, "Combustion of Boron Particles at Atmospheric Pressure," Combustion Science and Technology, vol. 1, no. 3, pp. 181–191, Nov. 1969.

[10] S. A. Hashim, S. Karmakar, A. Roy, and S. K. Srivastava, "Regression rates and burning characteristics of boron-loaded paraffin-wax solid fuels in ducted rocket applications," Combustion and Flame, vol. 191, pp. 287–297, May 2018.

[11] S. Sisi and A. Gany, "COMBUSTION OF PLAIN AND REINFORCED PARAFFIN WITH NITROUS OXIDE," International Journal of Energetic Materials and Chemical Propulsion, vol. 14, no. 4, pp. 331–345, 2015.

[12] M. Z. Akhter and M. A. Hassan, "Characterisation of paraffin-based hybrid rocket fuels loaded with nano-additives," Journal of Experimental Nanoscience, vol. 13, no. sup1, pp. S31–S44, Feb. 2018.

[13] D. Komornik and A. Gany, "Study of a hybrid gas generator for a ducted rocket," Combustion, Explosion, and Shock Waves, vol. 53, no. 3, pp. 293–297, May 2017.

[14] G. Young, G. A. Risha, A. G. Miller, R. A. Glass, T. L. Connell, and R. A. Yetter, "Combustion of alane-based solid fuels," International Journal of Energetic Materials and Chemical Propulsion, vol. 9, no. 3, pp. 249–66, 2010.

[15] S. C. Shark, C. R. Zaseck, T. L. Pourpoint, and S. F. Son, "Solid-Fuel Regression Rates and Flame Characteristics in an Opposed Flow Burner," Journal of Propulsion and Power, vol. 30, no. 6, pp. 1675–1682, Nov. 2014.

[16] S. A. Hashim, S. Karmakar, and A. Roy, "Combustion Characteristics of Boron-HTPB-Based Solid Fuels for Hybrid Gas Generator in Ducted Rocket Applications," Combustion Science and Technology, vol. 191, no. 11, pp. 2082–2100, Nov. 2018.

[17] S. A. Hashim, S. Karmakar, and A. Roy, "Effects of Ti and Mg particles on combustion characteristics of boron–HTPB-based solid fuels for hybrid gas generator in ducted rocket applications," Acta Astronautica, vol. 160, pp. 125–137, Jul. 2019.

[18] S. A. Hashim, P. K. Ojha, S. Karmakar, A. Roy, and D. Chaira, "Experimental Observation and Characterization of B−HTPB-based Solid Fuel with Addition of Iron Particles for Hybrid Gas Generator in Ducted Rocket Applications," Propellants, Explosives, Pyrotechnics, vol. 44, no. 7, pp. 896–907, Apr. 2019.

7. BIOGRAPHIES

Dr. Syed Alay Hashim is an Associate Professor at Sandip University Nashik and working in the field of Propulsion and Combustion.

Dr. Srinibas Karmakar is an Associate Professor at IIT KGP and working in the field of Propulsion and Combustion.

Dr. Arnab Roy is an Associate Professor at IIT KGP and working in the field of Computational Fluid Dynamics.

Miss. Shifa Sheikh is an undergraduate student at Sandip University Nashik.

Sensitizing Gaseous Mixtures for Practical Applications in Rotating Detonation Engines

1. D Santosh Kumar, Graduate Student, *IIT Kanpur*, 2. Ajay V. Singh, Assistant Professor, *IIT Kanpur*

Abstract - Rotating and Pulse Detonation Engines are being pursued as a more viable form of detonation-based engines that combine high thermodynamic efficiency with a simple design. The very high detonation temperatures have limited its progress, and its continuous operation remains a challenging task. The addition of diluents like CO_2, He, Ar, and H_2O (water vapor) will reduce the post-detonation temperatures and velocity, which in turn may cause degeneration of a detonation wave into a deflagration wave. This issue can be eliminated by sensitizing the given fuel-oxidizer mixture by doping it with small quantities of O_3 and H_2O_2. Fuel sensitization of a given fuel-oxidizer mixture with O_3 and H_2O_2 could alter the ignition chemistry of such mixtures significantly and can be used as a potential tool for widening the detonation propagation limits.

***Index Terms* — Detonations, Deflagration-to-Detonation Transition (DDT), Fuel Sensitization, Ignition Delay Time (τ_{ign}), Induction Zone Length (Δ_i), Detonation products temperatures (T_{CJ}), Rotating Detonation Engines (RDEs), Pulse Detonation Engines (PDEs), Detonation Velocity (V_{CJ}).**

1. Introduction

The research on Jet Engines has made significant progress since the 1930s and has left minimal scope towards further development. The lower efficiencies in ramjet and SCRAM jet engine due to significant stagnation pressure loss has shifted the research towards detonation based engine cycles. Detonation has an advantage over deflagration combustion in being more efficient and can release more energy **[1],[2]**.

Rotating and Pulse Detonation Engines (RDE's and PDE's) are being pursued as a more viable form of detonation-based engines that combine high thermodynamic efficiency with a simple design. The understanding of detonation chemical kinetics and gas dynamics is very important in the design of detonation cycle engines. Gaseous detonations have self-sustained combustion that couples the shock dynamics and chemical kinetics, which can be analyzed numerically by the ZND model. Detonation structures are both complex and multi-dimensional and are comprised of incident shock, Mach stems, and transverse waves whose intersection forms triple points, exhibiting cellular like structures [2]. The critical parameters associated with ZND structure are ignition delay time (τ_{ign}), induction zone length (Δ_i) and detonation cell size (λ). These critical parameters depend on the fuel-oxidizer mixture, dilution ratios, promoters and inhibitors, initial pressure, temperature, etc. Through experimental and numerical simulations, various researchers have tried to establish a relation between the key parameters like Δ_i, τ_{ign}, detonation cell size, and detonation velocity (V_{CJ}) **[3-8]**.

However, to date, many of the physics associated with detonation cycle engines have yet to be fully understood. The questions that remain unanswered to date include the initiation, sustainment, and stabilization of a detonation wave in the presence of hot spots and fluid flow instabilities **[2]**. For instance, detonation cycle engines currently employ very complex cooling mechanisms to cool the walls of an engine core. The temperatures in a detonation wave can be of the order of 3000 K, depending on the chemical makeup of the mixture. Generally, detonation cycle engines employ a stoichiometric fuel-oxidizer mixture in order to initiate a detonation wave easily inside such engine cores **[1]**. However, burning mixtures at stoichiometric conditions increases the flame temperatures drastically, where the resulting temperatures could be as high as 3000 K. In order to cool engine cores in such scenarios is a challenging task, especially when it is desired to run these engines for a considerable amount of time, which is an essential need for their use in military and civilian aircraft **[9-20]**. The answer to these questions is critical to the development of a miniaturized and full-scale RDE and thus broaden its areas of potential applications.

The high temperatures in the post equilibrium detonation products can be addressed with the addition of diluents like CO_2, H_2O, Ar, and He. However, the addition of diluents tends to increase the ignition delay

1. Squadron Leader D Santosh Kumar is presently undergoing MTech, in Aerospace Engineering at IIT Kanpur. (e-mail: dsantosh@iitk.ac.in).

2. Dr. Ajay Vikram Singh is working as Assistant Professor in the Department of Aerospace Engineering at IIT Kanpur, U.P, India. (e-mail: ajayvs@iitk.ac.in).

time (τ_{ign}) and induction zone length (Δ_i) which in turn causes the detonation wave velocities (V_{cj}) to drop and is largely responsible for the degeneration of a detonation wave into a deflagration wave **[21],[22]**. This issue can be eliminated by sensitizing the given fuel-oxidizer mixture by doping it with O_3 and H_2O_2 at smaller concentrations. The overall effect of such fuel sensitization is that it alters the ignition chemistry tremendously of a given fuel-oxidizer mixture without significantly impacting mixture properties that would influence the gas dynamics and final thermodynamic state after combustion, including the speed of sound, specific heats, heating value, adiabatic flame temperature, viscosity and conductivity of the initial reactant mixture.

Initially, Magzumov et al. **[23],** in their numerical calculations has shown that for hydrogen-air mixtures, the addition of small amounts of dopants like Ozone and H_2O_2 (up to 4000 PPM) could reduce the Δ_i and τ_{ign}. For H_2-O_2 detonations, Crane et al. **[5]** has experimentally shown that reduction in cell widths up to 70% can be achieved with the addition of 3000 ppm of Ozone. Lesser cell width signifies stronger detonation wave, which signifies that Ozone acts as an ignition promoter and can be used to sensitize a given fuel-oxidizer mixture.

The aim of this numerical study is two-fold:

(a) To study the effects of O_3 and H_2O_2 on various Detonation parameters for Hydrogen-Oxygen/Air mixtures.

(b) To study the effects of O_3 and H_2O_2 and various diluents (CO_2, H_2O, Ar, and He) on the post-detonation parameters for Hydrogen-Oxygen/Air mixtures.

2. ZND-NUMERICAL CALCULATIONS

The recently developed Foundation Fuel Chemistry Model Ver 1.0 (FFCM1) **[24]** chemical kinetic mechanism is used for numerical computations. Additionally, the Princeton Ozone sub-model **[25]** is used in conjunction with the FFCM1 model for calculations with Ozone as a dopant. Numerical computations are carried out with CANTERA 2.4 **[26]** open-source software integrated with MATLAB R2018b and Python Ver 3.7. ZND calculations were performed with the modified version of Detonation toolbox ver.2018 **[27]**.

Initially, the effects of H_2O_2 and Ozone dopants on various Detonation properties like T_{cj}, V_{cj}, M_{cj}, T_{vn}, V_{vn}, Ignition Delay Time (τ_{ign}) and Induction Zone Length (Δ_i) are studied for stoichiometric Hydrogen-Oxygen/Air mixtures. Further, the effect of diluents like CO_2, H_2O, Ar, and He are also studied. All the ZND Calculations in the present study are made at stoichiometric equivalence ratios, with initial pressure and temperature of 1 bar and 295 K, respectively.

3. RESULTS AND DISCUSSIONS

3.1 Effect of H_2O_2 and Ozone on hydrogen-oxygen/hydrogen-air Detonations.

Stoichiometric Hydrogen Oxygen/Air mixtures were doped with H_2O_2 and Ozone up to 10^4 PPM. The variations in detonation parameters like M_{cj}, V_{cj}, T_{cj}, τ_{ign}, and Δ_i were calculated and are given in Table 1 and Fig. 1(a) and (b) respectively. It is clearly evident from Table 1 and Fig-1 (a) and (b), that M_{cj}, V_{cj}, T_{cj} does not change with the addition of dopants up to 10^4 PPM, however, the ignition chemistry is tremendously altered which causes a reduction in Δ_i and τ_{ign}.

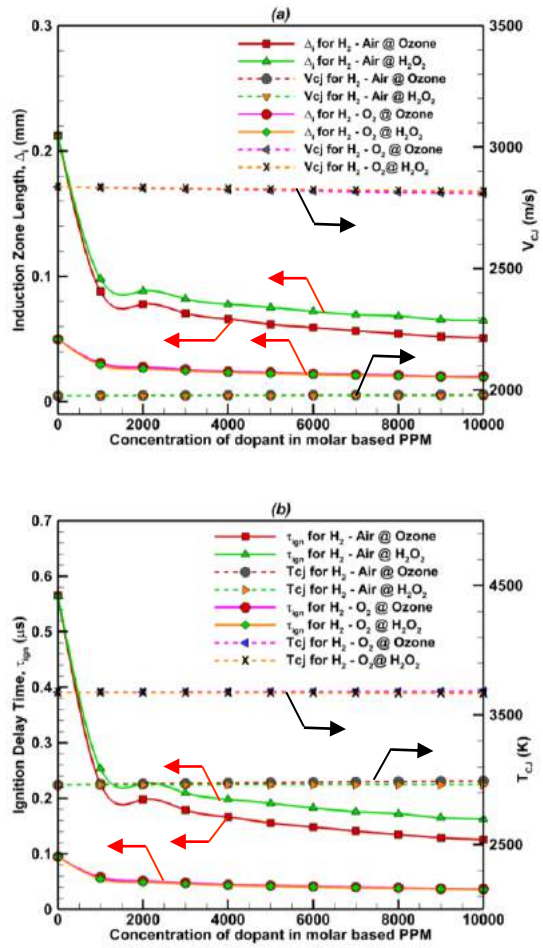

Fig. 1 (a) Effects of dopants on Induction Zone Length and V_{cj} for Hydrogen Oxygen/Air mixtures **(b)** Effects of dopants on Ignition Delay Time and T_{cj} for Hydrogen Oxygen/Air mixtures (solid lines indicating τ_{ign} and Δ_i and dashed lines indicating T_{cj} and V_{cj})

Table 1. Effects of Dopants on Detonation parameters for Hydrogen Oxygen/Air Mixtures.

	Dopant Conc in PPM		T_{CJ} (K)	V_{CJ} (m/s)	M_{CJ}	τ_{ign} (μs)	Δ_i (mm)
H_2-O_2	-	-	3675	2836	5.3	0.09	0.05
	O_3	3000	3677	2828	5.3	0.05	0.03
		6000	3680	2820	5.3	0.04	0.02
		10000	3682	2809	5.3	0.036	0.02
	H_2O_2	3000	3673	2831	5.3	0.05	0.025
		6000	3671	2825	5.3	0.04	0.02
		10000	3668	2818	5.3	0.035	0.02
H_2-Air	-	-	2959	1976	4.9	0.6	0.2
	O_3	3000	2971	1977	4.9	0.18	0.07
		6000	2980	1979	4.9	0.15	0.06
		10000	2989	1980	4.9	0.12	0.05
	H_2O_2	3000	2960	1976	4.9	0.2	0.08
		6000	2961	1977	4.9	0.18	0.07
		10000	2961	1977	4.9	0.16	0.065

**Calculations were carried out at stoichiometric Hydrogen-Oxygen/Hydrogen-Air mixtures with initial pressure and temperature of 1 bar and 295 K, respectively.*

It is evident from Fig. 1(a) and (b) that the addition of Ozone and H_2O_2 in small concentrations (up to 10^3 PPM) can cause a sharp reduction in Δ_i and τ_{ign}. Beyond doping levels of 10^3 PPM, a gradual reduction was seen in both Δ_i and τ_{ign}. Also, Ozone serves as a better ignition promoter/dopant when compared to H_2O_2.

3.2 Effects of H_2O_2 and Ozone dopants with Argon and Helium diluents for Hydrogen Oxygen/Air Detonations

ZND Calculations for stoichiometric Hydrogen Oxygen/Air mixtures at varying concentrations of Argon and Helium in the presence of Ozone and H_2O_2 were also carried out to simulate the post-detonation properties.

3.2.1 Hydrogen-Oxygen Detonations with Ar and He as a diluent

The addition of Ar or He at 90% molar fraction can reduce the post-detonation temperatures from 3675 K to 1792 K. A significant decrease in temperatures (T_{cj}) was seen when Ar and He mole fraction was higher than 70%. Fig. 2 shows the variation of ignition delay time with the diluent concentration. Without *H_2O_2 and Ozone*, τ_{ign} was found to increase exponentially in the presence of diluents, resulting in a weaker detonation wave. Sensitizing fuel-oxidizer mixtures with Ozone and H_2O_2 at 10^4 PPM could result in a lower τ_{ign}, even at a higher dilution of inert gases. This prevents the detonation wave from degenerating into a deflagration wave.

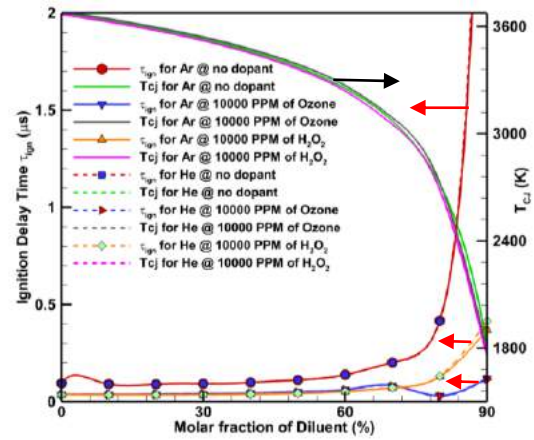

Fig. 2. Effects of H_2O_2 and Ozone dopants with Argon and Helium diluents for Hydrogen Oxygen mixtures. (solid lines indicate Ar and dashed lines indicate He)

3.2.2 Hydrogen-Air Detonations with Ar and He as a diluent

The addition of Ar or He at 90% Molar Fraction for stoichiometric hydrogen-air detonations will reduce the post equilibrium temperatures from 2960 K to 1073 K. Fig. 3 shows the variation of T_{cj} and τ_{ign} as a function of diluent concentration. Without O_3 and H_2O_2, τ_{ign} increases exponentially when diluent percentage crosses 60%. This, in turn, could cause a substantial increase in Δ_i and detonation cell size, depicting a weaker detonation wave. Fuel sensitization with Ozone and H_2O_2 dopants at 10^4 PPM even at higher concentrations of diluents could substantially decrease τ_{ign} suggesting a stronger detonation wave with smaller cell size. It is observed that a stronger detonation can be achieved with Ozone up to 90% dilution, however, with H_2O_2 stronger detonation can be achieved up to 80% dilution. This suggests that Ozone works as a better ignition promoter than H_2O_2 under the same operating conditions.

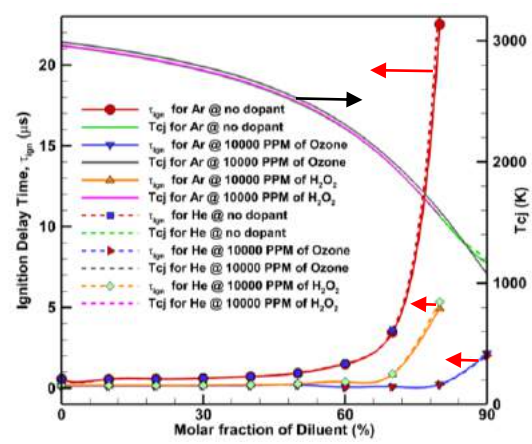

Fig. 3. Effects of H_2O_2 and Ozone dopants with Argon and Helium diluents for Hydrogen Air mixtures (solid lines indicating Ar diluent and dashed lines indicating He diluent)

It can be seen from Figures 2 and 3 that Argon and Helium will have a similar effect on τ_{ign} and T_{cj}. Lower detonation temperatures can be achieved for Hydrogen-Air when compared to Hydrogen-Oxygen mixtures. Ozone will have lower τ_{ign} (stronger detonation wave) compared to H_2O_2 at higher dilution ratios under the same operating conditions.

3.3 Effects of H_2O_2 and Ozone dopants with H_2O diluent for Hydrogen Oxygen/Air Detonations

ZND calculations for stoichiometric Hydrogen-Oxygen/Hydrogen-Air mixtures were carried out by varying concentrations of H_2O and CO_2 in the presence of ignition promoters like Ozone and H_2O_2.

3.3.1 Hydrogen Oxygen Detonations with H_2O as a diluent

The addition of H_2O at high concentrations can reduce the post-detonation temperatures from 3675 K to 2010 K as seen in Fig. 4. The reduction in post-detonation temperature (T_{cj}) is linear with the addition of H_2O. In the absence of an ignition promoter, τ_{ign} is observed to increase exponentially up to 40% dilution by H_2O. In the presence of an ignition promoter, stronger detonations can be achieved up to 70% dilution by H_2O.

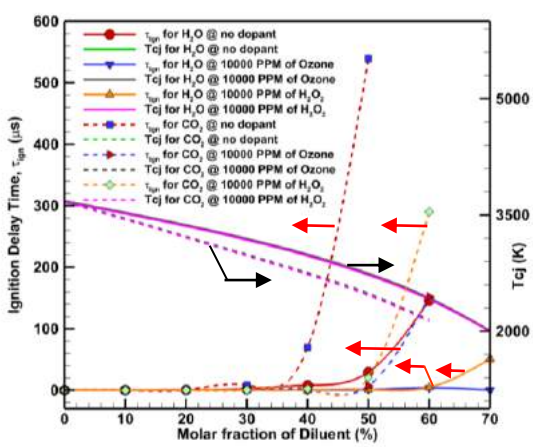

Fig. 4. Effects of H_2O_2 and Ozone dopants with H_2O and CO_2 diluents for Hydrogen-Oxygen mixtures. (solid lines indicating H_2O diluent and dashed lines indicating CO_2 diluent).

3.3.2 Hydrogen-Oxygen Detonations with CO_2 as a diluent

The addition of CO_2 at 40% Molar Fraction for stoichiometric Hydrogen Oxygen detonations will reduce the post-detonation temperatures from 3675 K to 2753 K, as seen in Fig.4. In the absence of any ignition promoter, τ_{ign} increases exponentially when CO_2 molar fraction in Hydrogen-air system crosses 40%. With the addition of Ozone at 10^4 PPM, a stronger detonation wave can be sustained up to 40% dilution, however, H_2O_2 is effective up to 30% dilution only.

3.3.3 Hydrogen-Air Detonations with H_2O as a diluent

The addition of water vapor as a diluent at 40% Molar Fraction for stoichiometric Hydrogen-Air detonations will reduce the post-detonation temperatures from 2959 K to 2028 K, and this can be easily seen in Fig. 5. In the absence of any ignition promoter, τ_{ign} increases exponentially beyond 10% molar fraction of water vapor. The addition of Ozone and H_2O_2 at 10^4 PPM, result in an interesting behavior of ignition delay time and the same can be discerned from Fig. 5.

3.3.4 Hydrogen-Air Detonations with CO_2 as a diluent

The addition of CO_2 diluent at 30% Molar Fraction for stoichiometric Hydrogen Oxygen detonations will reduce the post equilibrium temperatures from 2950 K to 2117 K (see Fig. 5). In the absence of any ignition promoter, τ_{ign} will increase exponentially beyond 10% molar fraction of CO_2 dilution.

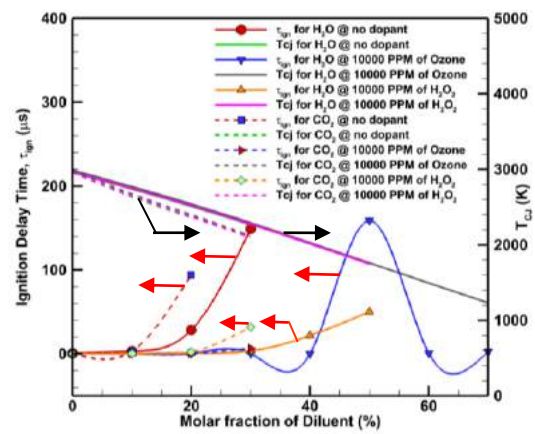

Fig. 5. Effects of H_2O_2 and Ozone dopants with H_2O and CO_2 diluents for Hydrogen-Air mixtures. (solid lines indicating H_2O diluent and dashed lines indicating CO_2 diluent)

The summary of the combined effects of ignition promoters and diluents is tabulated in Table 2 for hydrogen-oxygen and hydrogen-air mixtures. It can be inferred from Table 2 and from Figs. 2 to 5, that for a stoichiometric Hydrogen-Oxygen/hydrogen-Air mixture, Ar and He diluents will have lower τ_{ign} and T_{cj} when compared to H_2O and CO_2. Hence, Ar and He are better diluents to maintain stronger detonation wave at lower detonation temperatures. It can also be noticed that H_2O is a slightly better diluent than CO_2. Also, Ozone acts as a better ignition promoter than H_2O_2 at higher dilution percentages.

Table 2. Effects of Dopants with diluents for Hydrogen Oxygen/Air Mixtures

	Dopant	Diluent (dil)	dil %	T_{CJ} (K)	τ_{ign} (µs)	Δ_i (mm)
H_2-O_2	-	-	-	3675	0.09	0.05
	O_3 (10000 PPM)	Ar	90	1792	0.12	0.04
		He	90	1793	0.11	0.10
		CO_2	40	2753	0.5	0.16
		H_2O	70	2010	0.2	0.08
	H_2O_2 (10000 PPM)	Ar	90	1753	0.37	0.13
		He	90	1754	0.41	0.4
		CO_2	40	2733	2.3	0.7
		H_2O	70	1997	20.4	50.9
H_2-Air	-	-	-	2959	0.6	0.2
	O_3 (10000 PPM)	Ar	90	1073	2.14	0.66
		He	90	1073	2.0	1.6
		CO_2	30	2117	6.7	2.1
		H_2O	40	2028	0.18	0.06
	H_2O_2 (10000 PPM)	Ar	80	1562	1.8	5.0
		He	80	1562	4.2	5.3
		CO_2	30	2097	32	9
		H_2O	40	2013	21.9	8.3

** Calculations made at Stoichiometric Hydrogen Oxygen/Air mixtures with 10^4 PPM of dopant addition, an initial pressure of 1 bar and initial temperature of 295 K.*

4. Conclusions

The following conclusions can be drawn from the present work:

(a) The addition of H_2O_2 and Ozone dopants to Hydrogen Oxygen/Air mixtures will alter the ignition chemistry tremendously without significantly impacting the gas dynamics and thermodynamic states of the gaseous mixture.

(b) The addition of diluents like Ar, He, CO_2 and H_2O and Helium to Hydrogen-Oxygen/hydrogen-Air mixtures will reduce the detonation product temperatures significantly, at the cost of increased τ_{ign} and Δ_i making detonation wave weaker. Stronger detonations at higher dilutions can be achieved by sensitizing the mixture with Ozone and H_2O_2 dopants. This will be one of the viable solutions, to reduce the post-detonation high temperature in RDEs for its continuous operation.

(c) Ar and He are better diluents when compared to H_2O and CO_2, however, H_2O is a slightly better diluent than CO_2. Ozone acts as a better ignition promoter than H_2O_2 at higher dilutions.

5. Acknowledgment

This work is supported by the Start-up research grant of Indian Institute of Technology Kanpur. Also, the author gratefully acknowledges the support from the Indian Air Force.

6. References

[1] Jiun-Ming Li, Chiang Juay Teo, Boo Cheong Khoo, Jian-Ping Wang, Cheng Wang (eds.), Detonation Control for Propulsion, 2018.

[2] John H.S Lee, The Detonation Phenomenon Hadi Sadat, "Power System Analysis, " Tata McGraw Hill, 2002.

[3] J. Kindracki, P. Wolanski, Z. Gut, Experimental research on the rotating detonation in gaseous fuels-oxygen mixtures. 22nd International Colloquium on Dynamics of Explosions and Reactive Systems-2009.

[4] Yunfeng Liu, Wei Zhand, Zonglin Jiang, Relationship between ignition delay time and cell size of H2-Air detonation, International Journal of Hydrogen Energy 2016.

[5] Jackson Crane, Xian Shi, Ajay V. Singh, Yujie Tao, Hai Wang, Isolating the effect of induction length on detonation structure: Hydrogen-oxygen detonation promoted by ozone, Combust. Flame 200 (2019) 44-52.

[6] A. A. Vasil'ev, Cell Size as the Main Geometric Parameter of a Multifront Detonation Wave by, Journal of propulsion and Power, Vol.22, No. 6-2006.

[7] Charles K. Westbrook and Paul A.Urtiew, Chemical Kinetic Prediction of Critical Parameters in Gaseous Detonations, Combust. Inst. 19 (1982), 615-623.

[8] K. Kailasanath, E.S. Oran, J.P. Boris and T.R. Young, Determination of Detonation Cell Size and the Role of Transverse Waves in Two-Dimensional Detonations, Combust. Flame. 61:199-209 (1985).

[9] D A Schwer and K. Kailasanath , Numerical Investigation of Rotating Detonation Engines by, 43rd AIAA/SAE/ASEE Joint Propulsion Conference, 2010

[10] William H. Heiser, Thermodynamic Cycle Analysis of Pulse Detonation Engines, Journal of Propulsion and Power, 2002

[11] Jiro Kasahara and Sergey Frolov, Present Status of Pulse and Rotating Detonation Engine Research, 25th ICDERS, 2015

[12] Bulat Pavel Viktorovich, About the Detonation Engine, American Journal of Applied Sciences 11 (18) : 2014 (1357-1364)

[13] D.F. Dausen, C.M. Brophy, R.G. Wright and J.D. Marder, Design of Optically-Accessible Rotating Detonation Engine, 48th AIAA, Joint Propulsion Conference and Exhibit-2012

[14] R. Mevel, D. Davidenko, F. Lafosse, G. Dupre, C.E. Paillard, Detonation in Hydrogen-Nitrous Oxide-Diluent Mixtures : An Experimental and Numerical Study, Combust. and Flame -2014

[15] J. Kindracki, A. Kobiera, P.Wolanski, Z.Gut, M.Folusiak and K. Swiderski, Experimental and Numerical Study of the Rotating Detonation Engine in Hydrogen Air Mixtures, Progress in Propulsion Physics 2 (2011) (555-582)

[16] K. Kailasanath, Review of Propulsion Applications of Detonation Waves, AIAA Journal, Vol 38, 2000

[17] Eric M. Braun, Frank K. Lu, Airbreathing rotating detonation wave engine cycle analysis, Aerospace Science and Technology 27 (2013) (201-208)

[18] Zhou Rui, Wu Dan, Wang Jianping, Progress of Continuously rotating detonation engines, Chinese Journal of Aeronautics, (2016), 29(1): (15-29)

[19] E. Winterberger and J.E Shepherd Thermodynamic Cycle Analysis for Propagating Detonations, Journal of Propulsion and Power, Vol. 22, No.3-2006.

[20] Andrew St. George, Robert Driscoll, Vijay Anand, Steve Randall, David Munday and Ephraim J. Gutmark, Development of a rotating Detonation Engine Facility at the University of Cincinnati, 53rd AIAA Aerospace Sciences Meeting-2015.

[21] Charles K. Westbrook, Chemical Kinetics of Hydrocarbon Oxidation in Gaseous Detonations, Combust Inst.-1982

[22] Schwer, D. A., and Kailasanath, K., "Numerical investigation of the physics of rotating detonation-engines," Proceedings of the Combustion Institute, 33, 2195-2202 (2011).

[23] A.E. Magzumov, I. Kirillov, V.Rusanov, Effect of small additives of ozone and hydrogen peroxide on the Induction zone length of hydrogen-air mixtures in one dimensional model of a detonation wave, combust. Exp. Shock 34 (1998) 338-341.

[24] G. P. Smith, Y. Tao, and H. Wang, Foundational Fuel Chemistry Model Version 1.0 (FFCM-1) http://web.stanford.edu/group/haiwanglab/FFCM-1/index.html, 2016.

[25] H.Zhao, X.Yang, Y. Ju, Kinetic studies of ozone assisted low temperature oxidation of dimethyl ether in a flow reactor using molecular beam mass spectrometry, Combust. Flame 173 (2016) 187-194.
[26] David G. Goodwin, Raymond L. Speth, Harry K. Moffat, and Bryan W. Weber. Cantera: An object-oriented software toolkit for chemical kinetics, thermodynamics, and transport processes. https://www.cantera.org, 2018. Version 2.4.0. doi:10.5281/zenodo.1174508.
[27] S. Browne, J. Ziegler, and J. E. Shepherd, Numerical Solution Methods for Shock and Detonation Jump Conditions, GALCIT Report FM2006.006 - R3, California Institute of Technology Revised September, 2018.

7. BIOGRAPHIES

Squadron Leader D Santosh Kumar has completed B.Tech in Mechanical Engineering from Sri Venkateswara University College of Engineering, Tirupati in the year 2010. Thereafter, joined Indian Air Force as Engineering Officer in 2010 and trained on Hawk Mk-132 aircraft systems. He is presently undergoing MTech programme in Aerospace Engineering (Propulsion) at IIT Kanpur.

Dr Ajay Vikram Singh is presently working as Faculty in the Department of Aerospace Engineering at Indian Institute of Technology, Kanpur. He completed his MTech in Aerospace Engineering (Propulsion) at IIT Kanpur in 2008 and received Doctor of Philosophy (Ph.D.) in Mechanical Engineering from University of Maryland, College Park, USA in 2015. Later, he worked as Postdoctoral Researcher in the Department of Mechanical Engineering at Stanford University, USA. His research interests are in advanced propulsion technologies including detonation cycle engines and hybrid turboelectric propulsion, soot formation and oxidation, flame-synthesized functional nanoparticles for renewable energy devices and fire dynamics with applications to both industry and academia.

Sensitising Ethylene-Air and Ethylene-Oxygen Mixtures for Optimal Performance of Detonation Cycle Engines

1. Kiran Ivin, Graduate Student, *IIT Kanpur* 2. Ajay V. Singh, Assistant Professor, *IIT Kanpur*

Abstract- A promising research area today is the detonation cycle engines where detonation waves associated with it are complex, multi-dimensional processes. The critical parameters associated with a detonation wave are the cell size, IDT and IZL. The addition of ignition promoters like Ozone and H_2O_2 to fuel mixture reduces IDT and IZL, making detonation stronger and addition of diluents like Argon and Helium reduces the post-detonation temperature at the cost of reduction in IDT and IZL. The optimal doping and addition of diluents to sensitize the Ethylene-oxidizer mixture will enable us to utilize it for continual operation of detonation cycle engines.

Keywords- Detonation, Cell Size, Cell width λ, Induction Delay Time(IDT), Induction Zone Length(IZL), Rotating Detonation Engines (RDE), Thermicity (σ), Chapman Jouguet Temperature(T_{cj}), Chapman Jouguet Velocity (V_{cj})

1. INTRODUCTION

The combustion efficiency of the petrol, diesel and the jet engines which employ deflagration mode of combustion have come to a standstill. The quest for development of more efficient and powerful engines have led us to the development of pressure gain engines which uses detonation mode of combustion.

Detonation cycles are based on the concept of Pressure Gain Combustion (PGC). In PGC, the combustion process is close to constant volume, which can be used to augment cycle output and reduce engine size. In comparison, typical gas turbines burn at constant pressure. It can be seen that under comparable conditions the detonation cycle produces a burned gas with lower entropy and potentially higher work output. The use of detonation cycle engines increases efficiency by nearly 15 % **[1]**. The higher efficiency of detonation cycle engines has opened up more promising engine technologies like the Pulse Detonation Engines (PDE) and Rotating Detonation Engines (RDE).

1. Squadron Leader Kiran Ivin is a sponsored student of Indian Air Force with the Department of Aerospace Engineering, IIT Kanpur, India.(e-mail:kiranaf@iitk.ac.in).

2. Dr Ajay V Singh is an Asst Professor with the Department of Aerospace Engineering, IIT Kanpur, India. (e-mail: ajayvs@iitk.ac.in).

Detonation waves are complex, multi-dimensional processes involving interactions between incident shocks, mach stems, and transverse waves and are subsequently affected by the dimensions of the channel or tube into which the detonation wave is propagating **[2]**. The behaviour of the detonation wave is seen to vary with the geometry of the combustion chamber, the injection mechanism, the chemical kinetics of reacting mixture, the initial conditions and backpressure. The critical parameters associated with the ZND structure in a detonation wave are the cell size interpreted through cell width λ, Ignition Delay Time (IDT) and Induction Zone Length (IZL) **[3-7]**. The detonation cell width λ of the multi-front detonation wave plays a major role in deciding the detonation wave behaviour and reduction in cell size will help to achieve stronger and stable detonations. This detonation cell size is strongly related with the ease with which a mixture can detonate and is found to be correlated with the ignition delay time (IDT), Induction Zone Length (IZL), detonation diffraction and shock wave interactions and also initiation and transition from deflagration to detonation parameters. The fuel-oxidizer chemistry effect is in many ways inferred by the correlation between the ignition delay time, reaction zone length and the cell size. The IDT and IZL is derived from the thermicity peaks in the thermicity distance graph. Thermicity is defined as the effective energy transfer from the chemical bonds to thermal and flow energy and is dependent upon the pressure, the reaction progress variable for the ith species, the density, the sound speed, the reaction rate, the internal energy, the specific volume **[4]**. The limiting parameters of detonation propagation like the diameter of the combustion chamber are also seen to be closely related to the detonation cell size.

Out of the detonation cycle engines PDE and RDE, the RDE is a more viable option due to its ability to produce continuous thrust and operate in wide range of operating conditions **[8-20]**. However, many practical hurdles should be taken care of for the design and development of a rotating detonation engine. At present most of the RDEs can operate for a short duration due to its very high operating temperature **[21-23]**. One of the most fundamental ways to alter the detonation wave characteristics is by addition of ignition promoters and adding diluents into the fuel-oxidizer mixture. It is seen that the addition of ignition promoters or dopants like

Ozone or Hydrogen peroxide significantly reduce the Ignition Delay Time (IDT) and Induction Zone Length (IZL) with significantly negligible change in exothermic and thermodynamic properties of the fuel mixture. This reduces the average cell size making the detonation stronger and enabling us to use a leaner fuel-air mixture. The addition of diluents like Argon, Helium, CO_2, N_2 and H_2O is seen to reduce the CJ temperature post-detonation thus making the combustion chamber of the RDE viable. However, this reduction in temperature is at the cost of increasing the IDT and IZL making the average cell size larger.

This paper mainly focuses on the use of Ethylene as a fuel for detonation cycle engines. The numerical calculations for ethylene-air and ethylene-oxygen detonations were carried out using the Foundation Fuel Chemistry model (FFCM-1). It is seen that addition of trace amounts of ignition promoters/dopants like ozone and hydrogen peroxide can reduce the ignition delay time (IDT) and induction zone length (IZL), thereby, reducing detonation cell width for ethylene-air and ethylene-oxygen mixtures. It is also seen that the addition of diluents like argon and helium up to 90% for ethylene-oxygen and ethylene-air mixtures tend to increase the detonation cell size and reduce the CJ temperature. It is envisaged that the optimal doping and addition of diluents for sensitization of the fuel-oxidizer mixture will enable us to increase the operating limits of detonation cycle engines.

2. NUMERICAL ZND CALCULATIONS

The Foundation Fuel Chemistry Model Ver 1.0 (FFCM1) **[24]** was used for numerical computations. The Princeton Ozone sub-model **[25]** was used for modeling the gas phase kinetics of Ozone. Numerical computations are carried out with CANTERA 2.4 [**26]** open-source software integrated with MATLAB R2018b and Python Ver 3.7. ZND calculations were performed with the modified version of Detonation toolbox **[27]**.

3. RESULTS AND DISCUSSIONS

3.1 Effect of dopants/ignition promoters without diluents

The effects of dopants or ignition promoters ozone and hydrogen peroxide on ethylene-oxygen and ethylene-air mixtures has been studied numerically. It must be noted that the shift of the thermicity peaks to the left indicates a decrease in IZL and IDT with a corresponding decrease in the cell width thereby making the detonation wave stronger and a shift of the thermicity peaks to the right indicates an increase in IZL and IDT with a corresponding increase in the cell width thereby making the detonation weaker. The effect of the addition of ignition promoters at 0, 6000, 10000 and 14000 ppm molar concentration of ozone and hydrogen peroxide on IDT, IZL, T_{cj} and V_{cj} is depicted in Table 1.

3.1.1 Ethylene-oxygen mixtures

The shift of thermicity peaks in Fig 1(a) and the decrease of IDT in Fig 2(a) indicate the effect of the addition of ignition promoters. Addition of ignition promoters like ozone and hydrogen peroxide up to 14000 ppm to ethylene-oxygen mixture showed a shift in the thermicity peaks to the left indicating a stronger detonation without significantly affecting the thermodynamic and gas dynamic properties of the given mixture. It is also evident from the graph that hydrogen peroxide is a better ignition promoter than ozone for ethylene-oxygen mixtures due to the greater shift of thermicity curve to the left. The smooth reduction of IDT with addition of dopant and minimal variation of temperature with addition of dopants can also be seen in Fig. 2(a).

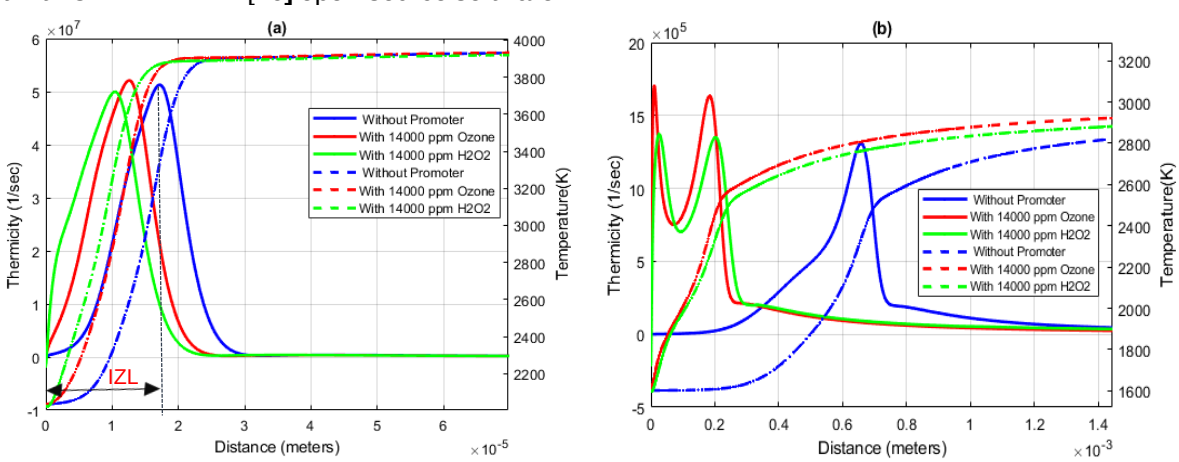

Fig. 1. (a) Variation of Thermicity and T_{cj} for Ethylene-O_2 mixtures with addition of 14000 ppm (molar concentration) of Ozone and H_2O_2 (b) Variation of Thermicity and T_{cj} for Ethylene-Air mixtures with addition of 14000 ppm (molar concentration) of Ozone and H_2O_2 (Solid lines indicate IDT and dotted lines indicate T_{cj}) (Calculations are made at φ = 1, P = 101325 Pa and T = 295K).

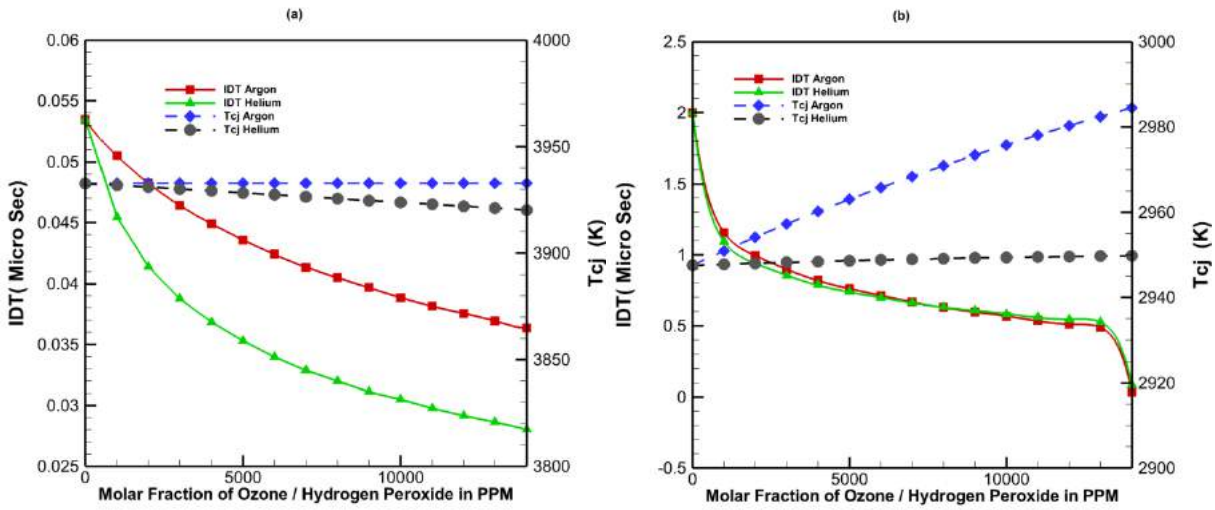

Fig 2. (a) Variation of IDT and T_{cj} for Ethylene-oxygen mixtures with addition of Ozone and H_2O_2 in molar based PPM (b) Variation of IDT and T_{cj} for ethylene-air mixtures with addition of Ozone and H_2O_2 in molar based PPM (Solid lines indicate IDT and dotted lines indicate T_{cj}) (Calculations are made at φ = 1, P = 101325 Pa and T = 295 K).

3.1.2 **Ethylene-air mixtures**

In case of Ethylene-air, the addition of ignition promoters up to 14000 ppm also shifts the thermicity peaks to the left and reduces IDT as shown in Fig. 1(b) and Fig. 2(a) respectively. However, in contrast to ethylene-oxygen mixtures, ethylene-air mixtures show that the effect of ozone is marginally better than that of hydrogen peroxide as seen in Fig. 1(a) with a greater shift of thermicity peak for ozone when compared with hydrogen peroxide. Another observation while comparing Figs. 2 (a) and (b) is that there is a smooth reduction in IDT for ethylene-oxygen mixtures whereas IDT encounters a sudden reduction at around 13000 ppm in case of ethylene-air mixtures. Also, the variation of post-detonation temperature with the addition of ignition promoter is seen to be minimal like in the case of ethylene-oxygen mixture.

Table 1. Detonation parameters for different molar concentrations of ozone and hydrogen peroxide in case of ethylene-oxygen and ethylene-air mixtures. (Calculations are made at initial P = 101325 Pa, T = 295K and ϕ = 1).

Fuel-Oxidizer	**X_{O3} ($x10^6$)**	**X_{H2O2} ($x10^6$)**	**IDT (μs)**	**IZL (mm)**	**$T_{CJ\ (K)}$**	**V_{CJ} (m/s)**
C_2H_4-O_2	0	-	0.053	0.017	3933	2374
	6000	-	0.042	0.014	3933	2371
	10000	-	0.039	0.013	3933	2368
	14000	-	0.036	0.012	3933	2366
	-	6000	0.034	0.012	3927	2371
	-	10000	0.030	0.011	3923	2370
	-	14000	0.028	0.010	3920	2368
C_2H_4-Air	0	-	2	0.66	2948	1833
	6000	-	0.71	0.27	2966	1837
	10000	-	0.56	0.22	2976	1840
	14000	-	0.035	0.010	2984	1841
	-	6000	0.7	0.27	2949	1835
	-	10000	0.58	0.23	2949	1836
	-	14000	0.08	0.02	2949	1836

3.2 **Effect of diluents (Argon and Helium)**

The effect of the addition of diluents on Ethylene Oxygen and Ethylene Air has also been studied numerically. The variation of IDT and the post-detonation temperature as seen in Fig. 3(a) change significantly with the addition of diluents. The effect of addition of diluents at zero, 30%, 60% and 90% concentration by molar fraction of Argon and Helium on IDT, IZL, T_{cj} and V_{cj} is depicted in Table 2. The effect of other diluents like N_2, CO_2 and H_2O have also been studied and it is seen that diluents like Argon and Helium are more effective in maintaining detonation even at higher diluent percentage. The slope of increase of IDT and IZL is also seen to be lower for Argon and Helium when compared to other diluents. The effectiveness of diluents can be arranged in the order Argon > Helium > Nitrogen > Water > Carbon dioxide. The IDT and IZL values are derived correspondingly from the thermicity curves.

3.2.1 **Ethylene-oxygen mixtures**

The addition of diluents like Argon and Helium show almost similar trend for of IDT and IZL for ethylene-oxygen mixtures. The IDT and IZL increase gradually up to 80 % thereafter show a steep rise with the addition of Argon and Helium. This clearly indicates that the addition of diluents reduces the detonation strength of the mixture. The main advantage of addition of diluents is a reduction in post-detonation temperature by nearly 1400 K. This significant reduction in post-detonation temperature will enable us to design a combustion chamber that can operate at lower temperature range. One observation where Argon and Helium differ is that with the addition of Argon the V_{cj} reduces whereas in case of Helium V_{cj} increases. This can be attributed to the difference in molecular weight of the two species.

3.2.2 **Ethylene-air mixtures**

The addition of Argon and Helium as diluents show a reduction in IDT and IZL for ethylene-air mixtures as in the case of ethylene-oxygen mixtures. The IDT and IZL increase gradually up to 70% and thereafter increases abruptly with the addition of Argon and Helium. The decrease in post-detonation temperatures up to 1800 K is seen for Argon dilution and up to 1200 K for Helium dilution. Helium dilution is also seen to quench the detonation earlier than in the case of Argon. A similar trend is also noticed in the case of ethylene-air and ethylene-oxygen mixtures where V_{cj} decreases for Argon dilution while it increases for Helium dilution.

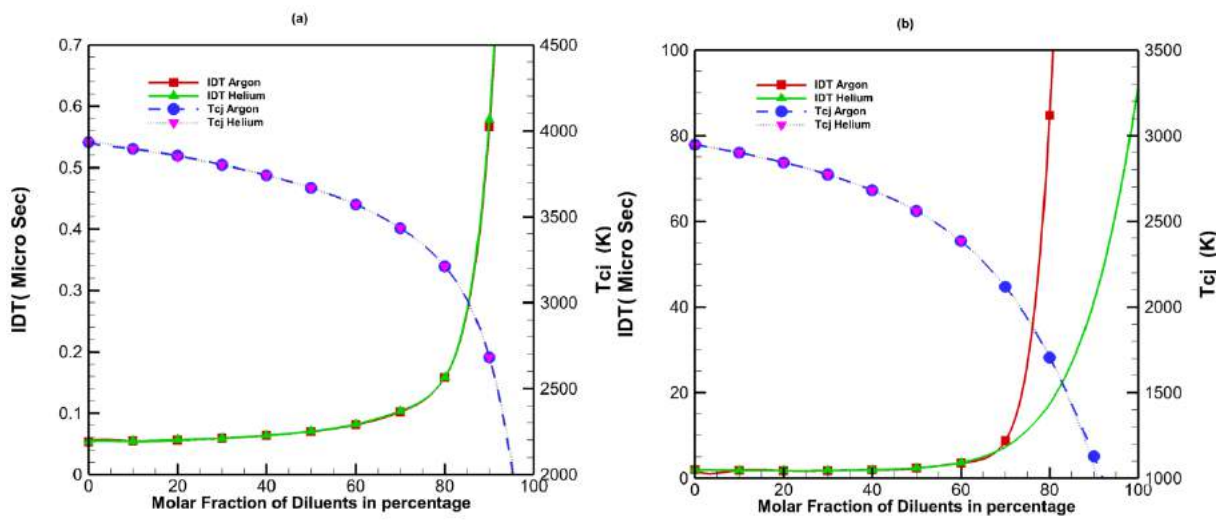

Fig 3. (a) Variation of IDT and T_{cj} for ethylene-oxygen mixture with addition of Argon and Helium in percentage molar fraction (b) Variation of IDT and T_{cj} for ethylene-air mixtures with addition of Argon and Helium in percentage molar fraction (Solid lines indicate IDT and dotted lines indicate T_{cj}) (Calculations are made at φ = 1, P = 101325 Pa and T = 295 K).

Fuel-Ox	X_{Ar}	X_{He}	IDT (μs)	IZL (mm)	$T_{CJ\ (K)}$	V_{CJ} (m/s)
	0	-	0.053	0.017	3933	2374
	0.3	-	0.058	0.020	3802	2134
	0.6	-	0.080	0.030	3571	1887
C_2H_4-O2	0.9	-	0.566	0.225	2682	1491
	-	0.3	0.059	0.024	3802	2588
	-	0.6	0.082	0.049	3571	2957
	-	0.9	0.578	0.554	2683	3560
	0	-	1.999	0.656	2948	1833
	0.3	-	1.771	0.614	2772	1670
	0.6	-	3.554	1.285	2384	1465
C_2H_4-Air	0.9	-	11.99	3.616	1129	943
	-	0.3	1.792	0.763	2772	2048
	-	0.6	3.654	2.111	2384	2339
	-	0.8	89.734	65.249	1706	2458

Table 2. Detonation parameters for different molar concentrations of Argon and Helium in case of ethylene-O_2 and ethylene-air mixtures (Calculations made at initial P = 101325 Pa, T = 295 K and ϕ = 1).

3.3 **Combined effect of ignition promoters and diluents**

The addition of dopants in small concentrations has shown a positive effect of making the detonation wave stronger due to decrease in IDT and IZL without significantly changing he thermodynamic and gas dynamic properties. The post-detonation temperature is of the order of 3500 K to 4000 K and it is difficult to design a combustion chamber that can operate continuously in this regime. The heat loads experienced by the combustion chamber at these temperatures are phenomenal which is a complex issue that needs to be resolved. The effect of diluents has shown that its addition weakens the detonation strength. However, one advantage of addition of diluents is the tremendous decrease in temperature, bringing the post-detonation products to a range of temperature where the combustion chamber can operate continuously without material failure. The optimal addition of dopants and diluents will enable us to reduce the post-shock temperature to desirable limits and maintain the detonation strength so that detonation is not quenched.

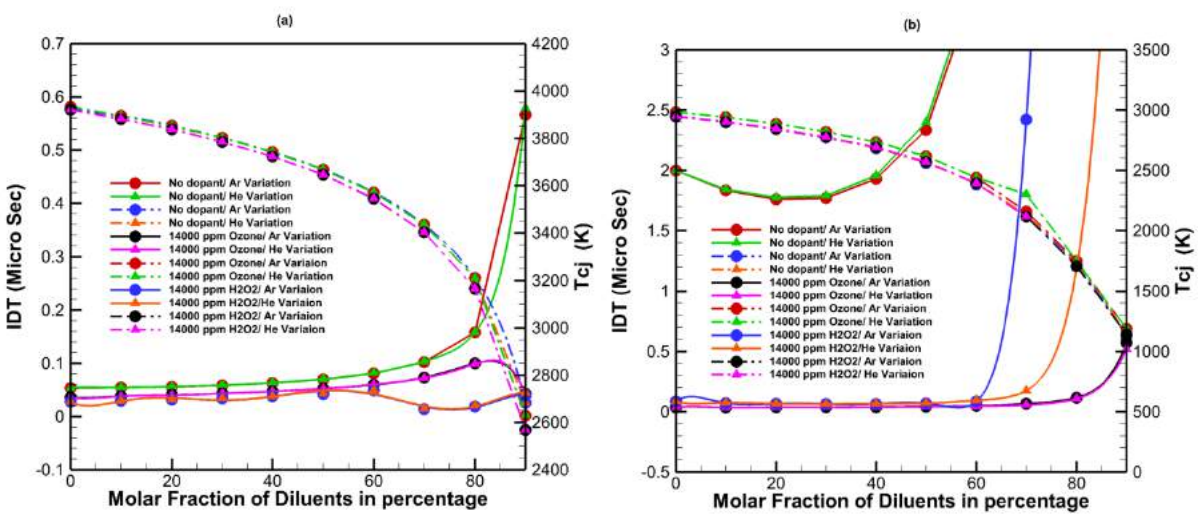

Fig 4. (a) Variation of IDT and T_{cj} for ethylene-oxygen mixture for a fixed doping level of Ozone and H_2O_2 (14000 ppm). However, percentage molar fraction of diluents is varied from 0-90%. (b) Variation of IDT and T_{cj} for ethylene-air mixture for a fixed doping level of Ozone and H_2O_2 (14000 ppm). However, percentage molar fraction of diluents is varied from 0-90%. (Solid lines indicate IDT and dotted lines indicate T_{cj}) (Calculations are made at φ = 1, P = 101325 Pa and T = 295 K).

3.3.1 **Ethylene-oxygen mixtures**

Now keeping the molar concentration of dopant Ozone and Hydrogen peroxide fixed at 14000 ppm and varying the concentrations of Argon and Helium for ethylene-oxygen mixture, we can find that the IDT and IZL values are maintained even at higher concentration of diluent addition. One major milestone that we are achieving here is maintaining stronger detonation with significant reduction in temperature even at higher concentration of diluent addition. Hydrogen peroxide as a dopant is found to be more effective than Ozone at all diluent concentrations and its effectiveness is found to improve further when diluent concentration exceeds 70%.

3.3.2 **Ethylene-air mixtures**

Keeping molar concentration of dopant i.e. Ozone and Hydrogen peroxide fixed at 14000 ppm and varying the diluents i.e. Argon and Helium for ethylene-air mixture, we found that the IDT and IZL values are maintained even at higher concentration of diluent addition. Here also we are able to maintain a stronger detonation with a significant reduction in post-detonation temperature even at higher concentrations of an inert diluent. The effect of dopants like ozone and hydrogen peroxide is seen to be more effective in case of ethylene-air in comparison to ethylene -oxygen.

4. CONCLUSION

The following conclusions can be drawn from the present work:

- The addition of H_2O_2 and Ozone dopants to ethylene-oxygen and ethylene-air mixtures will significantly alter the ignition chemistry (i.e reducing IDT and IZL) without significantly impacting the gas dynamics and thermodynamic states of the given mixture.
- The addition of diluents like Argon and Helium can reduce the temperature of the post-detonation products considerably at the cost of increasing IDT and IZL. This reduction in IDT and IZL can be compensated by the addition of dopants like Ozone and Hydrogen Peroxide.
- It is envisaged that the optimal doping and addition of diluents for sensitization of the Ethylene-oxidizer mixture will enable us to increase the operating limits of detonation cycle engines for practical applications.

5. ACKNOWLEDGEMENT

This work is supported by the Start-up research grant of Indian Institute of Technology Kanpur.

6. REFERENCES

[1] Jiun-Ming Li, Chiang Juay Teo, Boo Cheong Khoo, Jian-Ping Wang, Cheng Wang (eds.), Detonation Control for Propulsion, 2018
[2] John H.S Lee, The Detonation Phenomenon
[3] Yunfeng Liu, Wei Zhand, Zonglin Jiang, Relationship between ignition delay time and cell size of H_2-Air detonation, International Journal of Hydrogen Energy 2016
[4] Jackson Crane, Xian Shi, Ajay V. Singh, Yujie Tao, Hai Wang, Isolating the effect of induction length on detonation structure: Hydrogen-oxygen detonation promoted by ozone, Combust. Flame 200 (2019) 44-52.
[5] A. A. Vasil'ev , Cell Size as the Main Geometric Parameter of a Multifront Detonation Wave by, Journal of propulsion and Power, Vol.22, No. 6-2006.
[6] K. Kailasanath, E.S. Oran, J.P. Boris and T.R. Young, Determination of Detonation Cell Size and the Role of Transverse Waves in Two-Dimensional Detonations, Combust. Flame. 61:199-209 (1985)
[7] Charles K. Westbrook and Paul A.Urtiew, Chemical Kinetic Prediction of Critical Parameters in Gaseous Detonations, Combust. Inst. 19 (1982), 615-623.
[8] D A Schwer and K. Kailasanath, Numerical Investigation of Rotating Detonation Engines by, 43rd AIAA/SAE/ASEE Joint Propulsion Conference, 2010
[9] [William H. Heiser, Thermodynamic Cycle Analysis of Pulse Detonation Engines, Journal of Propulsion and Power, 2002
[10] Jiro Kasahara and Sergey Frolov, Present Status of Pulse and
[11] Rotating Detonation Engine Research, 25th ICDERS, 2015
[12] Bulat Pavel Viktorovich, About the Detonation Engine, American Journal of Applied Sciences 11 (18): 2014 (1357-1364)
[13] D.F. Dausen, C.M. Brophy, R.G. Wright and J.D. Marder, Design of Optically-Accessible Rotating Detonation Engine, 48th AIAA, Joint Propulsion Conference and Exhibit-2012
[14] R. Mevel, D. Davidenko et.al, Detonation in Hydrogen-Nitrous Oxide-Diluent Mixtures: An Experimental and Numerical Study, Combust. and Flame -2014
[15] J. Kindracki, A. Kobiera P.Wolanski, Z.Gut, M.Folusiak and K. Swiderski, Experimental and Numerical Study of the Rotating Detonation Engine in Hydrogen Air Mixtures, Progress in Propulsion Physics 2 (2011) (555-582)
[16] K. Kailasanath, Review of Propulsion Applications of Detonation Waves, AIAA Journal, Vol 38, 2000
[17] Eric M. Braun, Frank K. Lu, Airbreathing rotating detonation wave engine cycle analysis, Aerospace Science and Technology 27 (2013) (201-208)
[18] Zhou Rui, Wu Dan, Wang Jianping, Progress of Continuously rotating detonation engines, Chinese Journal of Aeronautics, (2016), 29(1): (15-29)
[19] E. Winterberger and J.E Shepherd Thermodynamic Cycle Analysis for Propagating Detonations, Journal of Propulsion and Power, Vol. 22, No.3-2006.
[20] Andrew St. George, Robert Driscoll, Vijay Anand, Steve Randall, David Munday and Ephraim J. Gutmark., Development of a rotating Detonation Engine Facility at the University of Cincinnati, 53rd AIAA Aerospace Sciences Meeting-2015.
[21] J. Kindracki, P. Wolanski, Z. Gut, Experimental research on the rotating detonation in gaseous fuels-oxygen mixtures. 22nd International Colloquium on Dynamics of Explosions and Reactive Systems-2009.
[22] Steven Randall, Andrew St. George, Robert Driscoll, Vijay Anand, and Ephraim J. Gutmark, Numerical and Experimental Study of Heat Transfer in a Rotating Detonation Engine,53rd AIAA Aerospace Sciences Meeting-2015

[23] Bykovskii, F.A., and Vedernikov, Heat Fluxes to Combustor Walls during Continuous Spin Detonation of Fuel-Air Mixtures, J.Phys.: 2009.
[24] Arnab Roy, Peter Strakey, Todd Sidwell and Don Ferguson, Unsteady Heat Transfer Analysis to Predict Combustor Wall Temperature in Rotating Detonation Engine, 51st AIAA/SAE/ASEE Joint Propulsion Conference, 2015
[25] G. P. Smith, Y. Tao, and H. Wang, Foundational Fuel Chemistry Model Version 1.0 (FFCM-1), http://web.stanford.edu/group/haiwanglab/FFCM-1/index.html, 2016.
[26] H.Zhao, X.Yang, Y. Ju, Kinetic studies of ozone assisted low temperature oxidation of dimethyl ether in a flow reactor using molecular beam mass spectrometry, Combust. Flame 173 (2016) 187-194.
[27] David G. Goodwin, Raymond L. Speth, Harry K. Moffat, and Bryan W. Weber. Cantera: An object-oriented software toolkit for chemical kinetics, thermodynamics, and transport processes. https://www.cantera.org, 2018. Version 2.4.0. doi:10.5281/zenodo.1174508
[28] S. Browne, J. Ziegler, and J. E. Shepherd, Numerical Solution Methods for Shock and Detonation Jump Conditions, GALCIT Report FM2006.006 - R3, California Institute of Technology Revised September, 2018.

7. BIOGRAPHIES

Squadron Leader Kiran Ivin has completed his bachelor's Degree in Aeronautical Engineering from Anna University in the year 2009. Thereafter, He was commissioned to Indian Air Force in 2010 in the Engineering Branch. He is trained in the Sukhoi-30 MKI aircraft systems. He is presently doing his M Tech in Aerospace engineering (Propulsion) in IIT Kanpur.

Dr Ajay Vikram Singh is an Assistant Professor in the Department of Aerospace Engineering at Indian Institute of Technology, Kanpur. He completed his MTech in Aerospace Engineering (Propulsion) at IIT Kanpur in 2008 and received Doctor of Philosophy (Ph.D.) in Mechanical Engineering from University of Maryland, College Park, USA in 2015. He worked as Postdoctoral Researcher in the Department of Mechanical Engineering, Stanford University, USA. His research interests are in advanced propulsion technologies including detonation cycle engines and hybrid turboelectric propulsion, soot formation and oxidation, flame-synthesized functional nanoparticles for renewable energy devices and fire dynamics with applications to both industry and academia.

Study the Effect of Axi-swirl Injector on the Regression Rate of the Hybrid Rocket

Pragya[a] and Shelly Biswas[b]

Department of Space Engineering and Rocketry,

Birla Institute of Technology, Mesra, Ranchi-835215 (India)

[a]pragyaberwal16@gmail.com, [b]shellybiswas@bitmesra.ac.in

***Abstract*- The performance of a hybrid rocket is dependent on the injection pattern of the oxidizer into the combustion chamber as the combustion process takes place. The flame is established inside the boundary layer. This boundary layer formation acts as hindrance in the interaction between the oxidizer and the fuel grain surface which reduces the heat feedback to the fuel surface. This can be achieved by reducing the boundary layer thickness and altering the attachment locations of the oxidizers over the fuel surface. The present work has investigated two injector patterns i.e. shower head and axi-swirl injectors to reduce the boundary layer hindrance and enhance combustion efficiency of a hybrid rocket using paraffin wax and Polyvinyl chloride (PVC) fuel. An axi-swirl injector was designed to create recirculation zone inside the chamber high enough to increase the regression rate of the fuel with stable combustion. Regression rate and combustion efficiency of paraffin wax fuel increased by 6% and 8.85% using the novel injector. For PVC fuel, regression rate shows no significant changes but combustion efficiency was raised by 5.5% using novel injector.**

***Index Terms*- Hybrid Rocket, Paraffin wax, Polyvinyl chloride, combustion efficiency, regression rate, shower head, axi-swirl injector, recirculation zone.**

1. INTRODUCTION

A hybrid rocket is a type of chemical rocket in which fuel and oxidizer are present in different phases. The fuel is present in combustion chamber in solid phase and the liquid or gaseous oxidizer is injected into the combustion chamber through an injector. The ignition is achieved with the help of an external heat source. The solid fuel surface is subjected to pyrolysis and hence it is decomposed and gasified. Thevapours further mix with the oxidizer to undergo combustion and the combustion products are expanded through the nozzle to develop the thrust [1]. The hybrid rockets have several distinct advantages over the solid and liquid propellant rockets. Simplicity, safety, lower cost and thrust tailoring are among the most attractive features of a hybrid rocket. The solid fuel regression rate is the key parameter for the characterization of the hybrid rocket's internal ballistics [2]. It was widely demonstrated, both theoretically and experimentally, that in the absence of radiation, the regression rate of the solid fuel depends on the convective heat transfer from the flame to the fuel surface. Marxman and Gilbert [3] developed a turbulent boundary layer regression rate ($\dot{r}$) model yielding that mass flux (G) is the fundamental factor governing the rate of fuel consumption ($\dot{r} \alpha G^{0.8}$).

Apart from the various advantages, hybrid rocket motors face some technical challenges such as low regression rate, changing O/F ratio, reduced combustion efficiency, combustion instability and sliver loss [4]. Several techniques have been proposed to increase the regression rate of solid fuel in hybrid rocket which includes use of protrusion [5], use of multi-port grain, use of paraffin-wax fuels, high mixture ratio values, swirling the flow inside chamber, particle additives in solid fuel, energetic compounds like plasticizers and binders with solid fuel [6], and manufacturing of grains with inner helical shape [7].

The combustion process in a hybrid rocket is achieved by oxidizer flow over the solid fuel grain leading to the formation of a turbulent diffusion boundary layer and the flame is established inside the boundary layer. This boundary layer formation acts as a hindrance in the interaction between the oxidizer and the burning surface of fuel grain and hence reduces the heat feedback to the fuel surface. The two different injection patterns that can be used to reduce this hindrance due to boundary layer is either by creating recirculation zones in the chamber or by direct impingement of the oxidizer flow onto the fuel grain surface. Several researches have been conducted on various injector designs such as converging nozzle injector, shower head injector, swirl injector and radial injector to enhance the fuel regression rate and reduce the combustion instability in the hybrid rockets.

Pucci (2002) [8] studied the flame holding instability in the hybrid rocket using axial, radial and swirl injectors. He concluded that swirl injector with super-critical swirl flow does produce stable combustion possibly due to the establishment of a central toroidal recirculation zone (CTRZ) and also an increase in regression rate by 182% in comparison to the axial injector. He also concluded that swirl injector with sub-critical swirl flow does pro-

duce unstable combustion because of weak swirling flow instabilities.

Carmicino and Sorge (2005) [9] studied the role of injection on the regression rate of hybrid fuel using a converging nozzle injector with exit diameter of 8 mm. They concluded that regression rate, at same oxidizer mass flux and chamber pressure, exhibited weaker dependence upon the mass flux. The researchers also observed that the non-uniform oxidizer injection and the oxidizer impinging jet zone dynamics strongly influence the heat transfer mechanism to the fuel grain surface which enhances the regression rate.

The direct impingement of the axi-radial oxidizer on the fuel surface was observed to enhance the interaction of fuel and oxidizer by delaying the boundary layer formation. Martino, Malgieri, Carmicino and Savino, 2016 [10] has carried out numerical analysis in Ansys-Fluent to conclude that uniform fuel consumption can be obtained in an injector configuration midway between axial and radial patterns. They experimentally observed an enhancement in the regression rate at the head end by 5 times in comparison to the axial injector. Also, the fuel consumption was observed to be uniform reducing the combustion instability as compared to the radial injector. Thus, the present work deals with designing a novel injector consisting of aaxi-swirl injection pattern. This leads to recirculation zone formation of the oxidizer over the fuel surface which would in turn increase the regression rate of the fuel and lead to uniform burning throughout the grain.

2. Experimental set up

The experimental setup used for the current study consists of hybrid motor combustion chamber of length 188mm and inner diameter of 50mm. The converging-diverging nozzle used has a throat diameter of 10mm and exit diameter of 25mm. The schematic of the lab scale hybrid rocket motor is shown in figure 1.

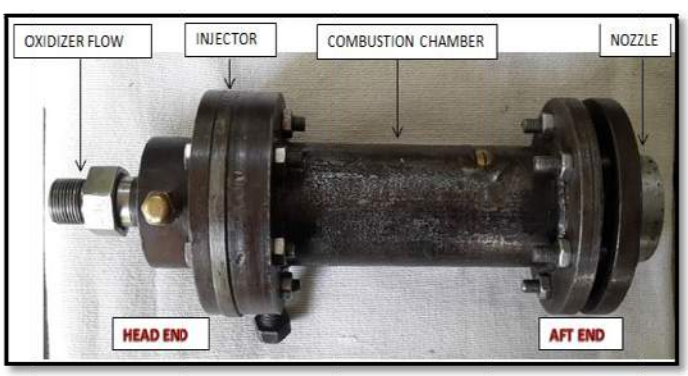

Fig 1 – Lab Scale Hybrid rocket motor

The port diameter of the fuel grain is taken to be 21mm as the diverged holes of the novel injector had a pitch circle diameter (PCD) of 20mm.The two injectors used are shower head injector and novel axi-swirl injector. The shower head injector plate has 21 holes of 1mm hole diameter as shown in figure 2. The axi-swirl injector has 10 holes of 1.5 mm diameter each with 6 axial holes, 5 holes at a PCD of 7 mm and 1 hole at the centre, and 4 tangential holes at angle of 45^0 as shown in figures 3.

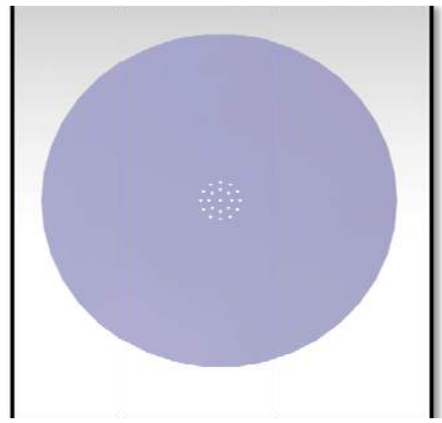

Fig 2-Shower head injector (3-D)

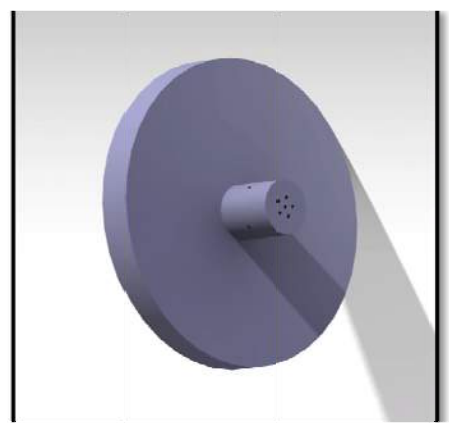

Fig 3 – Axi- swirl injector

The polymer based fuel used in the present study is polyvinyl chloride (PVC) plastisol grain. The compatible plasticizer used is di-octyl phthalate (DOP). The PVC fuel and the plasticizer were mixed thoroughly using a sigma blade mixer at a high rpm for 1 hour and then casted in a mould. The aluminiummould used has a length of 188mm and inner diameter of 50mm. The aluminium mandrel used is of 21mm diameter to create a tubular port in the fuel grain. The mould was kept at 120^0C for 4 hours in the hot air oven for curing and then the grain was allowed to cool down slowly to avoid cracks. The grain was extracted from the mould and loaded in the combustion chamber of the motor using silicon grease as an insulator. The other fuel i.e. paraffin wax was melted and then casted in the aluminium-

mouldwith mandrel of 21mm diameter. The curing of wax was done for 2 hours at ambient temperature. The wax fuel grain was loaded in the combustion chamber using PVC tube. Gaseous oxygen stored in cylinders is used as an oxidizer for both the fuels. The oxygen cylinder is placed on the digital weighing balance with a least count of 1 gm and maximum capacity up to 150 kg. The mass flow rate of the oxygen is measured using this weighing balance and a constant mass flow rate of 30gm/s is maintained for the experimentation purpose. The oxygen flow is controlled by a solenoid valve connected to a sequential timer. The sequential timer was used to control the operation of solenoid valve and the igniter battery. An igniter, made up of solid composite propellant bead with nichrome wire, is supplied with a power supply of 12Volts for 2 seconds which is sufficient for a small hybrid propellant to burn effectively. The pressure gauge is installed at various locations of the oxygen flow lines to visualize the pressure at each location.

3. Results and Discussion

In the current experimental study, polyvinyl chloride (PVC) and paraffin wax were used as fuel and gaseous oxygen was used as oxidizer. The port diameter of the fuel grain was 21mm and the length of grain was 188mm. The interrupted test firing of 2 seconds was done for 4 times with a total burn time of 8 seconds for PVC fuel grain. For paraffin wax fuel grain, the interrupted test firing of 0.75 seconds was done for 4 times with a total burn time of 3 seconds. This method of interrupted test is considered to be the best method suited for regression rate calculations as it mimics the actual situation in a hybrid rocket motor to the closest [11]. The oxidizer mass flow rate of 30 gram/second was maintained for both the injector designs. The injectors used in the present study were shower head injector and aaxi-swirl injector and the regression rate was obtained by weight loss method. The results are shown in figures 4a and 4b.

The figure 4a depicts the regression rate study using both the injector types for PVC fuel grain. The use of axi-swirl injector is observed to decrease the average regression rate of the hybrid fuel grain. For both shower head injector and axiswirl injector, the regression rate of the fuel grain increases with increase in oxidizer mass flux. The regression rate improvement with the axi-swirl injector was around 4% at higher oxidizer mass flux as compared to the shower head injector. This overall decrease in regression rate using axi-swirl injector may have occurred due to the interference of oxidizer molecules flowing through axial holes as compared to the molecules flowing through the tangential hole at an angle of 45^0. This interference would have led to decrease in the length of the swirling motion and direct impingement of oxidizer flow on the fuel grain surface is not attained.

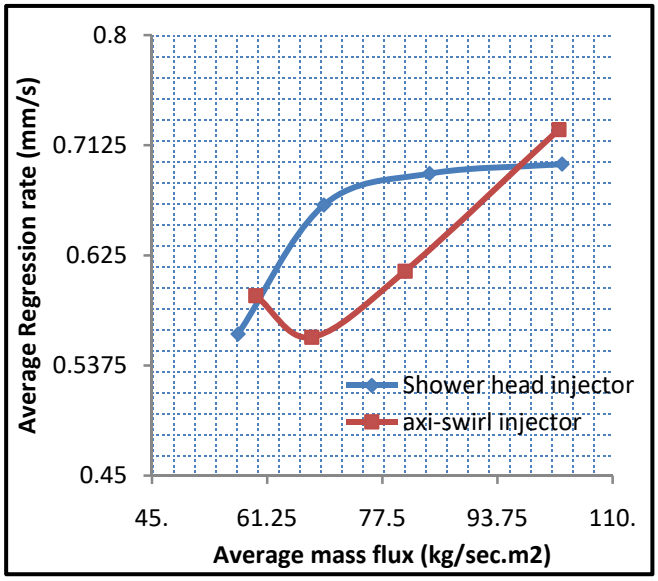

Fig 4a- Regression rate vs Oxidizer mass flux for PVC fuel grain using shower head and axi-swirl injector

The figure 4b depicts the regression rate of paraffin wax fuel grain using both the injector designs. The novel injector design improves the average regression rate of the wax fuel by 6%. In case of axi-swirl injector, the swirl motion of oxidizer particles and droplet entrainment phenomenon exhibited by wax fuel leads to a higher average regression rate as compared to the shower head injector.

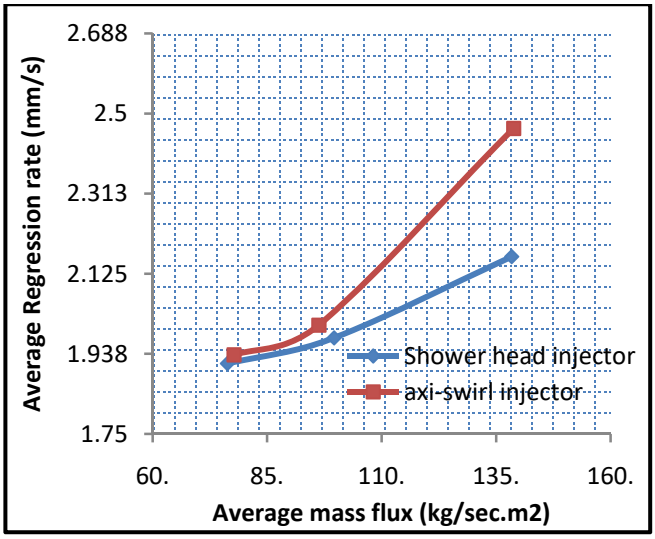

Fig 4b- - Regression rate vs Oxidizer mass flux for Paraffin wax fuel grain using shower head and axi-swirl injector

The novel injector design pattern actually shows a good improvement in the regression rate of both the fuel grain types at low and high oxidizer mass flux depicting the increase in heat feedback to the grain surface during

combustion. Also, the combustion of the fuel is enhanced due to disruption of boundary layer over the grain surface and better mixing of oxidizer and pyrolyzed fuel.

The local regression rate of PVC fuel grain from head end to aft end for both the shower head and multi-angle diverging injectors is shown in figure 5. Figure 5 shows that the local regression rate at aft end is more than at head end for the shower head injector. The graph also suggests that there is a high sliver loss at head end and non-uniform fuel consumption takes place. On contrary, axi-swirl injector leads to uniform fuel consumption.A rise in local regression rate at head end of around 42.3% was observed using axi-swirl injector for non-liquefying fuel i.e. PVC+DOP in comparison to shower head injector.This rise in local regression rate at head end for axi-swirl injector is because of the higher thermal energy of oxidizer particles at the head end. The collision of axial and swirl motion of oxidizer particles create a turbulence zone which increases the heat flux at the head end.

The paraffin wax fuel grain was completely consumed during the firing as it is a liquefying fuel which forms a melt layer enhancing the regression rate. Thus, no local regression rate studies were done for paraffin wax fuel.

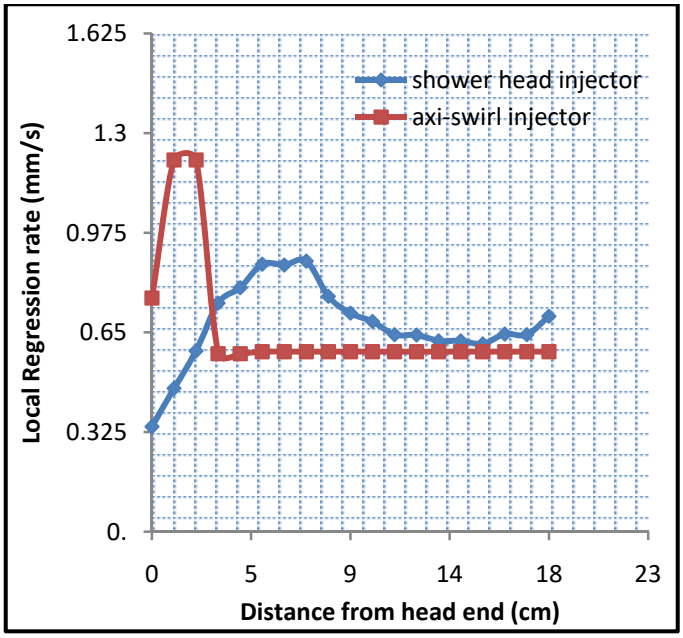

Fig 5- Local regression rate along the PVC fuel grain length using shower head and axi-swirl injector

Table 1 shows the comparison of combustion efficiency for the two injector types utilized in the present study for the two fuel types. Axi-swirl injector shows an increase in combustion efficiency by 5.5% and 8.85% as compared to the shower head injector for PVC and paraffin wax fuel types respectively. Although, a decrement in average regression rate was observed using axi-swirl injector but vortex created by the swirling flow of oxidizer particles has enhanced the mixing of reactants. This in turn leads to proper combustion process inside the combustion chamber.

Table 1: Combustion efficiency data for present study

Fuel type	Injector type	Average Chamber Pressure (Psi)	O/F ratio	Theoretical characteristic velocity (m/s)	Combustion Efficiency	% rise in efficiency
PVC + DOP	Shower head injector	74.26	2.55	1558.5	61.9	-
PVC + DOP	Axi-swirl injector	74.52	2.96	1524.5	65.3	5.50
Paraffin wax	Shower head injector	93.83	0.96	1382.3	60.23	-
Paraffin wax	Axi-swirl injector	101.63	0.98	1389.8	65.56	8.85

4. Conclusion

In the present study, a novel injector pattern was designed to improve the regression rate and combustion efficiency of the hybrid fuel grain at same oxidizer mass flow rate. The following conclusions can be deduced from the present study:

1. A rise in local regression rate at head end of around 42.3% was observed using axi-swirl injector for non-liquefying fuel i.e. PVC+DOP in comparison to shower head injector.
2. Uniform burning downstream of the combustion chamber and sliver loss reduction was observed using axi-swirl injectors for PVC+DOP fuel in comparison to non-uniform burning observed using shower head injector.
3. Axi-swirl injector showed 5.5% rise in combustion efficiency for non-liquefying fuel i.e. PVC+DOP as compared to the shower head injector.
4. An increase in the average regression rate using axi-swirl injectors was observed to be 6% respectively as compared to shower head injector for liquefying fuel i.e. paraffin wax.
5. Enhancement of combustion efficiency of 8.85% using axi-swirl injectors respectively as compared to shower head injector was obtained for liquefying fuel i.e. paraffin wax.
6. Axi-swirl injector shows a negligible decrease in regression rate with better combustion efficiency for

PVC+DOP fuel as compared to the shower head injector.

5. References

1. D. Altman, R.Humble, 'Hybrid rocket propulsion systems', in: R.W.Humble, G. N. Henry, W.J.Larson (Eds.), 'Space propulsion analysis and design', 1st edition, McGraw–Hill, New York, 1995, pp.365–401.
2. G.P.Sutton, O.Biblarz (Eds.), 'Hybrid propellant rockets', in: 'Rocket propulsion elements', 7th Ed., John Wiley & Sons, 2001, pp.585–593.
3. G. A. Marxman, and M. Gilbert, "Turbulent boundary layer combustion in the hybrid rocket," Ninth International Symposium on Combustion, Academic Press, New York, 1963, pp. 371–383.
4. V. Sankaran, 'Computational fluid dynamics modeling of hybrid rocket flow-fields' in: 'Fundamentals of hybrid rocket combustion and propulsion', edited by K. Kuo, M. Chiaverini, Vol.218. Progress in Astronautics and Aeronautics, AIAA, Reston, VA, 2007, pp.323-349.
5. Rajiv Kumar, P.A. Ramakrishna, "Effect of protrusion on the enhancement of regression rate", Aerospace Science and Technology, 39 (2014),pp.169–178.
6. P. Dario, "Approaches to low fuel regression rate in hybrid rocket engines", Review Article, International Journal of Aerospace Engineering, Volume-2012,DOI:10.1155/2012/649753.
7. C. Lee, Y. Na, J. W. Lee and Y. H. Byun, "Effect of induced swirl flow on regression rate of hybrid rocket fuel by helical grain configuration", Aerospace Science and Technology, Volume 11, No.1, 2007, pp.68-76.
8. J. M. Pucci, "The effects of swirl injector design on hybrid flame-holding combustion instability", 38th AIAA/ASME/SAE/ASEE Joint Propulsion Conference & Exhibit, 7-10 July 2002, Indianapolis, Indiana.
9. C. Carmicino and A. R. Sorge, "Role of injection in hybrid rockets regression rate behaviour", Journal of Propulsion and Power, Volume-21, No. 4, July-August 2005.
10. G. D. Di Martino, P. Malgieri, C. Carmicino, R. Savino, "A simplified computational fluid-dynamic approach to the oxidizer injector design in hybrid rockets", ActaAstronautica 129 (2016), pp.8-21.
11. R. Kumar and P. A. Ramakrishna, "Issues related to the measurement of regression rate of fast burning hybrid fuels", Journal of Propulsion and Power, Vol-29, No-5, 2013, pp. 1114-1121.

6. Biographies

a). Ms. Pragya is pursuing Ph.D. at Aerospace Department, I.I.T Bombay, Mumbai (2019 onwards)
M.E. Rocket Propulsion, Space Engg. & Rocketry Department, B.I.T Mesra, Ranchi (2016-2018)
B.Tech Aerospace Engg with specialization in Avionics, U.P.E.S Dehradun (2012-2016)

b). Dr. Shelly Biswas
Assistant Professor
Department of Space Engineering & Rocketry
Birla Institute of Technology Mesra (2016-till date)
Assistant Professor, Vel Tech University, Avadi, Chennai (2014-2015)
Ph.D., IIT Delhi (Nov 2007-Nov 2013)
M.Tech. (Fuels & Combustion)BIT Mesra, Ranchi (2005-2007). The author has published 14 papers in International Journals and conferences. The Author is a reviewer for many international journals of repute.

CFD Analysis of Convergent - Divergent Jet Nozzle of a Fighter Aircraft Gas Turbine Engine

1. VED PRAKASH, PhD student, Mechanical Engineering. DIAT, Pune, India.
(Email: vedprakash.sp@gmail.com)
2. SUNIL CHANDEL, Assistant professor, Mechanical Engineering, DIAT, Pune, India.
(Email: suniliitd2003@gmail.com)
3. R.K. MISHRA, Scientist G, CEMILAC, DRDO, Bengaluru, Karnataka, India
(Email: rkmishra.drdo@gmail.com)

Abstract--The purpose of this paper was to do CFD analysis of a 2D convergent-divergent nozzle. The use of such kind of nozzle is essential for supersonic aircraft. Many researchers had worked in the development of this nozzle in early days. For different pressure inlet conditions analysis has been performed. The finite volume method has been used for the numerical analysis. Mach number, static pressure and Temperature contours have been plotted for the Convergent-divergent nozzle. The reversed flow at the exit of convergent-divergent nozzle has been found and analysed.

Index terms-- convergent-divergent nozzle, different pressure inlet conditions, finite volume analysis, reversed flow.

1. INTRODUCTION

A nozzle is a varying cross-sectional area tube, which is usually axisymmetric in nature. It is use to increase the speed of an outflow by controlling direction and shape of the flow. Nozzle flow always generates forces associated to the change in flow momentum, as we can feel by hand- holding a nose and opening the tap. In the simplest case of rocket nozzle, relative motion is created by ejecting mass from a chamber backwards through the nozzle, with the reaction forces acting mainly on the opposite chamber wall, with a small contribution from nozzle walls. As important as the propeller is to shaft-engine propulsions, so it is the nozzle to jet propulsion, since it is in the nozzle that thermal energy (or any other kind of high- pressure energy source) transforms into kinetic energy of the exhaust, and its associated linear momentum producing thrust. A convergent-divergent De Laval nozzle is typically used to convert the heat liberated in the combustion chamber into kinetic energy for propulsion. Thrust is mainly produced by the momentum imparted to the products of combustion when discharging through the exhaust nozzle. During their passage, the gases are continuously accelerated from low subsonic to high supersonic velocities [1].

The convergent-divergent nozzle may be divided into three parts:

1. The convergent subsonic section whose design influences the mass flow of the exhaust gases and, to some extent, the combustion efficiency achieved in the chamber,

2. The throat section which determines, with the operating conditions in the combustion chamber, the mass flow rate through the nozzle, and

3. The divergent supersonic section whose wall configuration, together with the exit area, determines the additional velocity imparted by the expansion of gases through this portion of the nozzle.

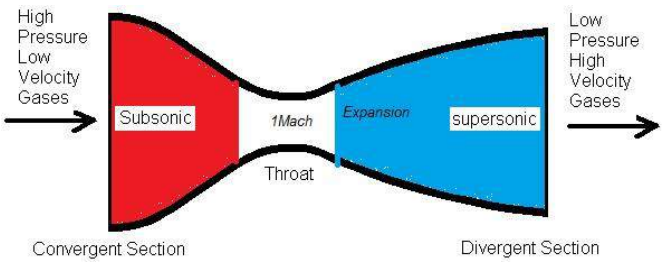

Fig.1. Convergent-Divergent nozzle [8]

David Munday and Ephraim Gutmark[2] has done acoustic radiation analysis. To reduce the effective velocity exiting the exhaust nozzle without increasing the bypass ratio of the engine or reducing effective thrust, the jet flow should mix faster and entrain more of the surrounding ambient flow. Dragan Kozulovic[3] has

seen that velocity non-uniformity reduce the propulsive efficiency. At diverging section, velocity vector also vary in other direction, which causes the thrust reduction. Gary G. Podboy et.al.[4] has visualized a very high levels of jet noise produced by high performance military aircraft during take-off and landing operations. Which causes serious health risks to personnel working on aircraft carriers.

2FINITE VOLUME ANALYSIS

2.1. Modelling of convergent-divergent jet nozzle:

The half convergent-divergent 2D nozzle specimen considered for the present analysis is shown in Fig.2. The length of the nozzle is taken as L= 580mm, inlet diameter d_1 = 375mm, outlet diameter d_2 = 370mm, throat diameter d_{th} = 350mm.

Convergent-divergent nozzle is made up of Titanium alloy. The fluid is taken air, which is considered as ideal gas for the analysis. The boundary conditions are mentioned in table 1.

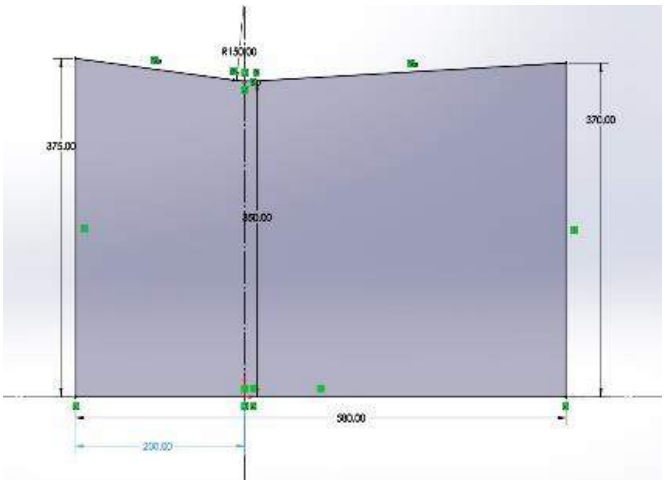

Fig.2. Convergent-divergent 2D nozzle

Table 1. Boundary conditions for Fluent Analysis

Inlet Pressure (KPa)	Inlet Temp (ºK)	Mach No.	Outlet Pressure (KPa)	Outlet Temp (ºK)
400	1050	0.3	100	300

2.2. Meshing of convergent-divergent 2D nozzle:

A good meshing with quality 0.998 has been developed of a 2D model in ANSYS ICEM CFD software. Total number of elements and nodes are 25368 and 25050 respectively. Maximum aspect ratio is 4.11058e-3.

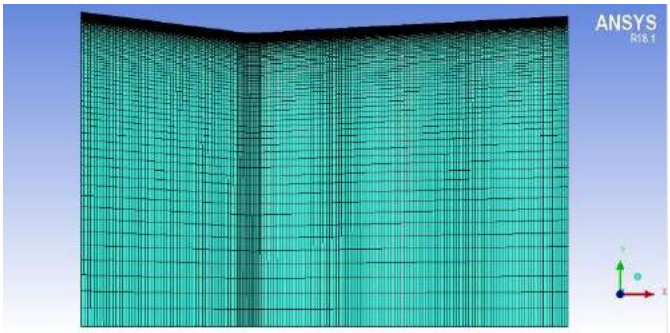

Fig.3. Finite volume mesh

3. RESULTS AND DISCUSSIONS

Two dimensional finite volume analysis have been carried out on the convergent-divergent 2D nozzle. Mach number, static pressure and temperature contours have been plotted. As it can be seen from the contours, velocity is increasing in the divergent section and velocity profile can also be seen. Pressure is decreasing as velocity increases after throat section. Temperature will also decrease because as it moves in forward direction, it loses its thermal energy. For better visualization, half as well as full convergent-divergent 2D nozzle contours have been plotted. Figure 4 & 5 are showing increment in Mach number from throat to exit. Which means, the aircraft will get accelerated.

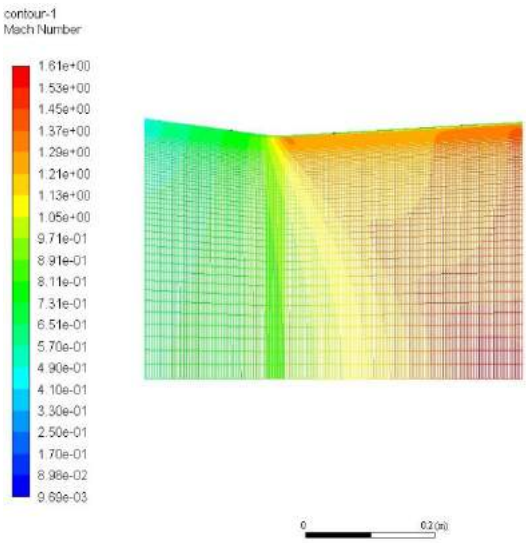

Fig.4. Mach number distribution in convergent-divergent half 2D nozzle

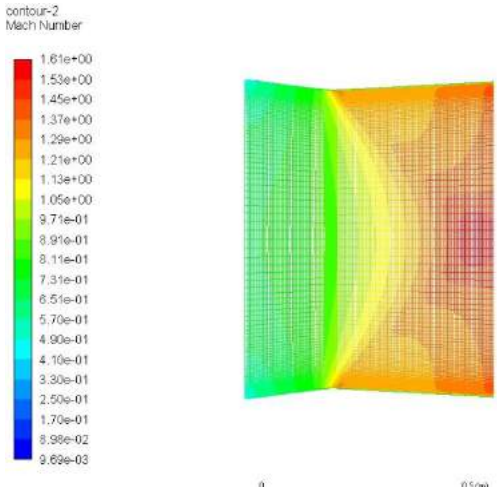

Fig.5. Mach number distribution in convergent-divergent full 2D nozzle

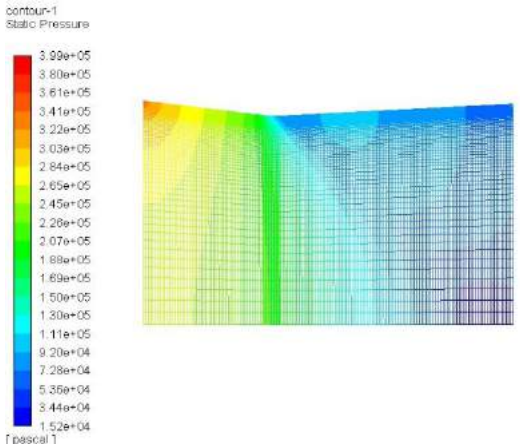

Fig.6. Static pressure distribution in convergent-divergent half 2D nozzle

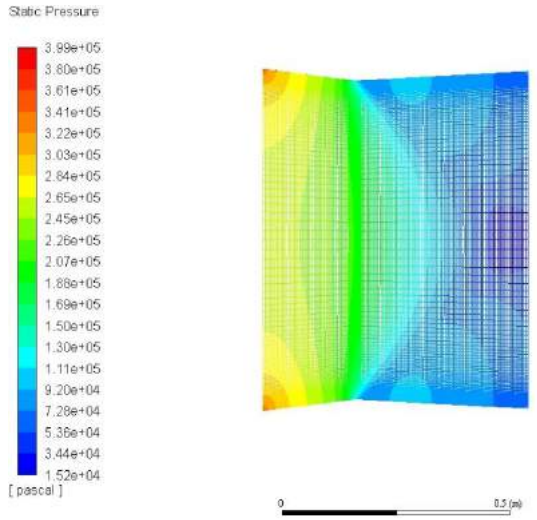

Fig.7. Static pressure distribution in convergent-divergent full 2D nozzle

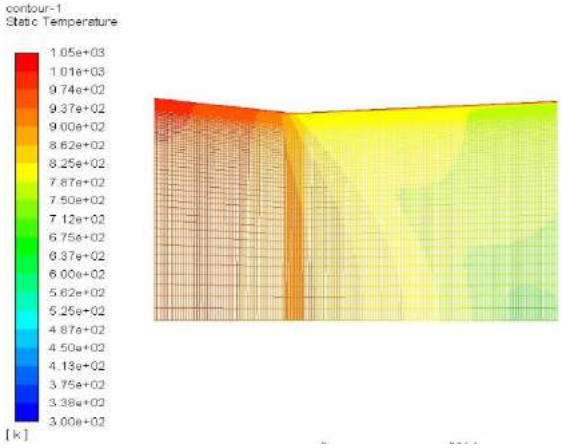

Fig.8. Static temperature distribution in convergent-divergent half 2D nozzle

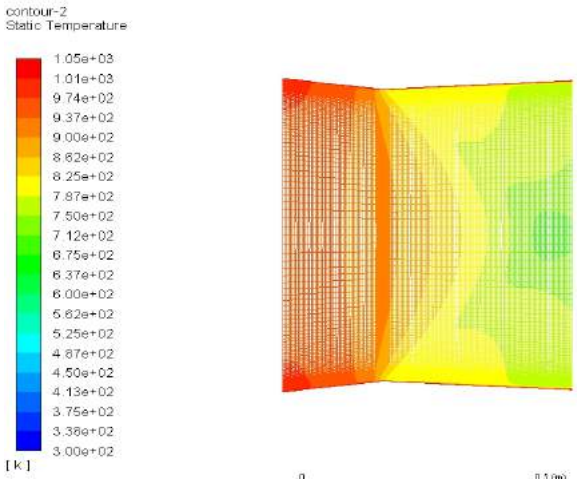

Fig.9. Static temperature distribution in convergent-divergent full 2D nozzle

4. CONCLUSION

A numerical analysis of convergent-divergent 2D nozzle has shown that the Mach number, presuure and temperature contours will vary according to the boundary conditions. As we know, pressure and temperature changes with the altitude. So analysis can be perform at different altitude for different boundary conditions. In future, variable area nozzle analysis can be done for different altitude conditions.

REFERENCES

[1] Haddad, A. "Supersonic nozzle design of arbitrary cross-section." (1988).

[2] Munday, David, et al. "Flow and acoustic radiation from realistic tactical jet CD nozzles." *14th AIAA/CEAS Aeroacoustics Conference (29th AIAA Aeroacoustics Conference)*. 2008.

[3] Kozulovic, Dragan. "Propulsive Efficiency of Plane and Axisymmetric Nozzles With Non-Uniform Velocity Distributions." *ASME Turbo Expo 2010: Power for Land, Sea, and Air*. American Society of Mechanical Engineers, 2010.

[4] Podboy, Gary G., James E. Bridges, and Brenda S. Henderson. "Phased array noise source localization measurements of an F404 nozzle plume at both full and model scale." (2010).

[5] Munday, D., et al. "Flow structure and acoustics of supersonic jets from conical convergent-divergent nozzles." *Physics of Fluids* 23.11 (2011): 116102.

[6] Mohanta, Prasanta Kumar. "Shock cell structure decay and spread characteristics of noncircular supersonic jets." (2017).

[7] Munday, David, et al. "Flow structure of supersonic jets from conical cd nozzles." *39th AIAA Fluid Dynamics Conference*. 2009.

[8] http://sahil34935.blogspot.com/2013/03/nozzles.html

Turbulent Boundary Layer Combustion in a Free Convective Environment

Akash Malaviya[1], Abhinandan Singh[1] and Ajay V. Singh[2]

***Abstract*—The present work aims to study the fundamental understandings of turbulent boundary layer combustion and focuses on the turbulence characteristics of the free convection boundary layer diffusion flames. Two different liquid fuels, namely ethanol and heptane are studied. In this study, fuel pyrolysis of a condensed fuel wick of size 10cm x 20cm is simulated using Fire Dynamics Simulator (FDS) in a free convective environment. The present study aims at understanding the complex interaction between gas-phase flames and condensed-phase fuels in the presence of turbulence. To understand the turbulence behavior of the ethanol and heptane, turbulent intensity and auto spectral density is plotted at various stream-wise location.**

***Index Terms*—Turbulence, Boundary Layer Combustion, Convection , Autospectral Density**

1. Introduction

The fire play an important role in our day to day life due to its various application of the controlled fire ranging from cooking food to industrial processes. The real concern related to fire when it goes uncontrolled during accidents. The fire accidents that happened all over the world has costed millions of lives and caused heavy damage to the property and also to the atmospheric pollution. Hence it is very important to prevent and control the uncontrolled fire. Fires most commonly can result in conflagration i.e. large and destructive fire caused naturally, begin accidentally or intentionally created – which has likely to cause physical destruction through burning. Numerous methods are developed to control fire, still, the research is primitive in estimation of the fire spread and related phenomenon. The basic understanding and the physics behind fire phenomena is necessary for better control and to prevent havoc during fire accidents.

Most of natural and manmade fire are generally in diffusion dominated, hence called diffusion flame. Generally, in diffusion flame, the fuel and oxidizer are transported into the reaction zone due to the concentration gradient, and this phenomenon is called diffusion. In nature, mostly the combustion that occurs is in the form of diffusion flame. The flame from a small match stick to the forest fire and from candle to building fire accidents and flashover, etc., are basically the diffusion flames. These diffusion flames will be either laminar or turbulent and in general, turbulent diffusion flames are mostly found in nature.

The physics behind fire phenomena in building fire, forest fires include the concept of boundary layer combustion. The combustion in such fires will happen in the boundary layer which is diffusion dominated. When sufficient amount of heat is supplied to the fuel surface, it gets vaporised and vapours diffuses perpendicularly away from fuel surface towards surrounding air and reverse of this happens to oxygen in air which diffuses towards the fuel surface. The combustion will occur at stoichiometric fuel and oxygen at the flame surface. The flame location is between thermal and hydrodynamic boundary layers. The fuel transport from the solid or liquid surface of a given shape mainly dependent on the mass transfer. D.B. Spalding **[1]** experimentally carried out the combustion of liquid fuels and concluded that rate of mass transfer from the fuel or liquid surface of a given shape in a gas stream is mainly dependent upon the mass transfer number. B.H.W Emmons **[2]** investigated combustion of the liquid fuels on a flat plate on boundary layer of an airstream and tried to address the problem of boundary layer combustion on a flat plate by giving the mathematical model. Ahmed and Faeth **[3]** investigated transport characteristics and structures of turbulent natural convection fire at the base of a vertical wall and proposed a theoretical description of the turbulent wall fire. It was concluded the radiation contribution to wall heat flux was at most 10 to 20% of the wall heat flux **[3]**. Orloff et al. **[4]** carried out research on large scale vertical surfaces and concluded that flame radiation is the dominant mode of energy transfer to the fuel surface and therefore dominates the local burning rates which in turn increases the flame heights.

A.V. Singh and Gollner **[5]** developed a correlation between local mass burning rate and the surface temperature gradient. This correlation was validated numerically and experimentally for a wick size 0f 8cm x 8cm. It is known **[6,7]** that as the flame progresses along the wall it transitions from laminar to turbulent which subsequently changes the dominant form of heat transfer from convection to radiation.

In this study, free boundary layer diffusion flames are

[1] Akash Malaviya and Abhinandan singh are student of M.Tech and MS by Research in the Department of Aerospace Engineering, IIT Kanpur, Email - akashjm@iitk.ac.in

[2] Ajay V. Singh is an Assistant Professor in the Department of Aerospace Engineering, IIT Kanpur ,Email: ajayvs@iitk.ac.in

simulated using a wick which is 20cm in length and 10cm in width. The fuel wick is kept in a vertical orientation and temperature and velocity are measured in the direction of the flow and also perpendicular to it. To study the turbulent behavior of the flame RMS measurements are presented along with the mean profiles. Auto-spectral density is also plotted against the frequency at various locations along the flow field to measure the dominant frequency of the flame. These measurements help predict the flame structure and turbulence behavior of the flame.

2. Numerical Solver and Configuration

In the present study, numerical simulations were carried out for the steady burning of an ethanol and heptane pool kept in a vertical configuration to generate free convective boundary layer diffusion flames.

2.1 Numerical solver

Numerical simulations of turbulent diffusion flames established over ethanol or heptane under a free convective environment are carried out using Fire Dynamics Simulator (FDS), developed by National Institute of Standards and Technology (NIST). It is a computational fluid dynamics(CFD) software, widely used for thermally-driven flows**. [8]**

The turbulent flow contains a wide range of length and time scale. The coupled fluctuations present at many scales makes turbulence modeling one of the challenging problem in real life. FDS uses Large eddy simulation(LES) employing discretized governing equations (mass, momentum, energy, and species) and spatio-temporal filtering to filter out the small scale eddies from large scales. The governing equations are solved up to the filter width and additionally the small scale fluid motion effects are included by sub-grid scale (SGS) modeling. SGS models are used to provide the value of turbulent viscosity, which solves the closure problem of turbulence. The general form of governing equations for a chemically reacting flow having n participating species, in conservation form are given below*:*

1) Mass Conservation:

$$\frac{\partial \rho}{\partial t} + \nabla \cdot (\rho \mathbf{v}) = 0$$

2) Momentum Conservation:

$$\frac{\partial \rho \mathbf{v}}{\partial t} + \nabla \cdot (\rho \mathbf{v} \times \mathbf{v}) = -\nabla p + \nabla \cdot \tau + \rho \sum_{i=1}^{N} Y_i f_i$$

3) Species Conservation:

$$\frac{\partial \rho Y_i}{\partial t} + \nabla \cdot (\rho Y_i \mathbf{v}) = -\nabla \cdot \mathbf{j}_i + w_i$$

4) Equation of State

$$p = \rho R T M^{-1}$$

where,

$$M = \left(\sum_{i=1}^{N} \frac{Y_i}{M_i}\right)^{-1}$$

5) Energy Conservation:

$$\rho \frac{\partial \rho e_t}{\partial t} + \nabla \cdot \{(\rho e_t + p)\mathbf{v}\} = -\nabla . \mathbf{q} + \nabla \cdot (\tau \cdot \mathbf{v}) + \rho \sum_{i=1}^{N} Y_i \mathbf{f}_i \cdot \mathbf{v} + \sum_{i=1}^{N} \mathbf{f}_i \cdot \mathbf{j}_i$$

$$e_t = h - \frac{p}{\rho} + \frac{1}{2}\mathbf{v} \cdot \mathbf{v}$$

The governing equations in FDS are approximated using 2nd order finite difference method and solved for the computational domain having a structured grid. In this study, Deardorff's eddy viscosity model is used for momentum equation closure. Single-step fast chemistry is considered and Eddy Dissipation Concept (EDC) is used for combustion modelling. For radiation, the gray gas model is used to solve radiation transport equation **[9].** For validation of numerical results, average mass loss rate of ethanol and heptane boundary layer diffusion flame had been compared with the experiments conducted by the author using baked super-wool wicks soaked with liquid fuels. Both the data having good agreement with a maximum percentage error of 15**%.**

2.2 Numerical Configuration

LES is conducted on the rectangular fuel surface of size 10cmx20cm- using FDS for the computational domain of size 13cm x 26cm x 80cm (see fig.1). The flow field within computational domain is assumed to be quiescent. Air is present at an ambient temperature, T_a=293K, and ambient pressure, P_a=101325 Pa. The adiabatic wall on

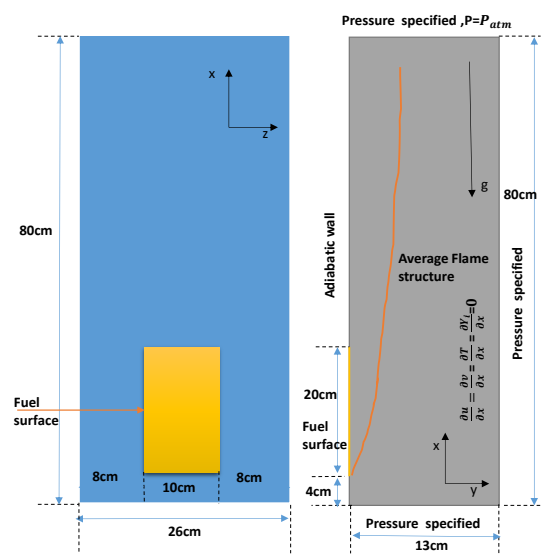

Fig. 1: Schematic diagram of a computational domain.

the left side of the domain having zero thickness and with fuel surface mounted over it as shown in Fig.1. At the wall, normal gradients of the velocity, temperature, and mass fractions of other species are fixed at zero. No-slip condition prevails at the adiabatic wall. All other boundaries are opened, and respective boundary conditions are specified as shown in Fig.1

In the present study, the grid resolution of $\Delta x = \Delta y = \Delta z$ =2mm and 5mm(results not shown) chosen. Heptane and Ethanol-free convective boundary layer diffusion flames were simulated for a time of 10 seconds.

3. Results and Discussions

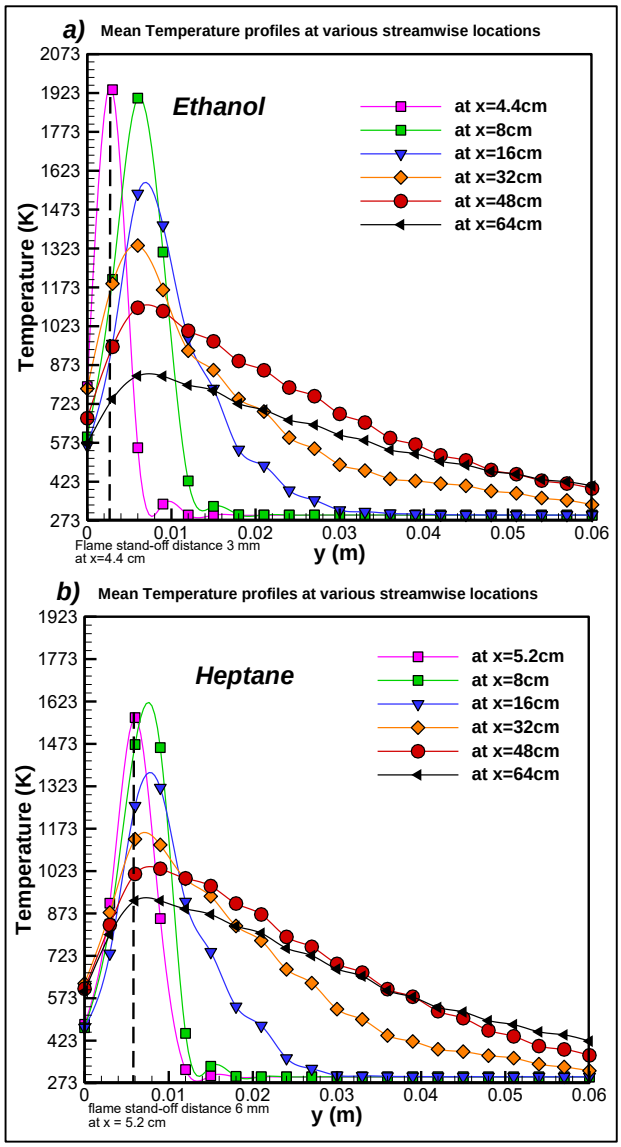

Fig. 2: Mean Temperature variation at different stream-wise location. a) ethanol b)heptane

3.1 Mean variation

For the flame on a vertically-oriented fuel surface, the temperature increases in the normal direction to a peak value and then decreases to an ambient temperature as we move away from the fuel surface. Fig. 2 shows the variation of the mean temperature along the different stream wise location for ethanol and heptane for a 10cm x 20cm rectangular fuel wick.

On comparing the mean temperature profiles of ethanol (fig. 2a) and heptane (fig. 2b) it can be seen that ethanol obtains a peak temperature at a distance of 3mm from the fuel surface and at around x = 4.4cm which is 0.4 cm from the flame edge while heptane attains its peak at x = 5.2cm which is 1.2 cm from the flame edge and around 6mm from the fuel surface. This shows that heptane has a thicker boundary layer with a lower peak temperature for the same size of fuel wick in vertical configuration. This behavior can be explained by comparing the mass burning rate of the two fuels, where heptane has a lower mass burning rate which shifts the flame away from the fuel surface, as stoichiometry is necessary for a diffusion flame to occur.

It is seen that, flame initially moves away from the fuel

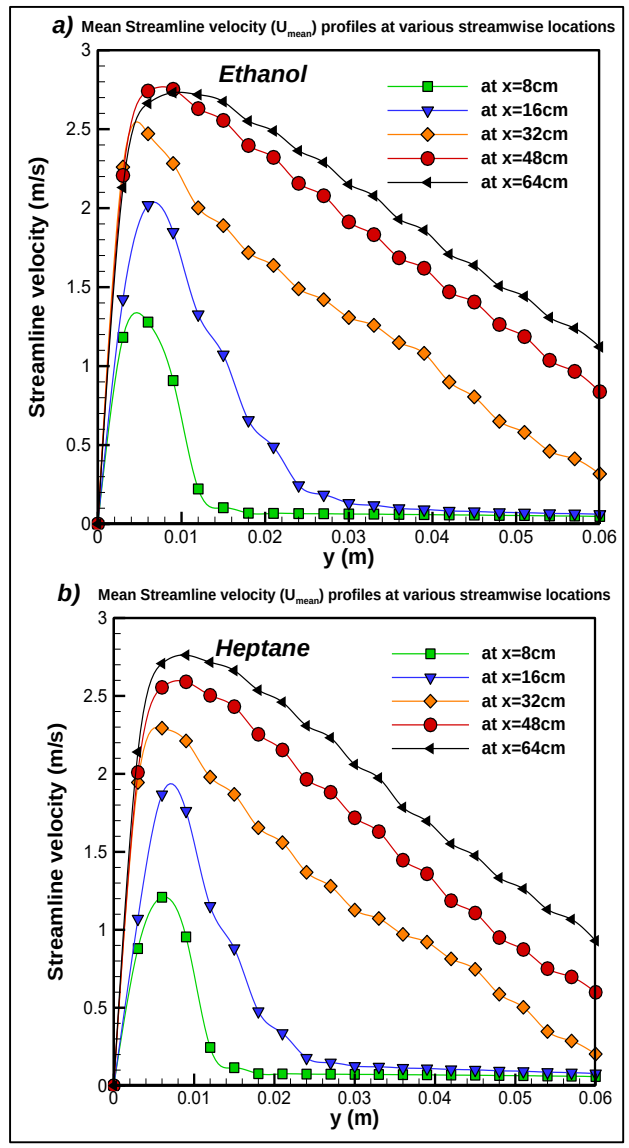

Fig 3 :Mean Streamline Velocity U_{mean} variation at different stream-wise location. a) ethanol b)heptane

surface but on crossing the fuel surface at x = 16 cm, the flow transitions to turbulence which decreases the

hydrodynamic boundary layer thickness, eventually decreasing the flame stand-off distance. This behavior is not affected by the fuel type as the trend observed is same for both the fuels. At the fuel surface the fuel mass fraction is maximum, so the fuel vapor travels a short distance before it mixes with the oxidizer. This leads to a lower flame stand-off distance, which ultimately results in higher heat transfer to the fuel surface. The flame stand-off distance is lower near leading edge and increases further downstream up to trailing edge.

Similarly, the mean streamline velocity profile in fig.3

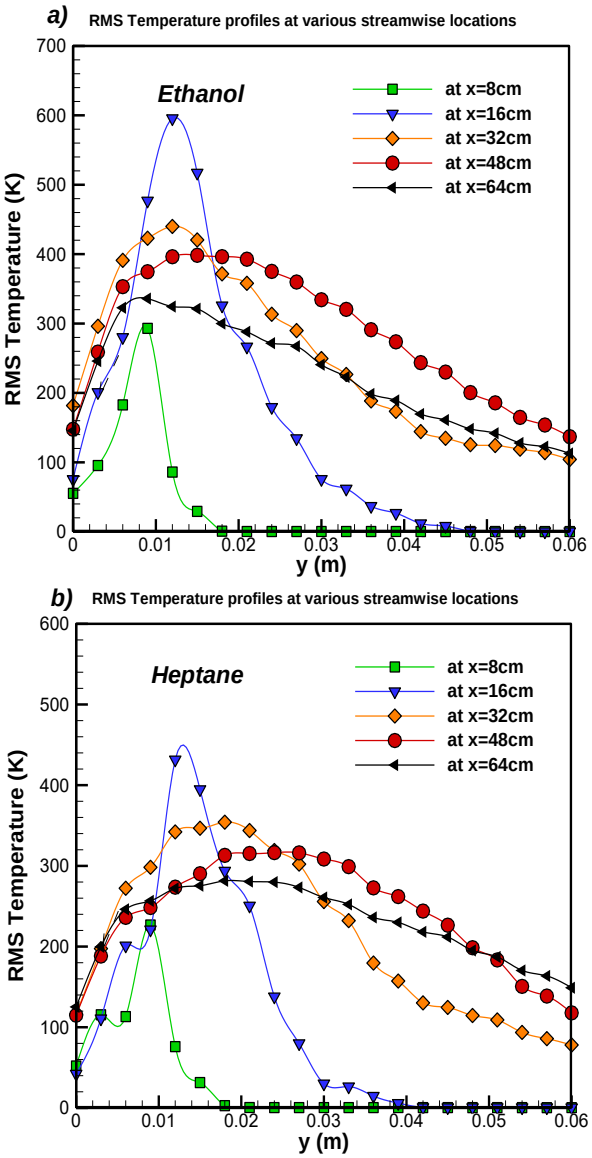

Fig. 4: Mean Temperature variation at different stream-wise location. a) ethanol b) heptane

shows that U increases (for both cases) in the perpendicular direction from a zero value at the surface to a peak value at the flame zone and then decreases nearly to zero value as we move away from the fuel surface. Here, the maximum velocity occurs behind the trailing edge in downstream of the flow. Due to the acceleration of the hot gaseous products around the fuel surface region. The maximum velocity observed in both-ethanol and heptane are almost at the same locations.

3.2 RMS Variation

The maximum RMS temperature is observed (fig 4a and fig 4.b) at about x= 16cm for different y locations that is y = 1.4 cm and y = 1.2 cm for ethanol and heptane, respectively. This due to transition of the laminar flow to turbulent flow, occurring at the x= 16cm.

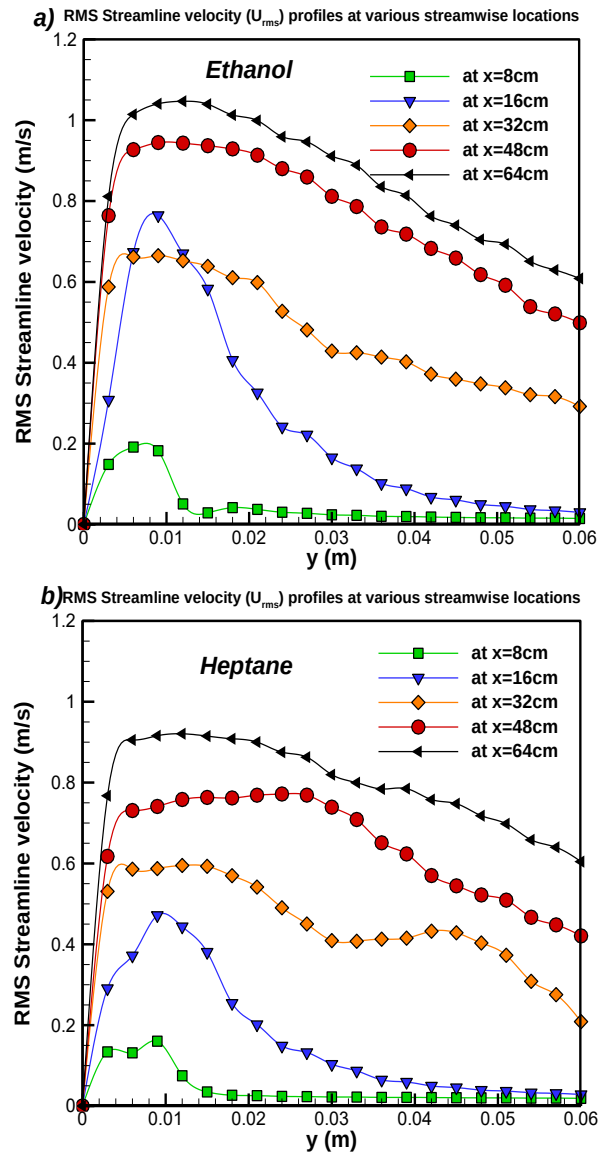

Fig 5: RMS Streamline Velocity U_{rms} variation at different stream-wise location. a) ethanol b) heptane

In fig.5, RMS streamline velocity U_{rms} variations showed. Similar trend of increasing RMS velocity in the stream-wise location is observed for the both. (ethanol and heptane) Since, initially the diffusion flame was laminar, subsequently it turns to turbulent diffusion flame after x = 16cm.This is due to buoyancy effects becomes dominant after fuel surface due to momentum processes accelerated by the hot gaseous products. RMS velocity in

both cases subsequently increase in stream-wise direction, eventually tells about the turbulent behavior the flow.

3.3 Turbulent Intensity profiles

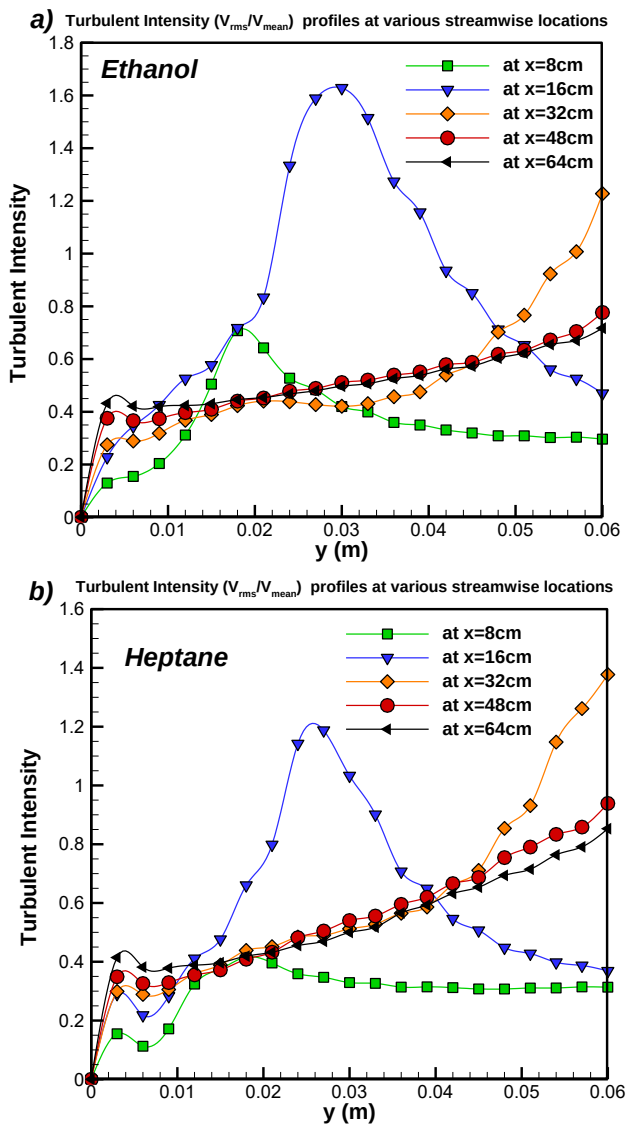

Fig. 6: Turbulent Intensity variation at different stream-wise location. a) ethanol b) heptane

It is observed that the turbulent intensity for ethanol and heptane (fig.6) initially increses till transition of the flow (x=16 cm) and then starts decreasing in stream-wise direction. Whereas the in normal to fuel surface. In both case, turbulent intensity increase in normal direction to fuel surface because of air entrainment from the right side of the flame. On comparing both fuels ethanol has higher turbulence intensity was observed.

3.4 Auto spectral Density plots at various locations

At the start of the boundary layer diffusion flame, the fluid flow was laminar until the fluctuations of velocity increased rapidly after x = 16cm in stream-wise direction. In fig.7 and fig.8 shows the auto-spectral density calculated for normal velocity (v) and streamline velocity (u) at two different locations, i.e. x= 48 cm, x= 64cm and y= 3mm, y= 6mm. The values are plotted against frequency in a log-log curve for 10cm x 20cm fuel wick in boundary layer combustion using both ethanol and heptane. The slopes of these plots help to identify turbulent behavior of the flame, that the flow is highly intermittent and is in turbulent inertial subrange.

At start of the boundary layer diffusion flame, the prominent frequency at which the flame fluctuates and the different locations show which region has the strongest fluctuation and how this fluctuation dies down along the stream-wise direction.

4. Conclusion

This study emphasizes on the turbulent behavior of free convection boundary layer flames developed by burning liquid fuels in a vertically oriented soaked fuel wick. It is concluded that similar to a hydrodynamic boundary layer, flame transitions from laminar to turbulent along the streamline. The eddies generated at the anchoring point and due to air entrainment move along the flow and become prominent at a distance of 12cm from the flame edge.On comparing the two fuels, i.e. ethanol and heptane it can be concluded that there is no significant variation in mean stream-line velocity profile is observed. It is observed that in ethanol boundary layer combustion, had obtained higher mean temperature compared to heptane. This shows that heptane has a thicker boundary layer with a lower peak temperature for the same size of fuel wick in vertical configuration due to lower mass burning rate, which necessary shifts the flame away from the fuel surface, as stoichiometry achieved for diffusion flame. Turbulent intensity increses in normal direction to fuel surface, due to air entrainment from the right side of the flame. Auto spectral density plots at different locations in computational domain conform the turbulent flow after x= 16 cm (transition point).

5. Acknowledgment

The authors would like to thank the High-Performance Computing (HPC) Facility of Indian Institute of Technology Kanpur for providing the resources to carry out the CFD computations for the given paper. This work is supported by the Startup Research Grant of Indian Institute of Technology Kanpur.

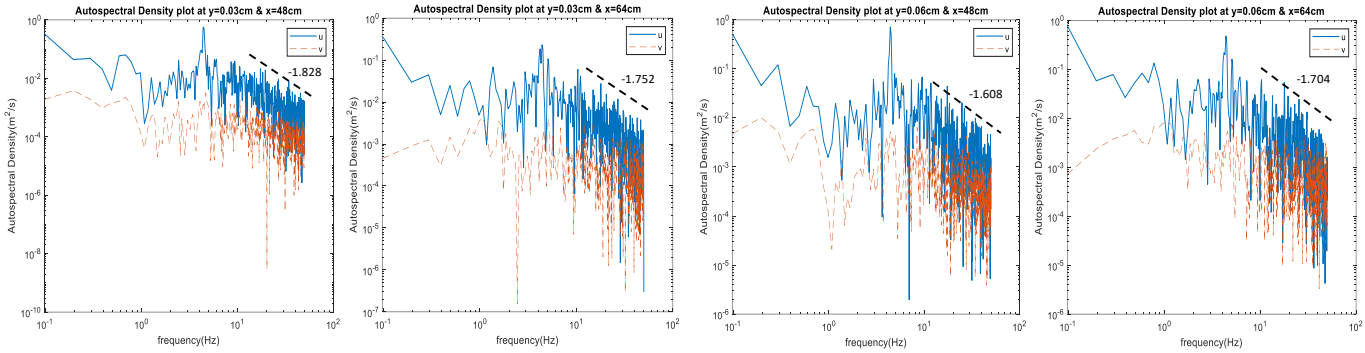

Fig. 7: Autospectral Density Plot for ethanol at x= 48 cm, x= 64cm and y= 3mm, y= 6mm.

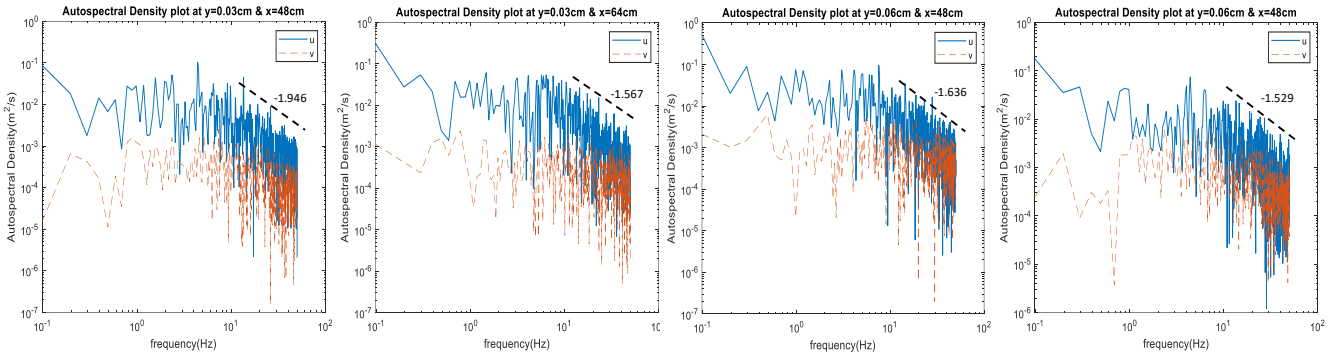

Fig. 8: Autospectral Density Plot for heptane at x= 48 cm, x= 64cm and y= 3mm, y= 6mm.

6. References

[1] D.B. Spalding, "The combustion of liquid fuels," Proceedings of the Combustion Institute, Vol. 4, pp. 847-864, 1953

[2] H. Emmons,' The film combustion of liquid fuel,''ZAMM –Journal of Applied Mathematics and Mechanics, vol. 36, no. 1-2, pp 60-70,1956

[3] T.Ahmed andFaeth,"Turbulent wall Fire,'Symposium(International) on Combustion, Vol.17 ,Issue 1,1979, pp.1149-1160, 1979

[4] L.Orlkoff, J.De Ris ,and G. Markstein, "Upward turbulent fire spread and burning of fuel surface," Proceedings of the Combustion Institute , vol.15, no.1, pp. 183-192, 1975

[5] Ajay V Singh,' A Fundamental Study Of Boundary Layer Diffusion Flame," Ph.D. Thesis , The University of Maryland, College Park,2015

[6] K. Saito, J. Quintiere, and F. Williams, "Upward turbulent flame spread," in Fire Saftey Science –Proceedings of the First International Symposium, pp. 75-86, 1986

[7] K. Saito, F. Williams, I. Wichman, and J. Quintiere, \Upward turbulent flame spread on wood under external radiation," Journal of Heat Transfer, vol. 111, no. 2, pp. 438{445, 1989

[8] K. McGrattan, S. Hostikka, R. McDermott, J. Floyd, C. Weinschenk, and K. Overholt, "Fire Dynamics Simulator technical reference guide," NIST Spec. Publ. Commer. Natl. Inst. Stand. Technol. Gaithersburg, MD., vol. 1, no. 5, p. 175, 2016

[9] H. Bockhorn, Soot formation in combustion, mechanisms, and models; Springer series in chemical physics. Berlin: Springer-Verlag, 1994.

[10] H. Bockhorn, Soot formation in combustion, mechanisms, and models; Springer series in chemical physics. Berlin: Springer-Verlag, 1994.

Turbulent fuel-air mixing investigations within a cavity based hydrogen inoculated scramjet combustor

1. Kodamasimham Bharadwajan 2. Dr. Debi Prasad Mishra 3. Dr. P.V. Ramana Murti 4. Dr. Srinivasan Vathsal

***Abstract*-- Flow field within the combustor of a scramjet engine is extremely complex and poses considerable challenges in the design and development of operable free-flight supersonic combustor with a near optimized geometry. In this work, an attempt for comprehensive numerical predictions on the flow-field characteristics of a cavity based scramjet combustor with the injection of hydrogen fuel into a supersonic incoming free stream air was carried out for both non-reacting and reacting flow conditions. The numerical studies implemented 1st order implicit numerical scheme for a 2D steady, density based, k-ω SST turbulence model with a multi-component finite reacting species for predicting the turbulent-combustion energy spectrum. Five fuel inoculation locations on cavity floor and two locations viz., one each on cavity fore-wall and aft-wall were identified based on the earlier works of [1]. The effect of injection location on supersonic flow field is investigated. The analysis of cavity based supersonic combustor for efficient fuel air mixing and combustion is achieved by commercial computational fluid dynamics tool. The results depict a wide variety of flow features resulting from the interactions between multiple injector flows, pseudo-shockwave structures, turbulent boundary layer, and encapsulation of the cavity flow regimes. We conjectured that an optimized cavity is a good choice to improve flame-holding in the supersonic flow field, and it generates a strong recirculation zone for turbulent fuel-air mixing within scramjet combustor.**

***Index Terms* -- Scramjet; Cavity; Injectors; Fuel-air Mixing, Flame Stability, Supersonic combustor; Flame–holding; Shock-Turbulent structure.**

1. Kodamasimham Bharadwajan is a Research Scholar, JNTU-Hyderabad, India. (e-mail: bharadwajank@gmail.com).
2. Dr. Debi Prasad Mishra is Professor, Department of Aerospace Engineering, Indian Institute of Technology, Kanpur, India. (e-mail: mishra@iitk.ac.in).
3. Dr. P.V. Ramana Murti is Professor and Director Evaluation (Retired), Jawaharlal Nehru Technological University, Hyderabad, India (e-mail: pvrmurti@gmail.com).
4. Dr. Srinivasan Vathsal is Director ER & IPR (Retired), Defence Research Development Organisation, New Delhi, India. (e-mail: svathsal@gmail.com).

1. Introduction

SUPERSONIC combustion ramjet (scramjet) engine is recognized globally as the most promising air-breathing propulsion system for realizing the hypersonic flight envelope. In the recent years, research and development efforts put forth for understanding various scramjet engine operations promoting study of turbulent-combustion diagnostics in supersonic flows. Globally, extensive research is expended in realizing the feasible scramjet technology using hydrogen as fuel choice with a significant attention focused on realizing an all new generation space launchers and global fast-reaction reconnaissance missions.

In conventional ramjet, multiple shockwaves are generated by backpressures accumulated within the massive engine envelope thus slowing down incoming supersonic airflow to subsonic speeds incurring additional pressure losses. Later to this subsonic flow, fuel is supplemented allowing the mixture to combust, and accelerate the gasses to supersonic speeds through a narrow throat region (called as mechanical choke). But contrarily, for a pure scramjet operated vehicle, incoming free-stream air remains essentially supersonic throughout combustion process within the engine envelope disqualifying any choking mechanism, thus ensuring better optimal performance over a wider operating range of Mach numbers.

Scramjet vehicles will provide sophisticated integrated engine-to-vehicle design because the engine envelope section is occupied on the entire lower surface of the hypersonic transport vehicle body as shown Fig. 1. Its propulsion system includes five engine envelope components and two vehicle components. Major engine components include: internal inlet; isolator; combustor; internal nozzle; and fuel supply subsystem and major vehicle components: vehicle fore-body (required for inducting air at supersonic speeds) and aft-body (critical part required for expanding gases in nozzle component).

The induction system comprises of the vehicle fore-body and internal inlet, which essentially ingests and compresses incoming air required for processing by other components of engine. Contrary to conventional jet engines, these high-speed air-breathing engines, achieves enough compression (very high pressure ratio's) as the vehicle is operated at supersonic or hypersonic speeds, eliminating role of complex axial flow turbo-machinery mechanical components.

The next section in scramjet engine i.e. isolator is also a critical component which enables obtained supersonic flow to get adjusted to static backpressure higher than the inlet static pressure. A pre-combustion shockwave is formed in isolator region as soon as combustion process starts shear layer separation across combustor section. Additional functionality is augmenting combustor in obtaining required space heat release and successful handling of pressure rise induced inside. If this functionality is not satisfied, it leads to a criterion called as inlet un-start, in which pre-combustion shock waves generated refrain's airflow from entering into the isolator section.

Subsequently, combustor section ingests the required airflow from downstream of the internal inlet section and fuel is injected through various points located throughout the combustor length, allowing efficient fuel-air mixing, thus ensuring optimizing of engine thrust. Subsequent section is expansion system, which integrates internal nozzle and vehicle aft-body that governs expansion of the high pressure, high temperature gaseous mixture to generate thrust by converting potential energy generated by combustor into kinetic energy. Cavity geometry is characterized by its length-to-depth $\left[\frac{L}{D}\right]$ ratio. A cavity is termed open if $\left[\frac{L}{D}\right] < 10$ and for these ratios, the free shear layer will reattach to rear face of cavity. For $\left[\frac{L}{D}\right] > 10$ cavity is termed closed because shear layer will reattach on the cavity floor as shown in Fig. 2 [9].

In order to reach scramjet speeds, an air-breathing hypersonic vehicle has to forego several types of engine operations. At the very initial stage, to attain a speed of Mach 3 from take-off (usually at release point) the vehicle employs a propulsion system that might possibly incorporate several gas-turbine engines or rockets (placed internally or externally). In next stage (3<Ma<4 range), the scramjet vehicle takes a transition by escalating from a lower-end propulsion stage to a situation where-in shock system generated possesses sufficient strength capable enough to generate subsonic flow regions at the entrance region of combustor section. For generating desired engine thrust, a thermal throat region to obtain required choking effect is provided within the combustor, which ensures a right combination of area distribution, fuel-air mixing and heat release [11].

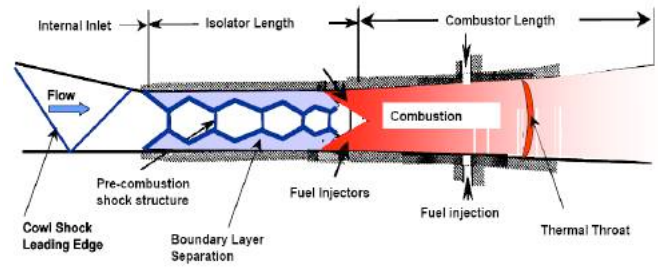

Fig. 1: Schematic of scramjet combustor

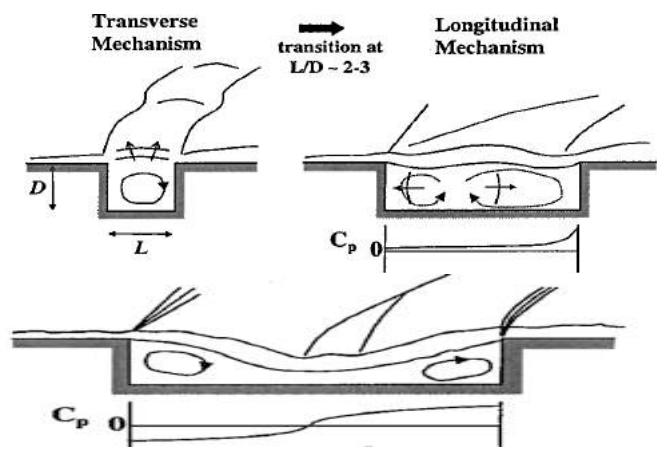

Fig. 2a: Open cavity flow for L/D < 7–10
2b: Closed cavity flow L/D> 10-13

At a further stage (3<Ma<8 range), a combination of ramjet and scramjet combustion takes place decreasing temperature rise and pressure inside the combustor, thus the pre-combustion shockwave produced at inlet throat area is pulled towards inlet plane of combustor (requiring weaker pre-combustion system). During this particular stage, pressure ratio across isolator section passes through a peak at Ma=6 and as the shock-train and boundary layer recedes (or fades-away), the vehicle operation mode completely takes transition from Dual-mode ramjet → Dual-mode scramjet (5<Ma<7) → Pure scramjet mode (Ma>7) [12].

Much of the complex physics entangled with above cited modes of operation provided varies with reference to: i) Flow behavior, ii) Placement of pre-combustion shock-train (which is terminated or moving along), and iii) Boundary layer (detached or attached) between different Mach numbers as shown in Fig 2. Observations from above indicate following: At Ma>5, higher performance levels are provided by supersonic combustion phenomena; between 5<Ma<6, engine efficiency dictates using the ramjet; At Ma~=6, airflow deceleration to subsonic speeds for combustion results

airflow halt which increases pressure and heat transfer rates; At Ma>7, combustion process no longer separate airflow, operates in complete scramjet mode without a pre-combustion shock-train with inlet shock propagating throughout engine module; At Ma>8, physics dictates supersonic combustion, engines inability to handle pressure and heat buildup caused by deceleration to subsonic speeds [10].

There exist many technological challenging aspects in meeting and fulfilling efficiency levels for these scramjet operated vehicles like mixing, ignition and flame holding in a scramjet combustor focusing on: i) Good and rapid fuel-air mixing ii) Minimization of total pressure loss iii) High combustion efficiency iv) Ground test facilities for testing of scramjet engine and v) Numerical simulation of scramjet flow spectrum.

2. Literature Review

Literature survey on cavity as a flame holder in supersonic flow were studied and previous contributions are reported here. Mishra D P and Sridhar K V [1] studied about fuel injection and fuel stabilization in a supersonic combustor and summarized the importance of cavity for enhanced mixing and better fuel entrainment. They observed oblique shock wave–fuel jet interactions and support extended enhancing molecular mixing between which supersonic air and gaseous fuel by the vortices generation. They concluded that mixing was enhanced by cavity induced oscillations and rate of enhancement was controlled by the cavity shape. Adela Ben-Yakar and Ronald K.Hanson [2] studied flow-field characteristics of cavities and summarized the research efforts related to cavities in low- and high- speed flows. They have also observed that cavities with aft ramp angle between 45° and 16° yields minimum drag penalties. K V Sridhar [3] simulated 2D supersonic combustor with direct fuel injection from cavity floor with various fuel injection angles. Low velocity recirculation regions assisted in flame holding. Heat release was also observed to have significant effects on various flow structures formed both in the main stream and cavity regions. In reacting conditions, the 120^0 injection angle shows highest combustion efficiency because of better mixing properties and in non-reacting conditions, injection at 135^0 shows maximum pressure losses. K H Yu and K C Schadow [4] studied about cavity-actuated supersonic mixing and combustion control using K-H instability method and concluded that for a required frequency excitation, transverse acoustic waves emanating within the cavities are powerful enough to affect mixing in a significant manner. F Xing, M M Zhao and S Zhan [5] studied performance of scramjet engine for non-reacting and reacting flow conditions with a corner plate at leading edge of cavity. They inferred, the distance of corner plate from front wall affects mixing characteristics inside a cavity region and controls fuel rich regions within the combustor. P Manna and D Chakraborty [6] simulated reactive flow fields of H_2-Air combustion behind backward facing step within constant area combustor by numerically solving 3D Navier-Stokes equations implementing k-ε turbulence model and fast-reaction rate chemical kinetics model. Zhiliang Xuxk, Myoungnyoun Kimxk, Wonho Ohzk, James Glimmzxk, Roman Samulyakx, Xiaolin Liz and Constantine Tzanos [7] simulated both reactive as well as non-reactive turbulent supersonic co-flowing jets using a Lagrangian turbulent-combustion interactions model in conjunction with an efficient RANS and AMA strategy.

3. Computational Methodology

A detailed study of the flow field characteristics of single cavity establishment with seven fuel inoculation zones was performed. Due to the combustor geometry model simplicity, the models were designed and grid topology or meshing was achieved in GAMBIT package. Meshed model was analyzed in commercial FLUENT package for a steady 2D density based Navier-Stokes equation and k-ω SST turbulence fluid dynamic model.

3.1 Numerical Analysis

3.1.1 Burner Geometry

A model of the combustion chamber implementing a cavity in the present numerical investigation is generated in GAMABIT as shown in Fig. 3. The dimensions are as shown in Table I.

Model	
$\left[\frac{L}{D}\right]$ ratio	4
Length of cavity	6.8 mm
Inlet diameter	5.1 mm
Exit diameter	6.58 mm
Length of divergence section	17 mm
Distance of cavity from inlet	5.1 mm
Divergence angle	2.5^0

Table I: Model dimensions

Fuel inoculation slots on cavity floor are represented by I_1, I_2, I_3, I_4, I_5 and on fore- and aft- walls are represented by I_6 and I_7 respectively as shown in Fig 4. If L is cavity length, then fuel slot positions on cavity floor are given by, I_1=0.1L, I_2=0.2L, I_3=0.3L, I_4=0.4L, I_5=0.6L respectively. If D is cavity depth, then fuel slot positions on fore- and aft- wall are given by, I_6=I_7=0.33D respectively. Width of all fuel slots is equal to 0.1mm. Hydrogen fuel is injected from the slots of width 0.1mm. Geometry and spatial discretization were generated using GAMBIT meshing tool.

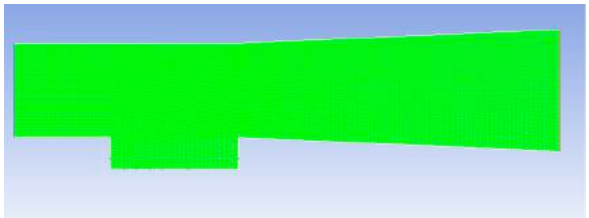

Fig. 3: Mesh of scramjet combustor region

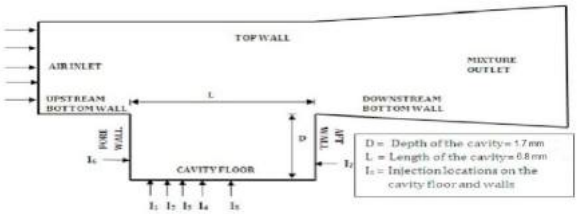

Fig. 4: Combustor geometry establishing fuel inoculation points

3.1.2 Boundary Conditions

Numerical studies have been performed implementing validated two-dimensional, coupled, implicit Navier-Stokes equations, shear stress transport k-ω turbulence model and finite-rate/eddy-dissipation reaction model. In parametric analytical studies, no-slip boundary condition is imposed at adiabatic wall (as heat transfer and shock-turbulent boundary layer interactions are not modeled). Flow through scramjet combustor domain is supersonic with suitable boundary conditions. At air- and fuel- inlets, turbulent kinetic energy, specification dissipation rate and species mass fractions are specified. In reacting flows, hydrogen is injected into the core flow at sonic velocity with an injection pressure of 0.5 MPa. Inlet conditions for Case A and Case B are specified below through Table II and Table III respectively.

Case A: Multi-Injection Non-Reacting Model

Zone	Boundary type	p (atm)	V (m/s)	T (K)	ρ (kg/m3)	M (kg/m-s)
Air-inlet	Pressure far field	1	833.0105	300	2.35	1.7894e-05
H_2-1	Pressure far field	5	416.5052	300	7.06	1.7894e-05
H_2-2	Pressure far field	5	416.5052	300	7.06	1.7894e-05
H_2-3	Pressure far field	5	416.5052	300	7.06	1.7894e-05
Mixture outlet	Pressure outlet	0	416.5052	300	7.06	1.7894e-05
Wall_1	Wall	0	416.5052	300	7.06	1.7894e-05
Wall_2	Wall	0	416.5052	300	7.06	1.7894e-05

Table II: Boundary conditions multi-injection non-reacting model

Case B: Multi-Injection Reacting Model

Zone	Boundary type	p (atm)	V (m/s)	T (K)	ρ (kg/m3)	M (kg/m-s)
Air-inlet	Pressure far field	1	834.5202	300	1.7894e-05	1.7894e-05
H_2-1	Pressure far field	5	1582.733	300	1.7894e-05	1.7894e-05
H_2-2	Pressure far field	5	1582.733	300	1.7894e-05	1.7894e-05
H_2-3	Pressure far field	5	1582.733	300	1.7894e-05	1.7894e-05
Mixture outlet	Pressure outlet	0	1582.733	300	1.7894e-05	1.7894e-05
Wall_1	Wall	0	1582.733	300	1.7894e-05	1.7894e-05
Wall_2	Wall	0	1582.733	300	1.7894e-05	1.7894e-05

Table III: Boundary conditions for Multi injection reacting model

3.2 Results and Discussion

Comprehensive numerical simulation was performed to understand the influence of scramjet combustors flow characteristics with injectors at different positions within the cavity domain. Implicit method along with an implicit first-order upwind discretization for the flow physics revelation; turbulence kinetic energy and turbulence dissipation rate were implemented for controlling the numerical calculation. Computations performed until residuals converged thus arriving towards a steady state solution. Spectrums for static- pressure, temperature, turbulence kinetic energy and total pressure were captured for the models.

Contours and trends of static pressure gradients benefit to visualize shockwave structures formation emanating from within cavity region. Contours of static temperature gradients are important to approximate flame anchoring capability within cavity region viz., higher the gaseous temperature, maximum is the ability to clutch flame propagation and provision for effective ignition of fuel-air mixture. Turbulent kinetic energy contours directly predicting vortices and eddies formation, its strength and mixing capability of the cavity territory. Contours of total pressure gradient estimates total pressure loss incurred due to the complex pseudo-shockwave structure(s) formation inside scramjet combustor region.

3.2.1 Non-Reacting- or Cold- Flow Model

Air arrives into scramjet combustor at a Mach number of 2.4 and the fuel is inoculated into scramjet combustor from total of seven locations from cavity floor, fore- and aft- wall locations at a Mach number of 1.2. While two flows at supersonic Mach numbers interact amidst each other, a complex change in flow topology (termed as jet in supersonic cross-flow) and a pseudo shock train structure are incurred at this juncture across which the flow properties change in a significant manner.

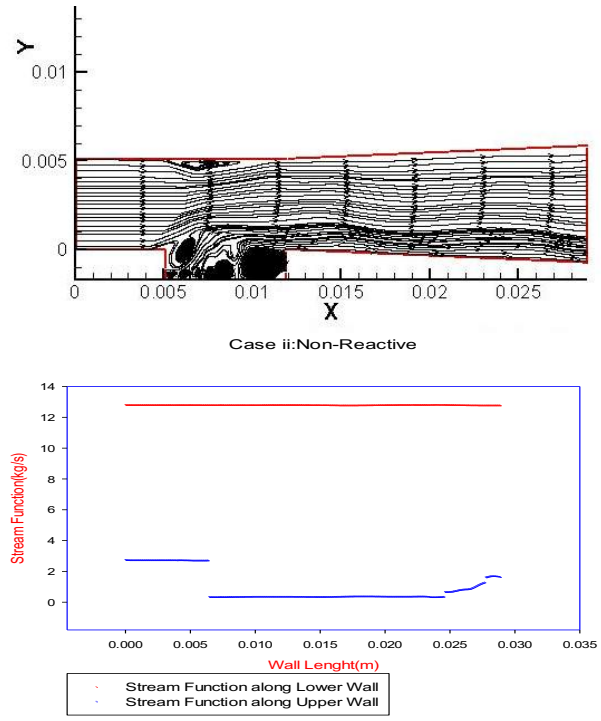

Fig. 5: Stream line function Contours & Plots for non-reacting or cold flow

Streamlines reflect the intense and strong recirculation zones of distinctive sizes that enhance fuel-air mixing which is an essential and most desirable characteristic of any combustor.

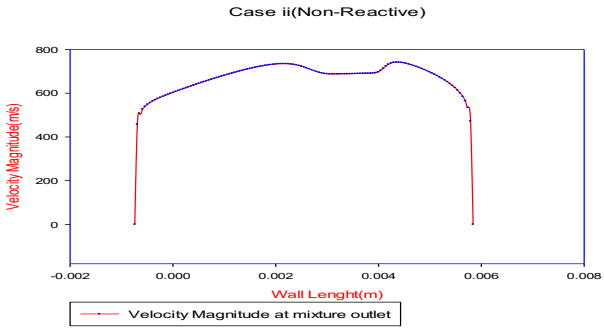

Fig. 6: Plots of Velocity magnitude for non-reacting or cold flow

Velocity is at maximum near combustor inlet and it decreases immediately after the formation of shock train. It is observed from the contours that the velocity behind the oblique shock is greater than that in the case behind the normal shock and it decreases across the shock train but is amplified marginally due to the multiple expansion fans produced along the cavity length and also due to diffusion of fuel-air mixture in the divergent section.

Shock interacts with the boundary layer of top wall and evident with the corresponding shockwave reflection occurrences. Stagnation zone is observed at the top wall of combustor and a recirculation zone is also witnessed along the same plane.

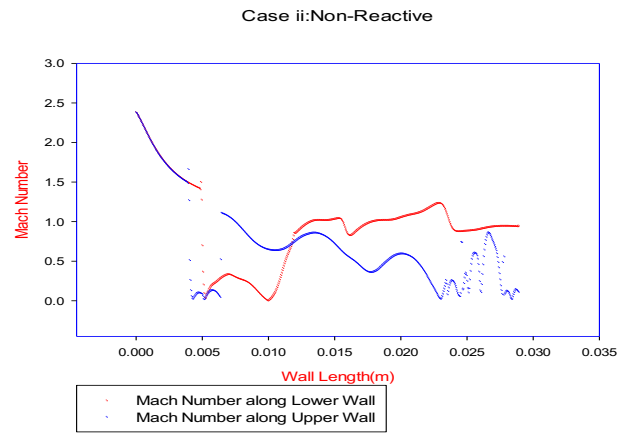

Fig. 7: Plots of Mach number for non-reacting or cold flow

Mach number decreases due to the formation of a strong normal shock wave structure placed exactly at the cavity onset plane. This is the reason for increase in the fuel residence time. Hence the time taken for mixing of fuel (H_2) and air is increased.

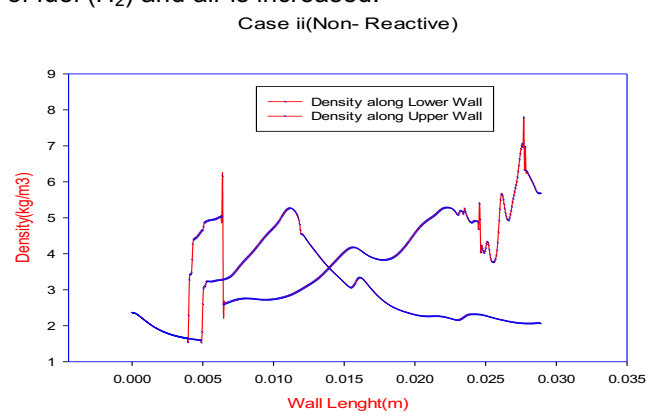

Fig. 8: Plots of density gradients for non-reacting or cold flow

Density contours and their relative trends significantly contribute to comprehend the complex compressible-turbulent flow physics along transverse- and crosswise-directions through emanated shockwave structures. Density across a shock wave increases drastically as observed. Therefore, we can clearly identify multiple shock interactions captivating cavity burner region thus increasing density gradient of flow. Shear layer growth is also clearly envisioned from obtained density contours.

Density increases to 5.77 $\left[\frac{kg}{m^3}\right]$ after fuel injection, but at the outlet, it is decreased to a minimum value of 2.7 $\left[\frac{kg}{m^3}\right]$ due to efficient fuel-air mixing. Shock formation can be visualized to augment for the abrupt increase in density just after fuel injection.

Contours of Total- and Static- Pressure Gradients

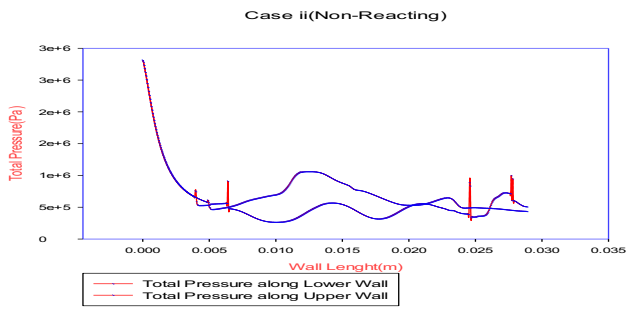

Fig. 9: Plots of Total pressure gradient for non-reacting or cold flow

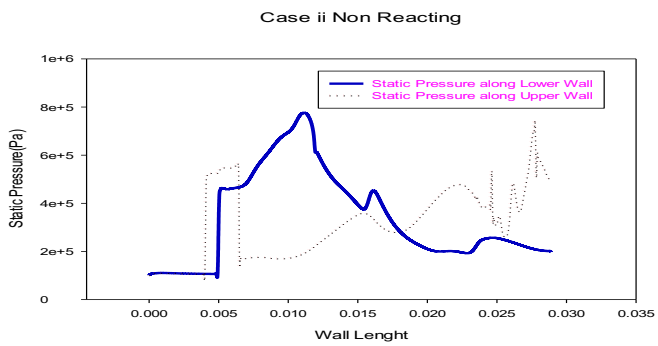

Fig. 10: Plots of Static pressure gradient for non-reacting flow

Static pressure variation inside the combustor was visualized. It remained constant up to the fuel injection point. Pressure rise caused by shock formation is clearly visible. There is a pressure rise of 11.92 [atm] across the shock. At outlet plane, pressure decreases to a minimum of 1.44 [atm]. Pressure rise on combustor top wall is a worthy indicator of the strength of flow structure(s) resembling shockwaves formed within flow stream. Moreover, the obtained results render in validating numerical results with experimental data.

Contours of Total- and Static- Temperature Gradients

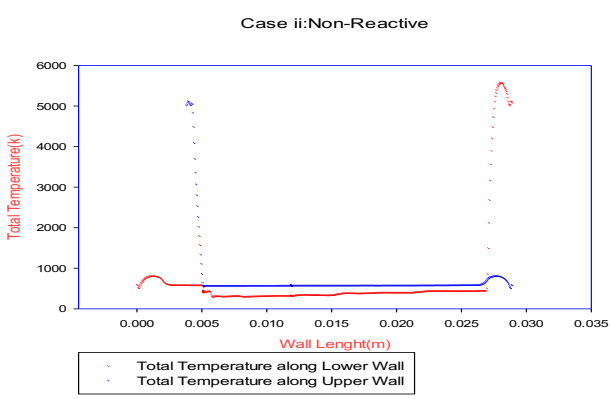

Fig. 11: Plots of Total temperature gradient for non-reacting or cold flow

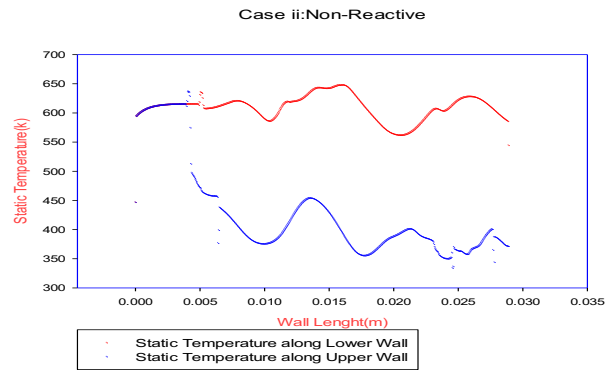

Fig. 12: Plots of Static temperature for non-reacting or cold flow

Static temperature is at a bare minimum at combustor inlet and it increases immediately after the shock wave formation. Due to shock-boundary layer interactions the temperature drastically increases at the surface of wall.

Contours of Turbulence Energy Spectrum

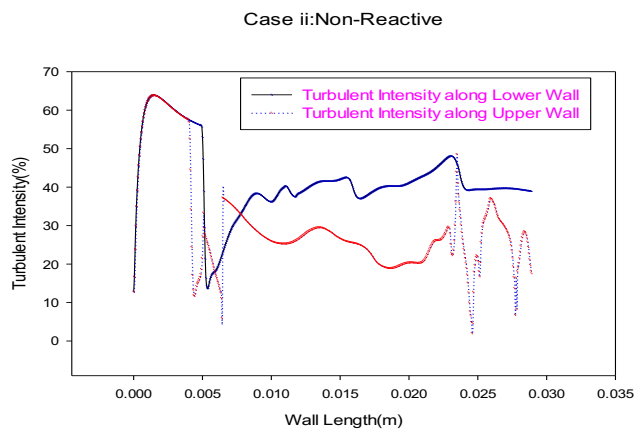

Fig. 13: Plots of Turbulent intensity for non-reacting flow

Turbulent intensity crosses 7000 mark at cavity region due to the intense turbulent physics triggered by vortices formation. These in particular viz., toroidal or the eddy like structures confirm strong encapsulation and efficient air-fuel mixing thus increasing the turbulent and overall mixing efficiency.

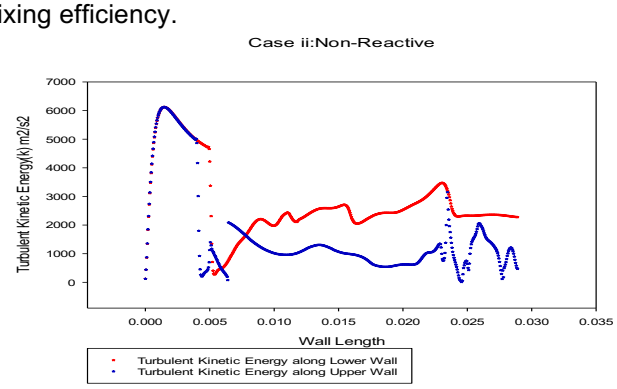

Fig. 14: Turbulent kinetic energy spectrum Plots for non-reacting or cold flow

Turbulent kinetic energy trends fortified to be constantly fluctuating throughout combustor length, although there was a substantial increase within the cavity region to 8350 [m^2/s^2] and with an increase at the top wall due to shockwave-boundary layer interactions.

Higher turbulent kinetic energy and turbulent intensity reflecting very strong, multiple vortex formation region(s) encapsulated within the cavity domain thus enhancing air-fuel mixing efficiency.

3.2.2 Reacting- or Hot- Flow Model

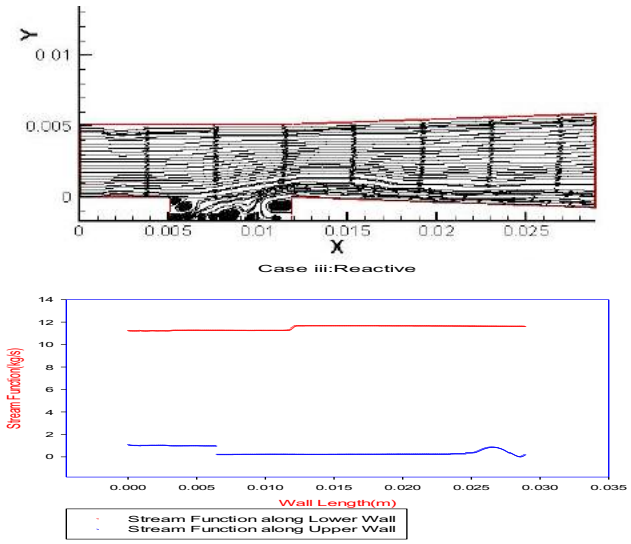

Fig. 15: Stream line function Contours & Plots for reacting flow condition

From Fig. 15, it is quite evident that a small recirculation region is formed around stagnation zone which helps in transportation of the fuel upstream of cavity region.

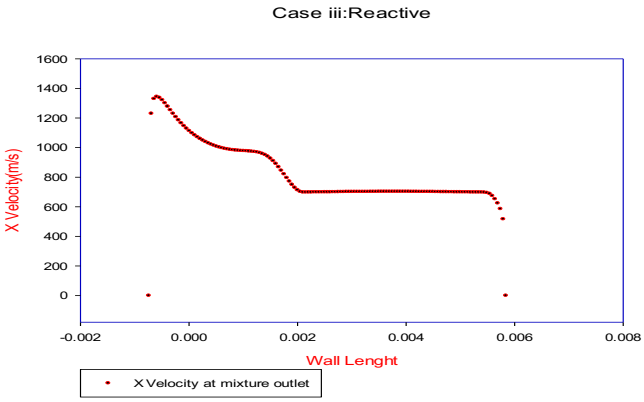

Fig. 16: Plots of Velocity magnitude for reacting flow physics

Strong normal shockwave is formed near combustor inlet motivating for reduction in the downstream velocity verifying the compressible physics.

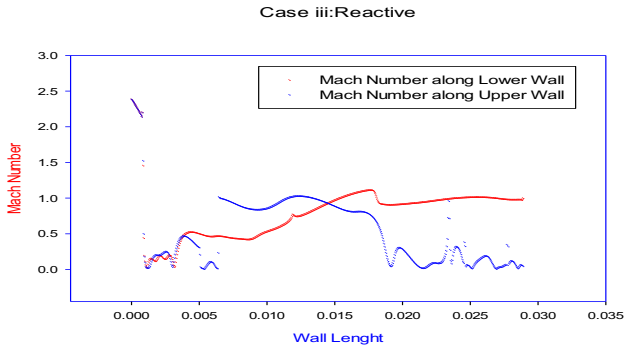

Fig. 17: Plots of Mach number for reacting flow

At the entry plane of combustor, a Mach number of 2.4 is observed and after the shockwave formation a Mach number of 0.653 is perceived. Substantial reduction in Mach number is outcome of the formation of a very strong standing normal shock wave that acts as a flame holder or flame anchoring and stabilizing zone.

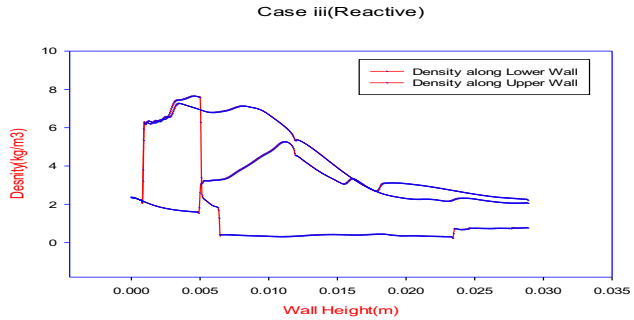

Fig. 18: Plots of Density gradient for reacting flow

There is an abrupt increase in density gradient near the inlet of combustor region; this indicates presence of a strong normal shockwave coupled with oblique shock structures terminating towards upper- and lower- walls of combustor. Closer observation also reveals propagation of shear layer growth over the surface of cavity. There is an increase in density of the fluid across the shear layer.

Density increased after fuel injection, but decreased to a minimal value at the exit with efficient mixing and combustion. Shock formation can be visualized by the abrupt increase in density just after fuel injection.

Contours of Total- and Static- Pressure Gradients

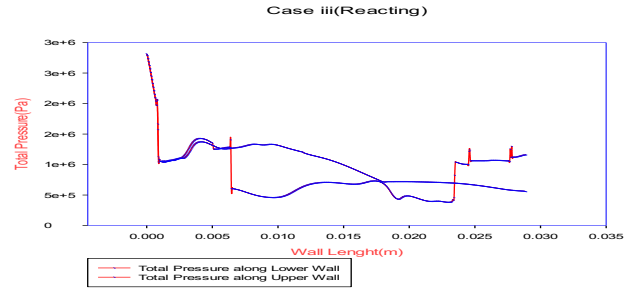

Fig. 19: Plots of Total pressure gradient for reacting flow

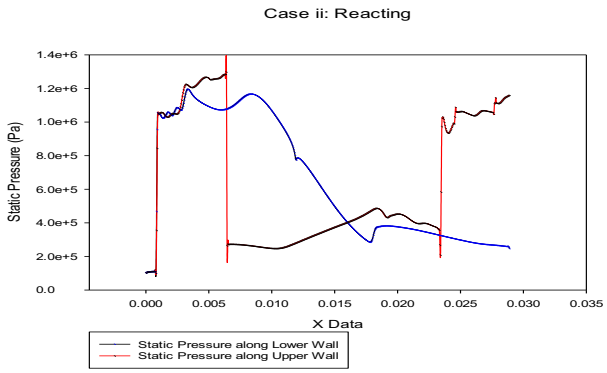

Fig. 20: Plots of Static pressure for reacting flow

In reacting flow model, chemical reaction takes place and there is a subsequent increase in the pressure at the cavity which is responsible for the disappearance of the shock train. With the increase in the pressure downstream, the shock moves upstream and almost a normal shock is observed at the inlet of the combustor. There is a minimal total pressure losses incurred supporting for a fundamental desirable characteristic of any combustor.

Contours of Total- and Static- Temperature Gradients

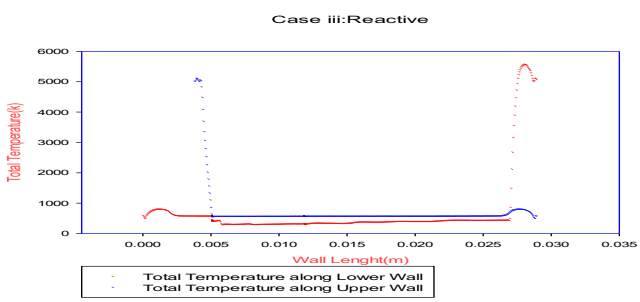

Fig. 21: Plots of Total temperature gradient for reacting flow

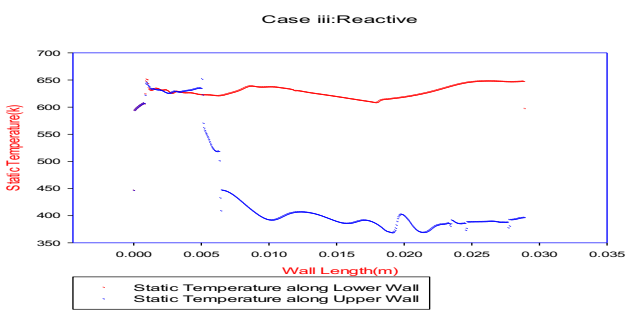

Fig. 22: Plots of Static temperature gradient for reacting flow

The static temperature gradient is appropriated as a profound, qualitative indication of combustion efficiency implementing hydrogen as an optimal fuel choice. Higher combustion efficiency means, greater percentage of the injected fuel undergoes combustion resulting in a higher static temperature at combustor exit. It is also observed that enthalpy (Fig. 30, next page) within the cavity is quite high.

From contours of total temperature gradient, it is apparent that across a shockwave there is no change in total temperature gradient in Fig. 21 and from contours of static temperature gradient in Fig. 22 it is recognizable for a relatively marginal increase in static temperature across a shockwave.

The steep temperature rise is along the shear layer growth direction fortifying occurrences of a very strong reaction(s) in the neighborhood within the shear layer region proximity exhibiting a profound multi-disciplinary compressible-turbulent-combustion physics.

Reaction zone is clearly visible in Arrhenius reaction rate contours of Fig 29 (next page). Temperature inside shear layer is noticeably visualized dissipating towards the downstream surroundings of combustor.

Contours of Turbulence Energy Spectrum:

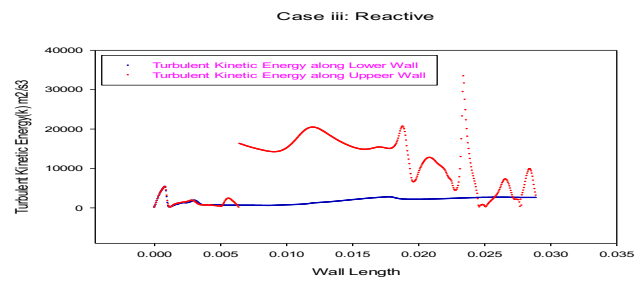

Fig. 23: Plots of turbulent kinetic energy for reacting flow

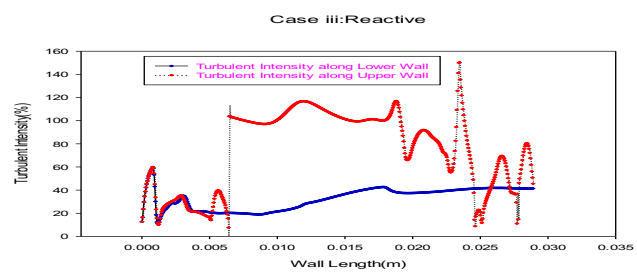

Fig. 24: Plots of Turbulent Intensity for reacting flow

It is clearly evident from depicted contours that turbulence is initiated downstream of shock wave and achieved prominently a high turbulent intensity value inside the cavity enriching turbulent mixing of fuel-air mixture. Strong recirculation zones present along upper- and lower- wall supplies fuel to the upstream flow for reactive mechanism to initiate and proceed further.

Turbulent kinetic energy spectrum depicted from Fig. 23 is an indication of resilient vortex cascade formation within the cavity enhancing air-fuel mixing.

Contours & Plots of Reactive Chemical Species:

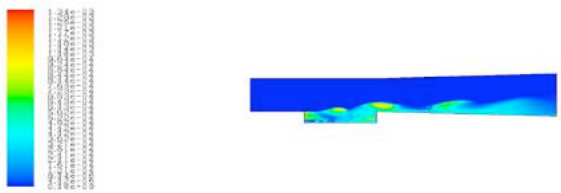

Fig. 25: Mass fraction of air flow distribution inside combustor

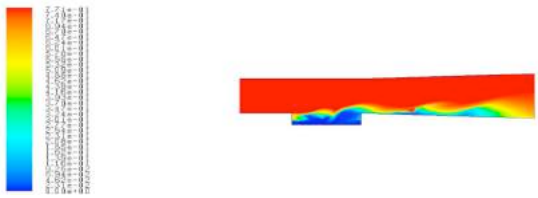

Fig. 26: Contours of mass fraction of N_2 species

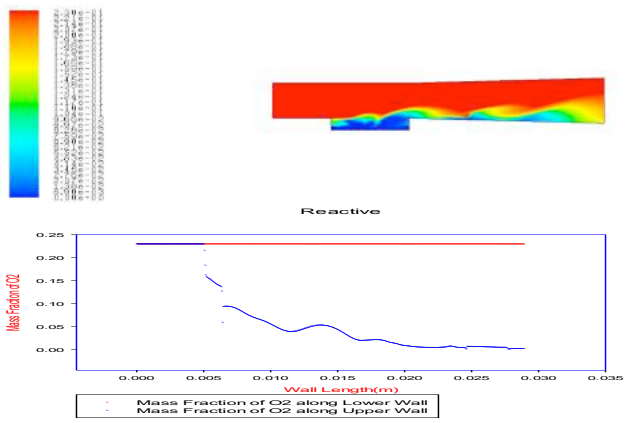

Fig. 27: Residuals & Plots of mass fraction of O_2 species

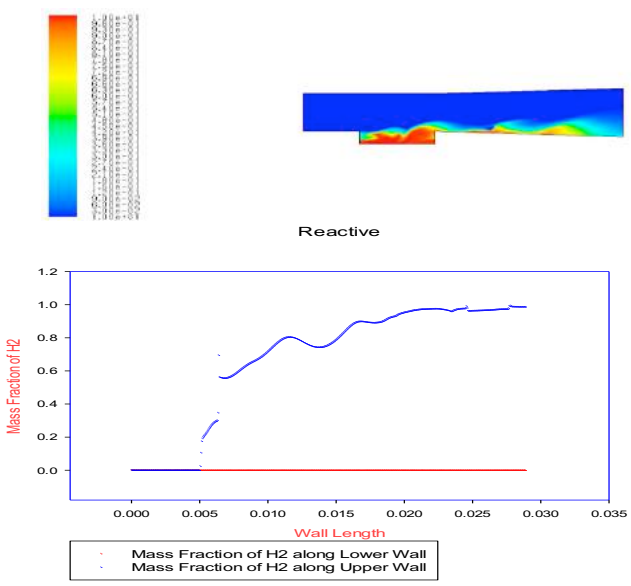

Fig. 28: Residuals & Variation of mass fraction of H_2 species

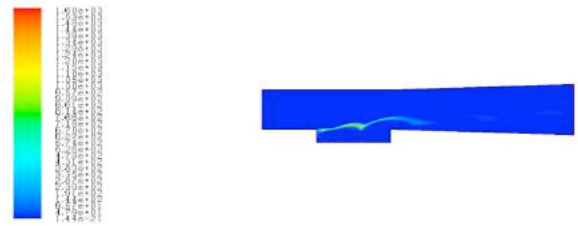

Fig. 29: Contours of Arrhenius rate of reaction

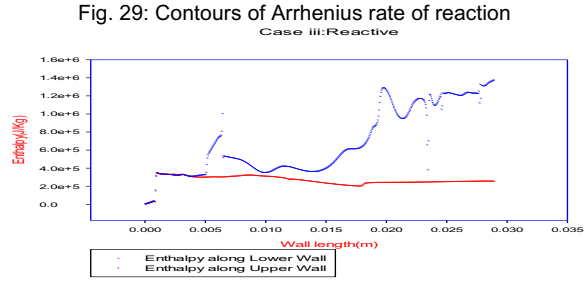

Fig. 30: Plots of Enthalpy within reaction zone of cavity

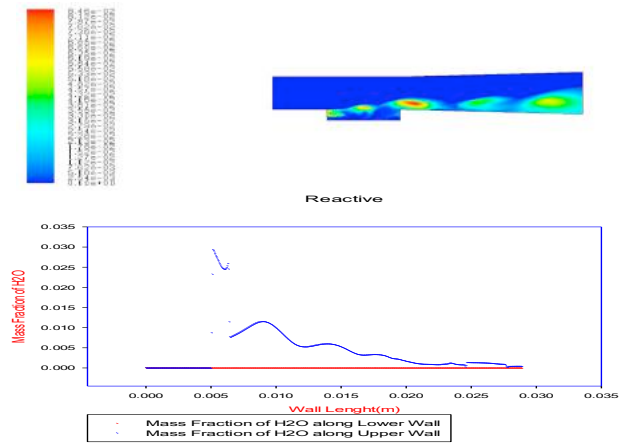

Fig. 31: Residuals & Variation of mass fraction of H_2O species

Comprehensive analysis of the mass fraction contours of H_2, O_2 and H_2O reflected significant evidence of appropriate fuel injection, effective turbulent mixing of fuel-air mixture, an substantial combustion manifestation within the scramjet combustor envelope.

Mass fraction of oxygen was at a maximum (=0.23) along air inlet of combustor. After fuel injection, mixing of oxygen and H_2 causes a variation in the mass fraction of O2 at any cross section of the combustor towards the outlet, as can be observed from the contour. The mass fraction varies from 0.23 at the interior of the combustor to almost 0 at the lower wall. Mass fraction of H_2 is zero up to the fuel injection port. An increase in the mass fraction of H_2 beyond the fuel injector location indicates the occurrence of fuel inoculations. The mass fraction continues to decrease, injector downstream due to occurrence of combustion which consumes hydrogen fuel. Mass fraction of H_2O was found to be zero at most places of the combustor to a maximum of 0.086 at the place where the reaction took place. The major changes are found to be across the turbulent shear layer.

4. Conclusion

Numerical analysis of fuel-air mixing investigations of cavity based inoculations inside a 2D supersonic combustor was performed for non-reacting and reacting flow conditions. The simulations were carried out for a cavity of $\left[\frac{L}{D}\right] = 4$. As fuel was injected into the combustor from the fore-, aft-, and floor- walls of the cavity, several upstream shock waves were observed. The small recirculation region which was present at the cavity and free stream interface helped in continuous transfer of fuel into the reacting zone. The low velocity recirculation region within cavity of scramjet engine definitely ensures for greater fuel-air residence times, thus signifying flame holding capacity of cavity based scramjet combustors.

In case of reacting flows, flow features downstream of coupled normal- and oblique- shockwave expansion fans are notably distinguishable. Accommodating a very high heat release occurring in this case, a small divergence angle should be provided on the upper wall. The flame was identified using contours of temperature and reaction rate and it was observed that flame anchored on the upstream wall of the cavity. The flame was formed at the cavity interface and main flow regime wherein the presence of strong turbulent re-circulating vortices facilitated for the flame holding capability.

5. Acknowledgment

The author gratefully acknowledges contributions of Dr RK Sharma, Distinguished Scientist and Director (Retired), HSTDV Project, DRDL, Kanchanbagh for his valuable suggestions during results discussion.

6. References

[1] Mishra D P and Sridhar K V, “Fuel Injection and Fuel Stabilization in a Supersonic Combustor”, International Conference on High Speed Trans-Atmospheric Air Space Transportation (ICHSTAST), June 2007.

[2] Adela Ben-Yakar, Ronald K. Hanson, “Cavity Flame-Holders for Ignition and Flame Stabilization in Scramjets: An Overview”, Journal of Propulsion and Power, Vol. 17, No. 4, Aug 2001.

[3] K V Sridhar and D P Mishra, “Numerical Investigation of Direct Fuel Injection from the Cavity Walls in a 2D Supersonic Combustor”, International Journal of Turbo & Jet Engines, 26, 155-168, 2009.

[4] K H Yu and K C Schadow, “Cavity-Actuated Supersonic Mixing and Combustion Control”, Combustion and Flame 99:295-301 (1994).

[5] F Xing, M M Zhao and S Zhan, “Simulations of a Cavity Based Two-Dimensional Scramjet Model”, 18th Australasian Fluid Mechanics Conference Launceston, Australia, 3-7 December 2012.

[6] P Manna & D Chakraborty, “Evaluation of Combustion Models for High Speed H_2/Air Confined Mixing Layer Using DNS Data”, Combustion and Flame 121:195–209 (2000).

[7] Zhiliang Xuxk, Myoungnyoun Kimxk, Wonho Ohzk, James Glimmzxk, Roman Samulyakx, Xiaolin Liz and Constantine Tzanos, “Atomization of A High Speed Jet”, April 14, 2005, U.S. Department Of Energy.

[8] D P Mishra “Fundamentals of Combustion”, Prentice Hall of India Private Ltd., New Delhi, 2008.

[9] Billing F S, “Research on Supersonic Combustion”, Journal of Propulsion and Power, Vol.9, No.4, 1996.

[10] Dean Andreadis, “Scramjet Engines Enabling the Seamless Integration of Air & Space Operations”, Pratt & Whitney Space Propulsion.

[11] David M Van Wie “Hypersonic Air-breathing Propulsion”, Johns Hopkins APL Technical Digest, Vol 26, 2005.

[12] Dean Andreadis, “Scramjets Integrate Air and Space”, July 2004.

7. Biographies

Kodamasimham Bharadwajan primary author obtained his Master of Science degree from Institute of Energy Technology campus, Aalborg University, Denmark with Fluids & Combustion Engineering discipline. His research interests are widely towards Numerical-, Experimental- modeling of Turbulent-Combustion, Aero-thermodynamics of high-speed propulsion systems and acquired research experience within the relevant Aeronautics subjects. He is a research scholar working towards doctoral degree from JNTU-H in same and is Life member of APS congress Mathematical sciences.

Dr Debi Prasad Mishra is well known and prominent personality in Aerospace Engineering community focused in the areas of Combustion and its applications related to propulsion, thermodynamics, fluid mechanics and experimental methods from IISc, Bangalore. He is Fellow of Institution of Engineers and proactive Life Member- The Combustion Institute (Indian section), Aeronautical Society of India, Solar Energy society of India, Indian society for Heat and Mass Transfer, India Society for Technical Education, Indian Science Congress Association, Indian Aerosol Science and Technology Association, designating administration portfolios with MHRD and several research projects.

Dr PV Ramana Murti is a familiar and prominent personality among the Mechanical Engineering community, specialized in areas of Machine Design and Machine Dynamics from IIT, Madras. He is Fellow of Institution of Engineers and Life Member of India Society for Technical Education and served various administration portfolios Viz., Convenor-BOS, Director- Evaluation, Academic and Planning at Andhra University-Waltair, JNTU-Hyderabad, Nagarjuna University and also contributed towards research projects.

Dr Srinivasan Vathsal is a distinguished personality of DRDO and close associate of formerly Hon’ble President of India Late Dr APJ Abdul Kalam and several other distinguished aerospace and defence personalities of VSSC, ISRO, and their associated laboratory’s. He earned 2 Post-Doctoral degrees from NASA-United States and DLR-Germany and several outstanding credentials for aerospace research contributions.

Design and Fabrication of a High Endurance, Cost-Effective, Auto-Stabilised Airship

Sohan Suvarna *†‡ Amogh S. Joshi § Avinash Dubey ¶ Rajkumar S. Pant †

Abstract – Unmanned Aerial Vehicles are flying vehicles capable of performing a wide variety of tasks such as package delivery, aerial surveillance and acting as disaster management aids. However, the most common UAV, viz. multi-rotorcraft have limited payload capacities as well as limited endurance. The use of airships could overcome these hurdles as they are energy efficient and can deliver high endurance and have higher payload capacity. The objective of this research is to demonstrate the design, fabrication and testing of high endurance, cost-effective and auto-stabilised airship for indoor applications. The proposed airship is an ideal means for long-duration indoor surveillance and advertising. A model indoor airship was designed and fabricated. This paper documents the details of envelope petal design and patterning. All of the airships subsystems, except for the controller board, were designed and fabricated in-house. In spite of the several advantages that airships provide, their applications are restricted since they are unsteady fliers and have an inherent directional instability. This research also proposes and describes the use of closed feedback loop for altitude hold, pitch regulation and to maintain directional heading. Primus-X autopilot system was used to implement the PID control law for realisation of the auto-stabilisation of the airship. Several flight tests of the model airship successfully validated all of its subsystems and exhibited nearly four times the longevity as compared to its multirotor counterpart with the same battery.

***Index Terms*– Micro-Airship, Lighter Than Air Systems, Unmanned Aerial Systems, Petal Design, Auto-Stabilization, Autopilot System**

*IITB Monash Research Academy, Mumbai

†Department of Aerospace Engineering, Indian Institute of Technology, Bombay

‡Department of Mechanical and Aerospace Engineering, Monash University

§Department of Electronics Engineering, K.J.Somaiya College of Engineering, Mumbai

¶Department of Mechanical Engineering, Indian Institute of Technology (Benaras Hindu University), Varanasi

1 INTRODUCTION

Unmanned Aerial Vehicle (UAV), commonly known as drones, are becoming an integral part of our lives. Most times, the word 'drone' is associated with the multi-rotor craft. These multi-rotor UAVs have a wide range of applications, but they also have limitations such as low payload capacity and low endurance. The present research explores the use of airships as a viable UAV.

Airships are lighter than air-craft that generate lift based on the principle of buoyancy. The main difference between a balloon and an airship is that it is possible to control and propel an airship, whereas a balloon relies solely on wind currents in order to maneuver itself. A conventional non-rigid airship contains a streamlined envelope which holds the lifting gas, a gondola suspended beneath which houses the propulsion system, avionics, and the payload.

Airships offer a stable, low-cost, long-lasting platform with low vibration, noise and wind disturbances that are otherwise common in aerial vehicles. Due to their large size, unmanned airships tend to be massive crowd pullers and are hence popularly used for advertising. They can also be used as mounting platforms for scientific sensors, for remote-sensing applications [18], for performing surveillance and for providing internet connectivity, amongst other things. The fabrication of Airship envelopes has been the subject of research for many decades now. Munson, Young and Okiishi [9], have provided a working knowledge of the concepts of fluid mechanics. Thiele's [17] paper on patterning technique is a comprehensive review of the merits of different envelope shapes with respect to stress distribution. The airship 'Simon', created by Rüegg, Lutz and Rüegg [12], demonstrated that a radio-controlled blimp could be designed and fabricated from scratch with minimal resources. An informative study of the materials used in envelope fabrication is found in Sonawane, Fernandes, Pant, Tandale and Pant [13]. Gawale, Raina, Pant and Jahagirdar [3] provide a detailed account of the envelope profiles, envelope materials and propulsion systems. Ilieva, Pascoa, Dumas and Trancossi [4] have conducted a detailed study of various propulsion systems used in airships.

The paper illustrates the necessary documentation relating to petal design. It also provides an easy method to fabricate smaller airships. The airship fabricated as part of this research also implements an active stabilisation system. Active stabilisation systems for airships have been fabricated previously. However, the system implemented in this research provided robust stabilisation while keeping the hardware footprint as low as possible. This system was implemented in C++, thus also keeping the software footprint low.

2 DESIGN METHODOLOGY

An indoor airship can be broadly divided into three components/subsystems - envelope and structure, propulsion and avionics . Methodology for design of a conventional airship is outlined in [3] [7] [11] and [16]. Main objective of the airship design methodology is to minimise the size of the envelope while fulfilling the design requirements. Other objective is to increase the flight endurance and the overall life of the airship.This paper documents the methodology to develop a low-cost, easy-to-fabricate, and easy-to-deploy indoor airship. In order to achieve these objectives, an iterative process was used to size the airship envelope, which is described in [15].

2.1 Design of Envelope

Envelope design consists of three important aspects viz. choosing an appropriate envelope profile, envelope size and envelope material. The envelope profile decides the lifting capacity and dynamic behaviour of an airship [8]. The modified-GNVR profile was chosen for this airship due to its good volume to surface area ratio and low aerodynamic drag. The aerodynamic data for GNVR profile was taken from Narayana and Srilatha [10] and Sundaram [14]. Envelope material was chosen based on the flying conditions as it should be ideally low in weight and highly durable. After that, an initial estimate of airship weight excluding envelope material's weight was made. Envelope dimensions were fixed by an iterative process to achieve a neutrally buoyant condition as shown by the yellow line in Fig. 1. The strategy utilised in deciding the diameter of the envelope has been aptly described by Suvarna et al. [16].

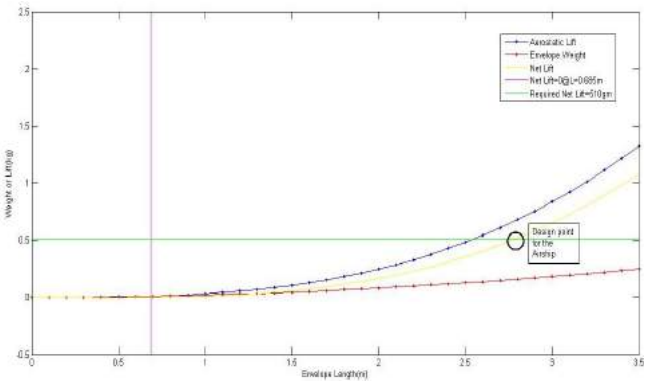

Figure 1: Net Lift v/s Airship Length

3 AUTOPILOT DESIGN

An autopilot system could be used to stabilise the airship, as well as to provide a friendly User Interface (UI) and robust control. The autopilot would perform simple functions such as actuation of the propulsion system along with complex functions such as altitude-hold, pitch regulation, and heading control. Complimentary filter was used on the data received from the barometer, accelerometers, gyroscopes and magnetometer, to get estimates for the attitude and altitude of the airship. In addition to providing a UI that enhances the user experience, this system would maintain controlled flight in case of UI failures or incorrect or extreme inputs on the part of the user. After due deliberation, it was decided to use an ARM Cortex M3 STM32 MCU in the flight controller. The controller is used to implement heading and pitch control, along with altitude control as well as alt-hold. Fig. 2 and Fig. 3 show the heading and integrated altitude-hold and pitch regulation algorithms, respectively. PrimusX, a miniature controller board based on the ARM Cortex M4 MCU, an enhanced version of the Cortex M3 was chosen as the autopilot system for the airship as the autopilot supported API (Application Program Interface) for programming. All of the desired functions were implemented in C++ on the PrimusX. The UI was provided by the PlutoPliot mobile application that came bundled with the PrimusX. To meet the specified power and noise level requirements, Coreless DC Motors were chosen as the propulsion actuators. The specifications of the motors are as given in Table 1

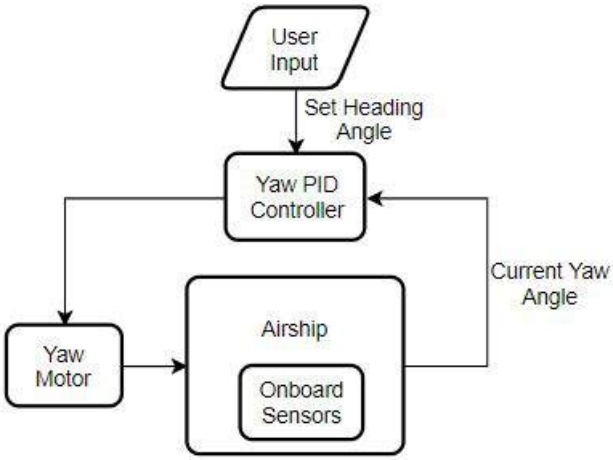

Figure 2: Heading Control Algorithm

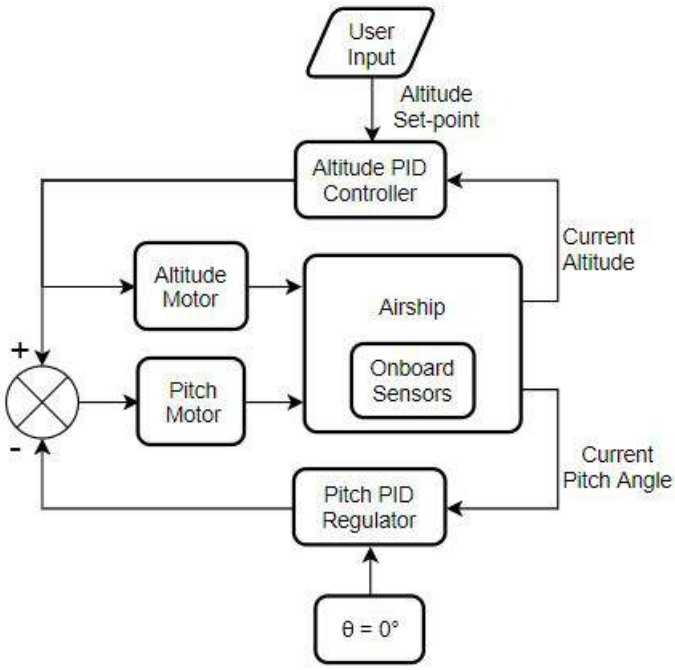

Figure 3: Integrated Althold and Pitch Regulation

3.1 Design of Propulsion System

The propulsion system is amongst the most critical subsystems on an airship. Airship propulsion systems can be divided into two types - Conventional Propulsion Systems, i.e., systems utilising IC Engines, and Electric Propulsion systems, i.e., systems utilising batteries and electric motors. Studies on conventional propulsion systems have been carried out by Gawale and Pant [2]. Since the airship being designed was meant primarily for indoor applications, where power requirements are low, and noise levels must be minimised, an all-electric propulsion system was chosen to power the airship. The locations of propulsion actuators for the airship were chosen such that the lateral and longitudinal controls could be easily decoupled. Five coreless DC motors were used, as shown in the Fig. 4.

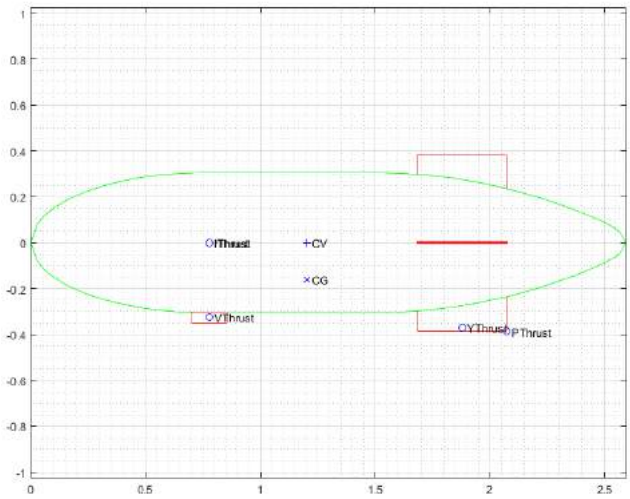

Figure 4: Positions of DC motors

As the airship was to be operated at much lower speeds, the effect of control surfaces would be less due to lower dynamic pressure. Hence two dedicated rotors were used to control yaw and pitch.

4 FABRICATION OF EXPERIMENTAL INDOOR AIRSHIP

After taking into consideration all of the points listed in the design methodology, the following design is proposed for the experimental airship.

4.1 Fabrication of Envelope

Several methods available for envelope fabrication as discussed in [17] [3]. Gore design method, as discussed in [7] was implemented for the envelope fabrication of this airship. This approach is best suited for a small envelope and is also simple in construction.

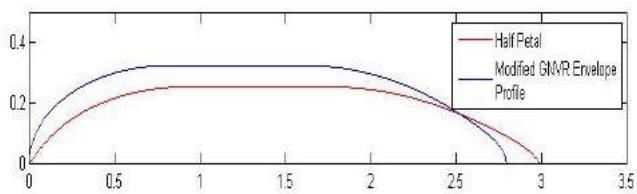

Figure 5: Modified GNVR and Half Petal Profile

In this approach, firstly, the number of gores (or petals) is decided. A large number of petals increase the weight of the envelope as the margin area for welding increases. Also, from the operation point of view, it increases the risk of leakage. On the other hand, a small number of petals will not be able to form a proper shape. Apart from this, the number of petals is constrained by the width of the material available. Therefore, incorporating the above factors, the number of the petal is decided. It is generally six in case of small envelopes. The profile is composed of different geometrical curves, e.g., the modified GNVR profile has four elements, namely, elliptical, circular, cylindrical, and parabolic. The gore design method produces polygonal cross-sections. Simple geometrical constructs are used to find coordinates of petals. X-coordinate, i.e. α is the true longitudinal length of the profile obtained using Pythagoras theorem. In contrast, the Y-coordinate i.e. β is obtained by dividing the circumference of that cross-section by the number of petals. For instance, in the elliptical section of the modified GNVR profile, if x and y represent the coordinates of the ellipse, then coordinates of the gore petal i.e.α and β would be

$$\alpha = \int_a^b \sqrt{1 + \left(\frac{dy}{dx}\right)^2}\, dx \tag{1}$$

$$\beta = \pm\pi \frac{y}{n} \tag{2}$$

Similarly, other coordinates can be found by replacing rele-

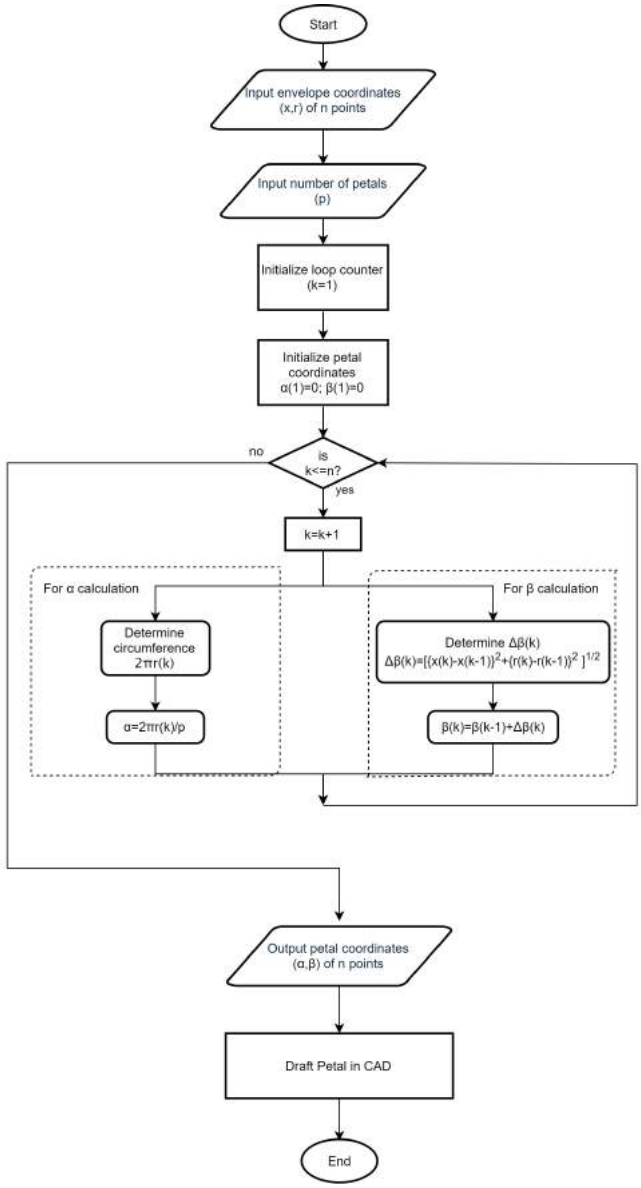

Figure 6: Petal Design Methodology

vant values in above equation.In Fig.5 Modified GNVR profile and corresponding petal profile is shown. A detailed flowchart of fabrication of envelope is given as Fig.6. Larger the number of points, more accurate is the profile of the petal. One thousand data points for the envelope profile were used to draft the petal for the airship discussed in this paper. Also, the margin for sealing is included in the petal by increasing the Y-coordinates. The obtained coordinates are now used to draft the template petal. After that, required number of petals are cut from the material and welded together with the help of heal-sealing machine. Once the fabrication was

complete, the envelope was initially tested for leaks by filling it with air. To reassure that envelope is leak free, it is then filled with helium and leaks if any, were detected using a extremely sensitive helium leak detector.

4.2 Propulsion System

Table 1: Specs of Coreless DC Motors

Weight	7gm
RPM	max. 39000 RPM
Power	6W

In all, five motors were used - two motors for forward thrust, and one motor each for pitch, yaw and altitude control.

Figure 7: PrimusX Controller Board

The Coreless DC Motors were actuated by the MCU by means of Pulse-Width-Modulation (PWM) signals. The PrimusX has eight PWM ports - four each for uni- and bi-directional motor control. The motors delivering forward thrust were connected to unidirectional control ports, while the pitch and yaw control motors were connected to the bi-directional control ports.

The BME280 [1] atmospheric sensor and MPU9250 nine-axis Inertial Motion Unit (IMU) [6] [5] provided the required sensory inputs.

The data received from these sensors, along with the inputs received from the PlutoPilot app were processed by the MCU to generate the PWM signal that was then used to drive the motors. When the altitude-hold function was enabled, the sensory input of altitude was given as input to a simple Proportional-Integral-Derivative (PID) control algorithm. The output of the PID algorithm was used to drive the altitude control motor in order to maintain the set altitude. Thus, the sensors and actuators functioned in tandem to create a highly effective control system. The fabricated indoor airship is shown in Fig. 8.

Figure 8: *'MiniEureka'* airship

4.3 Costing Details

An approximate costing analysis of the airship miniEureka was performed. The results of the cost analysis are as follows :

Table 2: Costing Details

Particulars	Cost
30gsm MPET	₹1000
Avionics suite	₹10000
Operating costs (LTA gas and power)	₹5000
Manpower	24 manhours

5 RESULTS

The designed airship, named 'MiniEureka', was subjected to three flight tests to validate its design and control system. The first flight test revealed certain flaws in its turn rate which were corrected in subsequent test flights. During the second test flight, one of the airship's two forward thrusting motors malfunctioned. However, the system proved to be robust enough to keep flying even with one motor down. It was later determined that the malfunction had been caused by a breakage in the wire connecting the motor to the PrimusX. In the final flight test, the airship and all of its systems functioned flawlessly. Fig. 9 contains samples of the airship's altitude plotted versus time when the Alt-hold system was ordered to hold an altitude of 4.5m (the red line) from an initial altitude of 4m (the blue line).

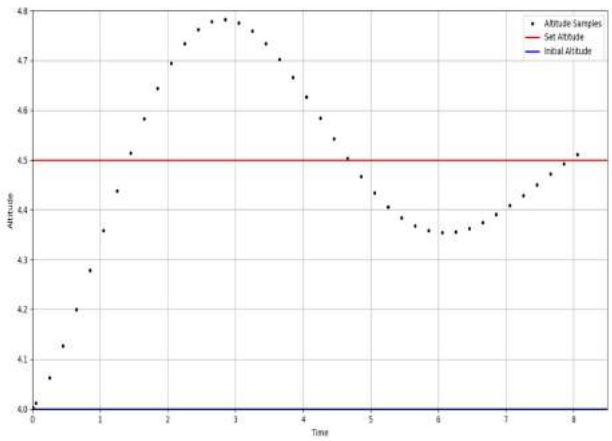

Figure 9: Response of Alt-Hold System

Owing to memory constraints, only the first 8 seconds of data could be recorded. However, this data is enough to validate the functioning of the althold system. The inherent sluggishness of LTA systems is reflected in the althold system too. In the final flight test, the airship was able to achieve an endurance of about 40 minutes on a standard 3.7v 600mAh LiPo battery. Videos of the flight test are available on YouTube[1]

Thus, the 'MiniEureka' demonstrated itself to be an easy-to-build and cost-effective solution to the problem of designing, fabricating and rigorously testing an Airship.

6 FUTURE PROSPECTS

The further development of airships, in spite of possessing great potential, is hindered by a few basic, and as yet, un-

[1] https://www.youtube.com/watch?v=JsCmCI2JVh8

solved problems. These problems are the inherent bulkiness of airships, the long time required to inflate, deflate and service them and their inherent instability in high winds, among other things. Therefore, work in any of these fields will not only further the present research, but research on airships as a whole. With respect to this airship, further optimisation of the control loops and enhanced endurance are the primary areas for further development.

References

[1] Bosch Sensortec. *BME280 Combined humidity and pressure sensor*, September 2018. Rev. 1.6.

[2] Amol Gawale and Rajkumar Pant. design studies of a powerplant system of non-rigid airship. In *5th International Convention of The Airship Association*, August 2004.

[3] Amol Gawale, Amool Raina, Rajkumar Pant, and Yogendra Jahagirdar. *Design, Fabrication and Operation of Remotely Controlled Airships in India*. 2009.

[4] Galina Ilieva, José Páscoa, Antonio Dumas, and Michele Trancossi. A critical review of propulsion concepts for modern airships. *Open Engineering*, Vol. 2, 2012.

[5] InvenSense. *MPU-9250 Register Map and Descriptions*, July 2015. Rev. 1.6.

[6] InvenSense. *MPU-9250 Product Specification*, June 2016. Rev. 1.1.

[7] Sohrab R Mistri and Rajkumar S Pant. Design and fabrication of a quick dismantlable remotely controlled semirigid finless airship. In *Innovative Design and Development Practices in Aerospace and Automotive Engineering*, pages 103–116. Springer, 2017.

[8] Nawaz I Motiwala, Irshad Ahmed Khan, Nitesh P Yelve, Balkrishna E Narkhede, and Rajkumar S Pant. Conceptual approach for design, fabrication and testing of indoor remotely controlled airship. In *Advanced Materials Research*, volume 690, pages 3390–3395. Trans Tech Publ, 2013.

[9] Bruce R Munson, Donald F Young, and Theodore H Okiishi. *Fundamentals of Fluid Mechanics*. Wiley, 4 edition, 1990.

[10] CL Narayana and KR Srilatha. Analysis of aerostat configurations by panel methods. *BLISS Project Document CF*, 10, 2000.

[11] Rajkumar Pant. Design, fabrication and flight demonstration of a remotely controlled airship for snow scientists. *Journal of Aerospace Technology and Management*, 6:19–27, 02 2014.

[12] Maurice Rüegg, Cyril Lutz, and Natalie Rüegg. The airship simon - design and construction of a radio controlled blimp. Technical report, Realgymnasium Rämibühl, Zürich, 1998.

[13] Bhushan Sonawane, Marvin A F Fernandes, Varun Pant, Madhukar S Tandale, and Rajkumar Pant. Material characterization of envelope fabrics for lighter than air systems. In *International Colloquium on Materials, Manufacturing and Metrology*, August 2014.

[14] S Sundaram. Wind tunnel tests on 1:7 and 1:28 scale aerostat models. *Experimental Aerodynamics Divisions, National Aerospace Laboratories, Bangalore, India*, 2000.

[15] Sohan Suvarna, Shoeb Ahmed Adeel, and Rajkumar S Pant. Design and development of an easily deployable indoor finless airship.

[16] Sohan Suvarna, Hoam Chung, and Rajkumar S. Pant. Design methodology of a small unmanned airship with optimized fins. pages 1136–1142, June 2019.

[17] James Thiele. *Patterning techniques for inflatable LTA vehicles*, pages 89–94. 1983.

[18] B. T. Walkenhorst, G. F. Miner, and D. V. Arnold. A low cost, radio controlled blimp as a platform for remote sensing. In *IGARSS 2000. IEEE 2000 International Geoscience and Remote Sensing Symposium. Taking the Pulse of the Planet: The Role of Remote Sensing in Managing the Environment. Proceedings (Cat. No.00CH37120)*, volume 5, pages 2308–2309, July 2000.

DESIGN AND FABRICATION OF AN INDOOR TETHERED AEROSTAT SYSTEM

M.Suhel U Karkun,[1] Aashna Seth[2], Raman Verma[3] & Rajkumar S. Pant[4]

[1]Summer Intern,Student, Department of Aeronautical Engineering, ASOIT, Ahmedabad, suhelkarkun786@gmail.com, 7405770602

[2]Summer Intern,Student, Department of Aeronautical Engineering, MIT Manipal, aashnaseth1256@hotmail.com, 9892813421

[3]Project Engineer, Lighter-Than -Air systems Laboratory, Department of Aerospace Engineering, IIT Bombay, Mumbai, raman.sr@iitb.ac.in,7708265423

[4]Professor, Lighter-Than-Air systems Laboratory, Department of Aerospace Engineering, IIT Bombay, Mumbai, rpant@iitb.ac.in, 9820084502

Abstract-- **This paper describes the design, fabrication and deployment of a tethered aerostat system for indoor purposes. To design this aerostat system an existing design methodology was referred to. An oblate spheroidal aerostat envelope was chosen to accommodate the sail, for ease of fabrication and for better stress distribution. A hand and motor operated portable winch system was designed and fabricated. A light-weight digital camera was mounted using a self-designed pan-tilt servo on a wooden payload carrying as a payload, and it provided steady and distortion-free HD image.**

Key Words-- LTA System, Indoor Tethered Aerostat,

1. INTRODUCTION

Aerostat is an aerodynamically shaped tethered body, belonging to the family of Lighter-than-Air (LTA) System, where static lift is produced on the basis of Archimedes principle. Archimedes principle states that the upward buoyant force that is exerted on a body immersed in a fluid, whether fully or partial, is equal to the weight of fluid that body displaces and acts in upward direction at the center of mass of displaced fluid. The volume of envelope is so designed that the displaced air should be able to produce sufficient lift to balance all the weight groups of all system (including payload).Payloads in modern day aerostats are usually radars, surveillance cameras or communication equipment. This paper discusses the design, fabrication, testing and deployment of the working model of oblate spheroid indoor aerostat system. The following are the principle parts of an Aerostat system,

1. Envelope- The main purpose of the envelope is to carry the LTA lifting gas (mostly hydrogen or helium).

2. Air ballonet- A ballonet is an air bag inside the outer envelope of an airship which is used for pressure and buoyancy control normally at very high altitudes.

3. Sail- The purpose of sail is to provide static and dynamic stability to the aerostat envelope.

4. Tether- It is an attachment between the envelope and the ground station.

5. Payload- It is the carrying capacity of the envelope system. In aerostats payload is mostly cameras, radars and transponders.

6. Ground Station- Winching System: The purpose of winching system or winch is to ensure that the envelope can be deployed at a particular height with safe ascend and descend speed.

Mooring system: The purpose of mooring system is to hold the inflated envelope at a particular position while attachment or detachment of payload takes place.

7. Payload Carrying Bay - The purpose of PCB is to attach payload with envelope. The PCB is attached to the envelope or it is at confluence point hanging through confluence lines from envelope.

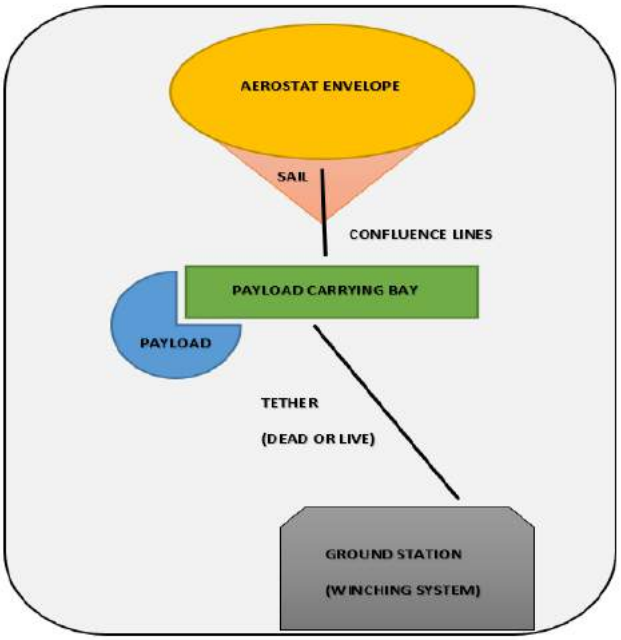

Figure 1. Basic Model of our Aerostat Systems

2. AEROSTAT CONCEPTUAL LAYOUT AND DESIGN

2.1 Conceptual Layout

As mentioned earlier, a sail based design was conceptualized to improve the stability of the system. Oblate spheroid was chosen to be the shape of the envelope to accommodate the sail and for ease of fabrication. A light weight custom designed Payload Bay was fabricated out of plywood. Its design was based on the payload and tether attachment. A hand and electrical motor powered winch was conceptualized and developed specially for this project. It has hand-locking mechanism and is easy to operate. A special PAN tilt servo was also conceptualized and developed in a 3D printer for attachment of camera and to cover 360^0 view.

2.2 Envelope Design

A crucial part of fabricating an aerostat, is to design an aerodynamically stable shape for its envelope. The shape should provide optimum stability even in turbulent wind conditions. Oblate spheroid shape was selected for the aerostat as it fit the major requirements for a tethered aerostat. The volume to surface area ratio of

the spheroid is greater than most shapes, therefore the overall weight of the aerostat decreases while providing a greater lift. A sail is provided for additional stability against strong winds.

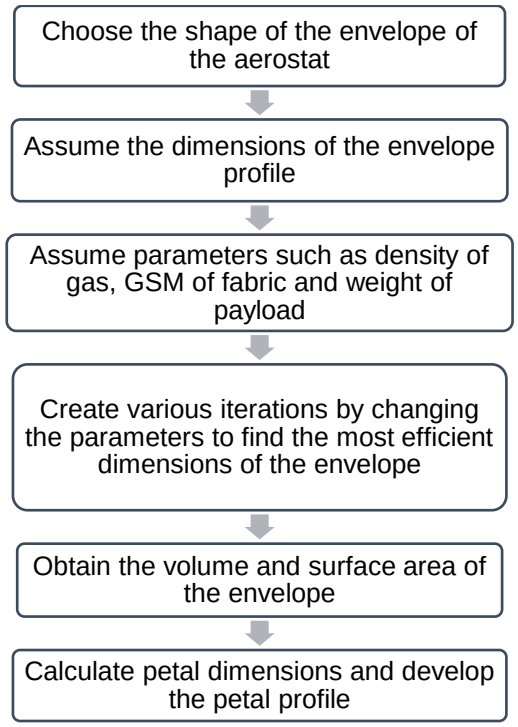

Figure 1. Flow Chart of the aerostat design methodology

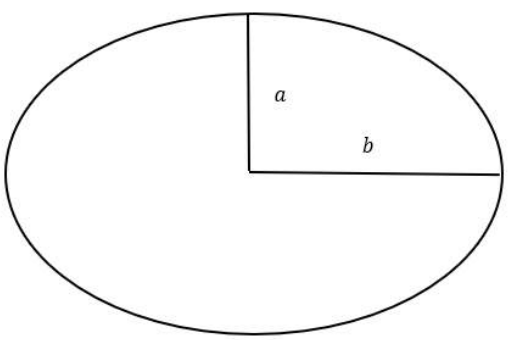

Figure 2. Envelope – 2D Profile of an Oblate Spheroid

Table 2. Envelope Specifications

Parameters	Specifications
Height (m)	0.66 (2a)
Width (m)	1.1 (2b)
Volume (m3)	0.4179
Material	MPET (22GSM)
No. Of Petals	6
Surface Area (m2)	2.8414
Self-Weight (N)	2.0

2.3 Material Selection

It is important that the material chosen for the fabrication of the aerostat be tough, light weight, and should not allow any leakage of gas. Materialized Polyethylene Terephthalate (MPET) and LDPE are commonly used for this purpose. MPET, being the lighter of the two materials and more easily available, was selected. It has a GSM((gram per square meter) value of 22. MPET is a polymer film coated by a thin layer metal(Aluminum). The metal coating reduces the permeability of the film to gases like hydrogen and helium. The properties of the film such as high toughness, the ability to be heat sealed, and lower density make the MPET material better suited. MPET being a thermoplastic can easily be linked together using a heat sealing machine.

2.4 Volume Estimation

The dimensions of the envelope, density of gas, GSM of fabric and weight of payload were taken into consideration to acquire an estimate value of the envelope. While sizing the envelope, it is important to maintain the L/D ratio. Equation 1 was used to find the volume and Equation 2 for the surface are of the spheroid. The buoyancy achieved by this volume is approximately 5.3N. With a GSM value of 22kg/m^2, the weight of the total fabric would ideally come to about 0.6N. That allows us to have a payload that weighs up to 400g.

$$v_{env} = \frac{4}{3}\pi\left(\frac{b^2}{2}\right)\left(\frac{a}{2}\right)$$

Equation 1

$$SA_{env} = 2\pi b^2\left(1 + \frac{(1-e^2)}{e * tan^{-1}e}\right)$$

Equation 2

Where,

$$e^2 = 1 - \frac{a^2}{b^2}$$

2.5 LTA Gas Selection

A tethered aerostat operates on the Principle of Archimedes. The atmospheric air surrounding the aerostat has a higher density than that of the gas filled inside it. The lighter gas is able to generate a lift equal to the weight of the displaced air, allowing the aerostat to rise up to the point of equilibrium. Helium

2.6 Petal Calculation

The area of each petal can be obtained by dividing the total surface area of the spheroid into 6 parts. For example, let the surface area of the spheroid be 60m^2, then the area of one petal would be 10m^2. It was

experimentally found that the outline of one half of the petal closely resembles a parabola. The area of any parabola can be calculated using equation 3. The equatorial circumference of the oblate spheroid was divided into 6 parts to get the width of each petal. By substituting the area and the width of a petal in equation 3, The outline of one half of the petal is determined by referring to the equation of a parabola, using the width and the area of the petal.

$$Area\ of\ petal = \frac{2}{3}(width)(height)$$

Equation 3

$$Eq.\ of\ petal : y^2 = -\alpha\left(x - \frac{width}{2}\right)$$

Equation 4

Using the x and y coordinates generated by equation 4, the exact shape of the entire petal can be generated.

3. Fabrication

3.1 Petal Fabrication

The gore outline was printed on a flex banner and then cut out. Using the flex banner as a stencil the petals were cut on the chosen material.

Figure 3. Cutting of Petals on MPET Material

The petals were joined together using a foot heat sealing machine as shown in the Figure 4. As mentioned earlier, due to the thermoplastic properties of the film, when two sheets of MPET are exposed to high temperature along with high pressure, they bond together forming an impermeable joint.

Figure 4. Heat Sealing the Petals

3.2 Payload Bay

Aerostat can be used for various functions. Aerostats are often used for surveillance and communication. The purpose of our aerostat was to use it for indoor surveillance. Therefore, a camera was installed. It is suggested to create Pan-tilt-servo for the camera from scratch, as it gives you the freedom to remove excess material and keep the it light-weight. The model was created on CatiaV5 and was then manufactured using a 3d printer. Two TGY-0025 sub micro Servos were used to permit the pan and tilt motion of the camera. In total, four parts were printed. All the components of the payload bay were assembled and fixed on a hexagonal plate as shown in the Figure 5.

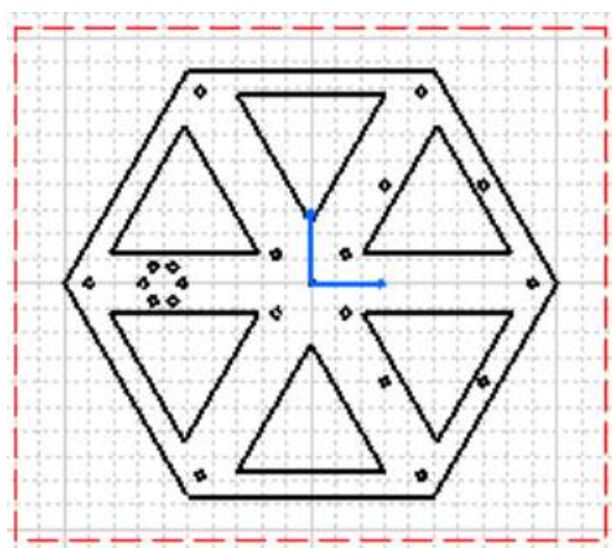

Figure 5. Design of Hexagonal base plate

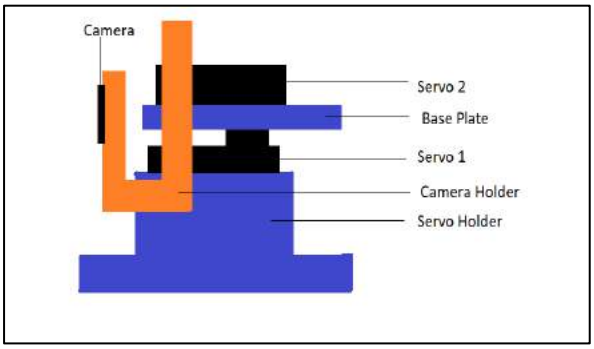

Figure 6. Design of the Pan-Tilt Servo with camera

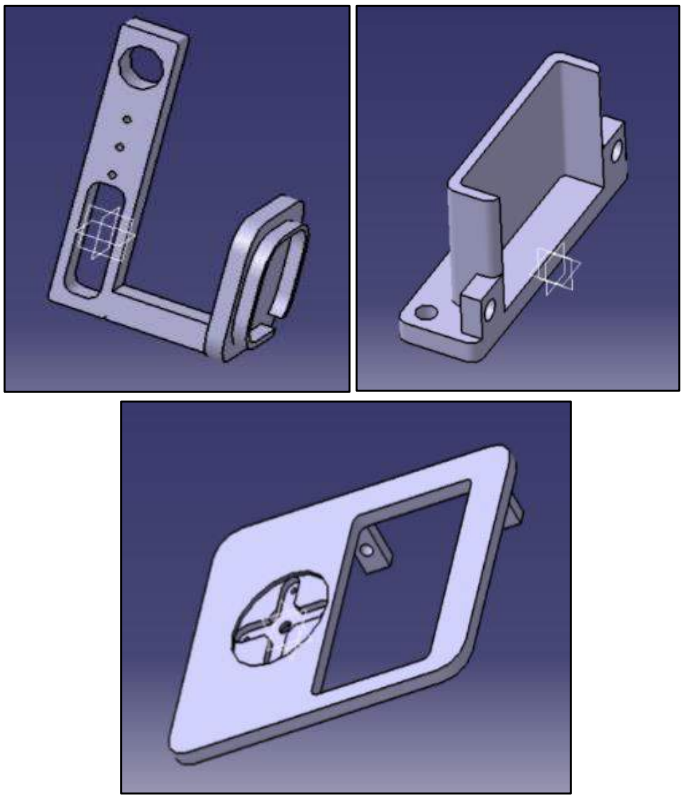

Figure 7.(a) Camera holder (b) Servo Holder and (c) Base Plate

3.3 Winching System

A winch system is meant to have good structural strength and should be easy to operate. In this model, an electric winch system, along with a hand crank for manual operation was designed. The model was constructed out of ply-wood and pvc pipes. A motor of 200 rpm was installed onto the winch system for winding and unwinding the tether ropes. In order to fix the aerostat at a certain altitude, a locking mechanism was installed as well.

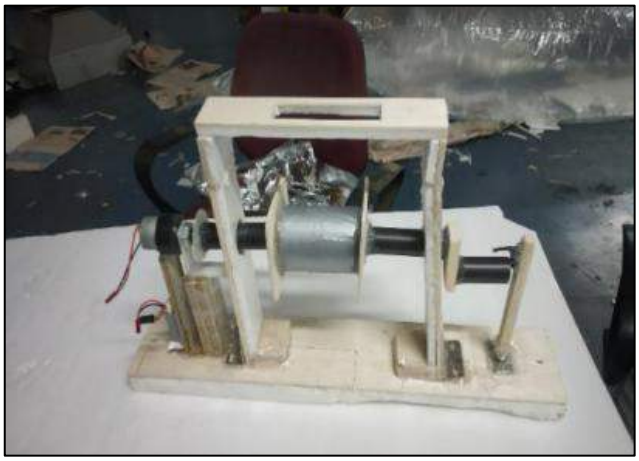

Figure 8. Model of Winching System

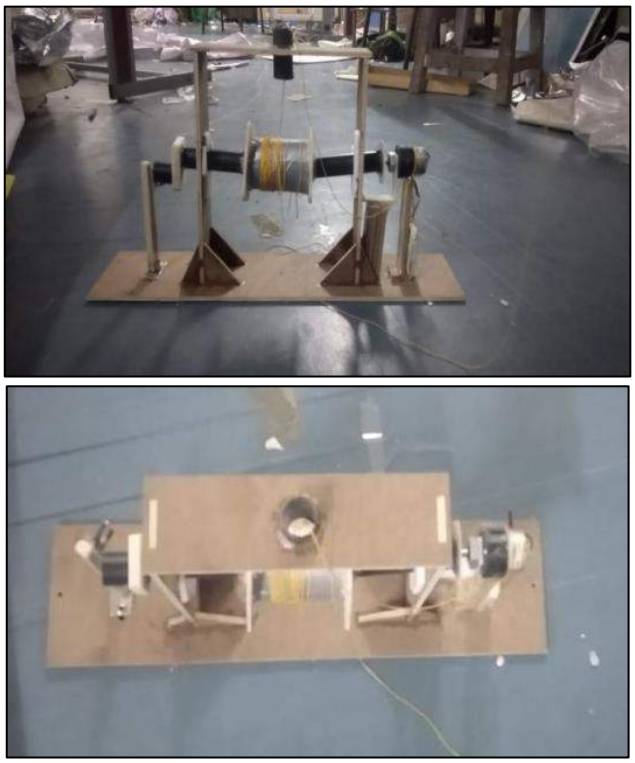

Figure 9. Model of our Second Winching System

3.4 Sail

An aerostat usually requires static and dynamic stability due to the presence of harsh wind conditions. This stability is provided by a sail, fins and/or kite. Since this aerostat was created for indoor purposes, there is less airflow and hence requires less stability. A sail provides enough stability without increasing the weight of the envelope. Therefore, in this model, a sail has been used in place of tail fins or kite. The dimensions of the sail are adapted from Reference [1]. Two petals were cut in half and then joined together using the heat sealing machine.

Figure 10. Sail Attached to the Envelope

3.5 Helium Leakage Test

LTA Gases have very small molecules, which can easily pass through the material of the envelope. Helium leakage tests are one way to check the leakage of envelopes as shown in the Figure 11.The leakage test performed showed positive results.

Figure 11. Helium Leakage Test

3.6 Indoor Field Trails and Observations

The first field trial of our aerostat system was conducted in the foyer/corridor of the Aerospace Department at Indian Institute of Technology Bombay. The foyer is approximately 50 feet high. As mentioned earlier, due to the high cost of helium, the aerostat was filled with helium as well air. This field trail was conducted for approximately 20-25 minutes. The figure 12 below shows field trail of our aerostat system in the corridor/foyer.

Figure 12. First Field Test of Aerostat System

4. Conclusion

This paper presents the design, fabrication and test observations of an aerostat system. It is essential to take some estimate values of certain variable parameters before beginning preliminary calculation. Various methods to obtain the outline of the petal (gore) have been tested and explained in this report. It was seen that the pan-tilt servo deigned for that servo motors was a bit small as not enough clearance was given. To rectify this, a pan tilt servo with more allowance should be fabricated. During the field tests, aerostat system performed better than expected. Due to the low weight of the payload and all its components, the aerostat was able to rise high enough even though it was filled partially with air.

5. Acknowledgement

The authors would like to thank to the members of Lighter-than-Air Systems Laboratory, Department of Aerospace Engineering, IIT Bombay, Mumbai.

6. References

[1] Dusane, C. R., Wani, A. V., Pant, R. S., Chakraborty, D., Chakravarthy, B. K., "An Elevated Balloon-Kite Hybrid platform for Surveillance", Proceedings of 23rd AIAA Lighter-Than-Air Systems Technology Conference, AIAA AVIATION Forum, (AIAA 2017-3995), Denver Colorado, USA, 5-9 June 2017.

[2] Gnanaprakash, K., Kamalraj, K. P., Pant, R. S., 'Design-Build-Fly of OSIRCA: Oblate Spheroid Indoor Remotely Controlled Airship', AIAA-2011-6914, Proceedings of 11th AIAA Aviation Technology, Integration, and Operations (ATIO) Conference, Virginia Beach, VA, USA ,20 - 22 September 2011, DoI: 10.2514/6.2011-6914

[3] Raina, A. A., Bilaye, P., Gawande, V. N. and Desai, U. B., "Low Cost Wireless Internet Access for Rural Areas using Tethered Aerostats", Proceedings of 2008 IEEE Region 10 Colloquium & Third International Conference on Industrial and Information Systems, IIT Kharagpur, 8-10 December 2008.

[4] Sharma, N., Sehgal, R., Sehgal, R. and Pant, R. S.," Design Fabrication and Deployment of a Tethered Aerostat System for Aerial Surveillance", National Level Conference on Advances in Aerial/Road Vehicle and its Application, MIT, Manipal, 18 - 19 July, 2014

[5] Raina, A. A., Bilaye, P., Gawande, V. N., Desai, U. B. and Pant, R. S.," Design and Fabrication of an Aerostat for Wireless Communication in Remote Areas", AIAA-2007-7832, Proceedings of AIAA 7th AIAA Aviation, Technology, Integration, and Operations (ATIO) Conference and 17th Lighter-Than-Air Systems Technology Conference, Belfast, Northern Ireland, UK, September 2007.

[6] Sharma, V., Dusane, C. R., Verma, R., Pant, R. S.," Design, Fabrication and Testing of an Aerostat System for Last Mile Communication", AIAA Aviation 2019 Forum, Reston, America, 15 June, 2019, https://doi.org/10.2514/6.2019-2979

[7] Mahto, N., Pant, R. S.," Feasibility study of a hot-air tethered aerostat system", 11th International Airship Convention and Regatta, Bedford, England, October, 2017, DOI: 10.31224/osf.io/zwmqx.

7. BIOGRAPHIES

1. 1st Student author

Name:- M.Suhel M.Umarbahi Karkun

College:-Aditya Silver Oak Institute of Technology, Ahmedabad, Gujarat, 382481

Year:- 3rd year, 5th semesters student

Coarse:- B.E. (Aeronautical Engineering)

University:- Gujarat Technical University

University Enrollment Number:- 171200101017

Mobile No.:- 7405770602

Email Id:- suhelkarkun786@gmail.com

Gender:- Male

2. 2nd Student author

Name:- Aashna Seth

College:- Manipal Institute of Technology, Manipal, Karnataka – 576104

Year:- 2nd year, 3rd semesters

Course:- B.E. (Aeronautical Engineering)

University-: MAHE

Enrollment Number:- 180933015

Mobile Number:- 9892813421

Email ID:aashnaseth1256@hotmail.com

Gender:- Female

3. 3rd Author

Name:- Raman Verma

Project Engineer, LTA Systems Labouratory, Aerospace Department, Indian Institute of Technology Bombay

4. 4th Author

Name:- Rajkumar S. Pant

Professor, LTA Systems Labouratory, Aerospace Department, Indian Institute of Technology Bombay

Design and Fabrication of Pluto-X Controlled Indoor Non-Rigid Airship

Saumya Sarawagi[1], Krishnakant Zope[2], Shreyas Sivan[3], Avneet Singh[4] & Rajkumar S. Pant[5]

***Abstract*-- An airship is a Lighter-than-Air system that has its application in various fields such as aerial photography, surveillance, advertisement, and coverage of sport events. This paper provides details regarding the design and fabrication of an indoor, non-rigid airship controlled with Pluto-X to make it maneuverable in all directions. The main intent of the project was to design and fabricate a small airship with 1m^3 volume, which can be flown within a confined location. For the envelope shape, three candidates (viz., modified GNVR, NPL, and Gertler 4621) were studied, and finally, the Gertler 4621 shape was chosen taking into consideration, the advantages it had over other shapes. The airship envelope was fabricated using a Metallized Polymer based fabric using Radio Frequency (RF) sealing. The fabricated envelope was extensively tested for leakages using a sophisticated Helium leak detector. The paper also describes a step-wise procedure for fabricating the airship, and assembling the various components, using which the payload capacity, net lift, and envelope gore design can be easily carried out. Flight tests revealed that the airship could be used for carrying out demonstration flights, and the Pluto-X controller was found to be an excellent means to provide sufficient control authority for its operation.**

***Index Terms*—Lighter-Than-Air systems, Airships, Blimps**

1. INTRODUCTION

Today's ever progressing world, where demand for fuel is increasing with the hour, calls for a dire need to cut down on the consumption of this perishable resource. While aircrafts are the commonly seen mode of air transport, they require power to generate lift. Airships have been in use form decades, for advertising and surveillance. Being a Lighter-Than-Air system, they generate Lift force through the principle of Buoyancy. They can be categorized as rigid and non-rigid airships. Non- rigid airships can be tethered and are called aerostats. This paper, dealing with the fabrication of the other non-rigid and dirigible kind of airships, demonstrates the simplicity and efficacy of employing this technology as substitutes of the more demanding technologies.

1. [1] Summer intern, Department of Mechanical Engineering, NIT, Durgapur, India. (e-mail: saumyasarawagi.dr81@gmail.com).
2. Summer intern, Department of Aeronautical and Automobile Engineering, MIT, Manipal, India. (e-mail: zopekrishna123@gmail.com).
3. Summer intern, Department of Aerospace Engineering, PEC, Chandigarh, India. (e-mail: shreyassiva271999@gmail.com).
4. Summer intern, Department of Aerospace Engineering, PEC, Chandigarh, India. (e-mail: avneets13@gmail.com).
5. Professor, Lighter-Than-Air Systems Laboratory, Department of Aerospace Engineering, IIT Bombay

2. DESIGN AND FABRICATION OF AIRSHIP

2.1. Stepwise flow of the designing process

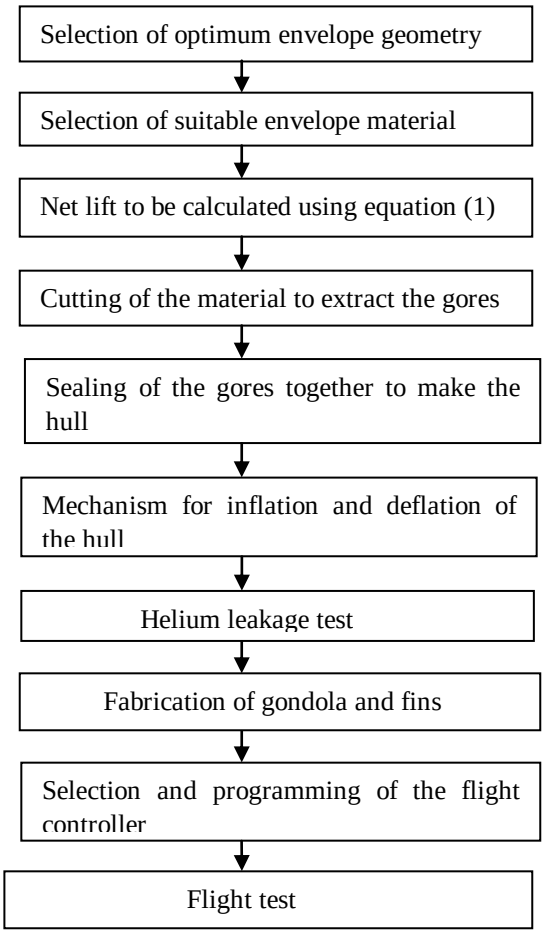

2.2 Envelope Fabric selection

Selection of an appropriate material for fabrication of the blimp is very important to ensure sufficient strength, durability and simultaneously maintaining low weight. The material was selected keeping in mind its permeability towards Helium gas. Two materials, namely, Low-Density Polyethylene (LDPE) and Metalized Polyethylene Terephthalate (MPET) were chosen due to low density and cost. LDPE has a transparent skin whereas MPET has a shiny silver colored skin. They were both tested for permeability towards Helium. It was found that LDPE (55 g/m^2) had higher permeability towards Helium than that of MPET (45 g/m^2). The metalized polymer based fabric was then selected for fabrication.

2.3 Envelope Shape

The geometry of the airship envelope is a crucial parameter that determines the relation between the gross lift produced by the airship and its slenderness. An airship traverses in air and analogous to a submarine in the ocean, it is subjected to drag forces as well. Increased interest of the David Taylor Model Basin in the behavior of streamlined bodies led to the development of families of bodies of revolution [1]. The main advantage of these mathematical equations over empirical methods were the precision and accuracy of the geometry obtained. Using these equations they developed Series 58, a series of 24 models, tested to establish criteria for minimum resistance [2]. A 6 degree polynomial is used and the values of these depend on the prismatic coefficient. Gertler Series 58 have since, been used for aircraft fuselages, submarines and airships as they provided well-streamlined bodies with minimum EHP.

Gertler 4621 shape generator was used to determine the geometry and size of the airship based on the design requirements of the indoor airship. The values of the prismatic coefficient, block volume and Fineness ratio fed in the generator determined the hull shape. The drag calculated could be neglected owing to the small velocity of the airship.

Table I lists the input parameters given to generate the envelope geometry and the gore pattern as shown in figure 1 and figure 2 respectively were generated. 50 uniformly spaced points were used to obtain the geometry of the curve that generates the hull on revolution.

Table I
Input Parameters for the Envelope Geometry

Input parameters	Input values
n_G (Number of Gores)	6
L/D (Fineness Ratio)	2.8
V_b (Block Volume)	2

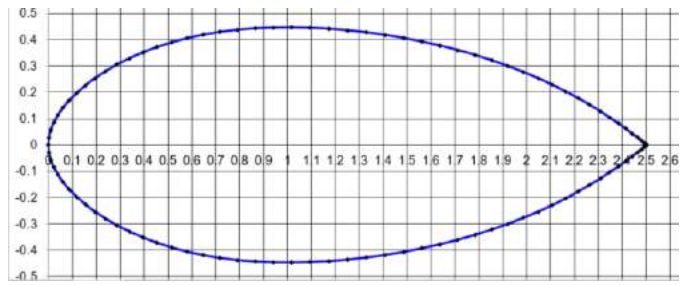

Fig. 1: Envelope Geometry

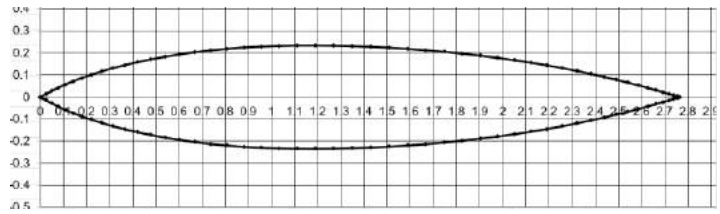

Fig. 2: Gore pattern

The optimum prismatic coefficient of 0.6 is maintained. The block coefficient hence becomes 0.4712. Table II lists the dimensions obtained

.

Table II
Dimensions of Airship

Envelope Volume (V)	0.7069 m^3
Length (L)	2.274 m
Diameter (D)	0.812 m
Surface area (A)	5.0685 m^2

These dimensions satisfy the volume restriction of less than 1m^3 and can fit through doors, at the same time, giving sufficient payload capacity.

2.1 Net Lift calculation

The volume occupied by the airship determines the amount of air displaced. The gross lift produced is the resulting buoyant force acting in the upward direction. This lift supports the weight of the airship and the payload. The net usable lift is obtained from equation:

$$L_d = ((\rho_{air} - \rho_{He}) * V * 1000) - W_{envelope} \quad (1)$$

where, L_d is the net lift. ρ_{air} and ρ_{He} are the air and helium densities respectively. V is the volume enclosed in the envelope and $W_{envelope}$ is the weight of the envelope which is calculated using equation (2).

$$W_{envelope} = \rho_{material} * A \quad (2)$$

$\rho_{material}$ is the material density and A is the surface area of the envelope. Weight of the envelope was found to be 228.08 grams. Substituting the values from Table III in equation (1), the net lift was calculated as 515 grams.

Table III
Performance Characteristics

Air density (ρ_{air})	1.223 kg/m^3
Helium density (ρ_{He})	0.169 kg/m^3
Envelope Volume (V)	0.7069 m^3

2.2 Envelope Fabrication

This section describes the fabrication method used for the envelope. The envelope is usually constructed by joining the gores together. 6 gores were used to form the envelope and figure 2 shows its geometry. The gores were then seamed together edge-to-edge using Radio Frequency (RF) sealing, leaving a small opening for the inflation system. This was followed by a helium leakage test, the results of which were within acceptable limits.

2.3 Gondola and Fin

Gondola is a payload base used in airships. In the current model, the gondola was designed so as to the house the Pluto-X flight controller, the forward/backward motor, and the battery needed to power the controller. Styrofoam and balsawood being lightweight were used to fabricate the gondola. It was installed slightly ahead of the C.G., on the airship's underside using two-sided tape. Gondola is as shown in figure 3 with the Pluto-X flight Controller and the motor mounted

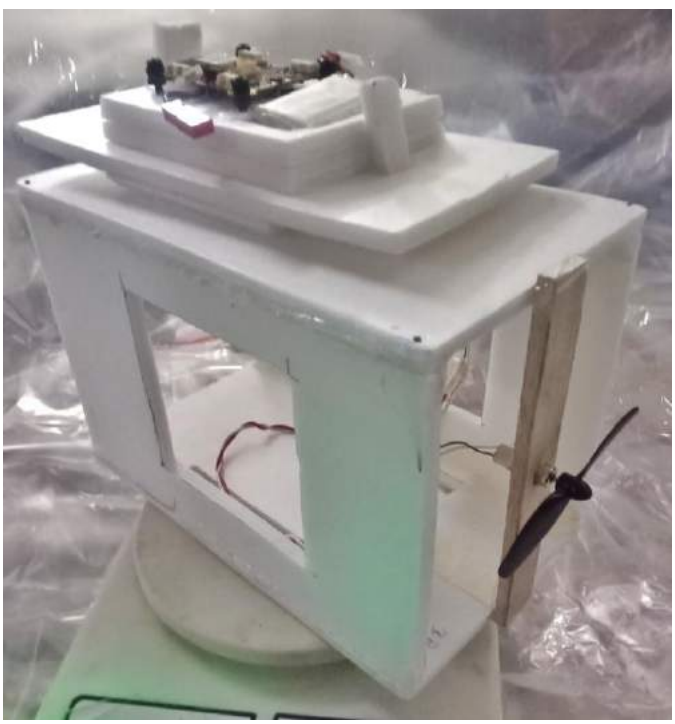

Fig. 3: Gondola side view with the Pluto-X flight controller

Fins are used for directional stability. In the current work, the fins were fabricated using styrofoam and were placed in a Y shape when viewed from aft or front face of the airship. Figure 4 shows the orientation of the fins. The vertical fin housed the second forward/backward thrust and yaw motors.

Fig. 4: Fin orientation in Y-shape

3. Propulsion and Control System

Pluto-X flight controller was used to control the airship. It is a commercially available product of Drona Aviation used to control nano drones. A drone uses 4 motors, each placed in the horizontal plane such that diagonal motors rotate in the same direction to produce lift. This balances the turning moments acting about C.G.. Maneuverability in all directions is obtained by reducing or increasing the speed of two motors depending on the direction of motion. The propulsion system consisted of four Coreless DC motors placed in different planes as shown in figure 5. Two motors were mounted in the vertical plane to provide thrust in forward and backward direction. The yaw motor was placed at the centre of the vertical fin. During yawing, this motor generated turning moment about the C.G.. Fourth motor was placed in the horizontal plane and produced downward force. These motors were positioned, balancing the moments and ensuring that the centre of gravity lied below the centre of the hull as shown in figure 5. The Pluto X was programmed using the Cygnus IDE. The freely available app Pluto that connects to the drone via Wi-Fi was downloaded and used as a controller.

4. Flight Test

After the final assembly and leak test, the airship was inflated. Additional ballast weight was required to attain stability. The flight demonstration was satisfactory and yielded smooth control during turning. The moments due to the thrust motors were balanced and provided sufficiently fast maneuver. The thrust during backward flight was found to be more than that obtained during forward flight owing to the difference in efficiency on the motors when rotated in the reverse direction. Figure 5 shows the completely assembled airship

Fig. 5: Final Assembled airship

5. Conclusion

The design process employed for the indoor airship considers the various options that can be used based on the application requirements. The blimp was successfully designed and fabricated and all the final tests revealed that the airship was suitable for demonstration purpose. Pluto-X flight controller proved to be an excellent means to provide sufficient control authority for its operation. The low cost of fabrication, safety of operation, low power consumption, feasibility in manufacturing and reliability of these airships for various applications is evident in this paper. With the constant progress, the difficulties faced during deployment and payload recovery for stratospheric airships will be minimized enabling their increased use for wireless connections and surveillance.

Acknowledgment

The authors would like to express their gratitude towards Raman Verma who constantly provided guidance and support.
The facilities and financial support provided by LTA systems Lab, IIT Bombay is highly appreciated.

References

[1] L. Landweber and M. Gertler, “Mathematical Formulation of Bodies of Revolution.,” vol. 3, no. September, p. 1981, 1981.

[2] M. Gertler, “Resistance Experiments on a Systematic Series of Streamlined Bodies of Revolution-For Application to the design of High-Speed Submarines,” 1976.

[3] G. Bansal, U. Bhardwaj, N. Jain, S. S. Mulay, S. Sawardekar, and R. S. Pant, “Design fabrication and flight testing of a non-rigid indoor airship,” AIAA Light. Syst. Technol. Conf. 2013, no. March, pp. 1–7, 2013.

[4] M. Biju and R. S. Pant, “Design and development of an indoor autonomous airship,” 23rd AIAA Light. Syst. Technol. Conf. 2017, no. June, pp. 1–14, 2017.

[5] A. C. Gawale, A. A. Raina, R. S. Pant, and Y. P. Jahagirdar, “Design, fabrication and operation of remotely controlled airships in India,” 8th AIAA Aviat. Technol. Integr. Oper. Conf., pp. 1–12, 2008.

[6] M. I. Alam, “MULTIDISCIPLINARY DESIGN OPTIMIZATION OF STRATOSPHERIC AIRSHIP,” 30th Congr. Int. Counc. Aeronaut. Sci. (ICAS 2016), Int. Counc. Aeronaut. Sci. Sep 2016, Daejeon, South Korea, 2017.

[7] N. I. Motiwala, I. A. Khan, N. P. Yelve, B. E. Narkhede, and R. S. Pant, “Conceptual approach for design, fabrication and testing of indoor remotely controlled airship,” Adv. Mater. Res., vol. 690 693, no. December 2014, pp. 3390–3395, 2013.

[8] T. Lutz and S. Wagner, “Drag Reduction and Shape Optimization of Airship Bodies,” AIAA J., pp. 1–11, 1997.

[9] R. S. Pant, “Design, fabrication and flight demonstration of a remotely controlled airship for snow scientists,” J. Aerosp. Technol. Manag., vol. 6, no. 1, pp. 19–27, 2014.

Design of Winching System for Tethered Aerostat

Saurabh Verma[1, a] • Avesh Cheulkar[1, b] • Rajkumar Sureshchandra Pant[2,c]

[a] Department of Mechanical Engineering, Punjab Engineering College, Chandigarh.
[b] Department of Mechanical Engineering, Bharti vidyapeeth College of Engineering , Navi- Mumbai.
[c] Aerospace Department, IIT-BOMBAY

Abstract- Aerostats have a place with the group of Lighter-Than-Air systems that conquer gravity by generating vertical lift by the utilization of a buoyant gas, for example Hydrogen, helium filled in adequately sized envelope which is fastened to the ground using tether. Winching system ensures that inflated envelope can be lowered or raised at a safe speed. This paper presents the design and structural details of such winch for a tethered aerostat. In previous studies, winch consisting of double drum each for tether and power cable was designed and fabricated. Further a modified winch was also designed and fabricated which used self reciprocating screw to ensure uniform winding of tether on winch. The present study started with a critical analysis of previously designed winches. This study aims to come up with a design of winching system which is able to address most of the shortcomings of previously designed winches. To ensure uniform winding of tether on drum, rolling ring linear reciprocating device is used. Drum has been grooved to further facilitate uniform winding. Thrust bearing is used to make it 360 degree rotating to align in any direction. Self locking is done using a suitable ratchet and pawl which can lock the system when the aerostat has reached the desired height. Hence an improved design of winch with careful design calculations is the basic outcome of the present work.

Index Terms- Winching - Aerostat - Ground handling - Uniform winding - 360° rotating – Lighter Than Air- LTA

List of Symbols

σ_c	Yield strength of material(N/mm)
s	Pitch of the grooves on the drum (mm)
c	Depth of grooves(mm)
w	Thickness of drum
L	Length of drum
F_t	Maximum tether tension
D_2	Outer diameter of drum
D_1	Inner diameter of drum
δ	Lead angle
β	Helix angle
q	Diameter factor
Z_{v1}	Virtual no. of teeth
A	Center to center distance
P_{cn}	Normal circular pitch
P_{dn}	Normal diametral pitch
M_n	Normal module
d	diameter of driving pulley
D	diameter of driven pulley
v_{mg}	Pitch line velocity of wheel
F_t	Transmitted load
K_w	Load wear factor
H_d	Heat dissipation capacity
H_g	Heat generated
P_e	Equivalent dynamic load
C	Dynamic capacity required
σ_b	Stress due to bending
T	Torque
η	Efficiency of gear drive
M_b	Max bending moment
M_t	Max torsional moment
Z	Number of starts
M_x	Axial module
Y	Lewis form factor
Z	Number of teeth on wheel

Introduction

Aerostats are most preferred aerial platforms for applications in which long endurance is the key requirement but weather conditions are not very harsh like military surveillance, meteorology, advertisements and providing last mile communication etc. During its deployment a number of forces viz. Buoyancy, aerodynamic forces, and gravity follow up on the envelope. This makes ground handling a challenging and cumbersome task. Winching system is considered as the backbone of the ground handling system. It ensures that inflated envelope can be

lowered or raised at a safe speed. It also has a suitable provision for locking the tether when the envelope reaches the desired height. According to Myers [**1**] winch can be relatively inexpensive manual winches used for small low altitude balloons or maybe power driven winches used for considerably bigger envelope size depending upon the specific applications. Tethered aerostat winches are rarely "off the shell" items and are rather custom tailored for specific requirements.

Critical Review of Existing Winches

The present study started with critical analysis of previously designed and fabricated winches, so as to identify the areas in which they can be improved further. Winch designed by Bhandari et al. **[2]** was cost effective as focus was primarily on using locally available material and fabrication techniques. It consisted of double drums both for tether and other one for data cable. A braking system was also designed by inversion of four bar link mechanism to regulate the ascending rate of aerostat with a line pull of over 70 kg. However, the braking system was not so efficient. Winch didn't have any provision for uniform winding. Moreover the winch was very heavy and bulky thereby making its transportation problematic.

Winch designed by Shah et al. **[3]** consisted of various sub-systems such as side frames, base frames with castor wheels, space rods and tether drum. A self-reversing screw was used in which one direction of rotation was required to achieve reciprocated bi-directional lateral movement. This movement is achieved using a follower blade in the nut that is matched to the particular groove width and screw turn round on the screw. However, it does not lead to perfect spooling and required perfect design of reversing screw, as any deviation in parameters lead to unwanted spooling. The winch is mounted on a four legged stand which gives it the required amount of stability. This winch too was bulky and not very comfortable to transport.

Winch described by Sharma et al **[4]** is a single drum winch, which can be grounded using long pegs. It was a very laborious and a time consuming activity to insert and take out the pegs which was experienced during the field trial of the aerostat. Buan Teck [**5**] has done detailed work on material selection for winch components so as to reduce the overall cost of winch. The stress analysis of winch drum is also carried out by the him.

Tiwari **[6]** describes about double acting winch type bucket elevator. The part of this elevator is more or less functional as the aerostat winch. So brief idea of the winch mechanism can be understood using this paper and most of calculation resemble like aerostat winch calculation. The work by Lambert [**7**] is about winch which consists of three major part Motor, Gear box and Drum. In this system the multi tether aerostat is used. Basically three winches are used to control the position of aerostat. The winch control system involves the integration of all the system's components, as feedback control based on GPS position measurements are used to adjust tether length in response to wind disturbances.US patent [**8**] was done to have uniform winding of drum of heavy load winch. In this the rope is at same position but drum can change the position to have uniform winding on the drum of winch.

Design Requirements for Winching System

Design requirements for the present winching system were came upon after requirements capture exercise with the experts. Experience gained during deployment of previous tethered aerostats helped in finalizing the requirements for winching system.

All subsystems of aerostat viz. Winching, mooring, inflation cylinders were to be integrated on a trailer which can be easily transported using a suitable vehicle. Winch must be bolted on the trailer itself, so as to be grounded even if the winch is made light weight that there is no chance of winch being lifted up by the upward pull of tether tension It was desired to have automatic uniform tether winding on drum to avoid wear and tear of tether. Also, winch should provide yaw freedom of 360 degrees. Additionally after reaching desired height, tether must be locked suitably so as to stop any vertical movement.

Design of Improved Winch

Taking note of the above stated requirements the winching system was designed to meet the requirements. The improved winch contains rolling ring drive linear reciprocator for smooth uniform winding of tether. Drum has been grooved to further facilitate uniform winding. Moreover it can be locked at any desired height using ratchet and pawl assembly. Housing assembly rests on a thrust bearing which makes it capable of rotating 360 degrees. The design is simplified which focus more on assembly and lightness of system. Winch can be easily bolted on a trailer to be carried away easily with the help of suitable vehicle.

Conceptual Design

Looking at the working and keeping in mind design for assembly (DFA) and design for manufacturing (DFM) conceptual design was made.

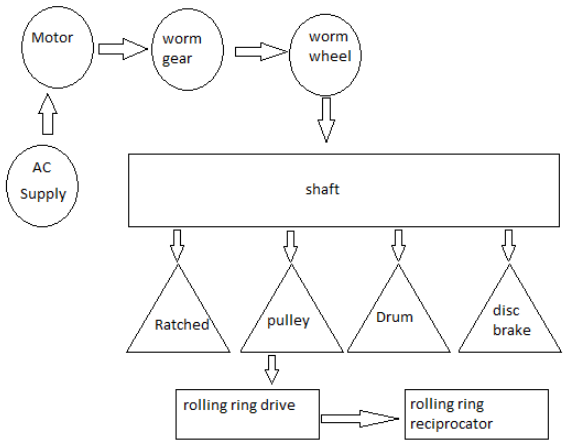

Figure 1: Block diagram of Winch

Motor

Present winch is powered using a DC motor so that system can be deployed even in extreme remote areas without being dependent on AC supply. Motor of adequate power is selected to control the ascent and descent of the aerostat at a desired rate.

Figure 2: CAD model of Motor

Maximum tether tension=1000N

Considering extra margin of 50 %, so that the safety of tether is ensured even in adverse or extreme situations like bad weather and windy atmosphere.

$$(\text{Max tether tension})_{\text{design}} = 1000\times1.5 = 1500\text{N}$$

Assuming dia of drum =12 cm =120mm

Required torque=1500×0.060

=90 Nm

$$\begin{pmatrix}\text{Length unrolled}\\ \text{in one revolution}\\ \text{of drum}\end{pmatrix} = \text{one circumference}$$

$$= \pi\times \text{ dia of drum}$$

$$=\pi\times0.12$$

$$=0.377 \text{ m}$$

For deployment altitude of 150m

$$\text{Total revolutions} = \frac{150}{0.377} = 398 \text{ revolutions}$$

We require aerostat to be able to reach the desired max height in 7.5 minutes (450 seconds), hence we require, 398 revolutions in 450 seconds, which is 0.8844 revolutions per second.

$$\text{Angular velocity}(\omega) = 2\times\pi\times\text{rps}$$

$$=2\times\pi\times0.8844$$

$$=5.55 \text{ rad/sec}$$

$$\text{Power requirements} = T\times\omega$$

$$=90\times5.557$$

$$=0.5 \text{ KW}$$

Considering losses in gears and system,hence an average efficiency of 0.7,

$$\therefore \text{ power} = \frac{0.5}{0.7} = 0.7 \text{ KW}$$

$\therefore$ select available DC motor of 0.75 KW (2800 RPM)

Gear Assembly

Worm and worm wheel connects motor to the main shaft on which drum is mounted. Worm and worm gear has a large gear reduction capacity and hence it is used to step down the revolutions of motor and rotate drum at the desired revolutions per minute. Worm and worm wheel are preferred as space is limited to make system compact. Additionally they perform smoothly and generate very less noise which results in added advantage.

Figure 3: Worm and Worm wheel

Table 1: Gear Specification

Sr. No.	Dimension	Worm (mm)	Worm Wheel(mm)
1.	Reference dia (PCD)	38.5	185.5
2.	Tip dia	45.5	192.5
3.	Bottom dia (clearance)	0.875	0.875
4.	Root dia	29.75	176.75
5.	Face width and Face length	L≥ 60.445	b=0.75 d_1=0.75(38.5) =28.875

Shaft Assembly

This assembly consists of main shaft on which drum, ratchet, and disc are mounted. It rotates at desired rpm after worm and worm wheel step downs motor shaft's rpm to a certain desired value. Carefully designed bearings are fitted across the shaft which support the radial loads and make the shaft to rotate in confined space.

Material selected=Mild steel

σ_{yield}=250MPa

Weight of various components

1) Worm wheel = 3.5 Kg

2) Ratchet = 0.85 Kg

3) Disc = 0.340 Kg

4) Pulley = 0.60 Kg

5) Drum = Vol × density of C 40

$$= \frac{\pi}{4}\left(D_2^2 - D_1^2\right)\times l\times\rho$$

$$= \frac{\pi}{4}\left((0.1428)^2 - (0.12)^2\right)\times 0.25\times 7850$$

=9.235 Kg

Power=0.75×η=0.75×0.71=0.5325KW

K_b=2

K_t=1.5

$$\text{Power} = \frac{2\times\pi\times N\times T}{60}$$

$$0.5325\times 10^3 = \frac{2\times\pi\times N\times 90}{60}$$

Hence,N=56.5 Rpm

Figure 4: Cad model of shaft

$$\text{Torsional moment } (M_t) = \frac{60\times 10^6\times KW}{2\pi N}$$

$$\text{Torsional Moment } (M_t) = \frac{60\times 10^6\times 0.5325}{2\times\pi\times 56.5}$$

=90,000 N-mm

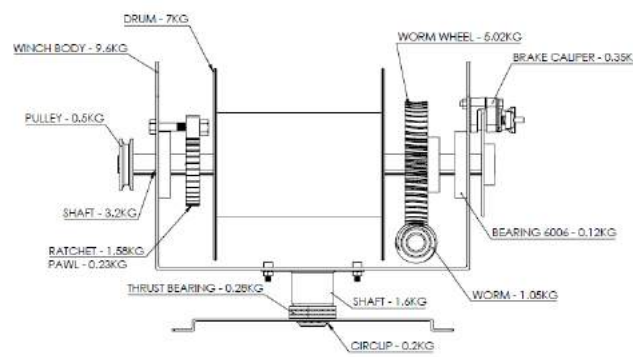

Figure 5: load on shaft

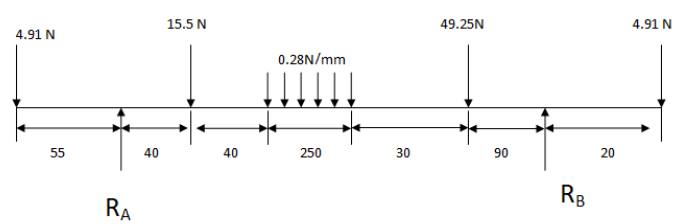

Figure 6: Free body diagram (length dimensions in mm)

$\Sigma F_y = 0$

$R_A + R_B$ =4.91+15.5+(0.25×250)

+49.25+4.91

=144.57N

ΣM about A =0

$$R_B\times 450 = (15.5\times 40) + [0.28\times 250\times (80 + \frac{250}{2})]$$

$$+(49.25\times 360) + (4.91\times 470) - (4.91\times 55)$$

$R_B = 77.2N$

$R_A = 67.37N$

Max bending moment $= -4.91(55+40+40+167.71)$

$+67.37(40+40+167.61)$

$-15.5(40+167.61)$

$-0.28\left(\frac{167.71}{2}\right)^2$

Max bending moment=8044.68 Nmm

Max Tether tension=1500 N

By ASME code

$0.3\sigma_{yield} = 0.3(280) = 84$ MPa

$\tau_{max} = 0.75\times 84 = 63$MPa

$$d^3 = \frac{16}{\pi\times\tau_{design}}\sqrt{(K_b M_b)^2 + (K_t M_t)^2}$$

$$(32)^3 = \frac{16}{\pi\times\tau_{design}}\sqrt{(2\times 8044.68)^2 + (1.5\times 90000)^2}$$

Taking shaft dia = 3.2 mm.

$\tau_{design} = 21.13$MPa

$$\text{Now, } \tau_{max} = \frac{0.5\times\sigma_{yield}}{FOS}$$

$$\text{Therefore, FOS} = \frac{0.5\times 250}{21.13} = 5.9$$

Hence shaft is safe

Selected Bearing = SKF 6006

Figure 7: CAD Model of Selected Bearing

Drum design:

A drum mounted on main shaft. It is designed so as to have a capacity of spooling around 450 meters of tether. It is mounted on the shaft using a key. To facilitate uniform winding of tether, grooves are provided on the drum.

After considering number of factors and inputs from various experts C40 alloy steel was selected for drum.

$\sigma_c = 330$ N/mm^2

$$\text{Max bending moment} = F_{max}\times\left(\frac{L}{2}\right)$$

$$(BM)_{max} = 1500\times\frac{0.25}{2} = 0.1875 \text{ KN-m}$$

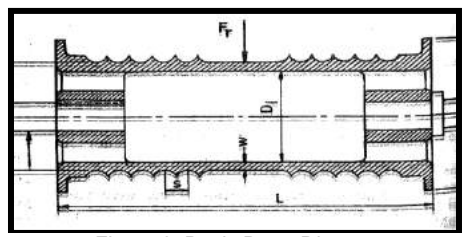

Figure 8: Basic Drum Diagram

$$\sigma_b = \frac{F_{max} L D_2}{(D_2^4 - D_1^4)\frac{\pi}{8}} = \frac{1500\times 250\times(120+2.48)}{\left[(120+2.48)^4 - (120)^4\right]\times\frac{\pi}{8}}$$

$$= 0.6615 \text{N/mm}^2$$

Total compressive stress $= \sigma_c + \sigma_b = 92.16$N/mm^2

Drum is also subjected to torsion ,

$$\text{Max torque} = 2\times F_{max}\times\frac{D_2}{2} = 2\times 1500\times\left(\frac{120+2.48}{2}\right)$$

$$= 0.18372\text{KNm}$$

$$\tau = \frac{T}{J} = \frac{0.183\times 10^6}{\frac{\pi}{16}\left[\frac{(120+2.48)^4 - (120)^4}{(120+2.48)}\right]} = 6.456 \text{ N/mm}^2$$

Principle stresses,

$$\sigma_1 = \frac{\sigma_{c\ total}}{2} + \sqrt{\left[\frac{\sigma_{c\ total}}{2}\right]^2 + \tau^2}$$

$$\sigma_1 = \frac{92.16}{2} + \sqrt{\left[\frac{92.16}{2}\right]^2 + (6.456)^2}$$

$$\sigma_1 = 46.08 + 46.53 = 92.61 \text{ N/mm}^2$$

$$\text{Permissible load} = \frac{\sigma_c}{FOS} = \frac{330}{3} = 110 \text{N/mm}^2$$

Since (σ_1) < (permissible load) Therefore, design is safe.

Figure 9 CAD Model of drum

Flange outer dia (x)

$$= \begin{pmatrix}\text{Dia of}\\ \text{drum}\end{pmatrix} + \begin{pmatrix}\text{No. of}\\ \text{windings}\end{pmatrix} \times \begin{pmatrix}\text{Dia of}\\ \text{rope}\end{pmatrix} + (\text{Clearance})$$

=120+15(4)+2(50)

=280 mm

Taking flange thickness=1 mm

Checking for shear failure,

Material = C 40 (σ_{yield} =330N/mm^2)

$$\left[\sigma_{yield}\right]_{permissible} = \frac{\sigma_{yield}}{FOS} = \frac{330}{10} = 33 \text{N/mm}^2$$

$$\text{Force} = \frac{1500}{2} = 750\text{N}$$

$$\sigma = \frac{750}{(x-d)\times 1} = \frac{750}{(280-40)\times 1} = 3.125 \text{N/mm}^2$$

$$\text{hence , } \sigma < \left[\sigma_{yield}\right]_{permissible}$$

Disc Brake

Disc brake is mounted on the shaft to control the ascent and descent rate of tether and to apply brake whenever required. Compact disc brake with adequate braking torque is selected.

Figure 10: CAD Model of Disc

Figure 11: CAD Model of lever and caliper of disc brake

Power = torque×ω

0.75×10^3 =torque×2×π×0.8844

torque=134.9 =135Nm

Selected Brake Now for the available torque , ME series of tolomatic brakes was found well enough and well suited. Moreover they have a compact structure which is an added advantage to being lightweight

Selected Brake

Disc Brake no. : ME10LA
Disc thickness: 5/32"
Lever type: lever
Assembly Number: 0732-003

Ratchet and Pawl

To lock the tether when the aerostat reaches the desired height, ratchet and pawl are used. They provide excellent locking for a system.

For selection of ratchet,

torque= F×r

=1500×0.060

=90 Nm

Assuming factor of safety of 1.5,

Design torque = 90×1.5

=135 Nm

Available ratchet KSRT3-40

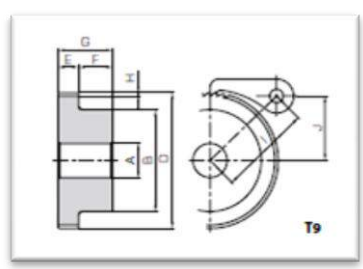

Figure 12: Dimension of Ratchet

Table 2: Dimension of Ratchet

Sr. No.	Dimension	Magnitude(mm)
1.	Pitch	9.42
2.	Number of teeth	40
3.	Shape	T4
4.	Bore (A)	20
5.	Hub dia (B)	-
6.	Outside dia (D)	160
7.	Face width (E)	25
8.	Hub Width (F)	-
9.	Total Length (G)	25
10.	Depth of teeth (H)	7.4
11.	Center of distance (I)	108.03
12.	Mounting distance	72.6

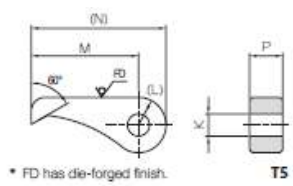

Fig. 13. Pawl dimension

Table 3: Dimensions of pawl

Sr. No.	Dimension	Magnitude(mm)
1.	K	12
2.	L	15
3.	M	65
4.	N	80
5.	P	20

Belt and Pulley

Main shaft and the shaft on which rolling ring drive linear reciprocator is mounted both are connected via belt and pulley assembly so as to provide drive to linear reciprocator. Both of them rotate at the same revolutions per minute and pitch of the linear reciprocator is set so as to provide uniform spooling.

Power=0.75 KW
i=1
N=56.5 Rpm
L_{years} =1year
F_a =Load correction factor=1.3
d=diameter of driving pulley
D=diameter of driven pulley
A= cross sectional area of belt
E= modulus of elasticity of belt material
n_b =number of belts
v= linear velocity of belt
T=Thickness of belt
w = width of belt

Figure 14: CAD model of pulley

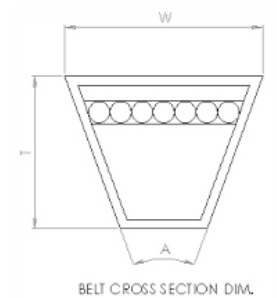

Figure 15 cross section of V belt

Selecting standard belt length from PSG [10]

L_b =950 mm

Exact center distance

$$A=\frac{L_b}{4}-\frac{\pi(D+d)}{8}$$

$$=\frac{950}{4}-\frac{\pi(80+75)}{8}=176.63 \text{ mm}$$

$$B=\frac{(D-d)^2}{8}=\frac{(80-75)^2}{8}=3.125 \text{ mm}$$

$$c=A+\sqrt{A^2-B^2}=353.25 \text{ mm}$$

Length correction factor (F_c) =0.87

Calculation of belt tension

Arc of contact(θ)

$$\theta=2\cos^{-1}\left(\frac{D-d}{2c}\right)=2\cos^{-1}\left(\frac{80-75}{2\times353.25}\right)$$

$\theta=179.18°=3.13$ radians

Number of belts

$L_{hrs}=L_{yrs}\times$number of days$\times$hours in a day

$=1\times365\times16$

$=5840$ days

Length correction factor $(F_c)=0.87$

Life in number of stress cycles

$$L_c=\frac{v}{L}\times L_{hrs}\times3600\times \text{ number of pulleys}$$

$$=\frac{0.22}{0.95}\times5840\times3600\times2$$

$$=9.73\times10^6$$

Maximum stress in belt

$$\left[\frac{\sigma\text{-}1}{\sigma_{max}}\right]^m=\frac{L_c}{10^7}$$

$\sigma\text{-}1=9\ N/mm^2$

m=8(for V belts)

$$\left[\frac{9}{\sigma_{max}}\right]^8=\frac{9.73\times10^6}{10^7}=0.973$$

$\sigma_{max}=9.03N/mm^2$

Now,

σ_{max} =tensile stress + bending stress + centrifugal stress

$$\sigma_{max}=\frac{T_1}{n_b\times A}+\frac{ET}{d}+\frac{mv^2}{A}$$

$$9.03=\frac{3498}{n_b\times80.68}+\frac{100\times8}{75}+\frac{0.106\times(0.22)^2}{80.68}$$

$=-26.71$

Negative sign indicates that we have selected belt of high cross section and therefore, using current section we can have only one belt that is one belt is sufficient. Number of belt = 1

Rolling Ring Linear Reciprocator

Rolling ring drives are friction drives which convert the constant rotary movement of a plain shaft into a traversing movement. They operate like nuts on a screw rod but have a pitch - either right-handed or left-handed - that can be precisely adjusted and can equal zero. This effect is achieved by using pivoted rolling rings that are mounted on roller bearings and have a specially shaped running surface which is pressed against the rotating shaft. A roller lever capable of making contact with cams arranged along the stroke path makes it possible to implement even complicated patters of motion

Figure 16: Rolling ring drive

Design of Vertical Shaft

By considering the space and other requirements for making winch rotate by 360 °, a thrust bearing mounted at the end of shaft is to be selected.
Diameter of shaft=40 mm
Length of shaft=80mm
Material= C40 alloy steel
Configuration= vertical
Checking for tensile failure,

$$\sigma_{yield}=\frac{F}{A}$$

σ_{yield} for C40 alloy steel=250MPa

As this shaft is an important components of the structure and supports the weight of all the components above, therefore considering factor of safety (FOS) of 10.

$$[\sigma]_{permissible}=\frac{\sigma_{yield}}{FOS}=\frac{250}{10}=25MPa$$

Now,
Max vertical load= 1500N

$$\sigma=\frac{1500}{\frac{\pi}{4}\times(40)^2}=1.19Mpa$$

Since it is less than permissible stress, therefore designed shaft is safe for compressive load.

Figure 17: CAD Model for Base Shaft

Checking for buckling failure

$$\text{Eulers critical buckling load}=P_{cr}=\frac{n\pi^2 EA}{\left(\frac{l}{k}\right)^2}$$

Where,

n=4 (since both the ends are fixed)
k=least radius of gyration of the cross section about its axis(mm)
E=young's modulus of elasticity
Slenderness ratio=l/k=80/10=8
Since, slenderness ratio (l/k)< 30
Therefore design is safe from bucking load

Bearing for 360 Degree Rotation

Bearing type = single thrust ball bearing
d=40mm
Radial force $(F)_r$=0
Axial force (F_a)=1500N =150 Kgf
N=60 rpm (assumed)
L =12000 hours hr

Selection of bearing for d=40 mm
Bearing number 51208
d=40mm, D=68mm, H=19mm, d=40.2min, r=1.5, C_o=7650Kgf, C=3450Kgf, N_{max}=5000Rpm

Checking the life of selected bearing

$$\frac{F_a}{C_0}=\frac{150}{7650}=0.0196$$

$$\frac{F_a}{F_r}=¥$$

$$F_a=0.019$$

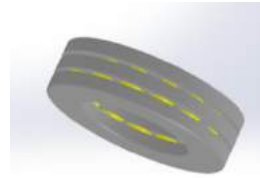

Figure 18: CAD model of Thrust bearing

$$\frac{F_a}{F_r}>e$$

Therefore, X=0.56 and Y=2 (where x,y,v are design coefficients)

$(P_e)=(XVF_r+YF_a)\times(s.f)\times K_t$
$(P_e)=[0+(2\times150)]\times1.2\times1$
(P_e)=360 Kgf
Million revolutions (L_{mr})

$$L_{mr}=\left(\frac{C}{P_e}\right)^k$$

where,
k =3 for ball bearings
P_e=Equivalent dynamic load
C=Dynamic capacity required

$$L_{mr}=\left(\frac{3450}{360}\right)^3=880 \text{ million revolutions}$$

Rated life in hours,

$$L_{hours}=\frac{L_{mr}\times10^6}{N\times60}=\frac{880\times10^6}{60\times60}=244444.4 \text{ hours}$$

This is greater than required 12000 hours. Hence selected bearing is safe and suitable.

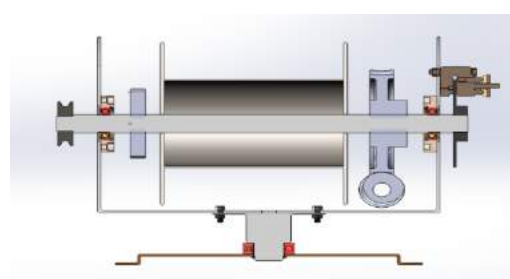

Figure 19 Sectional View

Conclusions and Suggestions for Improvement

This portable winch was 360° rotating which enable us to synchronize the alignment of balloon with tether. Beside this winch was very compact and can be fabricated very fast because we tried keeping minimum number of parts. Winch design is very lighter in weight with respect to previous winch designed hence can be carry anywhere when ever needed..

Size of the winch can be further reduced by using materials having good strength. Research can be done on using certain other materials for such applications which may result in winch having good amount of strength while having less weight. Hence this way winch can be made more compact and strong by using materials having good strength to weight ratio. Moreover, for further better control on aerostat positioning, automated smart control system can be integrated with winch system which can automatically detect any abnormality in the functioning of winch like non-uniform spooling of rope, or abnormally high tether tension and can automatically respond to such situations without any human interference.

Acknowledgments

The authors are highly thankful to the students, researchers and interns of the Lighter-Than-Air Systems Laboratory of Aerospace Engineering Department of IIT Bombay where this work was carried out. The authors are grateful to Mr. Chetan Dusane and Mr. Raman Verma, department of aerospace, for their encouragement and practical advice. Their insightful comments and constructive criticisms at different stages of my research were thought-provoking and they helped me focus my ideas. I am grateful to them for holding me to a high research standard and enforcing strict validations. I am also thankful to them for reading my reports, commenting on my views and helping me understand and enriching my ideas.

Reference

[1] P. F. Myers, "*Tethered Balloon Handbook ", Section V*, Goodyear Aerospace Corp., Akron OH, USA, Report No. GER-14142, 1968

[2] K. Bhandari, N. Wanjari, S. Kadam, and & G Sequeira, "Design, Fabrication and Field testing of Winch for Aerostat," in *Proceedings of National Seminar on Strategic Applications of Lighter-Than-Air (LTA) vehicles at High Altitudes (SALTA-07)*, pp. 12–13, 2007

[3] Harsh Shah, Vipul Rane, Utsav Chavda, Bhavesh Khatare, Bhushan Sonawane *and Rajkumar S. Pant, "*Design and Fabrication of a Winch for an Aerostat Indian Institute of Technology". AIAA -3994, 2017.

[4] V. Sharma, C. R. Dusane, R. Verma, R. S. Pant, and Design, "Fabrication and Testing of an Aerostat System for Last Mile Communication," in *Proceedings of 2019 AIAA Aviation and Aeronautics Forum and Exposition*, pp. 17–21, Paper AIAA 2019-2979, , 2019

[5] Lim Buan Teck, Danny, "improvement in the design of winches" Bachelor of Engineering, Department of Mechanical Engineering, National University of Singapore, 2004/2005

[6] Amit Tiwari, "DESIGN AND FABRICATION OF DOUBLE ACTING WINCH TYPE ELEVATOR", ISSN 2278 – 0149- ijmerr Vol. 4, No. 1. 2015.

[7] C. Lambert, A. Saunders, C. Crawford, and M. Nahon, "*Design of a One- Third Scale Multi-Tethered Aerostat System for Precise Positioning of a Radio Telescope Receiver", Proceedings of CASI Flight Mechanics and Operations Symposium*, Montreal, Canada, 2003.

[8] Albert Brauss "Level Winding Winch Mechanism and Heavy-Duty Drive Therefor" US Patent - US3690409A, Sept. 12, 1972.

[9] V.B. Bhandari, Design of Machine Elements, 8th reprint of 3rd edn, Tata McGraw Hill Education Private Limited, New Delhi, 2012.

[10] Complied by PSG College of Technology, Coimbatore-641004, "Design Data Book for Engineers", Published by: Kalaikathir Achchagam, Coimbatore-641037, 1978.

A Generic Approach for Geometry Generation of Multi-Lobed Airship Envelopes

1. Abhishek Kumar Shanklesha, Student, *NIT Trichy*, 2. Manikandan Murugaiah, Research Scholar, *IIT Bombay,* 3. Rajkumar S. Pant, Professor, *IIT Bombay*

This paper describes a methodology for shape generation of a tri-lobed airship envelope along with the estimation of its curved surface area and volume through B-spline interpolation. The approach behind the selection of shape parameters, formulation of the b-spline curves and formulation of the curved surface area and volume of the airship is discussed. The parameters for the generation of a cylindrical and a prismatic envelope were used for validation of the algorithm. However, the algorithm is restricted to the generation of geometries which are symmetric about two mutually perpendicular planes.

Keywords: **Multi-Lobed Airship, B-spline curves.**

1. Introduction

Multi-lobed airship technologies have emerged significantly from the mid of 20th century that offers unique operational advantages over conventional airships. Multi-lobed hybrid airship is a type of non-rigid and powered airship that combines the feature of lighter-than-air (LTA) system and heavier-than-air (HTA) system. The main advantage of the hybrid/multi-lobed airships are that up to 20 - 40% of the total lift comes from aerodynamics, whereas the conventional airships generate no more than 10% of their total lift from aerodynamics. The unique combination of buoyancy and varying aerodynamic lift makes the hybrid airships superior to conventional airships and other air vehicles.

Tri-lobed airship designs have emerged as an appropriate solution. Currently existing tri-lobed airship design involves three conventional single lobed ellipsoidal bodies with some lateral overlap between them. This paper is focused on a generic approach for geometry generation of multi-lobed airships.

1. Abhishek Kumar Shanklesha, Bachelor student, Department of Mechanical Engineering, National Institute of Technology Tiruchirappalli, Trichy, India.
(e-mail: abhishekshanklesha62@gmail.com).
2. Manikandan Murugaiah, Research Scholar, Department of Aerospace Engineering, IIT Bombay, Mumbai, India.
(e-mail: manikandan.m@aero.iitb.ac.in).
3. Rajkumar S. Pant, Professor, Lighter-Than-Air Systems Laboratory, Department of Aerospace Engineering, IIT Bombay, Mumbai, India.
(email: rpant@iitb.ac.in).

2. Geometry Generation

The generation of three-dimensional tri-lobed airship geometry was started by developing variably scaled cross-sections at various planes (as shown in Fig. 1) along its axis by interpolating a certain number of control points on the planes using B-spline curves. This is followed by interpolation of these cross-sections to generate the overall surface.

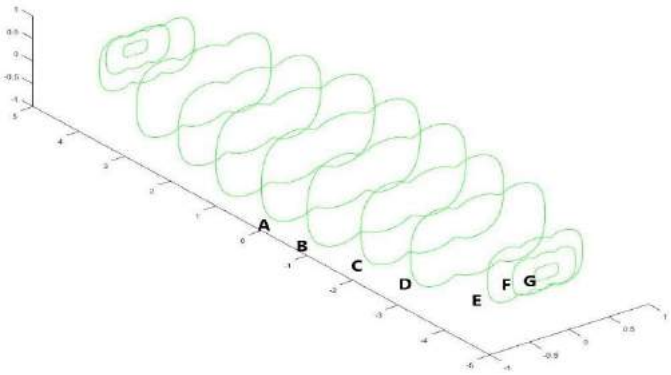

Fig. 1: Variably scaled standard cross-sections along the axis of the airship

2.1 Development of standard cross section

For developing a standard cross-section, which can be variably scaled and placed at different positions along the axis of airship, a geometry involving three overlapping circles was chosen (as shown in Fig. 2) so as to obtain optimum control points which can be interpolated by B-spline curves to give nearly same geometry.

To ensure that a minimum number of points be used to generate the curve as in Fig. 2, symmetry about both horizontal and vertical axis was considered. Next step was to determine the minimum number of control points that could generate the required curve by B-spline interpolation. To ensure slope continuity after adding the symmetrical pieces, points P_0 and P_1 were chosen so as to have same ordinate and points P_5 and P_6 were chosen to have same abscissa. So, a choice of 7 points (P_0, P_1,

P_2, P_3, P_4, P_5, P_6) was made so as to develop the cross-section of tri-lobed envelope. The coordinates chosen for the standard cross-section are shown in Table I.

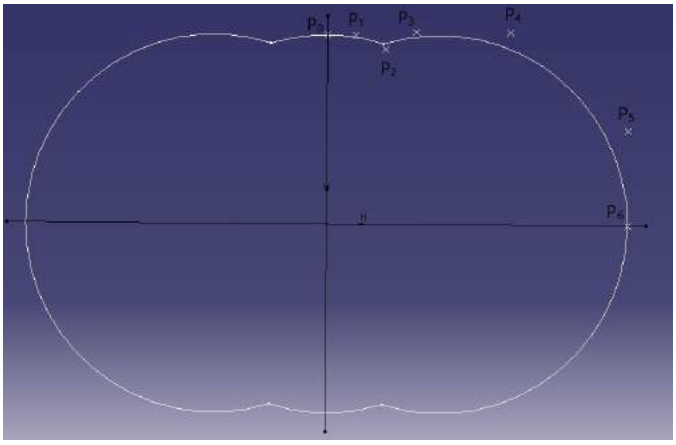

Fig. 2: Three circles with lateral overlap and symmetry about both axes for selection of control points

Points	Coordinates
P_0	(0,1)
P_1	(0.2,1)
P_2	(0.32.0.76)
P_3	(0.42,1)
P_4	(0.8,1)
P_5	(1,0.6)
P_6	(1,0)

Table 1: Control points for generation of standard cross-section

To ensure C-2 continuity, 3-degree B-spline curve was chosen. With the number of control points as 7 (n=6) and degree of curve as 3 i.e. k=4 (k=degree+1), the curve is obtained in 4 (n-k+2) segments [2]. The derived parametric equations of the 4 segments obtained are shown in Fig. 3.

For u=[0,1]

$$P(u)= (1-u)^3 \mathbf{P_0} + (7u^3-18u^2+12u)\, \mathbf{P_1}/4 + (-11u^3+18u^2)\, \mathbf{P_2}/12 + u^3\, \mathbf{P_3}/6$$

For u=[1,2]

$$P(u)= (2-u)^3\, \mathbf{P_1}/4 + (7u^3-36u^2+54u-18)\, \mathbf{P_2}/12 + (-3u^3+12u^2-12u+4)\, \mathbf{P_3}/6 + (u-1)^3\, \mathbf{P_4}/6$$

For u=[2,3]

$$P(u)= (3-u)^3\, \mathbf{P_2}/6 + (3u^3-24u^2+60u-44)\, \mathbf{P_3}/6 + (-7u^3+48u^2-102u+70)\, \mathbf{P_4}/12 + (u-2)^3\, \mathbf{P_5}/4$$

For u=[3,4]

$$P(u)= (4-u)^3\, \mathbf{P_3}/6 + (11u^3-114u^2+384u-416)\, \mathbf{P_4}/12 + (-7u^3+66u^2-204u+208)\, \mathbf{P_5}/4 + (u-3)^3\, \mathbf{P_6}$$

Fig. 3: Derived parametric equations of the four segments

Now to get various points for plotting the curve, values of u in steps of 0.01 (0, 0.01, 0.02, 0.02, 0.03, ….0.98, 0.99, 1, 1.01, 1.02, 1.03, ….2, …3, …4) were substituted in the respective segment equations. The smaller the value of step size more will be the number of coordinates used for obtaining the curve and thus smoothness of curve will be more as the curve is made by joining these points with the help of straight lines.

The curve generated by these four segments is shown in Fig. 4. By adding the symmetrical pieces, the standard cross-section as shown in Fig. 5 is generated.

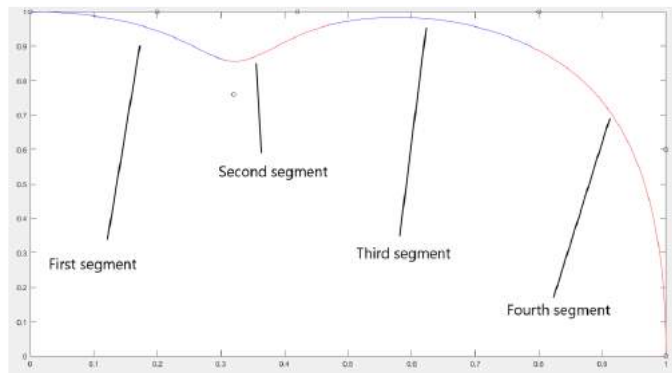

Fig. 4: Curve formed by combination of the four segments

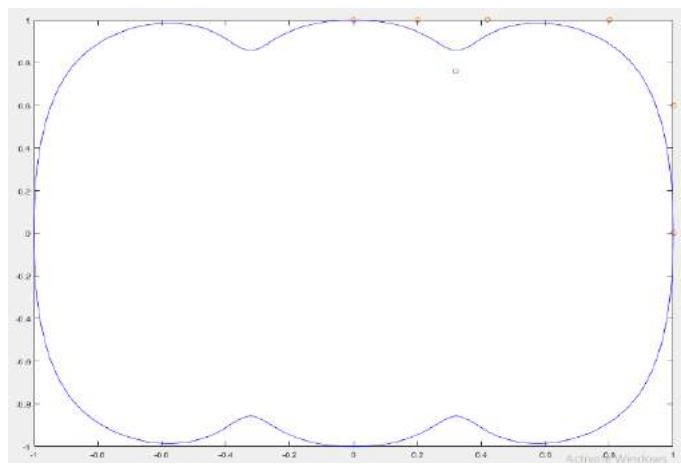

Fig. 5: Standard cross-section of the tri-lobed envelope surface

2.2 Generation of envelope surface

Similar to the generation of standard cross-section where seven control points were interpolated to generate the required geometry, seven such cross-sections (A, B, C, D, E, F, G) as shown in Fig. 1 which are obtained by scaling the standard cross-section to different values are interpolated to obtain one half of the airship surface along the axis. The other half of the airship is obtained by symmetry.

The same parametric equations which were used for interpolation to develop the standard cross-section with seven points were used to develop the surface by interpolation of these seven cross-sections. The coordinates of the points used for creating the seven cross-sections are used for the interpolation to generate the surface. Seven scaling factors are used to scale the x and y coordinates used for developing the standard cross-section shown in Fig. 5 so as to obtain x and y coordinates of the points for generating the seven cross-sections. Seven z coordinates were used for the positioning the seven cross-sections along the semi-axis of the airship.

The seven z-coordinates and seven scaling factors are chosen considering the side view of the airship just as the seven x and y coordinates were chosen for obtaining the standard cross-section. The half surface is obtained in 4 pieces in the same way as the curve for the cross-section was obtained in four segments,. The final generated shape is shown in Fig. 6 with one half indicating the four pieces.

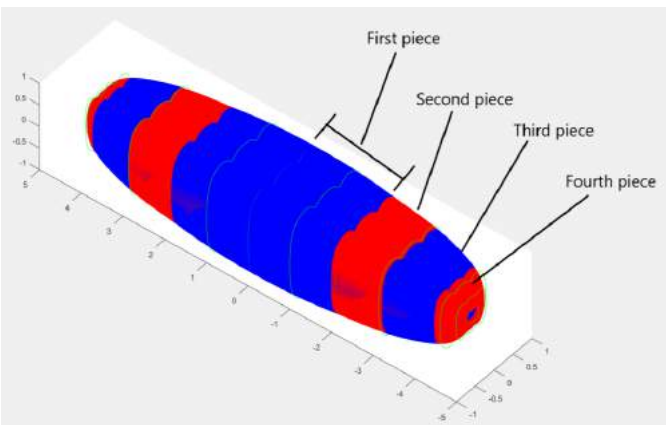

Fig. 6: Tri-lobed envelope surface obtained in two halves each divided into four pieces

An optimum step size was chosen for interpolation in generating the standard cross-section. The same is done in the case of interpolation of these cross-sections. Fig. 7 illustrates the variation of generated shape as step-size is increased from a large value to a very small size. As step-size decreases, the number of points generating the surface increases, resulting in a smoother surface.

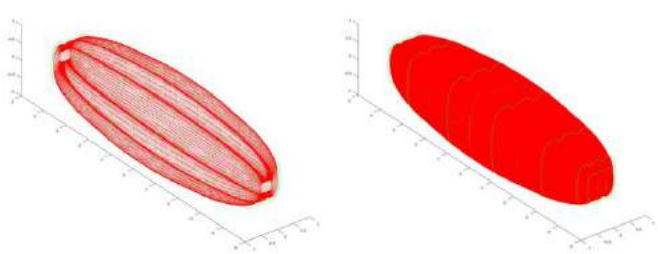

Fig. 7: Effect of step-size on accuracy of generation of surface

3. ESTIMATION OF CURVED SURFACE AREA OF THE AIRSHIP AND VOLUME ENCLOSED BY AIRSHIP

3.1 Curved surface area

Now that we have the coordinates of points used for generating the curve shown in Fig. 4, the sum of distances between each of the adjacent points would give the value of the perimeter of the curve. Multiplying that value by 4 will give the perimeter of the standard cross-section (say P). The perimeter of cross-sections at various intermediate locations along the axis was found by multiplying perimeter of the standard cross-section with the corresponding scaling factor obtained by interpolation techniques.

Since the overall shape of the airship is obtained by interpolating various cross-sections along the axis of airship, curved surface area of the surface is found by assuming the perimeter of cross-section over a small length (say dz) along the axis as constant so that curved surface area of the small element along that length is P*dz. Summation of curved surface area of these small elements along the axis will give the total curved surface area of the airship.

3.2 Enclosed volume

As we have the parametric equations of x(u) and y(u) which were used for the generation of the curve shown in Fig. 4, we can get the area under it by integration method. Express dx in terms of du by differentiating the equations. Then area under the curve by integration is given by $\int y(u).\ (du)$ after applying proper limits. Multiplying the value by 4 gives the value of the total area of the cross-section (say A). The area of cross-sections at various intermediate locations along the axis was found by multiplying area of the standard cross-section with the square of the corresponding scaling factor obtained by interpolation techniques.

The total enclosed volume, just like the curved surface area of the surface is found by assuming the area of cross-section over a small length (say dz) along the axis as constant so that volume enclosed within the small element along that length is A*dz. Summation of volume enclosed by these small elements along the axis will give the volume enclosed by the airship.

4. VARIANTS AND VALIDATION

Just as control points were estimated to generate a standard cross-section of a tri-lobed envelope, with appropriate manipulation of these points, circular cross-section and square cross-section can be achieved. Having equally scaled seven cross-sections of these lead to the development of cylindrical and prismatic surface as shown in Fig. 8.

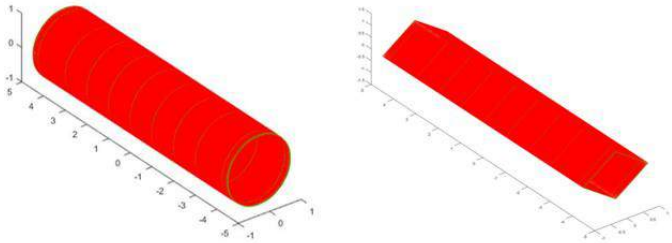

Fig. 8: Cylindrical and prismatic surfaces

Also, with a proper choice of points, Two-lobed and Four-lobed cross-sections (as shown in Fig. 9) can also be generated. The parameters used for the generation of cylindrical shape and prismatic shape were used for validation of measured curved surface area and volume. The relative error compared with actual curved surface area and volume was less than 0.5%.

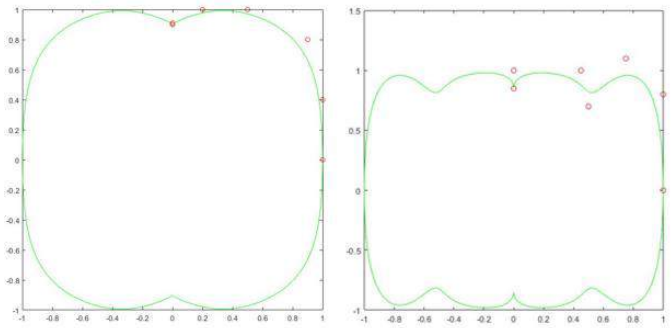

Fig. 9: Two-lobed and Four-lobed airship envelope cross-section

These values of curved surface area and enclosed volume can be used for drag and buoyant lift calculations for lighter than air applications.

5. Conclusion

A methodology for the generation of a tri-lobed airship envelope shape was successfully developed. It involves the input of boundary dimensions and few control points, which generates the surface by B-spline interpolation. The curved surface area and enclosed volume of the surface is also obtained as an output by discretization method which can be used by researchers in lift and drag calculations for various optimization studies.

The versatility of the method is proved by its ability to also generate the shapes of 2-lobed airship, 4-lobed airship and some standard shapes like cylinders and prisms. The parameters for the generation of cylindrical shape and prismatic shape were used for validation of measured curved surface area and volume.

Future work on the provision of more than one type of cross-section for the surface generation can be done for better customization of airship design.

6. Acknowledgement

We gratefully acknowledge the contributions of Raman Verma, Shweta Mahajan and Chetan Dusane for their timely help and the interns at Lighter than Air Systems Laboratory, Aerospace Department, IIT Bombay for their constant support.

7. References

[1] Manikandan M., Rajkumar S. Pant, “Conceptual Design optimization of High Altitude Airships having a Tri-lobed Envelope”, National Conference on Multidisciplinary Design, Analysis, and Optimization, 22nd - 23rd, March 2019, MSRUAS, Bengaluru.

[2] Sumimoto T., Chiba K., Kanazaki M., Hamada N., “Evolutionary Multidisciplinary Design Optimization of Blended-Wing-Body-Type Fly Back Booster”, AIAA SciTech Forum, 7-11 January 2019, San Diego, California.

[3] Ibrahim Z., Sivasubramanian R.: CAD/CAM: Theory and Practice, 2d ed., McGraw-Hill, India, 2009.

Hybrid Airship: More of a Faster Ship, Than a Slower Aircraft

Saurabh Vijay Bagare
Department of Aeronautical and Automobile Engineering
Manipal Institute of Technology
Manipal, India
saurabh.bagare@learner.manipal.edu

Rajkumar S. Pant
Department of Aerospace Engineering
Indian Institute of Technology Bombay
Mumbai, India
rkpant@aero.iitb.ac.in

***Abstract*—Hybrid Airships are a type of powered aircraft which obtain their total lift by means of aerodynamic forces (upto 30%) and thrust vectoring along with the buoyant force exerted by Lighter-Than-Air (LTA) gas. This combination helps the airship lift with a much higher weight and land with a much lighter weight as compared to conventional airships. Hybrid Air Vehicles (HAVs) have emerged as very efficient aerial transportation systems owing to their high endurance, greater payload carrying capacity, greater fuel capacity and eco-friendly nature. Though much work has not been done in the field of hybrid airships, they are an emerging source of aerial transport, both manned and unmanned. With the help of various mathematical and simulation tools like Multidisciplinary Design Optimization (MDO), advanced CFD techniques, it is expected that hybrid airships will soon be an everyday reality.**

***Index Terms*—Hybrid Airship, LTA System, High Endurance, Multi-lobed Envelope, Air Transportation**

I. Introduction

Lighter-Than-Air (LTA) systems are aerial vehicles whose majority of the lift comes from the LTA gas inside an aerodynamically designed envelope [1]. Helium and hydrogen are two of the most popular LTA gases. Though helium it is nearly twice as heavy [2], it has almost 92% of lifting capacity of hydrogen. Many other gases such as methane and ammonia are also lighter-than-air but the buoyant force that they provide is not enough for lift generation, hence they are not popular for use in LTA systems. The applications of LTA systems other than manned or unmanned transportation [3] include aerial surveillance [4], long distance communication [5], disaster management [6], generation of power [7] and military [8].

Since 1990s, a new type of airship has emerged which is popularly known as Hybrid Airship. Very little work has been done in the topic of multi-lobed hybrid airship. Furthermore, the development of complete design methodology of a multi-lobed hybrid airship is not available in the open literature. This poses a great challenge in the development of methodology for conceptual sizing and optimization of hybrid airships. A multidisciplinary analysis is needed for their conceptual design.

The Unique Selling Proposition (USP) of hybrid airships is their extremely high endurance. They have unique operational capabilities and flexibility that cannot be replicated by any fixed or rotary wing vehicles. A typical layout of a hybrid airship is shown in Fig. 1

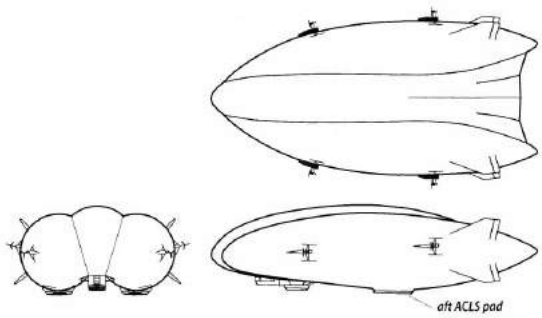

Fig. 1. Design Layout of a Hybrid airship [9]

Owing to its multi-lobed shape, a hybrid airship can have added features such as Advanced Cushion Landing System (ACLS) which gives it a unique ability to take-off, land, and taxi easily without any launching infrastructure. The first extensive work regarding hybrid airships is done by Colozza [10].

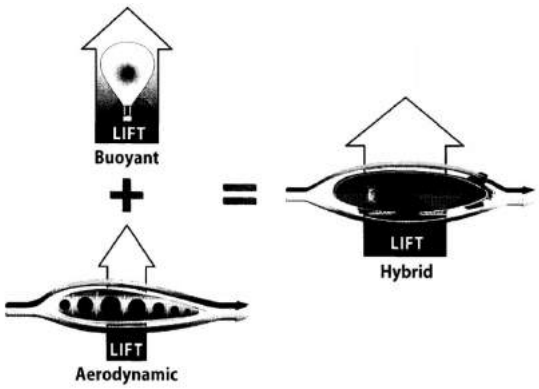

Fig. 2. Working Principle of Hybrid Airships [9]

II. Need for Hybrid Airships

Two significant gaps can be observed in the cargo transportation industry [11]. It can be seen that the world needs a mode of transport that is more eco-friendly than aircraft and trucks, but at the same time, more flexible than ships and rail. Hybrid airships can be a perfect mode of transport to bridge the gap between the common modes of cargo transport in the industry. An extensive cost-effect analysis is done by Prentice & Lau [12] and Mahzan [13].

From Fig. 3 we can observe that though airships may not be as efficient as cargo ships or rail network, they are certainly more efficient when compared to their main competitors in the local or global airspace.

A hybrid airship hence combines the strength of both aircraft and airship [14] to give adequate stability for station keeping and at the same time, swift and eco-friendly travel in air with significantly high endurance.

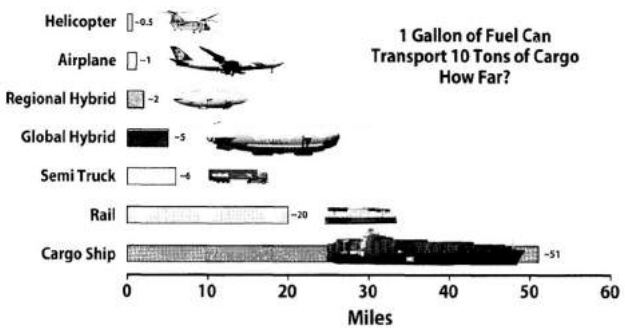

Fig. 3. Comparison of efficiency of various modes of transport [9]

The multi-lobed hybrid airship [15] is more aerodynamically efficient with the capability to generate and modulate dynamic lift during takeoff and landing, and the buoyant hull to generate static lift at low drag. The flat lower surface supports the installment of Air Cushion Landing System (ACLS) [16] which makes the hybrid airship to carry heavy equipment to any isolated regions.

III. Types of Hybrid Airships

Numerous hybrid airship designs have been explored in the past, namely, dynastats (airship+airplane) and rotastats (airship+helicopter) [17].

A. Dynastat

A dynastat is a hybrid airship with fixed wing and/or a lifting body that is typically intended for light transport and aerial surveillance applications. The presence of an aerodynamically streamlined hull creates lift [18] [19]. An airship with conventional hull attached to it is called as winged-hull dynastat whereas an airship with aerodynamic hull attached to it is called as lifting-body dynastat [20].

A number of winged-hull dynastat concepts exist, including Dynalifter (Ohio Airship Inc.), Dinosaure, and Aeroship proposed by Liu et al. [21]. An example of such a configuration is Dynairship (Fig.4) which is a proposed conceptual lifting-body dynastat for civil and military cargo purposes. Another example can be Wolverine as shown in Fig. 5 which is a delta-wing helium filled envelope capable of Short Take-Off and Landing (STOL).

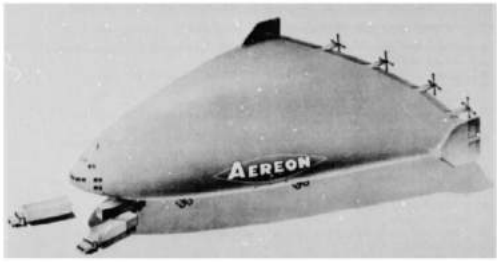

Fig. 4. The Dynairship [22]

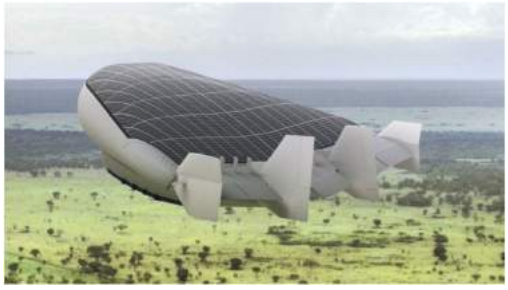

Fig. 5. Wolverine by Solar Ship

B. Rotastat

A rotastat [23] is a concept of hybrid airship with rotary wings capable of Vertical Take-Off and Landing (VTOL). It is very suitable for heavy lift operations as vertical thrust aids the net buoyant lift. SkyHook JHL-40 (Fig. 6) is a recent concept of rotastat which combines the best characteristics of an airship and a helicopter. It is capable of carrying 40 tons load without refuelling.

Fig. 6. SkyHook JHL-40 by Boeing

IV. Conventional vs Hybrid Airship

As shown in Table I, even though the drag for a hybrid airship is higher, it is compensated by high maneuverability, payload capacity and fuel efficiency.

TABLE I
COMPARISON BETWEEN CONVENTIONAL AND HYBRID AIRSHIP

	Conventional Airship	Hybrid Airship
Source of Lift	Aerostatic Force	Aerostatic+Aerodynamic
Aerostatic Lift	80%-100% from LTA gas	60%-70% from LTA gas
Maneuverability	Low	High
Drag	Low	High
Payload Capacity	Low	High
Ground Handling Cost	Low	High
Landing System	Fixed/Retractable LG	ACLS
Fuel Efficiency	Low	High
Susceptibility to weather change	High	Low
Dispatch reliability	Poor	Good

Buerge [24] has studied the suitability of hybrid airships compared to conventional ones in surveillance missions. From studies done by Schufele [25], on statistical comparison of hybrid and conventional airships at 20 tons of useful load, it is seen that hybrid airships have a greater range as compared to conventional ones.

V. DESIGN METHODOLOGY OF HYBRID AIRSHIPS

The envelope length, width, height, equivalent body diameter, diameter of lobes, aspect ratio, wetted surface area, tail area are estimated. Just like aircraft, aspect ratio plays a vital role in determining the Lift-to-Drag characteristics of the airship. The induced drag factor (k) varies with the aspect ratio irrespective of the geometry of the envelope. The non dimensional aerodynamic parameters could be estimated for given aspect ratio and fineness ratio using 3D panel method [26].

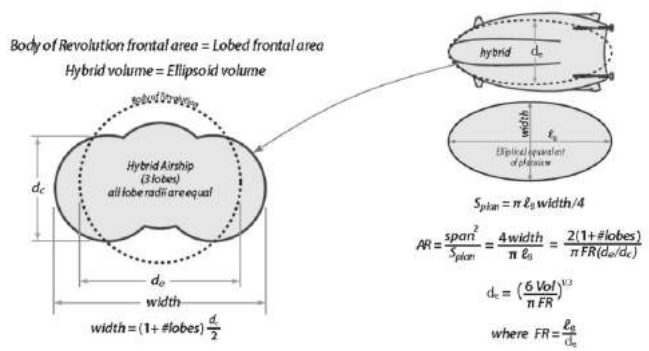

Fig. 7. Multi-lobed airship being approximated as ellipsoid [27]

$$V = \frac{\pi D^2 L}{6} \tag{1}$$

$$s = \pi(l^p w^p + l^p h t^p + w^p h t^p)^{(1/p)} \tag{2}$$

Where, L is the length of the ellipsoid and D is the Diameter of the ellipsoid

$$d_e = \left(\frac{6V}{\pi FR}\right)^{(1/3)} \tag{3}$$

Where d_e is the effective envelope diameter.

The ratio of the equivalent diameter (d_e) to the diameter of the lobes (d_c) is given as:

$$\frac{d_e}{d_c} = -0.0718(N_{lobes})^2 + 0.361(N_{lobes}) + 0.575 \tag{4}$$

$$L = L_b + L_{aero} + L_{vector} \tag{5}$$

Where L_b [28] is the net buoyant lift, L_{aero} is the net aerodynamic lift and L_{vector} is the lift due to vectored propulsion system. The effect of buoyancy ratio on various performance parameters can be seen in work done by Nicholai & Charichner [27] and Khurana et al. [29]. Further, the optimum aerodynamic and buoyant lift for a hybrid airship is demonstrated by Verma et al. [30].

A master constraint equation as shown in (6) is deduced by Agte et al. [31] which is similar to traditional fixed wing aircraft design and uses thrust-to-weight ratio, the wing loading and the volume to surface area ratio to size the airship.

$$\frac{T_{sl}}{W_{to}} = \frac{\beta}{\alpha}\left(\frac{qS}{\beta W_{to}}\left[k_1\left(\frac{n\beta W_{to}}{qS} - \frac{\rho g Q}{qS}\right)^2 + k_2\left(\frac{n\beta W_{to}}{qS} - \frac{\rho g Q}{qS}\right) + C_{D_0} + \frac{1}{v}\frac{dh}{dt} + \frac{1}{g}\frac{dv}{dt}\right.\right. \tag{6}$$

The constraint equation relating take-off distance to the three sizing variables is shown in (7)

$$\frac{T_{sl}}{W_{to}} = \frac{1.44\beta}{\alpha c_{L_{max}} S_{to}}\left[\frac{\beta W_{to}}{\rho g S} - \frac{Q}{S}\right] + \frac{0.71 C_{D_0}}{\alpha C_{L_{max}}}\left[1 - \frac{\rho q\left(\frac{Q}{S}\right)}{\frac{W_{to}}{S}}\right] + \frac{\mu}{\alpha}(\beta - 0.7) \tag{7}$$

$$Buoyancy\ Ratio\ (BR) = L_b/W_G \tag{8}$$

$$Heaviness = Aerodynamic\ Lift = W_G(1 - BR) \tag{9}$$

Heaviness is basically the measure of aerodynamic force exerted by the airship during an equilibrium or resting state. Since fuel is burnt during flight, BR constantly changes. Therefore, as the designer, we should take care of two conditions i.e BR@TO and BR@landing. Very low values of BR often result in airships having too much drag-due-to-lift and hence are rendered unable to generate sufficient lift during take-off. A detailed trade-off study is needed to identify the Aspect Ratio (AR), BR, thrust-to-weight ratio (T/W) etc. as low BR@TO results in longer take-off field length, bigger engines and more fuel burnt during the mission.

Ceruti and Marzocca [32] [33] have demonstrated the weight estimation of solar-powered and fuel-powered airship as a summation of all the individual component weights. Nicholai and Charichner [9] have also quantified the individual weight distribution for a hybrid airship equipped with an ACLS pad.

Zhang et al. [34] has proposed a methodology for conceptual design and analysis of multi-lobed hybrid airships for solar-powered and hydrogen powered cargo carrying applications. A brief methodology demonstrated by Nicholai and Charichner is shown in Fig. (8).

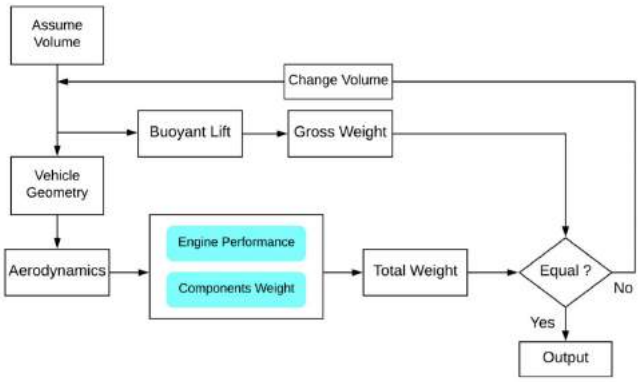

Fig. 8. Design and Analysis Process of Hybrid Airship

Furthermore, it is possible to have some special conceptual designs [35] for hybrid airships like ground-effect hybrid airship [36], winged hybrid [37], tandem wing [38], solar-powered [39] [40] [41] [42] [43] and delta-wing [44].

The innate design layout of a hybrid airship offers much flexibility in the positioning of the engines thereby giving much higher thrust vectoring capabilities [45]. Thrust vectoring is necessary for hybrid airships as they need to swiftly maneuver for on-ground operations. Certain amount of thrust vectoring is helpful for heavy take-offs and reverse thrust for braking. The design parameters like engine placement, engine cycle and propeller size is fundamentally same as that of conventional airships.

The main aerodynamic parameters of hybrid airships are studies by Carrion et al. [46] and the aerodynamic characteristics of the lifting-body are studied by Holt et al. [47].

The estimates of aerodynamic parameters of more complex geometries is obtained after validating CFD codes against 6:1 prolate spheroid. The Helicopter Multi-Block (HMB2) CFD solver developed by University of Liverpool is validated for various applications including turboprops and UCAVs. HMB2 solver uses arbitrary Lagrangian-Eulerian formulation for time-dependent domains with moving boundaries for solving Navier-Stokes Equations.

VI. Historical Development: Aereon III- The First Hybrid Airship

The Aereon III was an experimental rigid-body hybrid airship built by Aereon Corporation in early 1960s. It features three gas envelopes side-to-side, with aerofoil shaped connector structures to generate extra lift as the airship attains forward velocity. It was originally planned to be a prototype to precede the design and development of much larger airships, the Aereon III was built between 1959-1965 but was destroyed during taxiing tests in 1966 without executing a single successful aerial flight. It was the first 'rigid airship' to be constructed since Graf Zeppelin II.

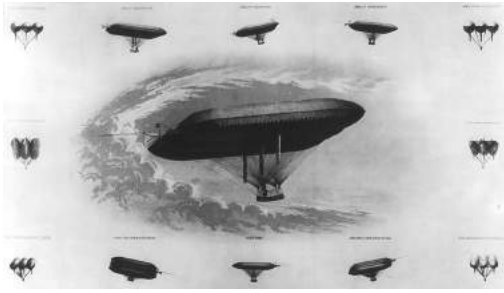

Fig. 9. Aereon III

VII. Present Progress

A. Lockheed Martin P-791

The Lockheed Martin P-791 is an hybrid airship developed by Lockheed Martin for experimental purposes. Its maiden flight took place on 31st January 2006 at Lockheed testing site at USAF Plant 42 in Palmdale, California.

Fig. 10. Lockheed Martin P-791 [48]

The P-791 has a triple hull shape with disk-shaped cushions for landing. It was born as a result of United States' Army's Long Endurance Multi-Intelligence Vehicle (LEMV) program, but ultimately lost the competition to Northrop Grumman's HAV-3.

B. Hybrid Air Vehicles HAV 304/Airlander 10

The Hybrid Air Vehicles HAV 304/Airlander 10 is a hybrid airship designed and built by Hybrid Air Vehicles (HAV), a British airship manufacturer. It was designed originally as a contention for United States' Army's LEMV program although it was cancelled in 2013. It has a helium filled envelope with auxiliary wing and tail surfaces. Production run of Airlander 10 is currently planned.

Fig. 11. HAV Airlander 10 [49]

Unlike most airships, it is devoid of a circular cross-section, instead it has an elliptical cross-section with flattened and contoured hull. It is purposely designed in such a way so that the shape inherently acts as a lifting body, thus contributing to the aerodynamic lift and aiding the buoyant lift produced by helium. It is designed to take-off from both terrain and water. 60%-80% of the weight is supported by Helium.

VIII. Conclusions

Seeing the current progress in the field of hybrid airships, the future of airships certainly looks bright. Their high efficiency coupled with very high endurance as compared to conventional aircraft makes it a very viable option for future air transportation involving civilian and military application both.

Better analytic and computational methods need to be developed for its aerodynamic modelling. Several papers have been published related to the design and optimization of hybrid airships but detailed study on conceptual and practical design methodology is yet to be done. A comprehensive analysis needs to be done on multidisciplinary optimization of multi-lobed airship envelope.

Also, a study on solar powered airships in in progress. The main advantage of such a system will be its extremely high efficiency and less polluting nature. Though many design aspects pose a potential challenge to the designers, keeping faith in the technological advancements will certainly make hybrid airships a reality in near future.

References

[1] C. Vijay Ram and Rajkumar S. Pant. Multidisciplinary shape optimization of aerostat envelopes. *Journal of Aircraft*, 47(3):1073–1076, 2010.

[2] P. V Hunt. *Advanced Airship Technologies and Design Approaches*. AIAA Education Series, 2015.

[3] Peter Tatham, Craig Neal, and Yong Wu. Hybrid cargo airships: a humanitarian logistic game changer? *Journal of Humanitarian Logistics and Supply Chain Management*, 7, June 2017.

[4] N. Sharma, R. Sehgal, and R. S. Pant. Design fabrication and deployment of a tethered aerostat system for aerial surveillance. In *Proceedings of National Level Conference on Advances in Aerial/Road Vehicle and its Application*, Manipal, India, 18-19 July 2014.

[5] P. Bilaye, V. N. Gawande, U. B. Desai, A. A. Raina, and R. S. Pant. Low cost wireless internet access for rural areas using tethered aerostats. In *Proceedings of 2008 IEEE Region 10 Colloquium and the Third International Conference on Industrial and Information Systems*, pages 1–5, IIT Kharaghpur, India, 8-10 December 2008.

[6] C. R. Dusane, A. V. Wani, R. S. Pant, D. Chakraborty, and B. Chakravarthy. An elevated balloon-kite hybrid platform for surveillance. In *23rd AIAA Lighter-Than-Air Systems Technology Conference AIAA AVIATION Forum, (AIAA 2017-3995)*, Denver, Colorado, 2017.

[7] R. S. Pant, A. Kar, and N. Komerath. Application of lighter-than-air platforms for power beaming, generation and communications. In *Proceedings of International Symposium on Electronic System Design (ISED-2011)*, pages 242–247, Kochi, Kerala, India, 2011.

[8] Christopher Bolkcom. Potential military use of airships and aerostats. In *Library of Congress Washington D.C, Congressional Research Service*, 2006.

[9] Leland M. Nicolai and Grant E. Carichner. *Fundamentals of Aircraft and Airship Design: Vol. 2 – Airship Design and Case Studies*. American Institute of Aeronautics and Astronautics, 2013.

[10] Anthony Colozza and James Dolce. Initial feasibility assessment of a high altitude long endurance airship. 2003. NASA/CR-2003-212724.

[11] Alexander Donaldson, Ioannis Simaiakis, Jonathan Lovegren, Nikolaos Pyrgiotis, Lishuai Li, Christopher Dorbian, and Chelsea He. Parametric design of low emission hybrid-lift cargo aircraft. *In 48th AIAA Aerospace Sciences Meeting Including the New Horizons Forum and Aerospace Exposition*, page 1395, 2010.

[12] Barry E. Prentice and Yui Yip Lau. Market potential for transport airships in service to hong kong. In *Proceedings of 8th International Forum on Shipping, Ports and Airports (IFSPA)*, November 2015.

[13] Muhammad Iyas Mahzan and Muhamad Sallehuddin. Cost analysis of a hybrid airship vehicle for cargo delivery. In *4th Mechanical and Manufacturing Engineering*, volume 465 of *Applied Mechanics and Materials*, pages 373–378, February 2014.

[14] Leland Nicolai and Grant Carichner. *Airplanes and Airships... Evolutionary Cousins*. Janary 2012.

[15] M. Manikandan and Rajkumar S. Pant. Design optimization of a tri-lobed solar powered stratospheric airship. *Aerospace Science and Technology*, 91:255 – 262, 2019.

[16] Jeffery Roger Munk. Hybrid air vehicle having air cushion landing gear, November 2005. US Patent, US6880783B2.

[17] Mark D Ardema. Feasibility of modern airships: Preliminary assessment. *Journal of Aircraft*, 14(11):1140–1148, 1977.

[18] David Arthur, David Newman, Jason Wheelock, and Raymond Hall. Options for strategic military transportation systems. In *Congressional Budget Office (US Congress)*, Washington DC, 2005.

[19] M. Spearman and Karen Feigh. A hybrid airship concept having twin-hulls and an inboard-wing. In *13th Lighter-Than-Air Systems Technology Conference, Norfolk,VA,U.S.A*, June 1999.

[20] Edwin Mowforth. *An Introduction to the Airship*. The Airship Association, 2007.

[21] Tianshu Liu, William Liou, and M Schulte. Aeroship: A hybrid flight platform. *Journal of Aircraft*, 46:667–674, March 2009.

[22] William McElwee Miller Jr. The dynairship. (structural design criteria and feasibility analysis of an airplane - airship). pages 441–455, 1975.

[23] Julius Dahms and Andreas Bardenhagen. Approach to a synthesis of hybrid unmanned aircraft systems (UAS) in rotastatic configuration. In *7th EASN International Conference on Innovation in European Aeronautics Research, Warsaw, Poland*, September 2017.

[24] Brandon Buerge. The suitability of hybrid vs. conventional airships for persistent surveillance missions. In *48th AIAA Aerospace Sciences Meeting Including the New Horizons Forum and Aerospace Exposition, Orlando, Florida*, 2010.

[25] Steffen Schaufele. Transport efficiency of conventional airships and hybrid airships in comparison. In *Deutscher Luft- und Raumfahrtkongress*, 2018.

[26] Alexander Donaldson, Ioannis Simaiakis, Jonathan Lovegren, Nikolaos Pyrgiotis, Lishuai Li, Christopher Dorbian, and Chelsea He. Parametric design of low emission hybrid-lift cargo aircraft. In *48th AIAA Aerospace Sciences Meeting Including the New Horizons Forum and Aerospace Exposition*, page 1395, January 2010.

[27] Grant E. Carichner and Leland M. Nicolai. Hybrids...the airship messiah? In *AIAA Lighter-Than-Air Systems Technology (LTA) Conference*, March 2013.

[28] J. A. Taylor. *Principles of Aerostatics: The Theory of Lighter-than-Air Flight*. CreateSpace Publishers, 2014.

[29] Parv Khurana, Manikandan M, and Rajkumar S. Pant. Conventional and multi-lobed lifting-body hybrid airships: A comparative study in sizing. In *11th International Airship Convention and Regatta*, 2017.

[30] Aman Raj Verma, K. Kiran Sagar, and Pankaj Priyadarshi. Optimum buoyant and aerodynamic lift for a lifting-body hybrid airship. *Journal of Aircraft*, 51(5):1345–1350, 2014.

[31] Jeremy Agte, Thomas Gan, Fabrice Kunzi, Andrew March, Sho Sato, Brandon Suarez, and Brian Yutko. Conceptual design of a hybrid lift airship for intra-regional flexible access transport. In *48th AIAA Aerospace Sciences Meeting Including the New Horizons Forum and Aerospace Exposition, Orlando, Florida*, January 2010.

[32] Alessandro Ceruti and Pier Marzocca. Conceptual approach to unconventional airship design and synthesis. *Journal of Aerospace Engineering*, 27(6), 2014.

[33] A. Ceruti, D. Gambacorta, and P. Marzocca. Unconventional hybrid airships design optimization accounting for added masses. *Aerospace Science and Technology*, 72:164 – 173, 2018.

[43] Durlabh Pande and Dries Verstraete. Impact of solar cell characteristics and operating conditions on the sizing of a solar powered nonrigid airship. *Aerospace Science and Technology*, 72:353 – 363, 2018.

[34] Lanchuan Zhang, Mingyun Lv, Junhui Meng, and Huafei Du. Conceptual design and analysis of hybrid airships with renewable energy. *Proceedings of the Institution of Mechanical Engineers, Part G: Journal of Aerospace Engineering*, 232, June 2017.

[35] Johannes Hartmann. *Conceptual Design of Air Vehicles with Hybrid Lift Concepts - A Design Space Exploration*. 2017.

[36] D. E. Calkins. Feasibility study of a hybrid airship operating in ground effect. *Journal of Aircraft*, 14(8):809–815, 1977.

[37] Anwar U. Haque, Waqar Asrar, Ashraf A. Omar, Erwin Sulaeman, and Jaffar M. Ali. Conceptual design of a winged hybrid airship. In *21st AIAA Lighter-Than-Air Systems Technology Conference*, 2014.

[38] Feng Li, ZhengYin Ye, and Chao Gao. Design of a new tandem wings hybrid airship. *Science China Physics, Mechanics and Astronomy*, 55(10):1886–1893, October 2012.

[39] Jun Li, Mingyun Lv, and Kangwen Sun. Optimum area of solar array for stratospheric solar-powered airship. *Proceedings of the Institution of Mechanical Engineers, Part G: Journal of Aerospace Engineering*, 231(14):2654–2665, 2017.

[40] John Gundlach IV. Unmanned solar-powered hybrid airships for mars exploration. In *37th Aerospace Sciences Meeting and Exhibit*, 1999.

[41] Lanchuan Zhang, Mingyun Lv, Junhui Meng, and Huafei Du. Optimization of solar-powered hybrid airship conceptual design. *Aerospace Science and Technology*, 65:54 – 61, 2017.

[42] Lanchuan Zhang, Jun Li, Junhui Meng, Huafei Du, Mingyun Lv, and Weiyu Zhu. Thermal performance analysis of a high-altitude solar-powered hybrid airship. *Renewable Energy*, 125:890 – 906, 2018.

[44] P. A. Mackrodt. Further studies in the concept of delta-winged hybrid airships. *Journal of Aircraft*, 17(10):734–740, 1980.

[45] B. L. Nagabhushan and G. D. Faiss. Thrust vector control of a v/stol airship. *Journal of Aircraft*, 21(6):408–413, 1984.

[46] M. Carrion, R. Steijl, G. N. Barakos, and D. Stewart. Analysis of hybrid air vehicles using computational fluid dynamics. *Journal of Aircraft*, 53(4):1001–1012, 2016.

[47] Jenny C. Holt, Kevin P. Garry, and Tony Smith. Investigation of the aerodynamic characteristics of a lifting body in ground proximity. In *34th AIAA Applied Aerodynamics Conference, Washington, D.C*, June 2016.

[48] Lockheed martin hybrid airship. http://www.lockheedmartin.com/us/products/HybridAirship.html.

[49] Hybrid aerial vehicles. hybridairvehicles.com.

Study of the Mechanical Properties of an Additively Manufactured IN718 Submitted to Tensile Tests

1 Mahesh Naik, PhD Scholar, Department of Mechanical Engineering, DIAT, Pune, India.
(email- mahesh.naik4144@gmail.com)
2 Dr. D. G. Thakur, Professor, Department of Mechanical Engineering, DIAT, Pune, India.
(*email- thakur@diat.ac.in*)

Abstract - Additive Manufacturing(AM) is a revolutionary technology which is bringing about path breaking changes in aerospace, automotive, biomedical and energy sectors. IN718 is a nickel based solid solution strengthening and precipitation hardening superalloy which is widely used in the aerospace and chemical processing industries. It has high temperature strength & hardness and also possess good wear and corrosion resistance. But due to its work hardening property it is a very difficult material to mould and machine. Hence AM is highly suggested for the fabrication of such parts and Direct Metal Laser Sintering (DMLS) is the most commonly used AM method for IN718. This study aims to determine some mechanical properties of an additively manufactured IN718 obtained through tensile tests. The additively manufactured IN718 was subjected to tensile tests with Solution Annealing the material at 980ºC for 1 hour and double aging treatment at 720ºC and 620ºC and a strain rate of 0.5 mm/min according to ASTM E-8 standard.

Keywords: Additive Manufacturing, DMLS, IN718, Tensile Test

1. INTRODUCTION

Developers of aerospace systems are increasingly employing additive manufacturing (AM) technologies to fabricate complex structural components used in fielded systems. Initially used to create models of design concepts and preliminary prototypes, applications of laser sintering to produce metallic components for end-use applications grew exponentially, beginning in the mid-1990s [1]. Introduction of commercial laser-sintering systems used to incrementally fuse layers of metal powder into solid objects generated the shift from “rapid prototyping” to “rapid manufacture” by 2005 [2]. Early selective laser sintering (SLS) systems utilized powders with polymer-coated powders, resulting in low density products requiring consolidation with hot isostatic pressure (HIP) to achieve near-full density [3]. Parallel innovations enabled the use of metal powders without coatings to be used in a “direct selective laser sintering” method [4]. Refinements of this concept grew into the AM process now referred to as direct metal laser sintering (DMLS), which is technically a special instantiation of SLS [5].

Direct metal laser-sintering (DMLS) is a production method for creating metal parts. It works by taking 3D geometry data such as a CAD file or scan data, which are sliced into layers by software. From this layer data, laser exposure vectors are calculated for each layer of the build process. In the production machine, very thin (typically between 20 and 60 µm) layers are exposed, creating a metallic bond to the surrounding exposed material including the previous layer. The process of applying and exposing layers is repeated, thereby creating solid metal parts additively, layer by layer, from the powder material. Figure 1 shows DMLS Process.

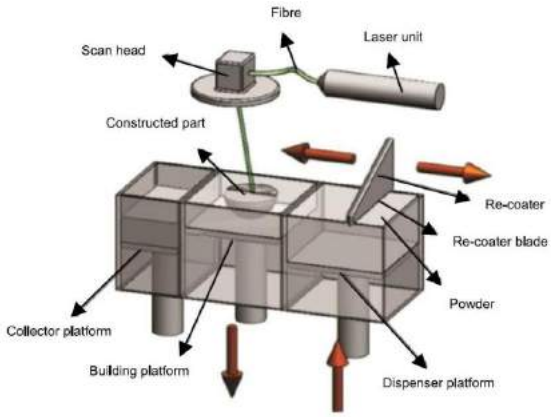

Figure 1: DMLS process [6]

Several reports of investigations of the characteristics of IN718 materials produced with layered AM techniques have been published recently. In the study carried out by authors in [7], the microstructure and

mechanical properties of as built specimens and after two different heat treatments were compared. Tests were carried out for specimens in two different orientations. The mechanical properties were almost equal for both the heat treatments and are comparable with that of wrought material. The specimens show anisotropic behaviour and horizontal oriented specimens have better tensile strength. Studies in [8] showed the changes in the properties of SLM IN718 with respect to change in the layer thickness taken as input parameter while printing the specimens. It was observed that samples with lower layer thickness showed better mechanical properties compared to higher layer thickness. It was also established horizontal specimens showed better results than vertical specimens. Studies were conducted in [9] to find the properties of as built and after heat treated IN718 samples under different conditions. The properties were found to be comparable to that of wrought material and the fractography analysis showed that the material failure can be characterized by ductile failure mode with some brittle fracture. The present study therefore aims to investigate in detail the mechanical properties of IN718 fabricated by DMLS in as-built and heat treated conditions by tensile test. For comparison purposes, samples produced by conventional techniques (henceforth as-cast samples) are also characterized.

2. Experimental Details

2.1. Powder-bed material fabrication:

Additive IN718 specimens were fabricated using an EOS M280, a DMLS system, also with argon gas and a laser having spot size of 100 mm. The laser power and travel rate are considered proprietary by the service provider. Powder for IN718 fabrication was also obtained from EOS GmbH, Nadcap certified with particle sizes ranging from 3µm to 30 µm. The resulting specimens had a layer thickness of approximately 40µm, and the temperature of the build platform during their fabrication was 35°C. The Chemical composition (weight %) of powder materials used in specimen fabrication is shown in Table 1.

Table 1: Chemical composition (weight %) of powder materials used in specimen fabrication.

Element	B	C	O	Al	Ti	Cr	Fe	Ni	Nb	Mo
% weight	4.08	12.95	1.34	0.42	0.96	16.22	14.48	42.34	5.34	1.87

2.2 Specimen preparation

The tensile specimens used in this study were traditional tensile “dog-bones,” contoured to dimensions consistent with ASTM Standard E8. The specimens used for the experimentation were printed at the Intech DMLS facility, Bengaluru using an EOS M280 metal 3D printer. The machine has many in built systems for its seamless operation. It consists of a building chamber with a recoater system, an elevation system, a heating system for the building chamber, a laser module, process gas module and a computer with an in built software. It uses an Ytterbium fibre laser with an optional power setting of 200W or 400W and has a scan speed of upto 7m/s. Figure 2 shows an EOSINT M280.

Figure 2: EOSINT M280 [10]

In total six tensile test specimens were printed. All the specimens were fabricated as per ASTM standards. Tensile specimens were designed as per ASTM E8/E8M standard with dimensions as given in Table 2. Fig 3 shows the dimensions of the fabricated specimens.

Table 2: Tensile specimen dimensions as per ASTM E8 standard

Parameters	Values(in mm)
Overall length	100
Gauge length	25
Width of gauge section	6
Length of reduced section	32
Width of grip section	10
Length of grip section	30
Thickness	6

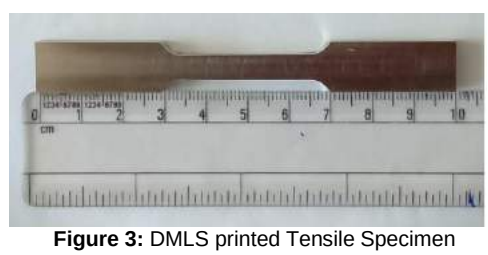

Figure 3: DMLS printed Tensile Specimen

2.3 Heat Treatment:

The heat treatment of the DMLS IN718 specimens were performed using the furnace facility (Figure 4) at Kalasalingam Academy of Research and Education (KARE), Krishnankoil. The heat treatments were carried out as per the SAE Aerospace standard AMS 5662, for Nickel alloys. It involved a three step process with Solution Annealing the material at 980°C for 1 hour and double aging treatment at 720°C and 620°C.

Figure 4: Tube furnace used for Heat treatment

2.4 Tensile Testing:

The tensile testing was carried out at the Metmech Engineers facility, Chennai. It was carried out in a computer controlled Universal Testing Machine with a capacity of 100kN. It uses a ball screw drive and has a cross head speed ranging from 0.5 mm to 200 mm per minute. Three samples of each as-built and heat treated were tested, using a non-contact video extensometer to measure strain; errors in the determination of elastic moduli, introduced by this instrument, may range from 1% to 3%. The values of various properties from tensile testing such as yield strength, elongation and stress strain graph were considered proprietary and were not shared.

3. RESULTS AND DISCUSSION

The mechanical properties of as-built and heat treated IN718 specimens using tensile test were measured on multiple samples and the average values were found and listed in Table 3.

Table 3: Mechanical properties (tensile test) of as-built and heat treated IN718 specimens

Condition	Tensile load (kN)	UTS (MPa)	UTS (MPa) (wrought material) [7], [12], [13]	UTS (MPa) (cast material) [14]
As built	43.35	1204.167	1275-1407	950
Heat Treated	46.14	1281.667		

The density of specimens fabricated using DMLS is very similar to that made using conventional means. The density of DMLS specimen is 8.209 g/cc which is almost equal to the currently proven industry standards. The various mechanical properties also shows similar behaviour, sometimes better properties than samples made using conventional methods. The as-built DMLS specimen's shows 26.7% higher tensile strength than a similar cast sample, while in the heat treated condition it shows a much higher strength, with an increase of up to 35%. It can also be noted that there is an increase in the tensile strength after heat treatment of the specimens. These UTS values of 1204.167 MPa and 1281.667 MPa for as built and heat treated conditions respectively is comparable to the tensile strength in the wrought condition.

4. CONCLUSION

- IN718 specimens were fabricated using DMLS process and was heat treated as per the AMS 5662 standard involving solution treating and double ageing.
- It was found that the as built specimens showed a tensile strength of 1204.167 MPa, a significantly better value than its cast counterpart with an increase of almost 27% and it was also noted that the value obtained was better than those found in the literature review.
- In the heat treated condition it showed higher strength of 1281.667MPa which is comparable to the strength in wrought condition and an increase of 35% in the value.

References:

[1] Kruth, J.P., Levy, G., Klocke, F. and Childs, T.H.C, "Consolidation phenomena in laser and powder-bed based layered manufacturing", CIRP annals, 56(2), pp.730-759, 2007.
[2] Kruth, Jean-Pierre, Ben Vandenbroucke, Jonas Van Vaerenbergh, and Peter Mercelis. "Benchmarking of different SLS/SLM processes as rapid manufacturing techniques." In Proceedings of the International Conference Polymers & Moulds Innovations PMI 2005, 2005.
[3] Shellabear, M., and O. Nyrhilä. "DMLS-Development history and state of the art." Laser Assisted Netshape engineering 4, proceedings of the 4th LANE, 21-24, 2004.
[4] Agarwala, Mukesh, David Bourell, Joseph Beaman, Harris Marcus, and Joel Barlow. "Direct selective laser sintering of metals." Rapid Prototyping Journal 1, no. 1, 26-36, 1995

[5] Kruth, Jean-Pierre, Peter Mercelis, J. Van Vaerenbergh, Ludo Froyen, and Marleen Rombouts. "Binding mechanisms in selective laser sintering and selective laser melting", Rapid prototyping journal 11, no. 1, 26-36, 2005.

[6] Singh, R., S. Singh, and M. S. J. Hashmi. "Implant materials and their processing technologies", (2016).

[7] Strößner, Johannes, Michael Terock, and Uwe Glatzel. "Mechanical and Microstructural Investigation of Nickel-Based Superalloy IN718 Manufactured by Selective Laser Melting (SLM)", Advanced Engineering Materials 17, no. 8, 1099-1105, 2015.

[8] Sufiiarov, V. Sh, A. A. Popovich, E. V. Borisov, I. A. Polozov, D. V. Masaylo, and A. V. Orlov. "The effect of layer thickness at selective laser melting", Procedia engineering, 174, 126-134, 2017

[9] Popovich, Anatoly A., Vadim Sh Sufiiarov, Igor A. Polozov, and Evgenii V. Borisov. "Microstructure and mechanical properties of Inconel 718 produced by SLM and subsequent heat treatment", In Key Engineering Materials, vol. 651, pp. 665-670. Trans Tech Publications, 2015.

[10] Technical Description of EOSINT M 280. © 2010 EOS GmbH – Electro Optical Systems. All rights reserved

[11] Wang, Zemin, Kai Guan, Ming Gao, Xiangyou Li, Xiaofeng Chen, and Xiaoyan Zeng. "The microstructure and mechanical properties of deposited-IN718 by selective laser melting", Journal of Alloys and Compounds 513 (2012): 518-523.

[12] Rao, G. Appa, M. Srinivas, and D. S. Sarma. "Influence of modified processing on structure and properties of hot isostatically pressed superalloy Inconel 718." Materials Science and Engineering: A 418, no. 1-2, 282-291, 2006.

[13] Trosch, Tanja, Johannes Strößner, Rainer Völkl, and Uwe Glatzel. "Microstructure and mechanical properties of selective laser melted Inconel 718 compared to forging and casting", Materials letters, 164, 428-431, 2016.

Topology optimization of aircraft fuselage wing lug bracket attachment

1. Akshay S, PG student, Defence Institute of Advanced Technology,
2. Dr.D G Thakur, Professor, Defence Institute of Advanced Technology,
3. Mahesh A N, Research scholar, Defence Institute of Advanced Technology, Pune

Abstract-The use of 3D printing for replacing conventional methods of manufacturing is been used widely. Aviation industry is one of the few which is striving hard to reduce the weight of the aircraft in order increase its performance whether it be the case of passenger, cargo and even the case of fighter aircraft. In this paper an attempt is made to implement topology optimization procedure applied to the 3D printed parts used in aircrafts. The parts of aircrafts are made such that they withstand the load of self along with the dynamic loads acting on it due to the environment of its operation. A lug bracket which is used for joining the wing to the fuselage is taken for analysis. The design of the bracket for the static loading is performed. A 67 percent of reduction in the mass of the part is obtained. The following discussion describes how to implement topology optimization along with additive manufacturing.

Index Terms- Additive Manufacturing – AM, Topology Optimization – TO, Computer Aided Design- CAD, Finite Element Methods-FEM

1. INTRODUCTION

Additive manufacturing is the change which is making the designer think of innovative methods to make the same component in the light of new idea. The use of additive manufacturing is not restricted to polymer materials. Gas turbine blades, supporting brackets are few of the applications of metal additive manufacturing. Also polymer based AM technology finds its application in product visualization in the initial stage of design process.

In the current scenario of the aviation industry in which all the companies are trying to reduce the emission of the aircraft as per the norms. In case of fighter aircraft used for defence purposes, maneuverability is major function for which it is supposed to be lighter without compromising the payload carried. As a result the aim is to reduce the weight of the aircraft.

Two methods are possible to reduce the weight of a component. Firstly, to decrease the weight of the component by scooping out unwanted material called topology optimization and secondly to make the component of a lighter material with the same physical properties. Topology optimization is the method mentioned first. It is an iterative process with which we remove unwanted material from the design space and add sufficient material at locations where it is required to add.

The use of topology optimization will reduce the weight of component without compromising its safety. TO process is actively used in the automotive industry for weight reduction of parts.

2. LITERATURE

The works associated with topology optimization started in the aviation industry after the general engineering competition taken as crowdsourcing given by Carter W.T[3]. In his work the different methods to implement topology optimization was shown from different domain experts of the world. The design of fuselage lug bracket for medium sized fighter aircrafts was studied by Shashikumar C[2] which constituted the load estimation on each wing and fatigue life estimation along with it.

Two cases of fatigue life estimation is discussed by Madiha Khan[8] for which the design changes has been done to check the fatigue life of components. In the work of Sriranga B K[12] the stress analysis in the lug bracket is performed and it is validated as problem of plate with a hole. The basics of aircraft parts was referred from [5].

3. PROBLEM DEFINITION

- Topology Optimization of the lug bracket.
- Design the bracket for static loads.

Flow chart shows the methodology of study associated in the present work

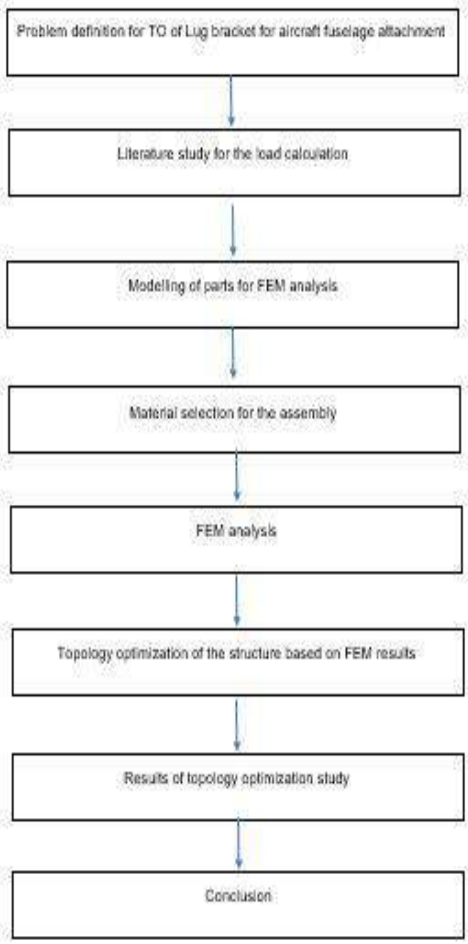

4. CAD MODELLING

The CAD model of the aircraft fuselage lug bracket is shown in figure 4.1. The solid object was modelled in Solidworks-18. The details of the modelling is referred from [1],[7],[12],[2]components which make up attachment are

- I spar beam on which wing surfacing are done.
- Lug with holes for connecting to the fuselage
- Top and bottom flanges.

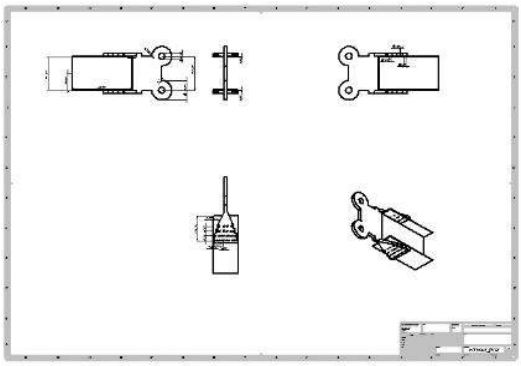

Fig: 4.1.a. planar views of the assembly

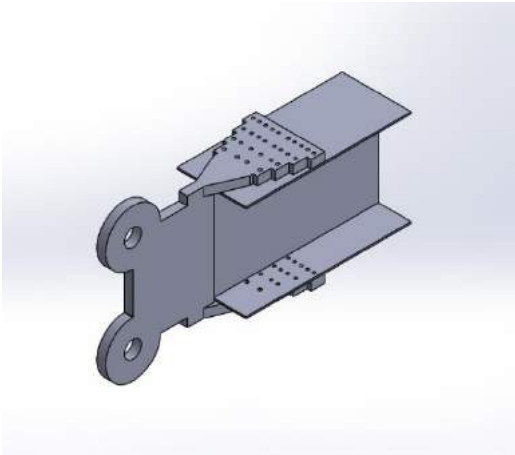

Fig: 4.1.b isometric view

5. MATERIAL SELECTION

The materials used for parts of aircraft are alloy to obtain the necessary properties. Many factors influence the selection of materials such as cost and performance. Costs are mostly initial material cost and maintenance cost. The properties of the material which are taken for the static analysis are

- Yield strength
- Ultimate strength
- Young's modulus
- Poisson's ratio
- Density

The material used for lug portion of the bracket is heat treated steel alloy AISI 4030. It has good ductility, toughness and strength. It finds application on power transmission gears, shafts, landing gear, and other structural parts of aircraft.

The material used for the I-spar beam is Aluminum alloy 2024 T351. It has high strength and is light weight. The material properties of both the materials are given in the table below which was inferred from the works of [6],

Table I from [1]

Sl. No.	Parameter	Al-2024 T351	AISI 4030
1	Youngs Modulus(Mpa)	72400	203000
2	Poissons ratio	0.33	0.32
3	Ultimate Tensile Strength(Mpa)	503.7	1835
4	Yield Strength(Mpa)	472.6	1550
5	Density(Kg/m^3)	2800	7850

6. FEM ANALYSIS

The finite element method originated due to the advances in the aircraft structural analysis. The procedure for fem analysis is carried out in Ansys-18 software. The geometry modelled in Solidworks-18 software is imported in stp format. Once the geometry is obtained it is discretized into number of tetrahedron elements in 3D called meshing of the model. The

process of meshing is done in a particular manner so that at regions of stress concentration, the mesh is made finer in order to get good results. The image of the part after meshing is depicted in fig6.1. It can be observed that at the regions of rivet holes and the lug hole, the mesh is finer.

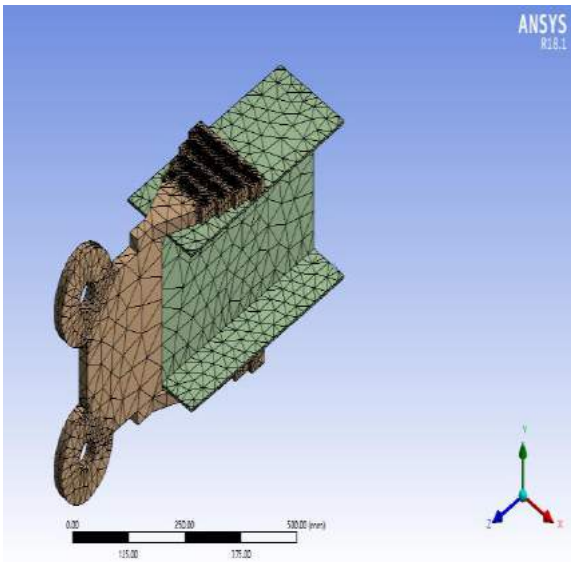

Fig: 6.1 Meshing of the model

The number of nodes are 166930 and elements are 104710.The software solves the equilibrium equation at each element of the mesh. The boundary conditions are defined for the flange portion of the bracket in which the semicircular portion of the bracket is fixed for all the six degree of freedom. A concentrated load is being applied at the end of the spar beam. The equilibrium equations are solved at each element and the results are obtained for each element.

Load calculation for wing fuselage lug bracket

- Category – medium sized aircraft
- Total weight = 6000kg = 58860N
- Load factor considered in design = 6g
- Design limit load for the structure = 353160
- FOS considered = 1.5
- Designed ultimate load = 529740
- Distribution of lift load = 35% on the bracket and 65% on wing
- Total load acting on wings = 529740*.65
  = 344331N
- Load acting on each wing = 172165.5
- Number of spars in the wing = 3
- Load sharing in spars is
  a)spar 1= 30% b)spar 2= 45% c)spar 3= 25%
- The bracket considered in this is spar 3
  = 0.25*172165.5 = 43041.375
- Hence the total load acting in is 90585

Figure6.2 depicts the boundary condition which is applied on the model.

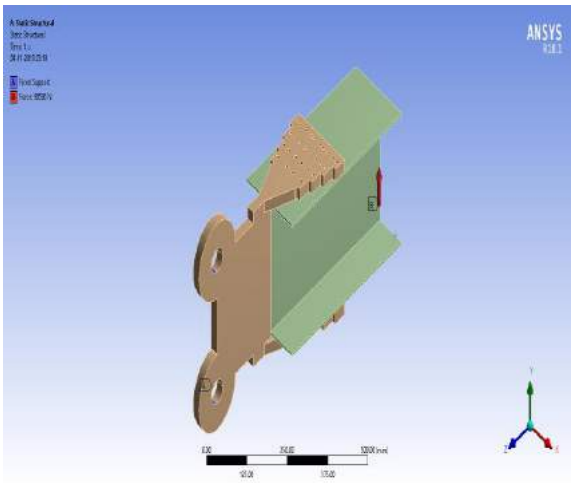

Fig: 6.2 Boundary conditions

7. RESULTS OF FEM

The setup is run and the results are obtained. It is observed that a maximum deformation of 6.3948mm in the I-spar beam as shown in fig7.1. From the stress plot shown in fig7.2, it is observed that the maximum stress of 1026.3Mpa is found to occur in the bottom lug hole. The yield strength of the material of lug bracket is 1550Mpa and the maximum stress is found to be 1026.3Mpa, the structure working under safe working condition. It can also be observed that there are regions at which it is not at all stressed. The material in this region if removed will not affect the strength of the structure. The removal of material causes wastage in case of conventional manufacturing. Whereas in case of additive manufacturing there is no material removal associated. Only addition of raw material at specific locations where the material requirement is needed.

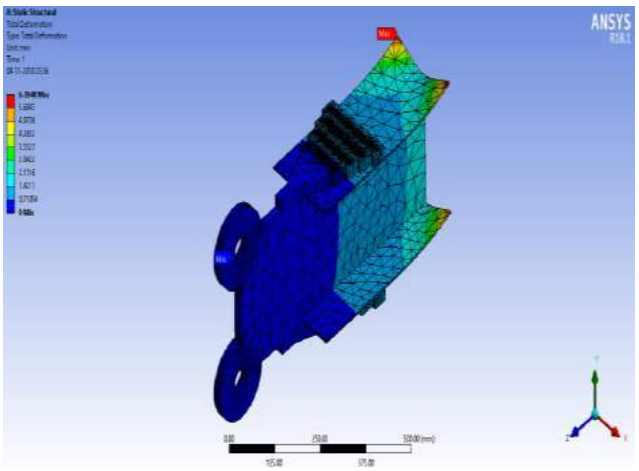

Fig: 7.1 Deformation plot

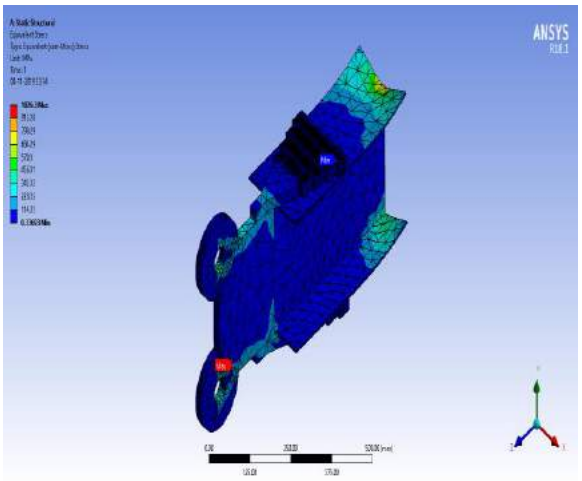

Fig: 7.2 Stress distribution

8. TOPOLOGY OPTIMIZATION PROCEDURE

The results of the FEM analysis is transferred to TO module in ANSYS in which we select only the bracket(out of the assembly) as the design domain since our consideration is to reduce the weight of the bracket alone. The process of topology optimization is iterative in nature and assumes a value of density(for 3D problem) at each element of the design domain and calculates the maximum density of element.

The design region is specified and the exclusion regions is also specified as shown in fig8.1. The minimum density of the element is also specified as 0.001. The optimality criteria method is used for the calculation. Our objective is to minimize the compliance i.e. to maximize the strain energy. The volume of the component is reduced to 50% as given by the response constraint.

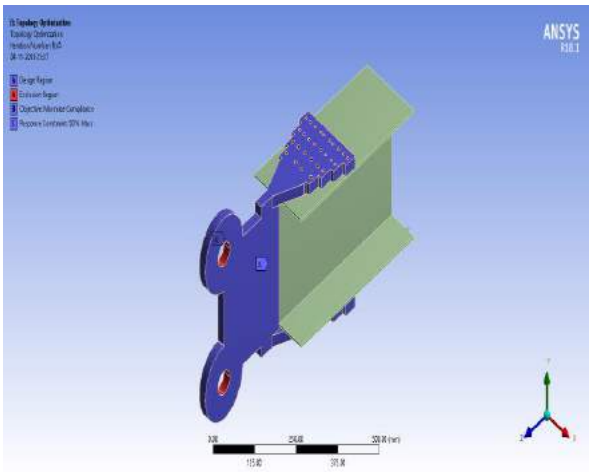

Fig: 8.1 Design space with the exclusion regions

The following flow chart shows the brief overview of the process of TO taken from [4].

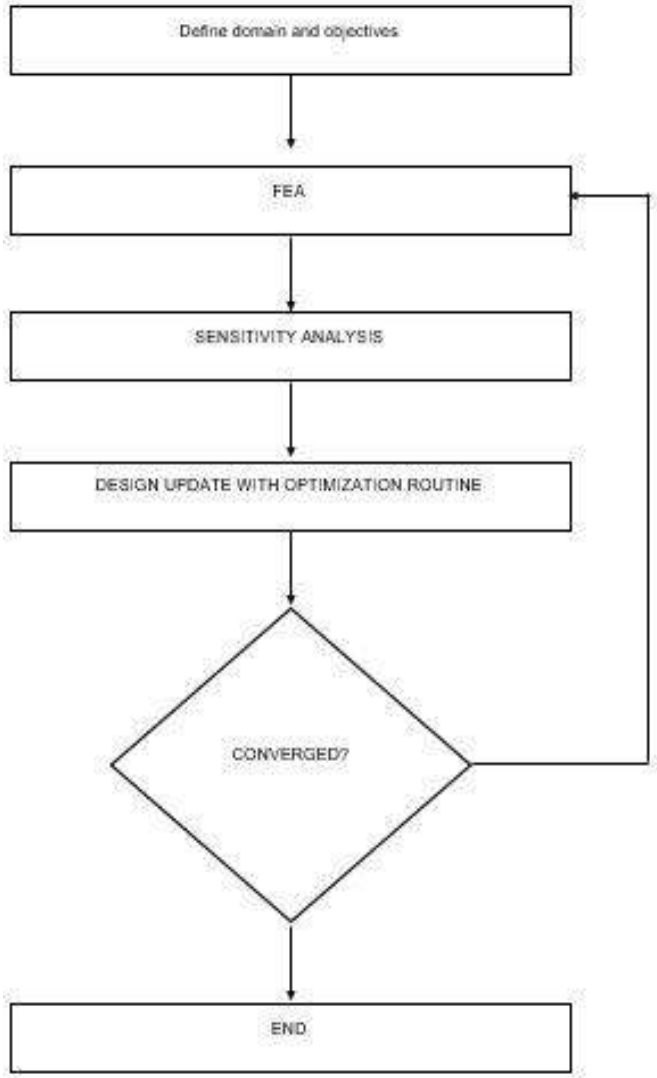

9. RESULTS OF TO PROCESS

The process of TO showed a 54% reduction of the mass of the component as given by the software. Fig9.1 shows the topology density distribution over the design space. The initial mass of 31.118kg was reduced to 16.861kg. But the resulting shape of the part is not uniform in nature as can be seen from fig9.1. inorder to manufacture a part like this using the conventional process is difficult and will result in the wastage of material. With the use of additive manufacturing these shapes can be obtained easily with much greater tolerance in it. From fig:9.2 it can be observed that the structure obtained as the result of TO cannot be manufactured using conventional manufacturing. Metal additive manufacturing can be actively implemented to obtain required shape. The strength of metal AM products are higher than those of products made by casting.

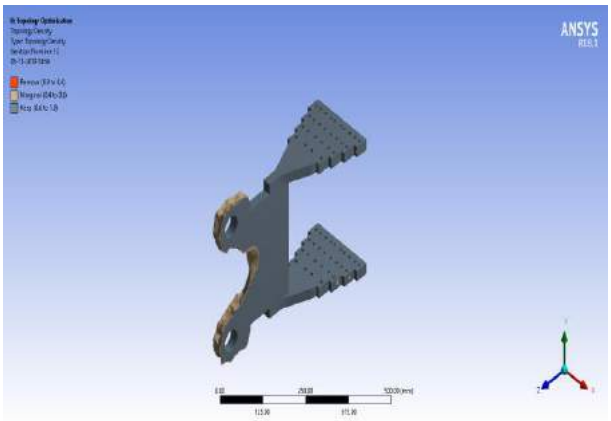

Fig: 9.1 Optimality criteria method (50% volume reduction)

Results	
Minimum	2.56e-003
Maximum	1.
Original Volume	3.9641e+006 mm³
Final Volume	2.659e+006 mm³
Percent Volume of Original	67.077
Original Mass	31.118 kg
Final Mass	20.873 kg
Percent Mass of Original	67.077

Fig: 9.2: Reduction of mass of the component

10. CONCLUSIONS

- Topology study was carried out in lug bracket of wing fuselage assembly for static loading condition.
- Considerable material savings is possible with the use of TO tool.
- Since the component is conventionally manufactured the removal of material causes wastage.
- Additive manufacturing can improve the properties as well as the wastage of material is reduced.
- Multi fold cost saving in case of aircrafts since fuel consumption can be reduced, material required for manufacturing is reduced.

12. ACKNOWLEDGEMENT

I would like to express my sincere gratitude towards Dr. CP Ramanarayanan for the support and motivation for doing this project. I would also wish to express my sincere thanks to Dr. S K Panigrahi for useful technical guidance and constant encouragement. I would also like to thank Mr. Abhijeet Kamble for helping me with the support of Mechanical System Design lab facility

11. REFERENCES

[1]. Sumanth M.H Ayyappa.T," Comparative analysis of aircraft wing fuselage lug attachment bracket", International Journal For Technological Research In Engineering in 11 July 2018.
[2]. Shasikumar.C Ngesh.N Ganesh," Design and analysis of Wing fuselage attachment for fighter aircraft", International Journal of Engineering Research and General Science in January 2016.
[3]. Carter Abbott Finkhousen Stevens," The GE Aircraft Engine Bracket Challenge: An Experiment in Crowdsourcing for Mechanical Design Concepts".
[4]. Davin.J Hossein.G Mohsen.T Ahmad.B," Developing Topology Optimization with Additive Manufacturing Constraints in ANSYS", Elsevier journal in November 2018.
[5]. Ramjan P," Aircraft structures".
[6]. Gulam.M Madhavi.M," STRESS ANALYSIS OF WING - FUSELAGE LUG ATTACHMENT BRACKET", International journal of Research in December 2018.
[7]. Harish.E.R.M Mahesha.K Satraj.P,"Stress Analysis for Wing Attachment Bracket of a six seater Transport Airframe Structure", International Journal of Innovative Research in Science, Engineering and Technology in July 2013.
[8]. Madiha.K Mohammed.R.K Smitha.D," Design And Analysis On Aircraft Wing To Fuselage Lug Attachment" International Conference Emerging Trends in Mechanical Science 2018.
[9]. Shambhu.K Jyoshi.A.K Nagaraj.Arali," Simulation of Wing-Fuselage Attachment Bracket Lug for Fighter Aircraft", International Journal for Ignited Minds in November 2017.
[10]. Ajith V S Ravikumar P Vidhya K," Study of Optimal Design of Spar Beam for the Wing of an Aircraft", International Journal of Engineering Development and Research,2017.
[11]. Vishruth G Chandan R Shivappa H A,"Structural analysis and optimization for spar beam of an aircraft ",International Research Journal of Engineering and Technology in 2017.
[12]. Sriranga B K Chandrappa C N Kumar R," Stress Analysis of Wing-Fuselage Lug Attachment Bracket of a Transport Aircraft", International Conference on Challenges and Opportunities in Mechanical Engineering, Industrial Engineering and Management Studies in july 2012.

System Engineering for Electrical Integration in Aerospace Industries: An Overview

Uttam G Salawade

Abstract: **The main objective of Integration of electrical system on the aircraft is to enhance the operational capability, reliability and safety of the aircraft. In this paper author has presented the methodology and his work experience for electrical system integration activity in aeronautical industry. All the related aspects starting from feasibility study, types of drawings / documents required, ground and flight testing activity till Local Modification Committee (LMC) ratification are covered and briefly explained. A particular focus on methodology adapted for documentation, system testing and industrial procedures are also made.**

Index Terms: **System integration, Aircraft modification, Design drawings, Test schedule.**

1. Introduction

Integration of new system / modification is a continuous process during exploitation of aircraft. The new systems are being integrated to enhance the operational capability and performance of the aircraft. Apart from enhancement of operational capability there are various other reasons such as improvement in terms of maintainability, safety and reliability of the aircraft [1]. To carry out these improvements we are making the provisions by way of integrating new and advance systems with existing one or modifying the existing systems [2]. To integrate the new system or modification of existing aircraft system is a challenging task which requires a pool of various engineering and management approaches [3]. In the literature various types of specifications are available which calls for testing requirements for new systems to be integrated on the aircraft as per airworthiness requirements.

These testing covers functional testing of electrical units, continuity checks, megger checks, voltage and current level checks, impedance matching etc [2].

Uttam G Salawade is working as Additional General Manager (Design), in Aircraft Upgrade Research and Design Center (AURDC) of Hindustan Aeronautics Limited Nasik, India (e-mail: uttam.salawade@hal-india.co.in).

Before integration of new electrical system, it is very much essential to carry out the feasibility study of the integration as per electrical specifications, preparation of interconnection diagrams, and test schedules coordinated by regularity authorities etc. During feasibility study electrical load analysis of the aircraft needs to be carried out to determine the spare power availability for the satisfactory operation of electrical units. The heat load analysis also needs to be carried out for safe operation and making the provision of the cooling [4]. Enabling minimum interconnection length and elimination of speed limiting components for any electrical signal is one of the major constraint to reduce the path loss during electrical system operation. Various factors such as effects of thermal, mechanical, electrical, magnetic and electromagnetic phenomena after integration of new electrical system on the aircraft needs to be considered during the integration process.

The paper is arranged as: Section 2 introduces the electrical system integration requirement. Section 3 describes about the steps involved in electrical system integration along with methodology and author experience starting from feasibility study till LMC ratification. Section 4 concludes the paper.

2. Electrical System Integration

2.1 Motivation / Requirements:

During the operation of the aircraft, time to time the need arises to enhance its operational capability, maintainability, reliability and safety with time to time based the future requirements and customer feedback. These requirements can be fulfilled by way of modifications in the existing systems of the aircraft or by integrating the new and advanced systems with existing one. The process of new system integration can be summarized in various steps. In this paper authors have presented their experience followed during system integration process.

2.2 System Integration Process:

The electrical system integration activity is performed in various steps throughout its life cycle management process. The task categories are diversified in nature

which involves the pool of various streams of engineering as well as management. The steps of electrical system integration process are related with interconnected knowledge and the interconnection of people who possess that knowledge. The system integration process starts from user requirements till LMC ratification with various intermediate stages such as feasibility study, documents / drawings preparation, design reviews , ground and in-flight system testing etc.

2.3 Steps Involved In Electrical System Integration

The system integration process can be mapped into various steps. The detailed description of each steps are summarized in subsequent para. The system integration steps are also diagrammatically represented in Fig. 1.

2.3.1 Analysis for User Requirements:

The first and foremost step for any system integration / modification activity is in depth analysis of user / customer requirement. This step gives the insights about what user needs and how we are going to achieve this, Is this requirement is feasible to materialize. In short all the user requirements needs to visualized from all possible perspectives.

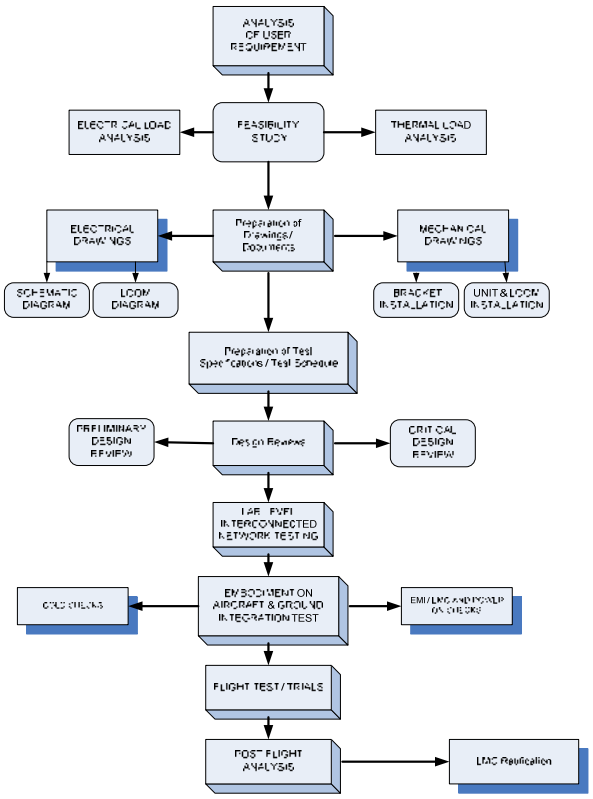

Fig.1. Electrical System Integration Process

2.3.2 Feasibility Study for New System Integration:

After obtaining the user requirement the feasibility study of new system integration needs to be carried out. In this phase, a road map must be planned for practicability / possibility for execution of the task. The feasibility study of integration are again subdivided in various modules such as feasibility for installation of electrical components / units, its electrical power requirement, cooling requirement, interconnection requirements, simulation study etc.

2.3.2.1 Mechanical Installation Trial:

In this phase, the mockup of electrical units / components are to be developed and its feasibility of installation within the available space on the aircraft needs to be carried out. Some time as per the requirement the mounting rack / shock absorber are also used for installing the electrical aggregate hence its mockup are also needs to be designed. The available space of installation must be properly selected so that, loom length requirement and signal losses can be minimized. For the installation study of communication / RF equipments, the possibility of EMI/ EMC effects with other electrical aggregates or EMI / EMC sources may also be considered.

2.3.2.2 Electrical Load Analysis:

Every electrical units requires electrical power supply for its operation. Two types of power supply are required by any electrical components / units the first one is Direct Current (DC) supply and second one is Alternating Current (AC) supply. The power consumption of these electrical units are calculated based on its operating voltage and current ratings as follows:

$$P = 3V_{ph} I_{ph} \cos\phi \qquad \text{(i)}$$

Here V_{ph} is the phase voltage, I_{ph} is the phase current, ϕ is the phase difference and P is the power required by the electrical units.

During integration study of these electrical units / components first we have to calculate the available spare power supply from aircraft side. The calculation of available spare power supply is termed as electrical load analysis. In this study we are listing the power generating sources and power consuming sources. The difference of electrical power generated through power generating sources and power consumed through power consumption sources are the spare power available for new system integration.

This electrical load analysis study needs to be carried out for calculation of both AC and DC power availability.

We must be fully ensure that sufficient amount of spare power (AC or DC) must be available as per new system power consumption requirement.

2.3.2.3 Thermal Load Analysis:

Every electrical unit generates the thermal energy in form of the heat when it operates. These heat load must be properly dissipated through suitable medium. The study of heat load dissipation process is termed as thermal load analysis.

The heat load dissipation technique is known as cooling. There are two means for providing the cooling to electrical aggregates the first one is convection cooling or natural cooling and second one is the forced cooling. The convection cooling is provided by making the suitable air passage around the electrical units so that generated heat can be dissipated through atmospheric air . The forced cooling is made by making the provision for passing of cold air in the closed vicinity of the electrical units. The calculation of mass flow rate of the cold air are carried out as follows:

$$Q_D = mC\Delta T \qquad \text{(ii)}$$

Here m is the mass flow rate of the cold air required for cooling the electrical units, C is the specific heat constant, ΔT denotes the temperature differences between outside and inside the electrical unit. Q_D denotes the dissipated heat energy.

If any electrical unit is operating for t times, then heat generated by that unit will be

$$Q_G = Pt \qquad \text{(iii)}$$

$$Q_G = 3V_{ph}I_{ph}\cos\phi \times t \qquad \text{(iv)}$$

The required amount of cooling will be calculated based on inequality

$$Q_G \le Q_D \qquad \text{(v)}$$

2.3.2.4 Simulation Study:

The simulation study for the electrical unit integration needs to be carried out by using various available software tools such as MATLAB / SIMULINK and LAB VIEW etc. The concept of model based engineering may be utilized in this step [5]. This study provides the initial insights for development of the product.

2.3.2.5 Preparation of Drawings / Documents:

As a part of system integration / modification activity the documentation one of the most important step. In this step we have to prepare and generate the various types of the drawing. In the broad sense the drawings can be categorized as electrical drawings and mechanical drawings. All the drawings must be coordinated with airworthiness regularity authorities.

2.3.2.6 Electrical drawings:

The electrical drawings represents the interconnection of host unit with other systems through which it receives the electrical inputs and provides the outputs.

It can be Single Input Single Output (SISO) , Single Input Multi Output (SIMO),Multi Input Single Output (MISO) or Multi Input Multi Output (MIMO) case. Based on our aircraft industry experience, the electrical drawings can be categorized as schematic circuit diagram and loom connection diagram, some times loom connection table is also prepared on requirement to requirement basis.

a) Schematic Circuit Diagram:

The schematic circuit diagram represents the interconnection of host unit with other associated units in block diagrammatic format.

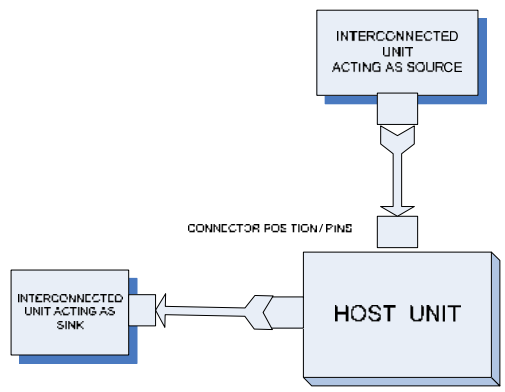

Fig.2. Schematic circuit diagram

It indicate the connector position / pins numbers of host unit which is going to be interconnect with other units (connector / pins). It lags about type of interconnecting wires and its cross-section area.

In general schematic circuit diagram gives the broad idea about interconnected networks. The representation of schematic circuit diagram is provided in Fig. 2.

b) Loom Connection Diagram:

In the loom connection drawings, the details about interconnection are available. Apart from information about interconnection as per schematic diagram it also provides the types of wire used, its cross-section area, nature of shielding / sheathing, wire tag etc. The loom connection diagram is also generally used for troubleshooting purpose. The representation of loom connection diagram is provided in Fig. 3.

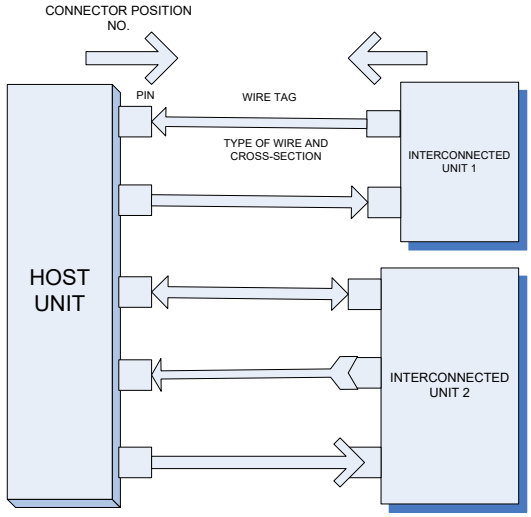

Fig.3. Loom connection diagram

2.3.2.7 Mechanical drawings:

The mechanical drawings are prepared from the installation aspects of the units on the aircraft. After selection of available space for installing the unit , the mechanical drawings are prepared. Both the first angle and third angle projection method can be used for preparation of installation drawings. The tolerance on the dimensions is incorporated as per standard practices. In general two types of mechanical drawings are prepared one for bracket installation drawings and other one is unit installation drawings.

a) Bracket Installation:

Some times for the installation of electrical units the mounting rack or bracket are required. These mounting rack and brackets are the interface between aircraft structure and electrical units. The other parts such as fasteners, washers, mounting screw also needs to be designed and its drawings also need to be developed.

b) Unit / Loom Installation:

Mechanical installation drawings pertaining to unit installation and loom routing also needs to be developed. In these drawings the dimension of the unit with suitable tolerance needs to be specified. The top view and side view drawings of the units are to be prepared. While routing of electrical looms through the aircraft structure appropriated clearance should be made with sharp edges of the structure, moving parts such as control rods and hydraulic / pneumatic pipelines. Keeping these aspects in the mind the loom routing drawings are prepared.

2.3.2.8 Preparation of Test Specifications / Test Schedules:

The test schedule is the document which list out all the necessary checks need to be carried out during system integration activity. It covers all the necessary steps to access the suitability and intactness of various units. The test schedule should be prepared by keeping the airworthiness requirement in the mind. It should cover functional testing of electrical units, continuity checks, megger checks, voltage and current level checks, impedance matching etc. The signal transmission network should be designed so that reflection loss, attenuation loss and transmission loss can be minimized. The test schedule should covers all these testing aspects. The test schedule must be coordinated with airworthiness regularity authorities

2.3.2.9 Design Reviews:

To assess the correctness of the design methodology used for system integration / modifications, the design review committee should be constituted. The committee comprises expert members in design domains. There are generally two types of design review which must be carried out to review the design schemes, the first design review is termed as Preliminary Design Review (PDR) and next one is the Critical Design Review (CDR).

a) Preliminary Design Review (PDR)

Preliminary design review is the first stage of design review which assess the design methodology up to component level inside the systems . Here the type of component used its specification , airworthiness requirement, embedded design, testing schemes , design drawings are reviewed. Keeping all these aspects PDR committee recommend for further improvements in design schemes on the requirement basis.

b) Critical Design Review (CDR)

The improvements in the system integration schemes suggested during PDR needs to be implemented before CDR meeting. In the CDR meeting similar type of committee as PDR are to be constituted with the design domain experts. This committee reviews the design scheme more comprehensively and thoroughly as compared to PDR. The CDR committee has two main objectives, the first one is, to check the implementation of design modifications as suggested by PDR committee and second one is the exhaustively and completely review the design schemes.

2.3.2.10 Lab Level Interconnected Network Testing

After the completion of design reviews the lab level testing of interconnected network are planned. In this stage the set of test equipment are used to assess the design parameters. The interconnected network are

formed as the mimicked version of aircraft layout keeping the loom length and other interconnections as per design drawings and testing are carried out as per test schedule or test procedure documents.

2.3.2.11 Embodiment on Aircraft and Ground Integration Checks

After obtaining the satisfactory test results during lab level testing the next task is embodiment of the electrical aggregates on the aircraft. The associated electrical units are installed on the aircraft and interconnected as per design drawings. The proper securing of electrical units and associated looms must be ensured on the aircraft as per standard practices. The next step after embodiment is ground integration checks. The ground integration checks need to be carried out as per the test schedule / test document duly coordinated by regularity authorities. The ground integration checks generally covers cold checks , Power ON checks, EMI/EMC checks, system checks during Engine Ground Run (EGR), system checks during taxi trials etc.

a) Cold Checks

This checks are to be carried out without POWER ON conditions, this checks generally covers loom continuity checks and Insulation resistance / meager checks.

b) Loom Continuity Checks

To assess the interconnectivity of electrical units the loom continuity checks needs to be carried out. Here as per design drawings we identify any two electrical units. The electrical connectors of both the units are de-mated as per standard technology and by using continuity tester pin to pin continuity of source and destination unit connectors are carried out. As per the standard practice the inter-pin shorting checks within the connector pins also need to be carried out.

c) Insulation / Megger Checks

Insulation cover on the metallic wire is used to provide the protection against short circuit with other metallic parts , protection against shocks, protection from mechanical damage etc. The megger checks are carried out to ensure the intactness of insulation material sheathings on metallic wire strands. This checks are also used to ensure the mechanical damage of insulation material sheathings. This checks are carried out by using the mega ohm meter instrument by applying around 500 V power supply. As per aviation industry requirement, the insulation resistance should be more than 20 Mega Ohm.

d) Power ON System Checks

This test are to be carried out with system POWER ON condition. In this test the electrical power supply to the kept ON during interconnected network testing.

In the supply ON condition for the pre defined time period the functioning of the electrical units in interconnected network should be ensured. This test also calls for measurement of voltage and current values at the connector pins of electrical units of interconnected network.

e) EMI / EMC Checks

EMI/EMC stands for Electro Magnetic Interference /Electro Magnetic Compatibility. This test is to be carried out to ensure the performance of electrical units in interconnected network in the event of any electromagnetic interference or radiation. In the interconnected network the test electrical unit is operated as EMI/EMC source mode and EMI/EMC victim mode. In both of the mode the performance of test unit must be satisfactory.

f) System checks during Engine Ground Run

The interconnected network must be checked during engine running conditions . On the ground engine is started and in supply ON condition the performance of network should be checked as per the test schedule approved by airworthiness regularity authorities.

g) System checks during Taxi Trial

In the taxi run aircraft moves on the ground in forward direction with engine thrust. The rudder control surfaces are operated to turn the aircraft in lateral directions. The interconnected network also needs to be checked in POWER ON conditions during taxi trials.

2.3.2.12 Flight Trials / Tests

After satisfactory ground run and taxi checks these test are to be carried out in the air by test pilot and flight test engineer. The aircraft is maneuvered in various attitude configurations and performance of the network is assessed as per test document.

2.3.2.13 Post Flight Analysis

The flight parameters of the aircraft should be recorded during the flight testing. After downloading the recorded flight parameters it must be analyzed by the experts for any deviation in the performance of the aircraft. The data analysis activity help us to ensure the satisfactory operation of the network during the flight.

2.3.2.14 LMC Ratification

After satisfactory ground and flight test reports a committee is form which is known as Local Modification Committee (LMC). This committee is headed by airworthiness authorities, and comprises design domain

experts. The committee studies the ground and flight test reports and based on discussions the system integration / modification activity are approved.

3. Conclusions

This paper presented a methodology / work experience of the author during electrical system integration activities on the aircraft. All the related aspects starting from feasibility study , types of drawings / documents required, ground and flight testing activity till LMC ratification are covered and briefly explained. In future we have to try to optimally utilize the latest simulation software and new technologies for system integration and modification activities.

4. Acknowledgment

The author want to express his sincere thanks to management of Hindustan Aeronautics Limited Nasik for providing the opportunity to present this work in this conference .

5. References:

[1] Maintenance Manuals / Operating Manuals of the General Aircraft.
[2] System Specifications and Testing procedures of General Purpose Aircraft.
[3] Chambers, J.R., “High-Angle-of-Attack Aerodynamics: Lessons Learned”, AIAA Paper 86-1774, June 1986.
[4] Chambers, J.R., “High-Angle-of-Attack Technology: Progress and Challenges”, NASA CP-3149, vol. 1, May 1992, pp. 1–22.
[5] B.L. Stevens and F.L. Lewis. Aircraft Control and Simulation. John Wiley & Sons, 2003.

6. Biographies

Uttam G Salawade graduated in Electrical Engineering from Shivaji University Kolhapur in 1985. He started his career in AURDC, HAL, Nasik in Oct 1986. Presently, he is HOD of Design Electrical Department, Design Indigenization Department & Central Lab of AURDC and holding a post of Addl. General Manager (Design). He has specialization in electrical & armament systems of fighter aircraft. He has made significant contribution in aircraft upgrade and responsible for several modifications/improvements on fighter aircraft of Russian origin for flight safety, reliability, maintainability, enhancement in operational capability, new/advanced weapon integration etc. He has participated in various pre survey and Court of Inquiry for accident investigations of the aircraft.. He has Presented and Published many Technical Papers at National & International seminars. He is a recipient of SODET Gold award and “R & D award” for his significant contributions in design & development. He is a life member (M-3362) of Aeronautical Society of India and presently holding the post of Honorary Secretary for The Aeronautical Society Of India, Nasik Branch.

Design and Analysis of Parachutes using PARAZ Software

1. Aniket Antre,2. Sumit Jana, 3. Basant Gupta
Zeus Numerix Pvt Ltd, Pune

***Abstract*-- Conventional and RAM air parachutes are widely used in military operations, sports and recreational purposes. Conventional parachutes works as drag producing devices whereas the RAM air parachutes are lifting wings. Paragliders are special type of RAM air parachutes which have high glide ratio. The planform shapes are generally elliptic to minimize induced drag and achieve longer range. These parachutes are primarily used in aero sports. As these parachutes acts as lifting wing, their performance is measured in terms of aerodynamic characteristics i.e. lift and drag coefficients. Selection of appropriate airfoil is important for desired performance as in the case of a fixed wing glider. This paper talks about parametric design methodology and development of parachutes using Zeus Numerix's in-house developed software, ParaZ. The software has a cloud interface, which provides design solutions for different type of parachutes including their manufacturing details, sewing allowance and tolerances. The software also provides a comprehensive interface for FSI simulation. This allows the user to analyze parachutes at conceptual level. Parachutes being a flexible structure, experiences large deformations and loadings till a steady inflated shape is achieved. Finite-volume based RANS solver withK-ε turbulence model is used for simulating air flows. This paper inspects the change in aerodynamic performance by varying certain design parameters likethe leading-edge cut, trailing edge configuration and aspect ratio (AR) of a parachute. The focus of this work is to present the capabilities of the parametric design and analysis tool and its advantages.**

***Keywords*:** Fluid-Structure Interaction, Paraglider, PARAZ, Leading-Edge Cut, Aerodynamic Characteristics

1. INTRODUCTION

Parachutes play an important role in sports, space and military applications. The shape of a conventional parachute is typically like a dome but varies with application. Most of time, different types of payloads are attached like food, medical equipment, people, space capsule, military equipment, transport devices, etc. The development of Ram-Airparachutes isa relatively tedious and time-consumingtask compared to conventional ones.There are many different fabric templates and its stitching timesare large. If any error creeps in the drawings, it can only be detected during stitching stage, leading to alarge delay in correction ofdrawings and re-stitching. Further, there are many options for planform shape, airfoil sections, rib cut-outs, fabric panels etc. Aerodynamic performance prediction of candidate parafoil design is also complex compared to conventional solid/slotted parachutes. For parafoil, accurate prediction of lift and drag with angle of attack is important. Additionally, prediction of accurate shape at different flight conditions is also important, which can be accomplished through FSI simulations.

In-view of the above challenges, a generic parachute design software, PARAZ - is developed. This essentially enablesa user to explore all design options before finalizing the design. Given the required inputs, the software generates a 2D CAD model of the fabric templates and lines in DXF format.It also generates a 3D CAD model thatcan be used for FSI simulations and analysis.

The software currently supports generation of two types of parachutes: (a) round canopy(b) ram-air parachute.Under these two main categories broad design variations are possible based on the input parameters. E.g. a conventional parachute can be flat circular, conical, slotted, skirted etc. A RAM-air parachute can be varied by planform shape (rectangular, elliptic and trapezoidal), volute shape (elliptic, user-defined), airfoil section (using database, user defined), location of suspension and brake lines, leading edge cut length/angle and so on. Both these types of parachute are used for personal and cargo application. The goal of this paper is to describe how easily one can generate and simulate different type of parachutes using PARAZ within a few easy steps. The turn-around time development costs for parachute manufacturing can be considerably reduced. The experimental design and testing are always expensive both in time and cost.Moreover it is often very difficult or impossible to obtain a proper test geometry that can be held in the test section, due to its flexible nature. So, any method which can eliminate the experimental process at least at the initial phase of design will really bring huge benefit for the designers.

Fluid-structure interactions are inherently difficult to simulate because of the unsteady interaction of the flow streamline with the deforming object. The difficulty is even more in case of aninflatable or large deformation object. Large deformations often cause self-intersection or penetrating surface elements. Such a situation compromise the mesh quality and the mesh generationitself which forces the process to terminate. To avoid such occurrence special algorithms like motion-damping, fabric-repulsion etc. are used.In the current study of Ram-air parachute, aerodynamic coefficients of a fully inflated canopy under steady air flow is estimated, to simulate its terminal descent. Satisfactorily lift-to-drag ratio and canopy shape are obtainedthrough the simulation.

2. METHODOLOGY

As a simulation tool PARAZ comprises modules for modeling, preprocessing, simulation and post processing. PARAZ outputs are through standard file formats which can be interfaced by any third party postprocessor for analysis. In the process the software also accommodates few standard open source tool and libraries. The major modules are

- Parametric CAD modeler
- TETGEN, the automatic mesh generator
- ZN-Inflation, the in-house structure dynamics code
- ZN-3DUNS, the in-house fluid dynamics code

The post-processing and visualizations are done in Paraview, an open software environment, versatile with a user-friendly interface. The PARA-Z GUIautomates the different steps of design and simulation of parachute.Complete steps for simulations are shown below.

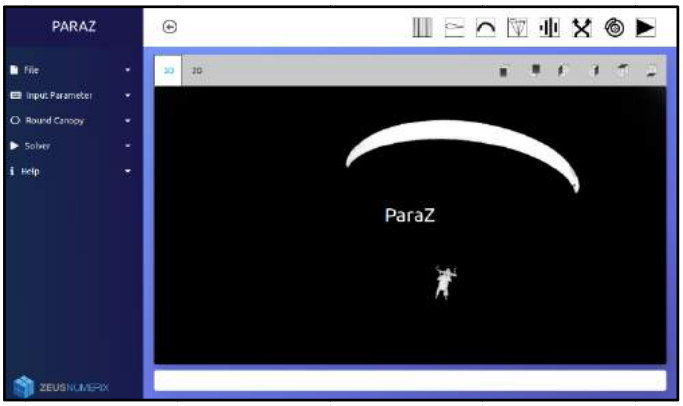

Figure 2-1 PARAZ GUI

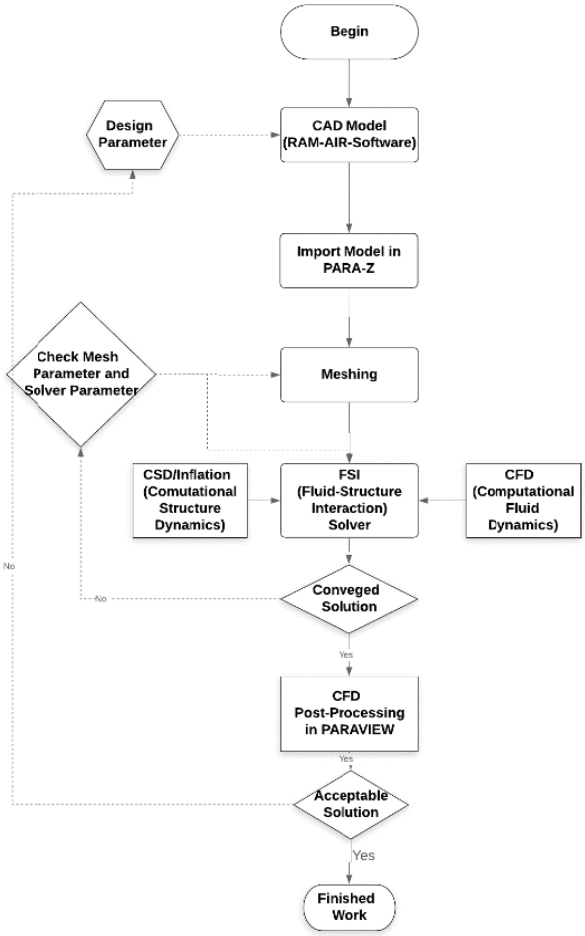

Figure 2-2Working of PARAZ (Flowchart)

- All the modeling inputs for Ram-air parachute come under '*Input Parameter*' label. Sub parameters are *Planform, Airfoil, Volute, Anchor Location, Flat Panels, and Rigging Lines* etc. Based on the values of those parameters the CAD of the parachute is created. The figure 2-2 shows the different input parameter in PARAZ GUI.

Figure 2-3 PARAZ GUI with Input Parameter

- The software generates a 3D CAD model as well as draw the fabric templates and lines in DXF format.
- Once the CAD is exported it is preprocessed through a mesh generator to produce triangulated surface and then a 3D volume mesh with the help of a predefined outer boundary.
- The FSI code are coupled with Computational Fluid Dynamics (CFD) and Computational Structure Dynamics (CSD). These two codes are iterated till a steady converged solution is obtained.

3. Fluid-Structure Coupling

Parachutesbeing a flexible structure, experiences large deformations and loadings till a steady shape is achieved.Realistic and accurate analysis requires sophisticated techniques in Fluid-Structure Interaction (FSI) which includes Computational Fluid Dynamics (CFD) and Computational Structure Dynamics (CSD) code.

The FSI code runs in iterative loops until parachute canopy gets fully inflated. Once the 3-D mesh is generated by theTETGEN code it will be transferred in FSI loop for simulation. Once the mesh is transferred in FSI loop, FSI code starts to calculate the pressure forces on parachute canopy.The pressure forces from CFD are transferred to the inflation code to inflate the flexible fabric canopy.

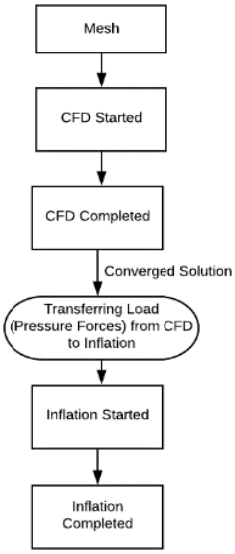

Figure 3-1 FSI Coupling

4. CFD Modelling – ZN3DUNS

The ZN-3DUNS code comprises the set of equations which are Reynolds Average Navier-Stokes coupled with K-ε turbulence model.

Equations:

X-momentum $\rho\frac{\partial u}{\partial t}+\rho u\frac{\partial u}{\partial x}+\rho v\frac{\partial u}{\partial y}=\mu\left(\frac{\partial^2 u}{\partial x^2}+\frac{\partial^2 u}{\partial y^2}\right)-\frac{\partial p}{\partial x}$

Y-momentum $\rho\frac{\partial v}{\partial t}+\rho u\frac{\partial v}{\partial x}+\rho v\frac{\partial v}{\partial y}=\mu\left(\frac{\partial^2 v}{\partial x^2}+\frac{\partial^2 v}{\partial y^2}\right)-\frac{\partial p}{\partial y}$

Z-momentum $\rho\frac{\partial w}{\partial t}+\rho u\frac{\partial w}{\partial x}+\rho v\frac{\partial w}{\partial y}=\mu\left(\frac{\partial^2 w}{\partial x^2}+\frac{\partial^2 w}{\partial y^2}\right)-\frac{\partial p}{\partial z}$

Continuity $\frac{\partial u}{\partial x}+\frac{\partial v}{\partial y}=0$

The equation for conservation of mass for steady flows, in Cartesian tensor form can be written as follows:

$$\frac{\partial}{\partial x_i}(\rho u_i)=S_m$$

Where u_i the velocity component in *i* is direction and ρ is the fluid density. Source term is defined as mass source termS_m.

For steady state flow, Cartesian tensor form of conservation of momentum equation is written as

$$\frac{\partial}{\partial x_j}(\rho u_i u_j)=-\frac{\partial p}{\partial x_i}+\frac{\partial \tau_{ij}}{\partial x_j}+F_i$$

Where p is the static pressure, τ_{ij} is stress tensor $F_i$are body forces which include any model dependent terms such as user defined sources.The stress tensor $\tau_{ij}$is given by

$$\tau_{ij}=\mu\left(\frac{\partial u_i}{\partial x_j}+\frac{\partial u_j}{\partial x_i}\right)-\frac{2}{3}\mu\frac{\partial u_k}{\partial x_k}\delta_{ij}$$

Where μ is dynamic viscosity of fluid and the second term indicates effect of fluid dilatation which is proportional to the divergence of fluid velocity.

5. Ram Air/Conventional Parachute Simulation

The aim of this paper is to define a process to carry out the numerical simulation of a 3D Ram Air/Conventional parachute using PARAZ. In fact, the objective of the simulation is to get the inflated shape of a Ram Air/Conventional parachute and its performances during a stabilized rectilinear flight. The simulation results can then be compared to real in-flight measurements.

5.1 Material Properties:

In order to calculate the parachute deformation, the mechanical properties of the different materials must be defined in the ZN-Inflation code. The various textile materials are modelled by membrane and cable elements, as following:

- Suspension lines = small cords modeled by cable elements;
- driving lines = small cords and semi-brakes modeled by cable elements;
- Various strengthening pieces = ribbons modeled by cable elements;
- Risers = ribbons modeled by cable elements.

The material properties needed by the PARAZ are as follow:

- Fabric:
  - Elasticity
  - Thickness
  - Poisson's Ratio
- Reinforcement and Suspension lines:
  - Elasticity
  - Section area
  - Density
  - Poisson's Ratio

6. Results

The drag, lift and side force coefficients as well as the yawing, pitching and rolling moment coefficients can obtain from FSI simulation. All the cases shown below are simulated for the velocity 25 m/sec. The contour plot shown below, defines the minimum and maximum Pressure Difference on parachute surface.

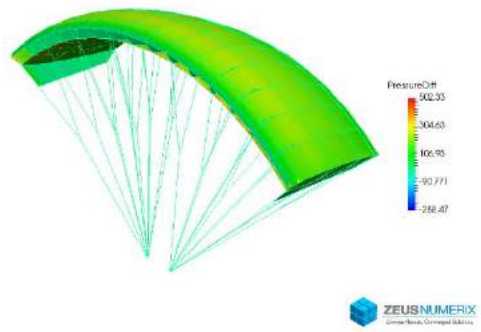

(a)

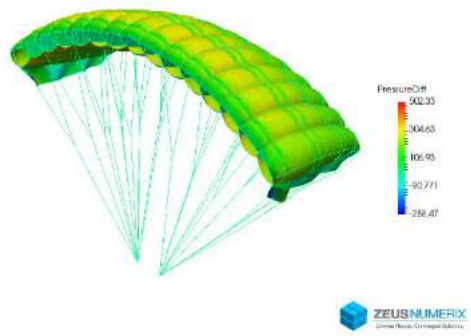

(b)

Figure (a) and (b) are representing initial and fully inflated Rectangular RAM-AIR Parachute.

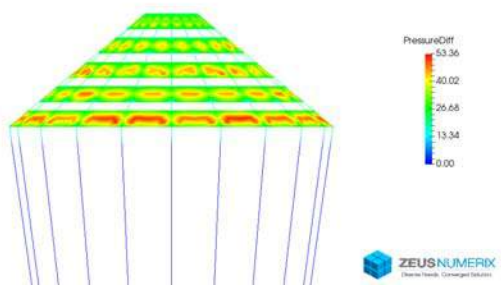

(c)

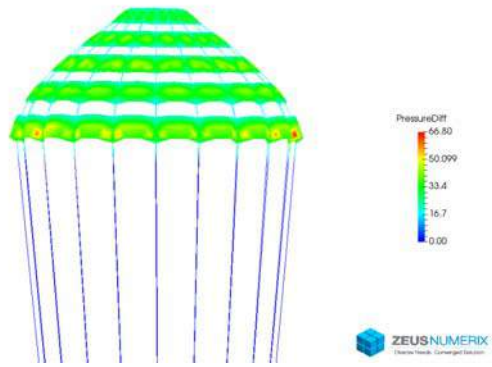

(d)

Figure (c) and (d) are representing initial and final shape of fully inflated Slotted Conical Parachute.

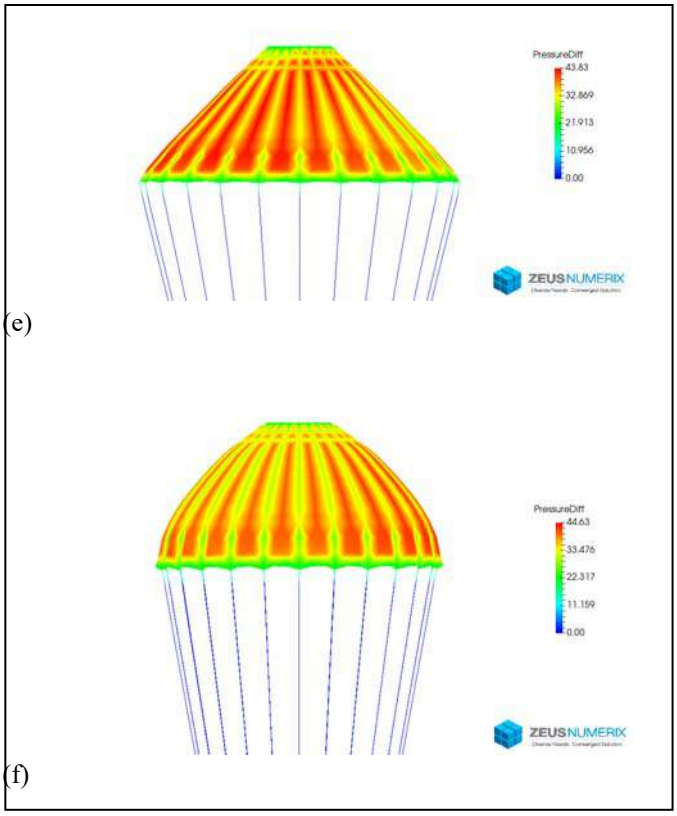

Figure (e) and (f) are representing initial and final shape of fully inflated Solid Conical Parachute.

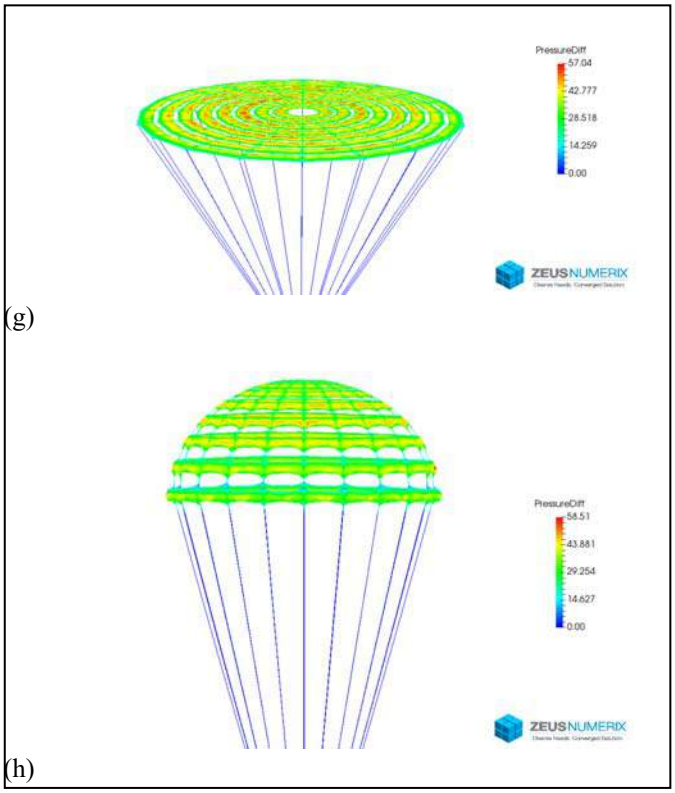

Figure (g) and (h) are representing initial and final shape of fully inflated Slotted Circular Parachute.

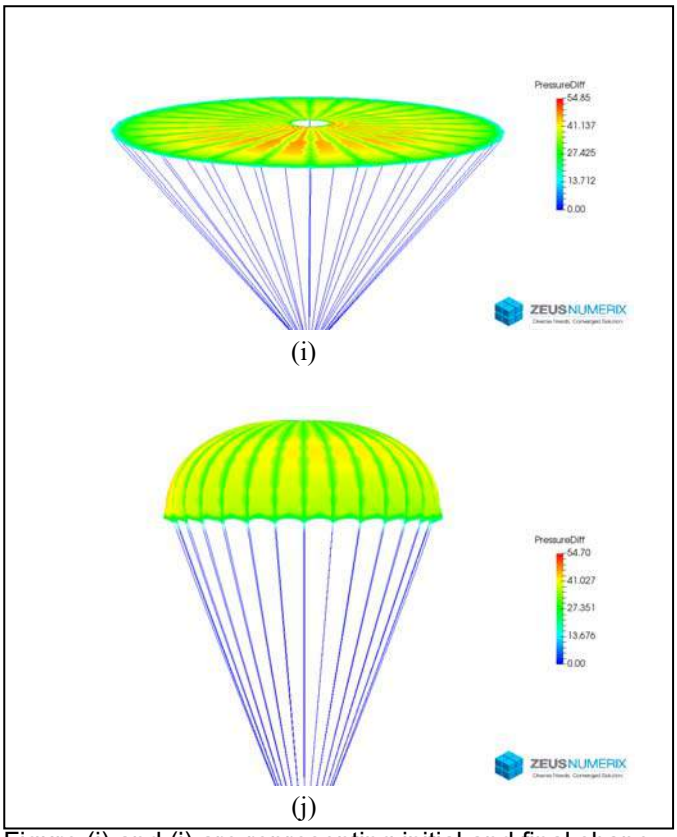

Figure (i) and (j) are representing initial and final shape of fully inflated Solid Circular Parachute.

7. Conclusion

PARAZ has been tested for different types and sizes of parachutes. The software is customized for parachutes as it runs several different solvers synchronously in the background and produces the final canopy shape, its aerodynamic characteristics and stresses. It is quite a simplified approach to a complex problem.This enables one to design a parachute without having to delve into the complexity of modeling, meshing and CAE analysis.

PARAZalso has a cloud interface, which can be used by anyone who wants to design his or her own customized parachutes. Its simulation interface can also be used to simulate and analyze the performance of the parachute. This also provides manufacturing drawings as output which can directly be used for fabricating the parachutes.

8. References

[1] Fogell, K. Bergeron, “Fluid-Structure Interaction Simulations of the Inflated Shape and Associated Flow field of the MC4/5 Parafoil during Steady Gliding flight”, 24th AIAA Aerodynamic Decelerator Systems Technology Conference, 5-9 June 2017.

[2] Ghoreyshi, Bergeron, Jirásek, Seidel, house, and Cummings, “Computational aerodynamic modeling for flight dynamics

simulation of ram-air parachute", Aerospace Science and Technology, 22 April 2016.

[3] Eslambolchi, Johari, "Simulation of Flow field around a Ram-Air Personnel Parachute Canopy", AIAA Aerodynamic Decelerator Systems (ADS) Conference, 25-28 March 2013.

[4] Fogell, Sherwin, Cotter, Pope, Iannucci, and Palacios, "Fluid-Structure Interaction Simulation of the Inflated Shape of Ram-Air Parachutes", Aerodynamic Decelerator Systems Technology Conferences, 25-28 March 2013.

[5] Kalro, Tayfun, Tezduyar, "A parallel 3D computational method for fluid-structure interactions in parachute systems", Compute. Methods Appl. Mech. Engg., 26 August 1999.